

Spring 2023

# Expanding Tailorable Nanomaterial Synthesis With Persistent Micelle Templates

Eric R. Williams

Follow this and additional works at: <https://scholarcommons.sc.edu/etd>



Part of the [Chemistry Commons](#)

---

## Recommended Citation

Williams, E. R. (2023). *Expanding Tailorable Nanomaterial Synthesis With Persistent Micelle Templates*. (Doctoral dissertation). Retrieved from <https://scholarcommons.sc.edu/etd/7235>

This Open Access Dissertation is brought to you by Scholar Commons. It has been accepted for inclusion in Theses and Dissertations by an authorized administrator of Scholar Commons. For more information, please contact [digres@mailbox.sc.edu](mailto:digres@mailbox.sc.edu).

EXPANDING TAILORABLE NANOMATERIAL SYNTHESIS WITH  
PERSISTENT MICELLE TEMPLATES

by

Eric R. Williams

Bachelor of Science  
University of North Florida, 2018

---

Submitted in Partial Fulfillment of the Requirements

For the Degree of Doctor of Philosophy in

Chemistry

College of Arts and Sciences

University of South Carolina

2023

Accepted by:

Morgan Stefik, Major Professor

Andrew B. Greytak, Committee Member

Brian C. Benicewicz, Committee Member

Jochen Lauterbach, Committee Member

Cheryl L. Addy, Interim Vice Provost and Dean of the Graduate School

© Copyright by Eric R. Williams, 2023  
All rights reserved.

## DEDICATION

To my family and friends

## ACKNOWLEDGEMENTS

I would first like to express my most sincere gratitude to my research advisor, Dr. Morgan Stefik. This thesis would simply not be possible without his mentorship over the last few years. Throughout my graduate career, he has not only supported me and my research in more ways than can be mentioned here, but he has also taught me how to think like a professional scientist – and for that I am beyond grateful. I also acknowledge the support and guidance provided by the members of my committee – Drs. Andrew B. Greytak, Brian C. Benicewicz, and Jochen Lauterbach. The track of my research progress and development as a scientist were improved by their contributions along the way. The friends inside and outside of my research group have also proven invaluable to me. Within my group: Taylor Larison, Dr. Wessel van den Bergh, Dr. Ben Lamm, Dr. Kayla Lantz, and Dr. Zachary Marsh along with more junior graduate students: Coby Collins, Sean Wechsler, C.J. Sturgill, Mengxue Zhang and undergraduate students Christian Ruff, Paige McMahon, Natalie Vest, and Mason Wright. Outside my group: Richard Ly, Dallas Abraham, Ethan Older, Eric Ruzicka, Caroline Rohlfing, Shaya Bension, Ian Baxter, and Luís Ramos. You all have contributed scientifically and non-scientifically in more ways than you know.

## ABSTRACT

The control of block polymer micelle dimensions while in solution is critical for a range of emerging applications in diverse fields from drug delivery and nanoreactors to use as sacrificial templates for porous nanomaterials. When under kinetic control, micelles will maintain a constant average size and thus aggregation number ( $N_{agg}$ ) through the suppression of chain exchange mechanisms. Such kinetic control effectively enables the decoupling of micelle dimensions from solution conditions. In other words, kinetically trapped micelles can resist reorganizations brought about by e.g., the addition of metal nanoparticles. However, such micelles are traditionally governed by a fickle  $\chi N$  activation energy barrier that is itself deeply dependent on solvent composition, temperature etc., with minute changes in any of these often resulting in the loss of kinetic control.

These challenges, however, can be resolved with an immobilized (glassy) core-forming segment. Here, the mechanism of kinetic control is now a function of core immobility as opposed to solvent composition. Such mechanisms are particularly useful for challenging chemistries which can e.g., involve slow cross-linking materials chemistries, protracted solvent evaporation, a critical transition from a solvent-rich to a material-rich environment, which could otherwise lead to losses in entrapment with analogous  $\chi N$  systems. To counter such shortcomings with  $\chi N$  control, glassy micelles were recently introduced to extend independent nanoscale tunability to the most challenging materials processing routes. Here, their wide tolerance for solution conditions

and extraordinary benchtop stability following the removal of all plasticizing solvents was found to make such micelles ideal candidates for a wide variety of applications. Furthermore, such micelles were also found to be receptive to swelling with core block homopolymer to affect an increase in micelle core dimension. This ultimately enables the faceted tunability of all material dimensions as both the walls and materials of the final material are independently tunable through the addition of material precursors and core block homopolymer, respectively.

## TABLE OF CONTENTS

DEDICATION .....	III
ACKNOWLEDGEMENTS .....	IV
ABSTRACT .....	V
LIST OF FIGURES .....	IX
LIST OF TABLES .....	XII
LIST OF SCHEMES .....	XIII
CHAPTER 1: OBJECTIVES AND INTRODUCTION.....	1
1.1 RESEARCH OBJECTIVES .....	2
1.2 DISSERTATION OUTLINE.....	3
1.3 REFERENCES.....	6
CHAPTER 2: TAILORED POROUS CARBONS ENABLED BY PERSISTENT MICELLES WITH GLASSY CORES .....	8
2.1 ABSTRACT.....	9
2.2 INTRODUCTION .....	10
2.3 EXPERIMENTAL METHODS .....	13
2.4 RESULTS AND DISCUSSION.....	21
2.5 CONCLUSIONS.....	43
2.6 REFERENCES .....	45
CHAPTER 3: UNIMER SUPPRESSION ENABLES SUPERSATURATED HOMOPOLYMER SWOLLEN MICELLE STATES WITH LONG-TERM STABILITY AFTER GLASSY ENTRAPMENT.....	51
3.1 ABSTRACT.....	52
3.2 INTRODUCTION .....	52
3.3 EXPERIMENTAL METHODS .....	55
3.4 RESULTS AND DISCUSSION.....	61
3.5 CONCLUSIONS.....	78
3.6 REFERENCES .....	78
CHAPTER 4: HIGH- $\chi$ , LOW- $N$ MICELLES FROM PARTIALLY PERFLUORINATED BLOCK POLYMERS .....	83
4.1 ABSTRACT.....	84
4.2 INTRODUCTION .....	84
4.3 EXPERIMENTAL METHODS .....	89
4.4 RESULTS AND DISCUSSION.....	95
4.5 CONCLUSION.....	115
4.6 REFERENCES .....	116
CHAPTER 5: SUMMARY AND SUGGESTIONS FOR FUTURE WORK .....	126
5.1 SUMMARY.....	127
5.2 SUGGESTIONS FOR FUTURE WORK.....	129
5.3 REFERENCES .....	129
APPENDIX A: CHAPTER 2 SUPPORTING INFORMATION .....	131

APPENDIX B: CHAPTER 3 SUPPORTING INFORMATION .....	141
APPENDIX C: CHAPTER 4 SUPPORTING INFORMATION .....	151

## LIST OF FIGURES

<p>FIGURE 2. 1 – SAXS (A) AND TEM (B) DATA FROM THE REPRESENTATIVE SAMPLES OS1-ETOH-1.00 AFTER CARBONIZATION. THE INSET 2D SAXS PATTERN HAS A COLOR SCALE CORRESPONDING TO THE LOG OF X-RAY INTENSITY. THE MOMENTUM TRANSFER <math>Q = 4\pi \sin(\theta)/\lambda</math>, WHERE <math>2\theta</math> REFERS TO THE TOTAL SCATTERING ANGLE AND <math>\lambda</math> IS THE WAVELENGTH. THE BRIGHT FIELD TEM IMAGE SHOWS THE LOCATION OF CARBON (DARK) AND POROSITY (LIGHT).....</p>	21
<p>FIGURE 2. 2 – SAMPLES THAT FAIL TO EXHIBIT PMT BEHAVIOR ENABLED THE REALIZATION OF DESIGN GUIDELINES FOR GLASSY-PMT. THE PMT MODEL PREDICTS LATTICE EXPANSION WITH INCREASING MATERIAL:TEMPLATE RATIO THAT FOLLOWS A QUASI-STRAIGHT-LINE (DASHED LINE) WITH A SLOPE OF 1/3 WHEN PLOTTED IN A LOG-LOG COORDINATE SPACE (A, C, AND E) OR ALTERNATIVELY A LINE WITH A QUASI-CUBE-ROOT DEPENDENCE (DASHED LINE) WHEN PLOTTED IN A LINEAR-LINEAR COORDINATE SPACE (B, D, AND F). TRENDS IN D-SPACING DERIVED FROM SAXS PEAK POSITIONS ARE SHOWN FOR SAMPLE SERIES F127-ETOH (A AND B), OS1-THF (C AND D), AND OS2-ETOH (E AND F). THESE DATASETS ARE INCONSISTENT WITH PERSISTENT MICELLE BEHAVIOR. ....</p>	26
<p>FIGURE 2. 3 – SCHEMATIC REPRESENTATION OF GLASSY-PMT PREPARATION WITH THE POLYMER OS1. DLS AFTER POLYMER DISSOLUTION IN A GOOD SOLVENT, THF (A), REVEALS UNIMERS IN SOLUTION. POOR-SOLVENTS ARE NEXT ADDED WHERE FIRST WATER INDUCES MICELLIZATION (B) BEFORE A LARGE EXCESS OF ETOH IS ADDED (C). THE THF IS THEN REMOVED BY ROTARY EVAPORATION TO YIELD MICELLES THAT ARE DISPERSED IN PURELY POOR SOLVENTS FOR THE CORE BLOCK (D). DLS DATA (E) SHOW THE HYDRODYNAMIC DIAMETER AT EACH STAGE OF PROCESSING. ....</p>	32
<p>FIGURE 2. 4 – TEM IMAGE OF OS1-ETOH MICELLES (A) AND THE ASSOCIATED MICELLE CORE SIZE DISTRIBUTION (B). THE MEAN DIAMETER AND STANDARD-ERROR-OF-THE-MEAN OF THE MEASURED CORES ARE 18.68 AND 0.22 NM, RESPECTIVELY. THE PEO CORONA WAS SELECTIVELY STAINED WITH 1 WT% URANYL ACETATE FOR CONTRAST (DARK) RELATIVE TO THE UNSTAINED PS (LIGHT). ....</p>	33
<p>FIGURE 2. 5 – SAXS OF AS-MADE OS1-ETOH SAMPLES WITH INCREASING MATERIAL:TEMPLATE RATIO. THE SHIFT IN PEAK POSITION TO DECREASING Q-VALUES CORRESPONDS TO AN INCREASE IN D-SPACING (<math>2\pi/Q</math>). THE DATA WERE OFFSET VERTICALLY FOR CLARITY.....</p>	34
<p>FIGURE 2. 6 – TEM IMAGES OF AGED SAMPLES FROM THE SERIES OS1-ETOH WITH MATERIAL:TEMPLATE RATIOS OF 0.85 (A), 0.95 (B), 1.00 (C), 1.05 (D), 1.10 (E), 1.20 (F). SAMPLES WERE STAINED WITH 1 WT% URANYL ACETATE TO IMPROVE CONTRAST. ....</p>	35
<p>FIGURE 2. 7 – ANALYSIS OF SAMPLES FROM SERIES OS1-ETOH BEFORE CARBONIZATION. THE TRENDS IN SAXS PEAK POSITION WERE EXAMINED USING THE SAME LOG-LOG (A) AND LINEAR-LINEAR (B) PLOTS AS BEFORE. THE REGION CONSISTENT WITH PMT LATTICE EXPANSION WAS IDENTIFIED (A) AND USED TO DERIVE A BEST-FIT TO THE MCT MODEL (B). THE AVERAGE PORE SIZE (C) AND WALL THICKNESS (D) WERE CALCULATED USING THE BEST-FIT MODEL AND WERE COMPARED TO THE DIMENSIONS DETERMINED BY DIRECT MEASUREMENTS FROM TEM IMAGES. THE SAXS AND TEM DATA WERE FROM AGED SAMPLES.....</p>	36
<p>FIGURE 2. 8 – SAXS OF CARBONIZED OS1-ETOH SAMPLES WITH INCREASING MATERIAL:TEMPLATE RATIO. THE SHIFT IN PEAK POSITIONS TO LOWER Q-VALUES CORRESPONDS TO AN INCREASE IN D-SPACING (<math>2\pi/Q</math>). THE DATA WERE OFFSET VERTICALLY FOR CLARITY.....</p>	38
<p>FIGURE 2. 9 – TEM OF CARBONIZED SAMPLES FROM THE SERIES OS1-ETOH WITH MATERIAL:TEMPLATE RATIOS OF 0.75 (A), 0.85 (B), 0.95 (C), 1.00 (D), 1.15 (E), AND 1.30 (F).....</p>	39
<p>FIGURE 2. 10 – NITROGEN PHYSISORPTION ISOTHERMS FOR SELECTED SAMPLES FROM THE SERIES OS1-ETOH (A) ALONG WITH THE CORRESPONDING BJH PORE SIZE ANALYSIS FROM THE ADSORPTION BRANCH OF THE ISOTHERM (B).....</p>	40
<p>FIGURE 2. 11 – ANALYSIS OF SAMPLES FROM SERIES OS1-ETOH FOLLOWING CARBONIZATION. THE TRENDS IN SAXS PEAK POSITION WERE EXAMINED USING THE SAME LOG-LOG (A) AND LINEAR-LINEAR (B)</p>	

PLOTS AS BEFORE. THE SLOPE OF DATA IN THE LOG–LOG COORDINATE SPACE IS 0.43 INSTEAD OF THE PREDICTED 1/3. THE BOUNDS OF THE AS-MADE PMT WINDOW ARE DENOTED WITH VERTICAL DASHED LINES. THE AVERAGE PORE SIZE (C) AND WALL THICKNESS (D) WERE CALCULATED USING THE BEST-FIT MODEL AND WERE COMPARED TO THE DIMENSIONS DETERMINED BY DIRECT MEASUREMENT FROM TEM IMAGES. .... 42

- FIGURE 3. 1 – DLS DATA DURING **OS** DISPERSION IN NON-SELECTIVE SOLVENT (PURE DCM) AND GRADUAL **OS** MICELLIZATION THROUGH THE ADDITION OF SELECTIVE SOLVENT (EtOH). FINALLY, SELECTIVE DISTILLATION RESULTED IN GLASSY-CORE MICELLES DISPERSED IN A PURELY SELECTIVE SOLVENT (PURE EtOH). THE VOLUME FRACTION OF EtOH IS GIVEN WITH RESPECT TO THE TOTAL SOLUTION VOLUME. THE PLOTS WERE OFFSET VERTICALLY FOR CLARITY. ....63
- FIGURE 3. 2 – REPRESENTATIVE SAXS AND TEM DATA FOR **OS** MICELLES IN PURE EtOH. THE 2D SAXS PATTERN (INSET, LOG(INTENSITY) COLOR SCALE) WAS RADIALLY INTEGRATED TO YIELD THE REDUCED PLOT WHICH WAS FITTED WITH A MICELLE FORM FACTOR MODEL (A). THE TEM MICROGRAPH OF **OS** MICELLES AFTER STAINING WITH 1% URANYL ACETATE TO ENHANCE THE CONTRAST BETWEEN PS (LIGHT) AND PEO (DARK) (B). ....64
- FIGURE 3. 3 – SCATTERING CURVES (A, C, E, G, I, K) FOR PURE **OS** MICELLES AS COMPARED TO THOSE WITH 40 WT% **hPS** (**OS-40hPS**) WERE MEASURED WITH DIFFERENT EtOH/DCM COMPOSITIONS FOR THE **OS** SOLUTION. FORM FACTOR ANALYSIS USING A SINGLE GAUSSIAN SIZE DISTRIBUTION (DASHED LINES) LED TO ILLOGICAL INTERPRETATIONS (E.G., MICELLES SHRINKING IN THE PRESENCE OF **hPS**). THUS, ADDITIONAL MONTE CARLO FITTING WAS USED TO REVEAL ADDITIONAL SMALLER SIZE CLUSTERS (B, D, F, H, J, L). THE ERROR BARS CORRESPOND TO UNCERTAINTY OF THE Y-VALUES. ....69
- FIGURE 3. 4 – SAXS AND TEM FOR **OS** MICELLES WITH INCREASING HOMOPOLYMER LOADING. SAXS CURVES (A) WERE FITTED TO DERIVE THE CORE DIAMETER DISTRIBUTIONS (B). TEM IMAGES FOR **OS** (C), **OS-60hPS** (D), **OS-80hPS** (E), **OS-100hPS** (F), **OS-140hPS** (G), AND **OS-180hPS** (H) ARE SHOWN WITH 1 WT% URANYL ACETATE STAIN TO IMPROVE CONTRAST. THE CORE DIAMETER DISTRIBUTIONS FROM THESE TEM DATA ARE ALSO PRESENTED ALONGSIDE THE SAXS FIT VALUES (B). SAXS PLOTS WERE OFFSET VERTICALLY FOR CLARITY. THE TEM BACKGROUND VARIED FROM DARK TO LIGHT DEPENDING ON THE AMOUNT OF UNBOUND STAINING AGENT PRESENT AFTER DRYING. THE DASHED LINE IN (B) IS BASED UPON EQ. B8 WHERE CONSTANT INTERFACIAL **OS** CHAIN DENSITY LEADS TO A LINEAR SWOLLEN MICELLE SIZE TRAJECTORY AS A FUNCTION OF **hPS** LOADING.....72
- FIGURE 3. 5 – SAXS DATA AND BEST-FITS FOR **OS** AND **OS-100hPS** MICELLE STOCKS MEASURED BOTH SEPARATELY AND AFTER COMBINATION IN PURE EtOH TO YIELD A BIMODAL DISTRIBUTION (A). THE MIXTURE WAS THEN MEASURED AGAIN AFTER THE ADDITION OF 30 VOL% DCM WITH STIRRING FOR 1.5 HRS TO YIELD A NEW EQUILIBRATED SIZE DISTRIBUTION (B). VALUES ARE PRESENTED IN  $IQ^4$  VS.  $Q$  COORDINATE SPACES TO HIGHLIGHT SMALL CHANGES IN MICELLE FORM FACTOR OSCILLATIONS. ....73
- FIGURE 3. 6 – THE SWOLLEN MICELLE AGGREGATION NUMBERS ( $N_{AGG}$ ) WERE CALCULATED USING EQUATION B.5 FOR VARYING EXTENTS OF SWELLING (A). THE INTERFACIAL AREA PER **OS** CHAIN WAS FOUND TO PLATEAU AT HIGH **hPS** LOADINGS, SUGGESTING A CRITICAL INTERFACIAL **OS** CHAIN DENSITY (B). THIS PLATEAU DENSITY (AVERAGE VALUE FOR 50–180 WT% **hPS**, B DASHED LINE) LED TO AN ANTICIPATED PARABOLIC SWELLING TRAJECTORY FOR  $N_{AGG}$  BASED ON EQUATION B.10 (A DASHED LINE). ERROR BARS CORRESPOND TO THE PROPAGATED UNCERTAINTY FROM A COMBINATION OF TEM AND SAXS MEASUREMENTS. ....74
- FIGURE 3. 7 – SAXS DATA OF (SWOLLEN) GLASSY-CORE MICELLES AS-MADE AND AFTER A 6-MONTH QUIESCENT PERIOD (6 MOS.) (A). THE BEST-FIT AVERAGE CORE DIAMETERS WERE COMPARED, INCLUDING THE ERROR OF THE FIT VALUES (B). SAXS DATA WERE OFFSET VERTICALLY FOR CLARITY. ....77
- FIGURE 3. 8 – SAXS OF AS-MADE CARBON MATERIALS TEMPLATED USING **OS** (A) AND **OS-80hPS** MICELLES (C). THE CORRESPONDING D-SPACINGS WERE COMPARED TO MODEL PREDICTIONS FOR PERSISTENT MICELLES (PMT MODEL) AS A FUNCTION OF THE MATERIAL : TEMPLATE RATIO (B, D). SAXS PLOTS ARE OFFSET VERTICALLY FOR CLARITY. ....78

FIGURE 4. 1 – DLS INTENSITY DATA FOR MICELLE SOLUTIONS $O_{45}F_{11}$ AND $O_{45}F_8$ IN MeOH (AQ) WITH 1.4 VOL% HCL. THE DATA WERE OBTAINED AT A CONCENTRATION OF $10 \text{ MG mL}^{-1}$ .	97
FIGURE 4. 2 – ABSOLUTE INTENSITY SAXS DATA FOR MICELLE SOLUTIONS $O_{45}F_{11}$ (A) AND $O_{45}F_8$ (B) IN MeOH (AQ) WITH 1.4 VOL% HCL. THE DATA WERE OBTAINED AT A POLYMER CONCENTRATION OF $10 \text{ MG mL}^{-1}$ . SOLID LINES CORRESPOND TO THE MODEL BEST-FITS.	101
FIGURE 4. 3 – REPRESENTATIVE DATA FOR SAMPLE $O_{45}F_{11}$ -1.00. THE INTEGRATED SAXS PATTERN IS SHOWN IN (A) WITH THE 2D PATTERN INSET. THE COLOR SCALE CORRESPONDS TO THE LOG-SCALE OF X-RAY SCATTERING INTENSITY. THE SEM IMAGE (B) HAS LIGHT AREAS CORRESPONDING TO TITANIA WITH THE DARK AREAS CORRESPONDING TO THE FORMER LOCATION OF THE MICELLE CORES (PORES) WITH THE FFT INSET.	103
FIGURE 4. 4 – ANALYSIS OF FILMS FROM THE $O_{45}F_{11}$ THIN FILM SERIES FEATURING INCREASING MATERIAL-TO-TEMPLATE (M:T) RATIO. THE MONOTONIC LEFTWARD SHIFT OF THE SAXS FIRST-PEAK POSITION IN (A) INDICATES LATTICE EXPANSION WITH INCREASING D-SPACINGS ( $D = 2\pi/Q$ ). THE LATTICE EXPANSION WAS QUANTITATIVELY CONSISTENT WITH THE PMT MODEL, SUGGESTING CONSTANT TEMPLATE/PORE DIAMETER (B). THE SAXS DATA WERE OFFSET VERTICALLY FOR CLARITY.	105
FIGURE 4. 5 – SEM IMAGES FOR A SAMPLE SERIES PREPARED USING $O_{45}F_{11}$ MICELLE TEMPLATES. THE IMAGES ARE ARRANGED IN ORDER OF INCREASING MATERIAL-TO-TEMPLATE RATIOS: (A) 1.0, (B) 1.5, (C) 2.0, (D) 2.5, (E) 3.0, (F) 3.5, (G) 4.0, (H) 4.5, (I) 5.0, (J) 6.0.	106
FIGURE 4. 6 – THE AVERAGE TEMPLATE/PORE DIAMETER (A) AND WALL THICKNESS (B) FOR $O_{45}F_{11}$ THIN FILMS WERE DETERMINED FROM HUNDREDS OF MEASUREMENTS ON SEM IMAGES AND WERE COMPARED WITH A BEST-FIT OF THE PMT MODEL (DASHED LINE). ADDITIONALLY, THESE METRICS WERE CALCULATED FROM SAXS D-SPACING BASED UPON THE BEST-FIT OF THE PMT MODEL. THE AGREEMENT OF MEASURED VALUES WITH THE PMT MODEL IS CONSISTENT WITH CONSTANT MICELLE CORE SIZE. ERROR BARS CORRESPOND TO THE STANDARD-ERROR-OF-THE-MEAN.	106
FIGURE 4. 7 – SAXS PATTERNS FOR $O_{45}F_8$ THIN FILM SERIES (A) DID NOT EXHIBIT THE EXPECTED MONOTONIC TREND IN PEAK SHIFT (DATA OFFSET VERTICALLY FOR CLARITY). THE CORRESPONDING PEAK D-SPACINGS WERE NOT CONSISTENT WITH THE PMT MODEL, SUGGESTING ACTIVE CHAIN EXCHANGE (B).	108
FIGURE 4. 8 – SAXS PATTERNS FOR A BULK CAST SERIES FROM $O_{45}F_{11}$ MICELLES. THE MONOTONIC LEFTWARD SHIFT IN Q-SPACE (A) INDICATES LATTICE EXPANSION WITH INCREASING MATERIAL-TO-TEMPLATE RATIO (OFFSET VERTICALLY FOR CLARITY). THE LATTICE EXPANSION WAS QUANTITATIVELY CONSISTENT WITH THE PMT MODEL (B), SUGGESTING CONSTANT MICELLE CORE SIZE.	111
FIGURE 4. 9 – SEM IMAGES OF BULK TITANIA SAMPLES PREPARED BY CASTING $O_{45}F_{11}$ MICELLE TEMPLATES WITH MATERIAL PRECURSORS. THE IMAGES ARE ARRANGED IN ORDER OF INCREASING MATERIAL-TO-TEMPLATE RATIOS: 1.50 (A AND E), 3.00 (B AND F), 3.50 (C AND G), 4.00 (D AND H).	111
FIGURE 4. 10 – THE AVERAGE TEMPLATE/PORE DIAMETERS (A) AND WALL THICKNESSES (B) WERE DETERMINED USING MEASUREMENTS ON SEM IMAGES. ADDITIONALLY, THESE METRICS WERE CALCULATED FROM SAXS D-SPACING BASED ON THE PMT MODEL USING BEST-FIT PARAMETERS. THE AGREEMENT OF MEASURED VALUES WITH THE PMT MODEL IS CONSISTENT WITH CONSTANT MICELLE CORE SIZE. ERROR BARS CORRESPOND TO THE STANDARD-ERROR-OF-THE-MEAN.	112

## LIST OF TABLES

TABLE 2. 1 – CHARACTERISTICS OF THE PS POLYMERS USED.....	28
TABLE 2. 2 – EXAMPLE SAMPLE RECIPES FOR SERIES OS1-THF WITH INCREASING M:T RATIOS.....	28
TABLE 2. 3 – PMT MODEL PARAMETERS FOR ALL SAMPLE SERIES.....	38
TABLE 2. 4 – NITROGEN PHYSISORPTION ISOTHERMS FOR SELECT SAMPLES FROM SERIES OS1-ETOH (A) ALONG WITH THE CORRESPONDING BJH PORE SIZE ANALYSIS FROM THE ADSORPTION BRANCH OF THE ISOTHERM (B).....	40
TABLE 2. 5 – MEASUREMENTS FROM SERIES OS1-ETOH AFTER CARBONIZATION .....	41
TABLE 3. 1 – MICELLE SIZE METRICS FROM ANALYSIS OF SAXS DATA FOR THE SWOLLEN <b>OS-hPS</b> MICELLES AS A FUNCTION OF STORAGE TIME. ....	77

## LIST OF SCHEMES

- SCHEME 2. 1 – CARBON PRECURSORS ARE COMBINED WITH MICELLES IN SOLUTION WHERE BOTH PHASES SEPARATE FROM THE SOLVENT AS THE CARBON-RICH BOTTOM LAYER (A) AND THE CARBON PRECURSORS (GREEN CIRCLES) SELECTIVELY ASSOCIATE WITH THE PEO CORONA BLOCK (BLUE SEGMENT) OF THE BLOCK POLYMER MICELLES (B). A CONTINUOUS SOLID IS PRODUCED AS THESE DECORATED MICELLES PACK TOGETHER WHILE PRESERVING THE TEMPLATE AND MATERIAL VOLUME FRACTIONS (C). WITH PERSISTENT MICELLE TEMPLATES, THE AVERAGE TEMPLATE SIZE IS CONSTANT, AND THE ADDITION OF FURTHER MATERIAL INCREASES THE WALL THICKNESS VIA LATTICE EXPANSION. THESE AS-MADE SAMPLES ARE SUBSEQUENTLY AGED AND CARBONIZED TO CONVERT THE CARBON PRECURSORS INTO AMORPHOUS CARBON WHILE REMOVING THE POLYMER TEMPLATE TO PRODUCE POROSITY (D). .....23
- SCHEME 2. 2 – CARBON PRECURSORS ARE COMBINED WITH MICELLES IN SOLUTION WHERE BOTH PHASES SEPARATE FROM THE SOLVENT AS A CARBON-RICH BOTTOM LAYER (A) AND THE CARBON PRECURSORS (GREEN CIRCLES) SELECTIVELY ASSOCIATE WITH THE PEO CORONA BLOCKS (BLUE SEGMENT) OF THE BLOCK POLYMER MICELLES (B). A CONTINUOUS SOLID IS PRODUCED AS THESE DECORATED MICELLES PACK TOGETHER WHILE PRESERVING THE TEMPLATE AND MATERIAL VOLUME FRACTIONS (C). WITH PERSISTENT MICELLE TEMPLATES THE AVERAGE TEMPLATE SIZE IS CONSTANT, AND THE ADDITION OF FURTHER MATERIAL INCREASES THE WALL THICKNESS VIA LATTICE EXPANSION. THESE AS-MADE SAMPLES ARE SUBSEQUENTLY AGED AND CARBONIZED TO CONVERT THE CARBON PRECURSORS INTO AMORPHOUS CARBON WHILE REMOVING THE POLYMER TEMPLATE TO PRODUCE POROSITY (D). .....25
- SCHEME 3. 1 – A STOCK SOLUTION OF **hPS** IS ADDED DROPWISE TO AN **OS** MICELLE SOLUTION (LEFT). THE **OS** UNIMER CONCENTRATION DEPENDS UPON THE AMOUNT OF SELECTIVE SOLVENT (TOP PANEL) AND DETERMINES THE OUTCOME FROM THE HOMOPOLYMER ADDITION (MIDDLE PANEL) AS WELL AS THE OUTCOME AFTER SELECTIVE DISTILLATION (BOTTOM PANEL). HERE, COMPOSITIONS WITH UNIMERS PRESENT (A) WILL FORM SMALL **hPS** AGGREGATES STABILIZED BY **OS** CHAINS THAT LATER PRECIPITATE. IN CONTRAST, HIGHER-SELECTIVITY COMPOSITIONS WITH MINIMAL UNIMERS (B) RESULT IN HOMOPOLYMER SWELLING OF THE MICELLE CORES WHICH REMAIN STABLE AFTER TRANSFER TO A SELECTIVE SOLVENT. ....67
- SCHEME 4. 1 – A SURVEY OF QUIESCENT MICELLE BEHAVIORS SPANNING FROM DYNAMIC MICELLES (DIAMONDS) TO PERSISTENT MICELLES (CIRCLES) AS A FUNCTION OF THE  $\chi N$  BARRIER TO SINGLE-CHAIN EXCHANGE AND DEGREE OF POLYMERIZATION ( $N$ ). THE  $\chi_{\text{CORE-SOLVENT}}$  VALUES WERE EITHER DERIVED FROM SCATTERING METHODS (BLACK BORDER) OR WERE ESTIMATED FROM SOLUBILITY PARAMETERS (BLUE BORDER). THE STAR AND SQUARE DENOTE THE HIGH- $\chi$  LOW- $N$  POLYMERS FROM THIS STUDY,  $O_{45}F_{11}$  AND  $O_{45}F_8$ , RESPECTIVELY. ....86

SCHEME 4. 2 – OVERVIEW SHOWING THE USE OF MICELLES AS TEMPLATES. A DIBLOCK POLYMER IS  
DISPERSED IN A SELECTIVE SOLVENT TO YIELD MICELLES (A). MATERIAL PRECURSORS  
(NANOPARTICLES) ARE NEXT ADDED WHERE THERE IS A PREFERENTIAL INTERACTION WITH THE  
MICELLE VIA HYDROPHILIC INTERACTIONS (B). IF THE MICELLE IS KINETICALLY TRAPPED (PERSISTENT)  
THEN THE TEMPLATE/PORE SIZE REMAINS CONSTANT WHILE THE WALL THICKNESS IS INDEPENDENTLY  
TAILORED BY THE AMOUNT OF MATERIAL PRECURSORS (C). SUBSEQUENT HEAT TREATMENT REMOVES  
THE POLYMER AND YIELDS POROUS NANOMATERIALS WHERE THE PORE SIZE ARISES FROM THE MICELLE  
CORE DIAMETER (D).....98

SCHEME 4. 3 – DEPICTION OF NANOPARTICLES PREFERENTIALLY INTERACTING WITH THE CORONA BLOCKS  
WHILE SIMULTANEOUSLY BEING LOCALIZED WITHIN THE CORE–CORONA INTERFACE. ....113

## CHAPTER 1: OBJECTIVES AND INTRODUCTION

## 1.1 RESEARCH OBJECTIVES

Porous nanomaterials are widely employed for catalysis and electrochemical devices<sup>1-4</sup> where device performance often relies upon specific and well-defined regular feature sizes.<sup>4,5</sup> The use of amphiphilic block polymers to this end affords unique opportunities as their union of chemically dissimilar blocks can yield discrete phase separation while tailorable block molar masses enable a range of achievable length scales.<sup>4-7</sup> When present in a selective solvent, block polymers can create dispersible moieties, known as micelles, through the partitioning of the solvophobic domains to the non-interacting core while the solvophilic blocks remain in contact with the solvent, constituting the exposed corona. While block polymer micelles have been the focus of much research over the last several decades, there remains a significant gap in micelle dimensional tailorability as well as their ability to impart independent dimensional control over discrete nanoscale architectures.

Kinetically trapped micelles represent a unique solution context for block polymers. Normally under thermodynamic control, polymer micelles will undergo changes in their size and/or morphology through the exchange of single chains in response to changes in solution conditions e.g., changes in solvent composition or temperature.<sup>8-11</sup> However, kinetic entrapment suppresses the exchange of block polymer chains (changes in aggregation number) through the imposition of a staunch thermodynamic barrier ( $\propto \chi_{\text{core-solvent}}$ ).<sup>6</sup> Traditionally, this is done through the addition of sufficient core block non-solvent

to create solution conditions that prohibit the formation of the excessive core block-solvent interface needed for extraction of block polymer chain into the solvent matrix. However, the continual usage of low glass transition ( $T_g$ ) core forming segments mean that excessive core block mobility is still present regardless of solution composition, ultimately limiting the extent of micelle dimensional tunability in any templated material.<sup>12-15</sup> This work focuses on expanding block polymer micelle utility through the modification of the core forming segment to feature a high- $T_g$  block for greatly enhanced persistence. The resulting micelles are examined with respect to their solution characteristics as well as after use as structure directing agents in the synthesis of fully tunable porous nanomaterials, where both datasets offer unique perspectives on micelle characteristics.

## 1.2 DISSERTATION OUTLINE

This dissertation concentrates on increasing the utility of kinetically trapped micelles for the controlled synthesis of porous nanomaterials through (1) the incorporation a high- $T_g$  core-forming segment, (2) micelle swelling through added core block homopolymer subsequent vitrification, and (3) the use of a high- $\chi$  core-forming segment to enable micelle persistence in the low- $N$  regime. The following discussion elaborates on the utilization of kinetically trapped block polymer micelles enables the tunable synthesis of nanostructured porous materials. Furthermore, this dissertation also expands upon path dependent synthesis guidelines needed to realize full glassy character. The resulting micelles are then examined in solution and after their use as templates for a series of nanostructured materials.

As discussed previously, mechanisms for kinetic entrapment of block polymer micelles relied upon a  $\chi N$  activation energy barrier where additions of core block non-solvent (e.g., H<sub>2</sub>O) would provide the thermodynamic incentive to arrest appreciable amounts of single-chain exchange. However, due to the highly mobile nature of the core block, micelles can resume dynamic behavior following only minor changes in their solution conditions through e.g., the depletion of water through the addition of water-reactive material precursors.<sup>12,13</sup> Thus, a more robust mechanism for micelle entrapment is needed to support the highly diverse current nanomaterial synthesis landscape. Micelles featuring a fully immobilized (glassy) core forming segment were found to be highly robust, resisting the exchange of single chains as detected through SANS experiments.<sup>16</sup> Thus a solvent processing pathway was developed that eventually led to micelles suspended in complete core block non-solvents. Such micelles were again found to be highly robust provided they (1) contain a sufficiently high- $T_g$  core block, feature sufficient molar mass to realize glassy character, and (3) are present in exclusively core block non-solvent e.g., EtOH, MeOH, H<sub>2</sub>O. This core immobility, which is a function of the  $T_g$  of the core block<sup>17,18</sup> rather than the solvent conditions, was found to support a wide variety of materials chemistries by imparting exceptional micelle persistence, speaking to their utility in a breadth of applications.

The controlled swelling of micelle core diameters by means of core block homopolymer addition in solution remains largely challenging due to the use of equilibrating conditions of the homopolymer and or the block polymer.<sup>19,20</sup> Such equilibrating conditions severely limit the achievable feature micelle sizes in addition to the longevity of the swollen micelles, with most of the homopolymer phase separating out

within a day.<sup>20</sup> Glassy micelles are well positioned in addressing both of these challenges as their vitrification through the removal of all plasticizing solvents ensures a highly immobile core block which does not permit “leaching out” of the homopolymer with time. In chapter 3, a path dependent route to swelling micelles with core block homopolymer was achieved. This process was found to be highly dependent upon solution conditions at each step of the processing pathway where proper tailoring of solvent/non-solvent mixtures were needed to drive homopolymer insertion while subsequent removal of the plasticizing solvents led to core block-homopolymer vitrification. This process not only led to the most tunable swollen micelles to date with core sizes spanning from 39.8 to 99.6 nm, but also lent fundamental insights into the governing energetic processes as well as possible mechanisms that enabled such rapid expansion of the micelle cores.

While the preceding discussions focused on the use of micelles featuring a high- $T_g$  segment, it is important to point out that a critical molar mass (or degree of polymerization,  $N$ ) is needed to properly realize glassy behavior. In other words, glassy character is not a candidate mechanism for kinetic control in the low- $N$  regime.<sup>21</sup> Thus, the choice of especially high- $\chi$  core-forming segments is motivated to provide a sufficient  $\chi N$  thermodynamic barrier in the especially low- $N$  regime. The use of a high- $\chi$  perfluorinated segment was herein adopted and found to enable kinetic entrapment with as few as 11 mer units. Micelle persistence was evaluated through a combination of solution characterization as well as analysis of templated nanomaterials where the especially high- $\chi$  perfluorinated micelles were found to enable the widest extent of wall thickness tunability to date across a 45-sample series, speaking to their deeply trapped kinetic state.

### 1.3 REFERENCES

- (1) Joo, S. H.; Choi, S. J.; Oh, I.; Kwak, J.; Liu, Z.; Terasaki, O.; Ryoo, R. Ordered nanoporous arrays of carbon supporting high dispersions of platinum nanoparticles. *Nature* **2001**, *412*, 169–172.
- (2) Sanchez, C.; Belleville, P.; Popall, M.; Nicole, L. Applications of advanced hybride organic–inorganic nanomaterials: from laboratory to marked. *Chem. Soc. Rev.* **2011**, *40*, 696–753.
- (3) Zhang, Q.; Uchaker, E.; Candelaria, S. L.; Cao, G. Nanomaterials for energy conversion and storage. *Chem. Soc. Rev.* **2013**, *42*, 3127–3171.
- (4) Li, C.; Li, Q.; Kaneti, Y. V.; Hou, D.; Yamauchi, Y.; Mai, Y. Self-assembly of block polymers towards mesoporous materials for energy storage and conversion. *Chem. Soc. Rev.* **2020**, *49*, 4681–4736.
- (5) Li, C.; Iqbal, M.; Jiang, B.; Wang, Z.; Kim, J.; Nanjundan, A. K.; Whitten, A. E.; Wood, K.; Yamauchi, Y. Pore-tuning to boost the electrocatalytic activity of polymeric micelle-templated mesoporous Pd nanoparticles. *Chem. Sci.* **2019**, *10*, 4054–4061.
- (6) Mai, Y.; Eisenberg, A. Self-assembly of block copolymers. *Chem. Soc. Rev.* **2012**, *41*, 5969–5985.
- (7) Karayianni, M.; Pispas, S. Block copolymer solution self-assembly: recent advances, emerging trends, and applications. *J. Polym. Sci.* **2021**, *59*, 1874–1898.
- (8) Eisenberg, A.; Yu, K. Multiple morphologies in aqueous solution of aggregates of polystyrene-*block*-poly(ethylene oxide) diblock copolymers. *Macromolecules* **1996**, *29*, 6359–6361.
- (9) Eisenberg, A.; Yu, G. Multiple morphologies formed from an amphiphilic ABC triblock copolymer in solution. *Macromolecules* **1998**, *31*, 5546–5549.
- (10) Eisenberg, A.; Luo, L. Thermodynamic size control of block copolymer vesicles in solution. *Langmuir* **2001**, *17*, 6804–6811.
- (11) Bhargava, P.; Tu, Y.; Zheng, J. X.; Xiong, H.; Quirk, R. P.; Cheng, Z. D. Temperature-induced reversible morphological changes of polystyrene-*block*-poly(ethylene oxide) micelles in solution. *J. Am. Chem. Soc.* **2007**, *129*, 1113–1121.
- (12) Lokupitiya, H. N.; Jones, A.; Reid, B.; Guldin, S.; Stefik, M. Ordered mesoporous to macroporous oxides with tunable isomorphic architectures: solution criteria for

- persistent micelle templates. *Chem. Mater.* **2016**, *28*, 1653–1667.
- (13) Sarkar, A.; Stefik, M. How to make persistent micelle templates in 24 hours and know it using X-ray scattering. *J. Mater. Chem. A.* **2017**, *5*, 11840–11853.
  - (14) Sarkar, A.; Evans, L.; Stefik, M. Expanded kinetic control for persistent micelle templates with solvent selection. *Langmuir* **2018**, *34*, 5738–5749.
  - (15) Lantz, K. A.; Clamp, N. B.; van den Bergh, W.; Sarkar, A.; Stefik, M. Full gamut wall tunability from persistent micelle templates via *ex-situ* hydrolysis. *Small* **2019**, *15*, 1900393.
  - (16) Choi, S.; Lodge, T. P.; Bates, F. S. Mechanism of molecular exchange in diblock copolymer micelles: hypersensitivity to core chain length. *Phys. Rev. Lett.* **2010**, *104*, 047802–047805.
  - (17) Fox, T. G.; Flory, P. J. Second-order transition temperature and related properties of polystyrene. I. Influence of molecular weight. **1950**, *21*, 581–591.
  - (18) Fox, T. G.; Flory, P. J. The glass temperature and related properties of polystyrene. Influence of molecular weight. **1954**, *14*, 315–319.
  - (19) Deng, Y.; Liu, J.; Liu, C.; Gu, D.; Sun, Z.; Wei, J.; Zhang, J.; Zhang, L.; Tu, B.; Zhao, D. Ultra-large-pore mesoporous carbons templated from poly(ethylene oxide)-*b*-polystyrene diblock copolymer by adding polystyrene homopolymer as a pore expander. *Chem. Mater.* **2008**, *20*, 7281–7286.
  - (20) Sarkar, A.; Thyagarajan, A.; Cole, A.; Stefik, M. Widely tunable persistent micelle templates *via* homopolymer swelling. *Soft Matter* **2019**, *15*, 5193–5203.
  - (21) Williams, E. R.; McMahon, P. L.; Reynolds III, J. E.; Snider, J. L.; Stavila, V.; Allendorf, M. D.; Stefik, M. Tailored porous carbons enabled by persistent micelles with glassy cores. *Mater. Adv.* **2021**, *2*, 5381–5395.

CHAPTER 2: TAILORED POROUS CARBONS ENABLED BY  
PERSISTENT MICELLES WITH GLASSY CORES<sup>1</sup>

---

<sup>1</sup> Reproduced from Williams, E. R.; McMahon, P. L.; Reynolds III, J. E.; Snider, J. L.; Stavila, V.; Allendorf, M. D.; Stefik, M. *Mater Adv.* **2021**, 2, 5381–5395 with permission from the Royal Society of Chemistry.

## 2.1 ABSTRACT

Porous nanoscale carbonaceous materials are widely employed for catalysis, separations, and electrochemical devices where device performance often relies upon specific and well-defined regular feature sizes. The use of block polymers as templates has enabled affordable and scalable production of diverse porous carbons. However, popular carbon preparations use equilibrating micelles which can change dimensions in response to the processing environment. Thus, polymer methods have not yet demonstrated carbon materials with constant average template diameter and tailored wall thickness. In contrast, persistent micelle templates (PMTs) use kinetic control to preserve constant micelle template diameters, and thus PMT has enable constant pore diameter metrics. With PMT, the wall thickness is independently adjustable *via* the amount of material precursor added to the micelle templates. Previous PMT demonstrations relied upon thermodynamic barriers to inhibit chain exchange while in solution, followed by rapid evaporation and cross-linking of material precursors to mitigate micelle reorganization once the solvent evaporated. It is shown here that this approach, however, fails to deliver kinetic micelle control when used with slowly cross-linking material precursors such as those for porous carbons. A new modality for kinetic control over micelle templates, glassy-PMTs, is shown using an immobilized glassy micelle core composed of polystyrene (PS). Although PS based polymers have been used to template carbon materials before, all prior reports included plasticizers that prevented kinetic micelle control. Here the key synthetic conditions for carbon materials with glassy-PMT control are enumerated, including dependencies upon polymer block selection, block molecular mass, solvent selection, and micelle processing timeline. The use of glassy-PMTs also enables the direct observation of

micelles cores by TEM which are shown to be commensurate with template dimensions. Glassy-PMTs are thus robust and largely insensitive to material processing kinetics, broadly enabling tailored nanomaterials with diverse chemistries.

## 2.2 INTRODUCTION

Prolific in functional nanomaterials are the porous carbons whose high surface areas with tunable nanoscale pore sizes and naturally low densities lend themselves well to a variety of applications spanning from adsorption<sup>1-5</sup> to separations,<sup>6-8</sup> catalysis,<sup>9,10</sup> and energy conversion and storage.<sup>11-13</sup> The direct assembly<sup>14-17</sup> of amphiphilic block polymer templates with carbon precursors affords a robust self-assembled product with ordered periodicity through low-cost reagents. These carbon precursors are often based upon the polymerization of phenol<sup>7,18,19</sup> and related analogs<sup>7,19-21</sup> which are able to be cross-linked and have a high carbon yield following carbonization.<sup>16</sup> Generally, the block polymers contain a poly(ethylene oxide) (PEO) or other hydrogen bonding polymer block to enable selective interaction with the carbon precursors. Simultaneously, the non-interacting (usually hydrophobic) polymer block phase separates from the material-PEO domain to form discrete hydrophobic regions. A subsequent heat treatment rigidifies the carbon precursors and pyrolysis then carbonizes the precursors and removes the block polymer template to yield ordered porosity.<sup>22,23</sup> The carbonization temperature is well known to determine the extent of graphitization.<sup>24-26</sup>

The pluronic family of block polymers are popular templates due to commercial availability, though their low molecular mass limits the achievable feature size. In contrast, custom-synthesized block polymers enable much larger feature sizes through increased

hydrophobic block molecular mass.<sup>27</sup> A wide range of nanoscale porous carbons have been prepared using these and similar polymers to yield pore sizes ranging from 3.8 to 108 nm.<sup>28,29</sup> Many custom block polymers are not directly soluble in alcohols and are thus processed from THF or other good solvents for both the polymer blocks and the carbon precursors. While convenient, this class of good-solvent approaches generally leads to dynamic micelles that change size in response to the specific solution conditions. From a materials perspective, this means that the feature dimensions (e.g., pores and walls) both change simultaneously with any recipe changes. Prior reports demonstrate this phenomenon where altering the amount of material precursors changes both the pore size and the wall thickness<sup>30-33</sup> and sometimes also leads to morphology changes.<sup>32,34-38</sup> These are natural limitations of equilibration-based synthesis approaches where all aspects of the architecture are determined through free-energy minimization. While recent porous carbon reports have added diversity to carbon precursor chemistry,<sup>4,7,39,40</sup> block polymer chemistries,<sup>29,41</sup> feature sizes,<sup>29,42-44</sup> and morphologies<sup>43,45</sup> none yet have demonstrated carbon materials with constant polymer template dimensions irrespective of the amount of material added.

Persistent micelle templates (PMTs) are uniquely based upon kinetically controlled micelles which enable the production of porous material series with constant pore size and varied wall thickness. The suppression of chain exchange mechanisms are needed to preserve constant micelle template diameter with an invariant micelle aggregation number. Furthermore, the use of a constant micelle template also enables isomorphic sample series where transitions to bulk phases (spheres, cylinders, lamellae *etc.*) are prevented. Thus, changing the amount of material precursors relative to the amount of persistent micelle

templates (material: template ratio) enables the production of isomorphic (constant morphology) sample series with constant template dimensions and monotonically varied wall thickness.<sup>46</sup> In contrast, monomicelle routes<sup>47,48</sup> rather react material precursors around dispersed and likely-equilibrating micelles to form a stable intermediate for later assembly and have not yet demonstrated independent wall thickness control. Prior demonstration of PMT used a large thermodynamic barrier ( $\chi N$ ) to inhibit chain exchange between micelles and thus preserve kinetic control of the template dimension. Here, the effective interaction parameter  $\chi$  is a largely enthalpic term corresponding to the interface of the solvent and the core block. In prior PMT examples, this  $\chi N$  barrier was adjusted based upon chain size,<sup>46</sup> trace water content,<sup>46,49–52</sup> or solvent selection.<sup>50</sup> In all of the prior examples, porous transition metal oxides were prepared via sol–gel chemistry where the material precursors were rapidly cross-linked by a high temperature “aging” treatment within seconds of drying *via* spin/dip coating. It was shown there that rapid material cross-linking was critical to preserve kinetic control.<sup>49</sup> In other words, there is a kinetic competition between the rates of material cross-linking and micelle reorganization. This limitation has thus far prevented the use of PMTs with slowly crosslinking material chemistries, such as those used for carbon materials. Here, we present a new modality for maintaining PMT control that does not rely upon a  $\chi N$  thermodynamic barrier, but rather uses an immobilized glassy core block to maintain kinetic control. Our unique solvent processing conditions remove all core block solvents from solution, effectively halting core mobility and prohibiting chain exchange. It will be shown that these glassy- PMTs significantly enhance the extent of micelle persistence, with templates lasting indefinitely under suitable conditions. Furthermore, demonstrations of PMT to date have relied upon

statistical measurements of porous materials to infer the micelle template dimensions after processing. Here, we report the first direct observation of the PMT mechanism with TEM images of glassy-PMTs as well as materials prepared therefrom. Glassy- PMTs maintain constant micelle core size after solvent removal for TEM whereas prior non-glassy PMTs could re-equilibrate following solvent removal. Additionally, a series of glassy-PMT design guidelines will be presented which also highlight why prior studies using e.g., PEO-*b*-PS<sup>14,38,42,53</sup> and PEO-*b*-PMMA<sup>54</sup> exhibited wide simultaneous variance of both pore and wall dimensions despite the apparent inclusion of a glassy core block.

## 2.3 EXPERIMENTAL METHODS

### MATERIALS

Anhydrous, inhibitor-free THF (>99.9%, Fisher), phloroglucinol (99+%, anhydrous, Acros), *N,N'*-dicyclohexylcarbodiimide (DCC) (99%, BeanTown Chemical) and Cu(I) Br (99%, Aldrich) were all stored in an argon glovebox and used as received. Formaldehyde (37 wt% in water stabilized with 7–8% methanol, Fisher) and styrene monomer (99%, Acros) were stored inside a refrigerator until use as received. Styrene monomer was passed over a basic alumina column prior to use to remove inhibitor. Concentrated hydrochloric acid (37 wt% ACS grade, VWR), 4-dimethyl- aminopyridine (DMAP) (99%, TCI Chemicals), the ligand *N,N,N',N'',N''*-pentamethyldiethylenetriamine (PMDETA) (99%, Sigma), 2-bromopropionic acid (98%, Alfa Aesar) and Cu(II) Br (99%, Aldrich) were all used as received. Poly(ethylene glycol) methyl ether (PEO) Mn 5000 g mol<sup>-1</sup> (Sigma) and Mn 2000 g mol<sup>-1</sup> (Alfa Aesar) were used as received. Hexanes (>98.5%, Fisher), methanol-free chloroform (99%, Aldrich), HPLC grade isopropyl alcohol (>99.9%, Honeywell), dimethyl sulfoxide (99.7%, Fisher), deionized water (ACS grade, Alfa Aesar)

and 22-gauge copper wire (McMaster-Carr) were all used as received. Ethanol (200 proof, Deacon Labs) was stored over 50 w/w% molecular sieves (3 Å, 8–12 mesh, Acros Organics) for one week prior to use.<sup>55</sup>

#### SYNTHESIS OF PEO-BR MACROINITIATOR

A Steglich esterification was used to produce a macroinitiator for atom transfer radical polymerization (ATRP). A typical synthesis involved the dissolution of 20 g of 5000 g mol<sup>-1</sup> (4.00 mmol) PEO methyl ether in 100 mL of chloroform. Next, 0.720 mL (8.00 mmol) of 2-bromopropionic acid was added dropwise with stirring. The flask was then chilled with an ice bath for 10 minutes prior to the addition of 1.65 g (8.0 mmol) of DCC and 0.391 g (3.20 mmol) of DMAP. The flask was then allowed to stir for another 10 minutes before the ice bath was removed. The reaction was then stirred at room temperature for 24 hours. Next, the crude reaction mixture was gravity filtered through a Whatman 2V filter paper with a diameter of 270 mm to remove the urea by-product. The solid by-product was then discarded, and the macroinitiator filtrate was then precipitated in 500 mL of hexanes by a dropwise addition. The solid product was collected and allowed to dry in a vacuum chamber without heat overnight prior to further purification. The product was then dissolved in 100 mL of chloroform and shook gently with an equal volume of deionized water to remove the urea by-product. This process was repeated for a total of three times. The chloroform was then removed by evaporation under reduced pressure.

## SYNTHESIS OF OS1

The PEO-*b*-PS diblock was prepared by ATRP using the following molar ratios: PEO-Br : PMDETA : Cu(I)Br : Styrene of 1 : 1.125 : 1.125 : 200. Styrene monomer was passed over a basic alumina column immediately prior to use to remove inhibitor. In a 100 mL round-bottom flask, 13.75 mL (120 mmol) of styrene was added to 3.00 g of the previously synthesized PEO-Br macroinitiator and sealed with a rubber septum. The solution was then sparged with nitrogen for 20 minutes to displace dissolved oxygen in solution. In an argon glovebox, 98.6 mg (0.675 mmol) of Cu(I)Br was combined with 140.9  $\mu$ L of (0.675 mmol) of PMDETA. This mixture was then transferred, *via* an airtight stoppered syringe, to the reaction flask and added *via* injection through the rubber septum to initiate the polymerization. The reaction was then placed in a preheated oil bath at 110°C and allowed to proceed until the solution became sufficiently viscous to arrest the stir bar, this took approximately 6 hours. The flask was then placed in the freezer for 3 hrs before exposure to air. The product was dissolved in THF and passed over a column of basic alumina to remove copper complexes. The majority of THF was then removed by rotary evaporation to yield a highly viscous liquid. The product was then precipitated in 500 mL of methanol at -78°C (achieved with a dry ice acetone bath) and collected by gravity filtration. The product was then dried under vacuum prior to characterization.

## SYNTHESIS OF OS2

The small PEO-*b*-PS diblock was prepared *via* a radically deactivated reversible polymerization (RDRP) route<sup>56</sup> using the following conditions PEO-Br : PMDETA : Cu(II)Br : Styrene of 1 : 0.05 : 0.36 : 30. A volume of 3.43 mL (30.0 mmol) of inhibitor-

free styrene was added to 2.00 g (1.00 mmol) of 2000 g mol<sup>-1</sup> PEO-Br macroinitiator (prepared with identical molar ratios and procedure as the 5000 g mol<sup>-1</sup> used previously) along with 3.43 mL of isopropyl alcohol in a 50 mL round-bottom flask. A 5 cm length of copper wire was activated by submerging in 37 wt% HCl, along with a stir bar, for 10 minutes. The wire was then wrapped round the stir bar in such a way as to secure it during normal stirring. An aliquot of 56 μL (0.05 mmol) of Cu(II)Br was taken from a 200 mg mL<sup>-1</sup> aqueous stock solution and added to the reaction flask. The mixture was sparged with nitrogen for 20 minutes to displace dissolved oxygen. Then, 72 μL of PMDETA was delivered *via* needle and syringe through the rubber septum and the reaction mixture placed in a preheated oil bath at 60°C. The reaction was allowed to progress for 12 hrs until becoming sufficiently viscous. The reaction flask was then placed in the freezer for 3 hrs before exposure to air. The product was dissolved in THF and passed over a column of basic alumina to remove copper complexes. The product was then dialyzed against pure THF for a total of 48 hrs with solvent exchange after the first 4, 18, and 24 hours, respectively.

## POLYMER CHARACTERIZATION

The molar mass of PS and molar mass dispersity ( $\bar{D}$ ) of all polymers were determined using nuclear magnetic resonance (NMR) spectroscopy and gel permeation chromatography (GPC), respectively. All proton (<sup>1</sup>H-NMR) spectra were measured using a Bruker Avance III HD 300. All GPC data were collected using a Waters gel permeation chromatography GPC instrument equipped with a 515 HPLC pump, a 2410 refractive index detector and three styragel columns (HR1, HR3, and HR4) in the effective molecular weight range of

0.1–5, 0.5–30, and 5–600 kg mol<sup>-1</sup>, respectively. The eluent was THF at a temperature of 30°C and a flow rate of 1 mL min<sup>-1</sup>. The instrument was calibrated with polystyrene standards (2570, 1090, 579, 246, 130, 67.5, 34.8, 18.1, 10.4, 3.4, and 1.6 kg mol<sup>-1</sup>) received from Polymer Laboratories. The GPC samples were prepared by dissolution in THF at a concentration of ~5 mg mL<sup>-1</sup> and were filtered through a syringe filter with a pore diameter of 0.2 µm just prior to injection.

#### F127–ETOH MICELLE PREPARATION

Owing to the weakly hydrophobic nature of F127, 1.00 g of this pluronic polymer was readily dispersed into 20 mL of solvent composed of 90 vol% EtOH (18 mL) and 10 vol% H<sub>2</sub>O (2 mL).

#### OS1–THF MICELLE PREPARATION

First, 1.00 g of OS1 was dissolved in 10 mL of THF. Next, 10 mL of deionized water was added dropwise with stirring. A volume of 80 mL of EtOH was then added gradually to yield the micelle solution.

#### OS2–ETOH MICELLE PREPARATION

The polymer OS2 was directly dispersible in EtOH with minor agitation. Typically, 100 mg of OS2 was dispersed directly into 10 mL of EtOH.

## OS1–ETOH MICELLE PREPARATION

A typical preparation involved dissolving 1.00 g of OS1 in 10 mL of THF. Next, 10 mL of deionized water was added by a dropwise addition with constant wrist stirring. Then 100 mL of EtOH added gradually to increase the amount of non-solvent for PS. Lastly, the THF was selectively removed by rotary evaporation and the removed volume replaced with EtOH to achieve a final micelle concentration of 30 mg mL<sup>-1</sup> with a final composition of 90 vol% EtOH and 10 vol% H<sub>2</sub>O. Dynamic light scattering (DLS) measurements were performed on the polymer OS1 at each stage of the micelle preparation. The DLS measurements of the micelle hydrodynamic diameter were performed using a Zetasizer Nanoseries ZEN3690 instrument. Solutions for DLS were prepared with OS1 at a concentration of 10 mg mL<sup>-1</sup> and were filtered through a 0.2 μm syringe filter prior to measuring. All measurements were performed three times to confirm measurement reproducibility. All DLS measurements were performed at 25°C. For pure THF, a viscosity of 0.455 cP and a refractive index of 1.405 were used. For solvent-water mixtures, the viscosities of 0.916, 0.784, 0.819 and refractive indices of 1.397, 1.366, and 1.362 were used for the 50/50 vol% THF/H<sub>2</sub>O, 80/10/10 vol% EtOH/THF/H<sub>2</sub>O, and 90/10 vol% EtOH/H<sub>2</sub>O, respectively.<sup>57,58</sup>

## POROUS CARBONS

A stock solution of 100 mg mL<sup>-1</sup> of phloroglucinol was prepared by dissolving 1.0 g of phloroglucinol in 10 mL of EtOH. In a 20 mL scintillation vial, one of the above micelle solutions containing 50 mg of polymer was combined with the desired amount of phloroglucinol stock. This combined mixture was then diluted with the solvent mixture (90

vol% EtOH, 10 vol% H<sub>2</sub>O) to achieve a concentration of 25 mg mL<sup>-1</sup> for the sum of material precursors and template masses (M + T) with respect to the total solution volume. The appropriate amount of 37 wt% HCl was added such that the final concentration of HCl was 10 μL per mL of total solution. Next, the appropriate amount of formaldehyde solution was delivered, and the reaction solution was inverted a few times and allowed to react unperturbed. A 1 : 1 molar ratio of phloroglucinol : formaldehyde was used for all samples. After ~18 hrs, two distinct phases were visible: the lower cloudy phase corresponding to carbon precursors and micelles and an upper clear phase rich in solvent. The supernatant solvent layer was discarded by decantation, and the material-micelle phase dried under vacuum without heat (termed “as made”). The samples were further cross-linked (termed “aged”) by the addition of 0.5 mL of formaldehyde solution and heating to 80°C for 48 hrs. The samples were carbonized under a N<sub>2</sub> atmosphere by heating at a ramp rate of 2°C min<sup>-1</sup> to 450°C and were held at this temperature for 4 hrs (termed “carbonized”).

#### SMALL-ANGLE X-RAY SCATTERING (SAXS)

Small-angle X-ray scattering measurements were performed at the South Carolina SAXS collaborative using a SAXSLab Ganesha instrument. A Xenocs GeniX3D microfocus source was used with a Cu target to create a monochromatic beam with a wavelength of 0.154 nm. The instrument was calibrated prior to use with a National Institute of Standards and Technology (NIST) reference material 640d silicon powder, with a reference peak position of  $2\theta = 28.44^\circ$ , where  $2\theta$  represents the total scattering angle. A Pilatus 300 K detector (Dectris) was used to collect the two-dimensional (2D) scattering pattern. The detector exhibits a nominal pixel dimension of  $172 \times 172 \mu\text{m}^2$ . The SAXS data were

acquired with an X-ray flux of ~4.1 million photons per second incident upon the sample and with a sample-to-detector distance of 1040 mm. The 2D images were azimuthally integrated to yield the scattering vector intensity. Peak positions were fitted using custom MATLAB software. SAXS simulations were conducted using SASFit.

#### TRANSMISSION ELECTRON MICROSCOPY (TEM)

Electron microscopy images were collected in bright-field imaging mode using a JEOL 1400 Plus Transmission Electron Microscope with an accelerating voltage of 120 keV. Cryoultramicrotomy was performed using a Leica UC7/FC7 cryoultramicrotome at  $-55\text{ }^{\circ}\text{C}$  using a eutectic mixture of DMSO and  $\text{H}_2\text{O}$ . Coarse sample cuts were performed using a freshly cut-glass edge with  $\sim 1\text{ mm}$  being removed before sectioning. Sectioning was performed with a diamond blade with a nominal sample thickness of 60 nm. The floating sections were transferred to bare copper grids. The micelles themselves were imaged by placing a  $20\text{ }\mu\text{L}$  drop at  $10\text{ mg mL}^{-1}$  concentration onto a carbon coated grid and allowing the sample to sit unperturbed for 10 mins. Staining was performed by adding a single  $20\text{ }\mu\text{L}$  drop of 1 wt% aqueous uranyl acetate solution and wicking the grid dry after 10 mins.

#### BET POROSITY MEASUREMENTS

Gas sorption isotherms were measured with an Autosorb iQ (Quantachrome Inc., USA) gas sorption system with  $\text{N}_2$  (Matheson, 99.999% purity) as the probe gas. Prior to measurement, samples were evacuated under dynamic vacuum at  $300\text{ }^{\circ}\text{C}$  for a minimum of 2 hrs and free-space correction measurements were performed with He gas (Matheson, 99.999% purity). All  $\text{N}_2$  isotherms were collected at 77 K using a liquid  $\text{N}_2$  bath in the pressure range from 0–1 bar. The specific surface area was determined using a multi-point

Brunauer–Emmett–Teller (BET) method in the pressure range between 0.05–0.20 P/P<sub>0</sub>. Pore size distributions were determined by application of the Barrett–Joyner–Halenda (BJH) method to the adsorption portion of the N<sub>2</sub> isotherm. Total pore volume (V<sub>t</sub>) was calculated at the relative pressure of ~0.99 P/P<sub>0</sub>.

#### DIFFERENTIAL SCANNING CALORIMETRY MEASUREMENTS

DSC measurements were performed on a Hitachi DSC7020 with two cycles ranging from 0 °C to 150 °C at a heating and cooling rate of 10 °C min<sup>-1</sup> in a nitrogen atmosphere. Samples were prepared in a crimped aluminum pan.

#### 2.4 RESULTS AND DISCUSSION

The control of micelle size through suppression of chain exchange is key to fabricating tailored nanostructures with independent tunability of pore and wall dimensions.

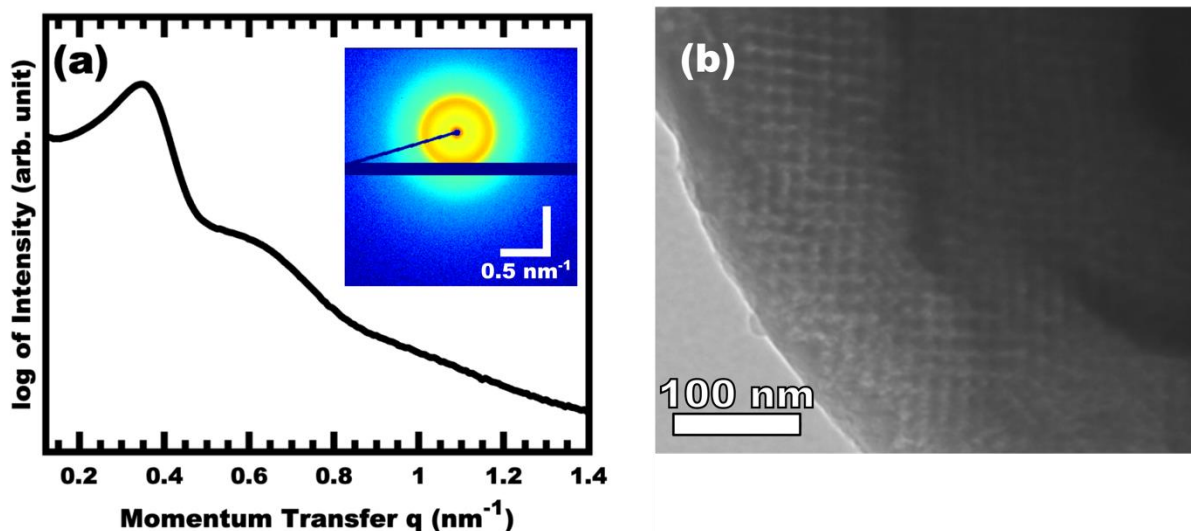
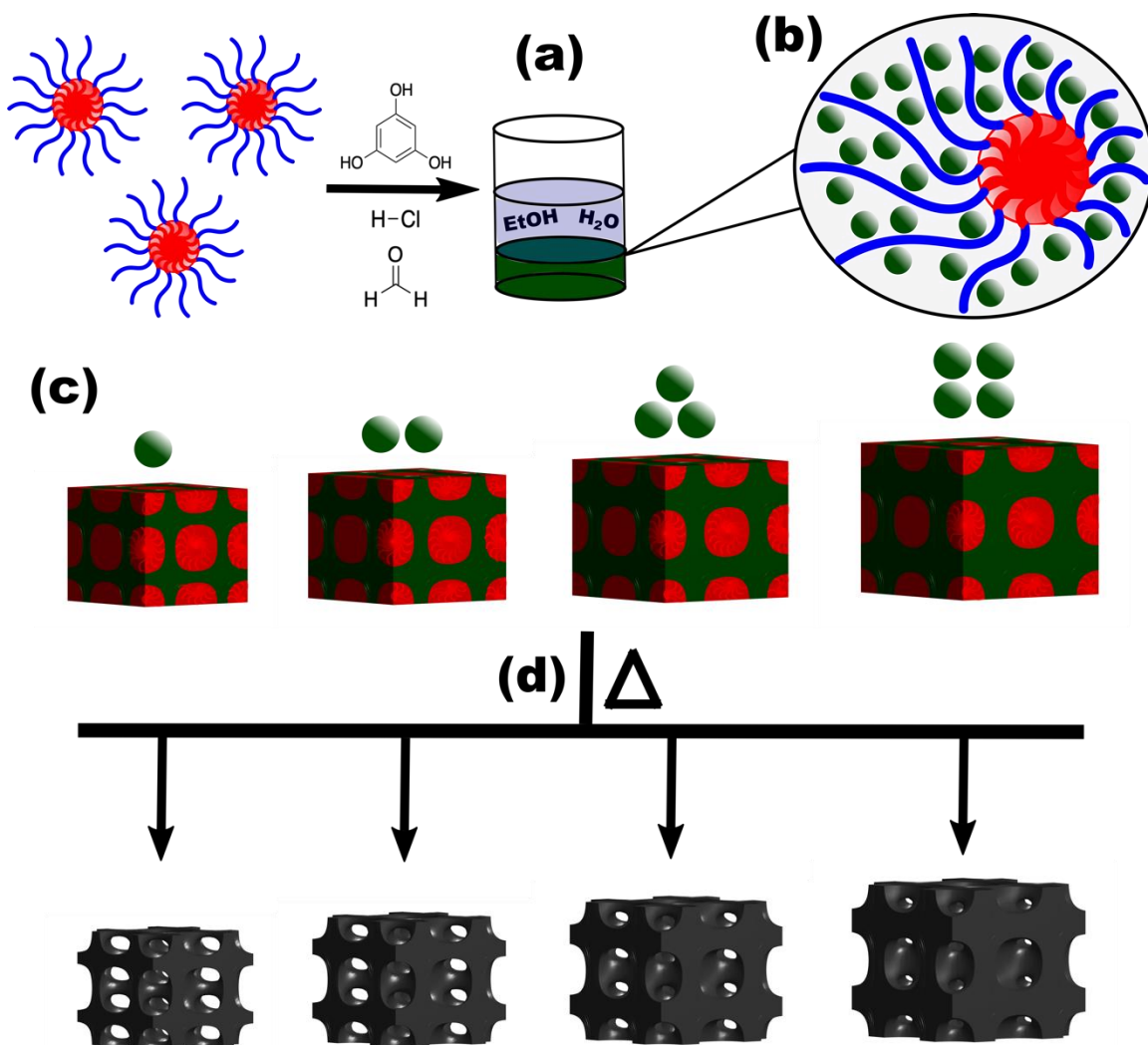


*Figure 2. 1* – SAXS (a) and TEM (b) data from the representative samples OS1-EtOH-1.00 after carbonization. The inset 2D SAXS pattern has a color scale corresponding to the log of X-ray intensity. The momentum transfer  $q = 4\pi \sin(\theta)/\lambda$ , where  $2\theta$  refers to the total

scattering angle and  $\lambda$  is the wavelength. The bright field TEM image shows the location of carbon (dark) and porosity (light).

All prior PMT examples<sup>46,49–52</sup> relied upon a  $\chi N$  thermodynamic barrier to inhibit chain exchange between micelles in solution as well as a rapid thermal crosslinking of the material precursors directly after evaporation. However, the slow cross-linking nature of carbon materials chemistry necessitates the development of a template with significantly enhanced degrees of persistence within a micelle–material rich environment. Within the context of block polymer micelles, the use of a glassy core block is known to suppress micelle core mobility<sup>59,60</sup> and halt chain exchange.<sup>61,62</sup> Such glassy core micelles would be the most deeply trapped PMT modality to date. Although glassy-PMTs would offer many benefits towards nanomaterial synthesis, the implementation of glassy-PMTs, however, is non-trivial where the solvent selection, solvent path dependence, and polymer molar mass each play critical roles, *vide infra*. An example dataset from a single condition is presented first before comparing different sample conditions. Figure 2.1 shows the SAXS and TEM data for OS1–EtOH–1.00, named for using polymer OS1 processed from EtOH and having M:T = 1.00. The TEM data is mostly consistent with a mixture of randomly packed spherical pores with regions of well-ordered domains. Hundreds of measurements were taken from TEM images to yield statistically significant metrics (Fig. B.2). Here the pore size (light circles) was determined to be 10.80 nm and the wall thickness 9.07 nm (dark). The SAXS pattern features two isotropic scattering peaks with an approximate  $q$ -ratio of 1 : 1.8, consistent with a randomly packed arrangement of spheres. The inset 2D SAXS pattern was isotropic, indicating a lack of preferred alignment as expected for a randomly ordered sample precipitated from solution. The  $d$ -spacing ( $2\pi/q$ ) for the first intensity

maximum was 19.32 nm, similar to the sum of the pore size and the wall thickness. This correlation is subsequently used to infer PMT behavior for sample series where prior

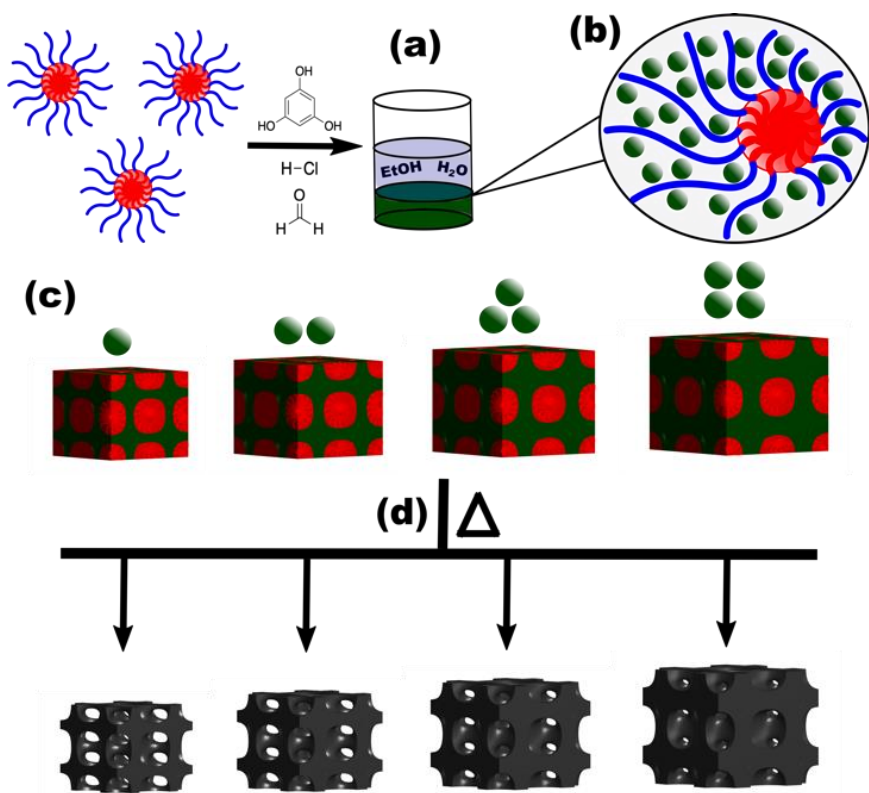


*Scheme 2. 1* – Carbon precursors are combined with micelles in solution where both phases separate from the solvent as the carbon-rich bottom layer (a) and the carbon precursors (green circles) selectively associate with the PEO corona block (blue segment) of the block polymer micelles (b). A continuous solid is produced as these decorated micelles pack together while preserving the template and material volume fractions (c). With persistent micelle templates, the average template size is constant, and the addition of further material increases the wall thickness *via* lattice expansion. These as-made samples are subsequently aged and carbonized to convert the carbon precursors into amorphous carbon while removing the polymer template to produce porosity (d).

modelling established a relationship between  $d$ -spacing and the material-to-template (M:T) ratio.

## NANOSTRUCTURE CARBON FROM A PLURONIC POLYMER

The prototypical use of poly(ethylene oxide-*b*-propylene oxide-*b*-ethylene oxide) (PEO-*b*-PPO-*b*-PEO, F127) as a template for carbon precursors is examined first. Here PPO is the hydrophobic block that forms the micelle core in typical aqueous and alcoholic solutions. The especially low ( $-60$  °C)  $T_g$  of PPO<sup>63</sup> is well below room temperature where the corresponding micelle chains have considerable mobility under normal processing conditions. Furthermore, the typical alcohol-rich solutions used with F127 and analogs are good solvents for PPO. This implies a very low effective interaction parameter,  $\chi$ , between the core block and the solvent, leading to relatively high chain exchange rates between micelles and facilitating a diverse range of bulk morphologies depending on the amount of material precursors.<sup>64,65</sup> Carbon precursors are often templated by phase separation from a solution where the arrangement of spherical micelles is frequently preserved<sup>7,17</sup> (Scheme 2.1). Prior works have widely varied such procedures with F127 where both pore and wall dimensions tend to vary simultaneously.<sup>32,37</sup>



*Scheme 2. 2* – Carbon precursors are combined with micelles in solution where both phases separate from the solvent as a carbon-rich bottom layer (a) and the carbon precursors (green circles) selectively associate with the PEO corona blocks (blue segment) of the block polymer micelles (b). A continuous solid is produced as these decorated micelles pack together while preserving the template and material volume fractions (c). With persistent micelle templates the average template size is constant, and the addition of further material increases the wall thickness via lattice expansion. These as-made samples are subsequently aged and carbonized to convert the carbon precursors into amorphous carbon while removing the polymer template to produce porosity (d).

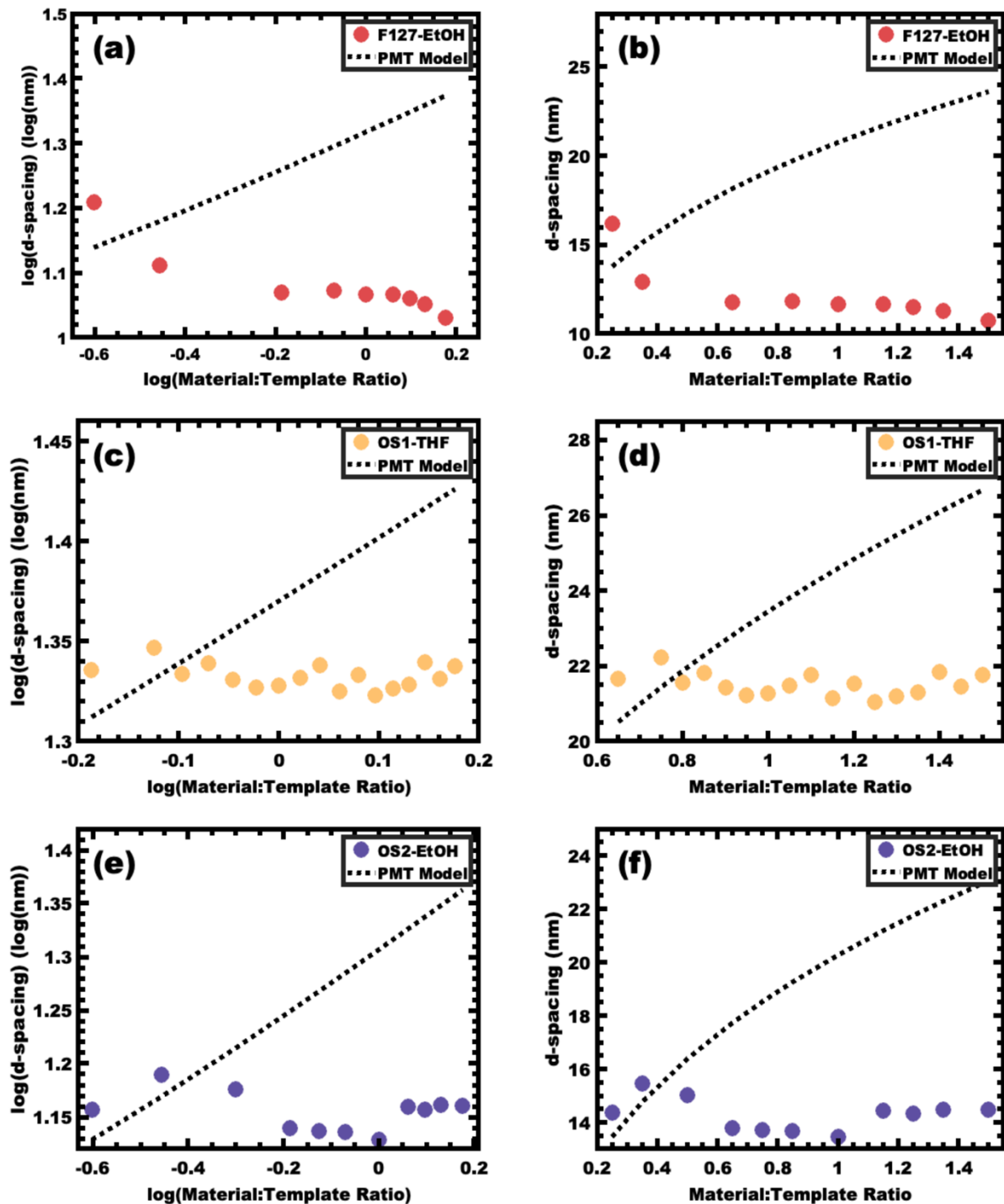


Figure 2. 2 – Samples that fail to exhibit PMT behavior enabled the realization of design guidelines for glassy-PMT. The PMT model predicts lattice expansion with increasing material:template ratio that follows a quasi-straight-line (dashed line) with a slope of 1/3 when plotted in a log–log coordinate space (a, c, and e) or alternatively a line with a quasi-cube-root dependence (dashed line) when plotted in a linear–linear coordinate space (b, d, and f). Trends in  $d$ -spacing derived from SAXS peak positions are shown for sample series

F127–EtOH (a and b), OS1–THF (c and d), and OS2–EtOH (e and f). These datasets are inconsistent with persistent micelle behavior.

Figure 2.2a and b presents the SAXS trends from sample series F127-EtOH where the  $d$ -spacing monotonically decreases with increasing M:T ratios. This material addition naturally increases the volume fraction of the walls however the SAXS lattice contraction indicates that this wall change is more than compensated for by a decrease in pore size throughout the series. In contrast, we previously reported a PMT model<sup>46</sup> that quantitatively predicts lattice expansions as materials are added between persistent micelles. Here the corresponding lattice dimension is simple to track *via* SAXS measurement of  $d$ -spacing where  $d = 2\pi/q$  and  $q$  is the position of the first structure factor peak. The model predicts a quasi-cube-root dependence for  $d$ -spacing *vs.* M:T ratio based upon a simple conservation of volume argument.<sup>49</sup> Later it was shown that a convenient log simplification of this model enables validation of SAXS data consistency with PMT behavior from SAXS data alone. Here the PMT model predicts a straight line with a slope of 1/3 in this log–log coordinate space.<sup>50</sup> One advantage of this approach is that consistency of the data with PMT behavior may be assessed prior to real space measurements with electron microscopy. This approach also identifies the M:T range of the PMT window (if applicable) prior to fitting. Thus the decreasing  $d$ -spacing with M:T for the F127-EtOH SAXS data (Fig. 2.2a and b) is prototypical evidence of dynamic micelles (not PMT behavior) where both the pore size and wall thickness change simultaneously. This gives rise to glassy-PMT design guideline (1): the polymer block residing in the micelle core must have a  $T_g$  above the processing temperatures, including any subsequent thermal cross-linking of the material precursors.

Table 2. 1 – Characteristics of the PS polymers used.

Polymer Name	$M_n$ , PEO (g mol <sup>-1</sup> )	$M_n$ , PS <sup>a</sup> (g mol <sup>-1</sup> )	Total $M_n$ (g mol <sup>-1</sup> )	Molecular mass dispersity, $\mathcal{D}$
OS1	5 000	15 500	20 500	1.17
OS2	2 000	880	2 880	1.10

<sup>a</sup>Calculated based upon <sup>1</sup>H-NMR spectra. <sup>b</sup>Determined using GPC analysis. Here,  $M_n$  is defined as the number average molecular weight of the polymer.

## NANOSTRUCTURED CARBON FROM PEO-*b*-PS AND SINGLE SOLVENT ROUTES

The simple inclusion of a high  $T_g$  polymer block to the micelle core, however, does not guarantee persistent micelle behavior. Indeed, none of the porous carbon reports using micelles with high- $T_g$  blocks were consistent with PMT behavior. These reports<sup>14,38,42,53,54</sup> used poly(ethylene oxide-*b*-styrene) (PEO-*b*-PS) and poly(ethylene oxide-*b*-methyl methacrylate) (PEO-*b*-PMMA) where PS and PMMA have  $T_g$ 's of ~90 and 105 °C, respectively.<sup>66-68</sup> Several PEO-*b*-PS block polymers were synthesized to evaluate possible factors leading to these behaviors (Table 2.1). The above-mentioned reports all used THF as a processing solvent. This is convenient since THF is a good solvent for PEO, PS, and PMMA and is thus able to directly dissolve these block polymers.

Table 2. 2 – Example sample recipes for series OS1-THF with increasing M:T ratios.

M:T Ratio	Mass OS1 <sup>a</sup> (mg)	Total material mass (mg)	Phloroglucinol (mMoles)	Phloroglucinol <sup>b</sup> (mg)	Formaldehyde (mMoles)	Formaldehyde <sup>c</sup> (mg)
0.75	60	45.00	0.28	36.34	0.28	8.65
0.95	60	54.00	0.34	43.61	0.34	10.38
1.00	60	60.00	0.38	48.46	0.38	11.54
1.10	60	66.00	0.42	53.30	0.42	12.69

1.25	60	75.00	0.48	60.57	0.48	14.42
1.40	60	84.00	0.53	67.84	0.53	16.15

<sup>a</sup>Delivered *via* a 30 mg mL<sup>-1</sup> micelle stock solution. <sup>b</sup>Delivered *via* a 100 mg mL<sup>-1</sup> phloroglucinol stock solution. <sup>c</sup>Delivered *via* a 37 wt% formaldehyde solution (see Experimental section).

Such good solvents, however, are also able to plasticize polymer domains that would otherwise be glassy. This possibility was examined using a custom synthesized PEO-*b*-PS polymer termed OS1 (Table 1.1), which was confirmed by DSC to have a glass transition temperature of 99.1 °C (Appendix B.2a). Micelles of OS1 were prepared in a mixture with 80 vol% EtOH, 10 vol% H<sub>2</sub>O, and 10 vol% THF. Here the only good solvent for PS (THF) is present as a minority. Please note that OS1 is not directly dispersible in the mentioned solvent mixture, but rather had to be dissolved in THF initially and gradually brought dropwise towards the final solvent composition. This observation suggests that unimers are not dispersible in this solvent mixture since micelles are not able to be directly formed. Such a lack of unimer exchange would indeed cause OS1 micelles to be present in the solvent mixture. A series of samples were prepared as previously described where the M:T ratio was gradually swept from 0.65–1.65. An excerpt from this data series is shown in Table 2.2. The corresponding SAXS *d*-spacing trends are shown in Fig. 2.2c and d. These data show that the *d*-spacing is relatively constant with increasing M:T ratio which is not consistent with the lattice expansion that is fundamental to the PMT model. Similar to the case with F127, this lack of lattice expansion suggests the presence of dynamic micelles (not PMT behavior) where further material additions lead to a decrease in micelle size thus yielding relatively constant lattice dimensions despite the shifting volume fractions of material and template. The notion of dynamic OS1 micelles here is perhaps surprising considering the noted lack of direct dispersibility for OS1 in this solvent mixture. It may

be that the micelles undergo dynamic chain exchange after combining with the carbon precursors and phase separating from solution. The resulting carbon-rich environment would be reasonably well swollen by THF, giving rise to a reduced effective interaction parameter  $\chi$  combined with plasticization of the PS core, enabling dynamic chain exchange between micelles. These observations led to glassy-PMT design guideline (2): glassy micelle cores require that plasticizing agents such as THF are not present when using the templates.

The exclusion of plasticizers alone also does not guarantee persistent micelle behavior from PEO-*b*-PS or related polymers. Polymer OS2 was prepared to mimic the low molecular mass of common pluronic polymers such as F127 with the substitution of PPO with a PS block. Unlike OS1, OS2 was able to be directly dispersed in EtOH despite it being a traditional non-solvent for PS. A series of samples were prepared as previously described where the M:T ratio was gradually swept from 0.25–1.30 and the corresponding SAXS data are shown in Fig. 2.2e and f. These data do not show a monotonic increase of *d*-spacing with increasing M:T ratio but rather relatively constant values with some scatter. Again, this lack of monotonic lattice expansion is consistent with dynamic micelles despite the presence of a PS block and the absence of traditional PS plasticizers. Two factors likely contribute towards this behavior. First, a polymer's selectivity towards non-solvents decreases as the molecular mass decreases. For example, styrene monomer itself is soluble in EtOH whereas  $> \sim 5000 \text{ g mol}^{-1}$  PS is not. Second, the  $T_g$  of a polymer while constant for large molar mass is typically suppressed in the low molecular mass regime. The well-known Flory-Fox relationship quantifies the  $T_g$  decrease for low molar masses where for PS the  $T_g = 100 - 1.0 \times 10^5 M^{-1} \text{ }^\circ\text{C}$ , with *M* being the polymer molecular mass in  $\text{g mol}^{-1}$

<sup>1,66,67</sup> This equation estimates the PS in OS2 to have a  $T_g$  of  $\sim -20^\circ\text{C}$ . This molar mass, however, is below the range used to derive the model fit and the resulting estimate thus has additional uncertainty. Regardless, this estimate shows that the  $T_g$  can certainly decrease below the processing temperature. Both of these factors enhance the mobility of low molar mass PS chains and can reasonably facilitate dynamic chain exchange when the  $\chi N$  barrier to chain exchange is relatively low due to the low molecular mass. These considerations give rise to two additional glassy-PMT design guidelines: (3) the molecular mass of the intended glassy block must be sufficiently large to realize a suitable  $T_g$  value and (4) the block polymer must not be directly dispersible in the processing solvent. That is, the ability to directly disperse the block polymer in the processing solvent indicates that the intended glassy core block is plasticized and thus not glassy.

## NANOSTRUCTURED CARBON FROM PEO-*b*-PS USING A MULTI-STEP PROCESSING ROUTE

The implementation of glassy-PMTs introduces an apparent paradox in the form of guideline (4): how can one achieve glassy micelle dispersion when the used block polymer must not be directly soluble? This implies an additional glassy-PMT guideline in that (5) an indirect dispersion route with multiple steps can satisfy guideline (4). Here the starting solvent must be a good solvent for both the polymer blocks to assure dispersion. The subsequent addition of solvent(s) that are good for the corona block and poor for the core block leads to micellization (*i.e.* “selective” solvent).

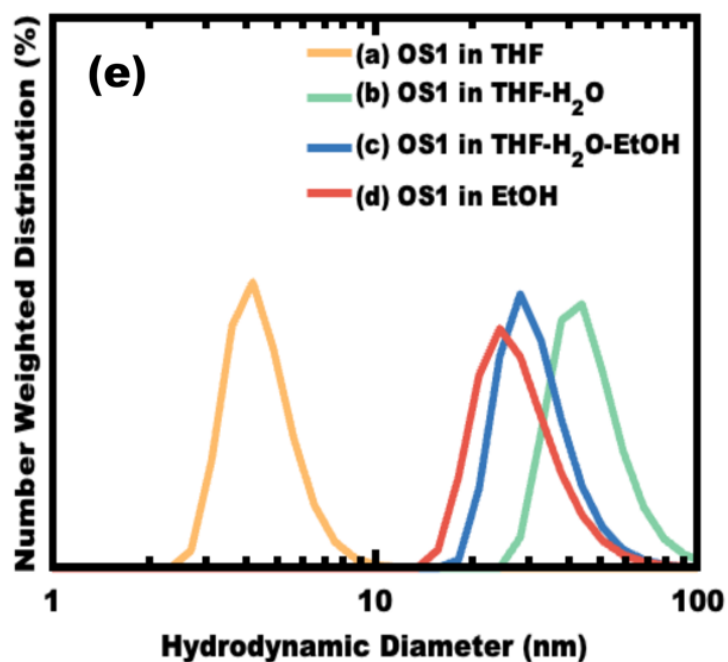
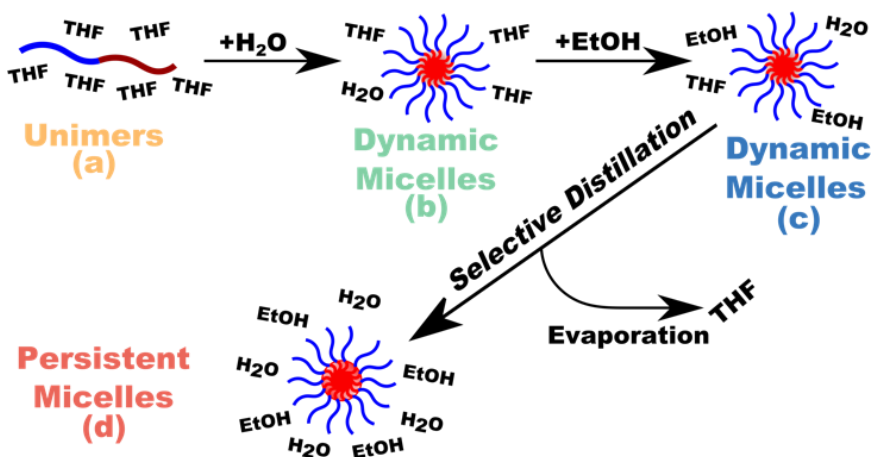


Figure 2. 3 – Schematic representation of glassy-PMT preparation with the polymer OS1. DLS after polymer dissolution in a good solvent, THF (a), reveals unimers in solution. Poor-solvents are next added where first water induces micellization (b) before a large excess of EtOH is added (c). The THF is then removed by rotary evaporation to yield micelles that are dispersed in purely poor solvents for the core block (d). DLS data (e) show the hydrodynamic diameter at each stage of processing.

We note that solvents and non-solvents for polymers are tabulated from various reference sources.<sup>68</sup> As demonstrated above with the OS1-THF, however, the resulting micelle cores can still be plasticized by any remaining trace good solvent at this point.

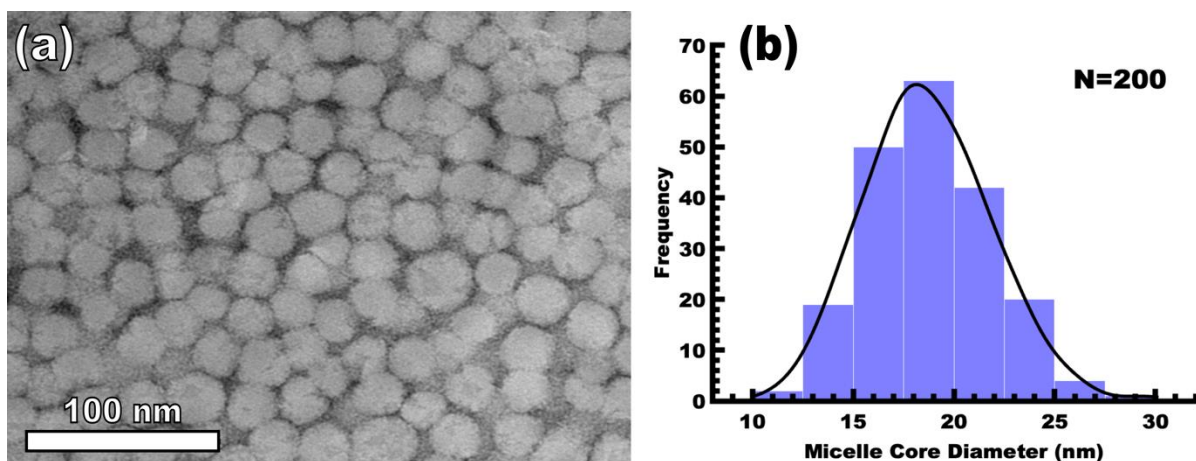
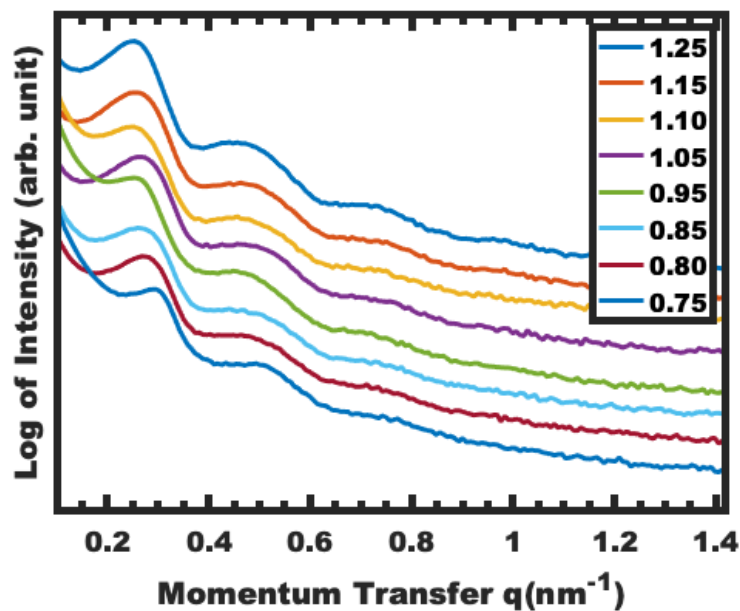


Figure 2. 4 – TEM image of OS1–EtOH micelles (a) and the associated micelle core size distribution (b). The mean diameter and standard-error-of-the-mean of the measured cores are 18.68 and 0.22 nm, respectively. The PEO corona was selectively stained with 1 wt% uranyl acetate for contrast (dark) relative to the unstained PS (light).

Thus, an additional purification step is necessary to remove any non-selective solvents for the core block, which are also simultaneously good solvents for the corona block. Guideline (5) was thus implemented with OS1 by dispersing the polymer in pure THF, followed by the slow addition of water to induce micellization and EtOH to quench molecular dynamics. Next rotary evaporation was used to remove the THF and yield a THF-free dispersion of OS1 in EtOH/H<sub>2</sub>O. This processing pathway along with the number weighted DLS of the micelle solution at each step is shown in Figure 2.3. The DLS results were consistent with OS1 unimers in THF and OS1 micelles in all subsequent solutions involving H<sub>2</sub>O or EtOH. We note that DLS is often unable to distinguish between persistent micelles and dynamic micelles since the concentration of unimers can be below the detection limit.<sup>50</sup> The resulting glassy micelles are able to be imaged by TEM at room temperature owing to the persistence of the glassy cores (Fig 2.4). In contrast, all prior PMT demonstrations utilized low  $T_g$  core blocks and would reorganize upon solvent removal. Statistics were collected from 200 TEM measurements of individual glassy OS1–

EtOH micelles to yield an average template diameter of  $18.68 \pm 0.22$  nm (Fig. 2.4). Please note that a uranyl acetate staining agent was used to selectively stain the PEO coronas for contrast at the core–corona interface. Thus, micelles OS1–EtOH were prepared and characterized before use as templates. A series of samples (OS1–EtOH) were again prepared with the M:T ratio spanning from 0.45–1.65. In contrast to all sample series presented above, series OS1–EtOH exhibited a region of monotonic lattice expansion (decreasing  $q$ -position) as the M:T ratio increased from 0.80–1.30 (Figure 2.5).



*Figure 2. 5* – SAXS of as-made OS1–EtOH samples with increasing material:template ratio. The shift in peak position to decreasing  $q$ -values corresponds to an increase in  $d$ -spacing ( $2\pi/q$ ). The data were offset vertically for clarity.

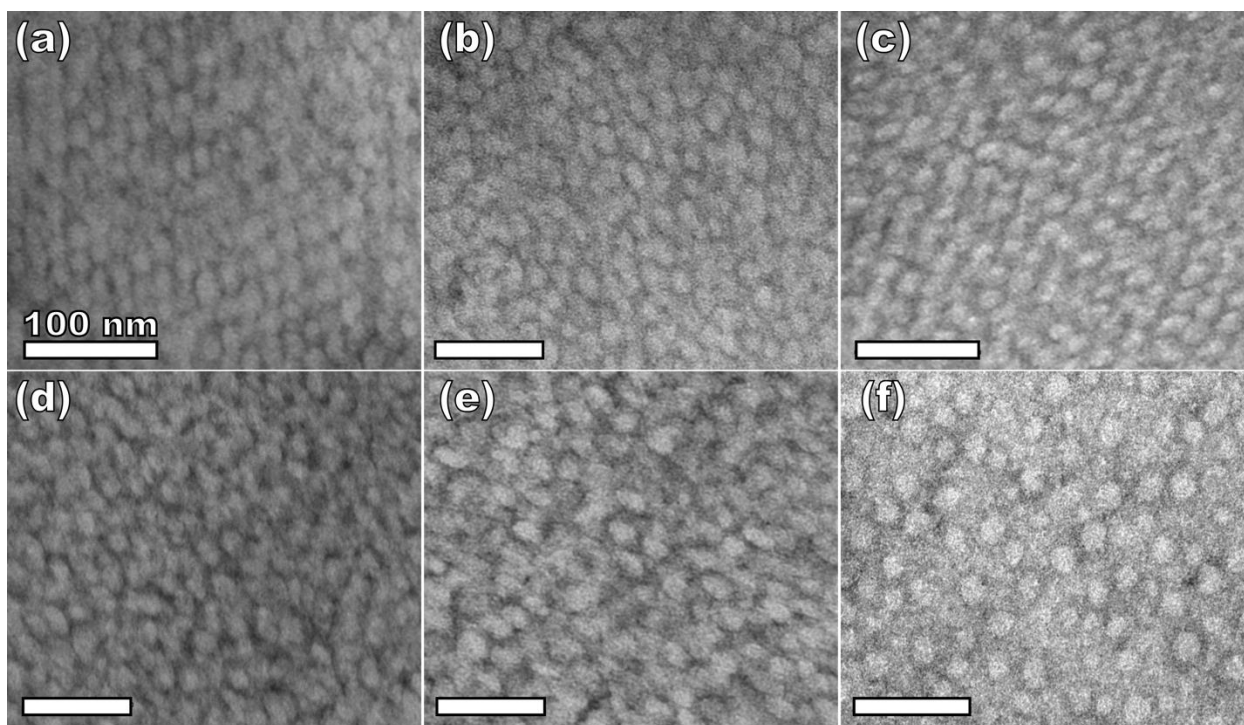


*Figure 2. 6* – TEM images of aged samples from the series OS1–EtOH with material:template ratios of 0.85 (a), 0.95 (b), 1.00 (c), 1.05 (d), 1.10 (e), 1.20 (f). Samples were stained with 1 wt% uranyl acetate to improve contrast.

TEM images of the as-made samples revealed a relatively constant template diameter of ~17.5 nm and increasing wall thickness from 8.00 to 10.74 nm across the series. This ~34% increase in wall thickness across the PMT window is apparent in Figure 2.6. Here we note that the material, but not the micelles, were relatively sensitive to beam damage where the carbon precursors would contract somewhat upon exposure to the electron beam. We direct the reader to Appendix A for clarification on the measurement of the pore and wall dimensions.

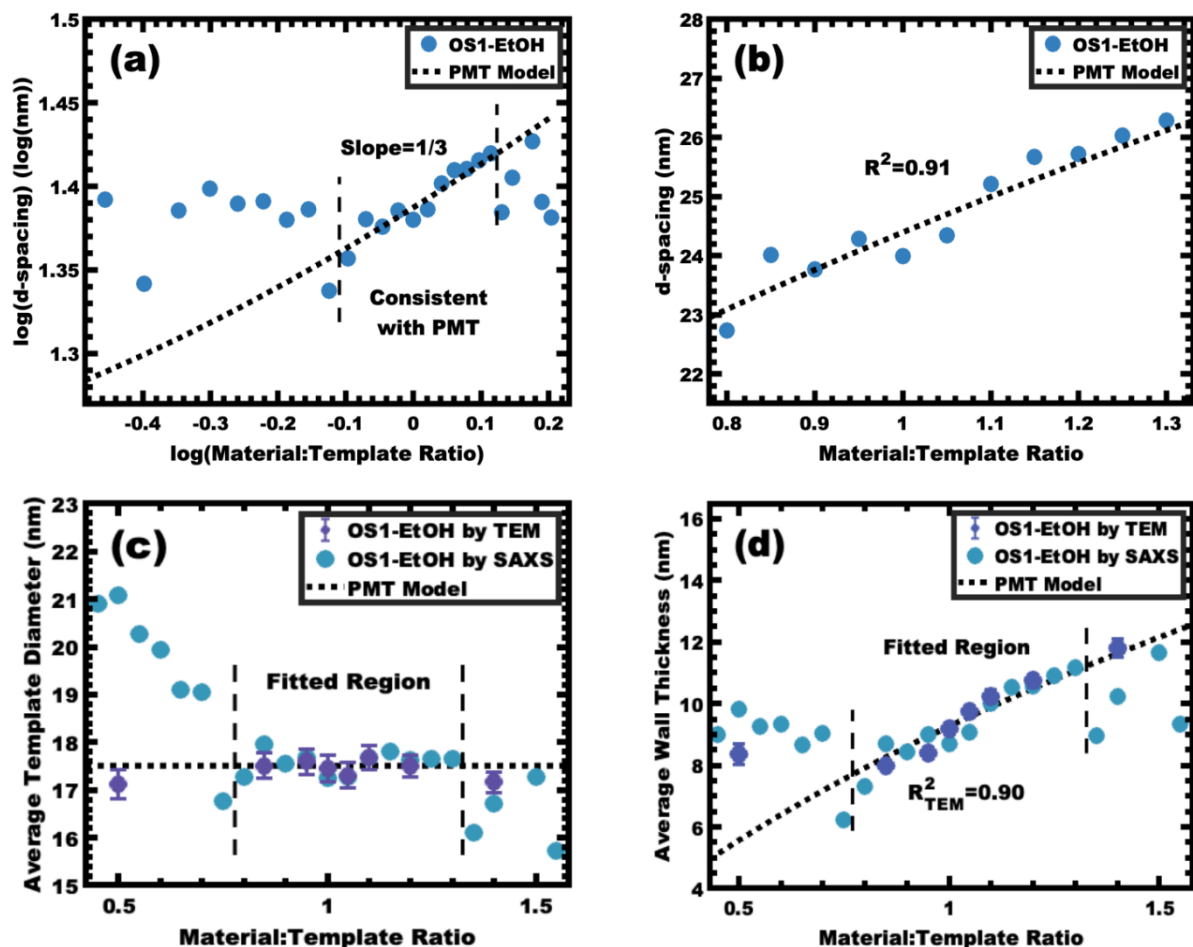


Figure 2. 7 – Analysis of samples from series OS1–EtOH before carbonization. The trends in SAXS peak position were examined using the same log–log (a) and linear–linear (b) plots as before. The region consistent with PMT lattice expansion was identified (a) and used to derive a best-fit to the MCT model (b). The average pore size (c) and wall thickness (d) were calculated using the best-fit model and were compared to the dimensions determined by direct measurements from TEM images. The SAXS and TEM data were from aged samples.

A plot of  $\log(d\text{-spacing})$  vs.  $\log(\text{M:T ratio})$  was used to identify a region with a slope of  $1/3$ , consistent with the PMT model for lattice expansion from  $\text{M:T} = 0.80\text{--}1.30$  (Figure 2.7a). Lower  $\text{M:T}$  ratios exhibited larger  $d\text{-spacing}$ s, presumably due to the low amount of material precursors limiting the contraction of the corona conformation (negative  $\chi_{\text{material-corona}}$ ). Similarly, samples with  $\text{M:T} > 1.3$  exhibited a relatively constant  $d\text{-spacing}$  (Figure

2.7c), consistent with the corona reaching a saturation where the addition of further material precursors leads to precursor phase separation (Figure A.10). The solvent phase was evaporated to recover and quantify the amount of material precursors partitioned into that phase. While most samples in the PMT window had a relatively constant yield of carbon precursors to the micelle phase of ~20%, there was a sharp decrease in the solution material content when M:T > 1.30 (Figure A.8). This observation combined with the lack of further lattice expansion for higher M:T ratios suggests some precipitation of excess material precursors without micelles. The identified window consistent with the PMT model was well-fitted using the previously shown PMT model (micelle core template model), having a goodness of fit  $R^2 = 0.91$  (Figure 2.7b and Table 2.3). Extraction of the pore size and wall thickness values from the SAXS data using the best-fit of the PMT model confirmed a relatively constant template diameter of ~17.5 nm. Here the 11 samples within the PMT window had a template diameter interpreted by the best-fit PMT model spanning from 17.30–17.68 nm, consistent with the TEM average diameter of 17.51 nm (Figure 2.7c). This nominal template dimension of ~17.5 nm closely matched the 18.68 nm core diameter of the glassy micelles themselves, thus providing the first direct evidence of the PMT mechanism. The minor ~1.2 nm difference was statistically significant and is perhaps associated with the carbon precursors residing partly within the PEO–PS interface region, or alternatively the latter formaldehyde treatment inducing minor expansion of the material precursors. The PMT model predicted the average wall thickness to range from 7.42–10.89 nm across the M:T range used for fitting (Figure 2.7d). Similarly, the TEM measurements of wall thickness increased monotonically from 8.00 to 10.74 nm. Regardless of the wall shrinkage from the beam damage, the overall trends were well fitted

by the PMT model with an  $R^2 = 0.90$ . Thus, the as-made/aged series OS1-EtOH was found to be consistent with PMT behavior by both SAXS and TEM measurements. To the best of our knowledge, this is the first report of a polymer template preserving constant dimensions while varying the amount of carbon precursors. As explained using the three counter examples above, equilibration enabled by several modalities leads to a loss of kinetic template control where glassy-PMTs circumvent these challenges.

Table 2. 3 – PMT Model parameters for all sample series

Series Name	Pore Size (nm)	$\beta$	S	$\gamma$	$\alpha$
F127-EtOH	13.50	3.75	1.00	1.00	N/A
OS1-THF	16.63	3.75	1.00	1.00	N/A
OS2-EtOH	13.34	3.75	1.00	1.00	N/A
OS1-EtOH (as-made/aged) <sup>a</sup>	17.51	3.75	1.00	1.00	1.092
OS1-EtOH (carbonized) <sup>a</sup>	10.69	9.98	1.00	1.00	1.044

<sup>a</sup>A best-fit approach was used to fit Model parameters  $\beta$  and  $\alpha$ .

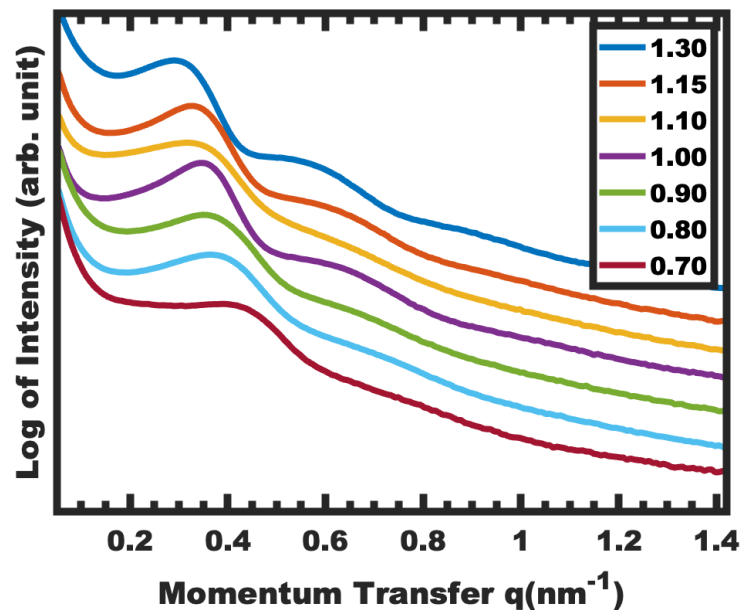


Figure 2. 8 – SAXS of carbonized OS1-EtOH samples with increasing material:template ratio. The shift in peak positions to lower  $q$ -values corresponds to an increase in  $d$ -spacing ( $2\pi/q$ ). The data were offset vertically for clarity.

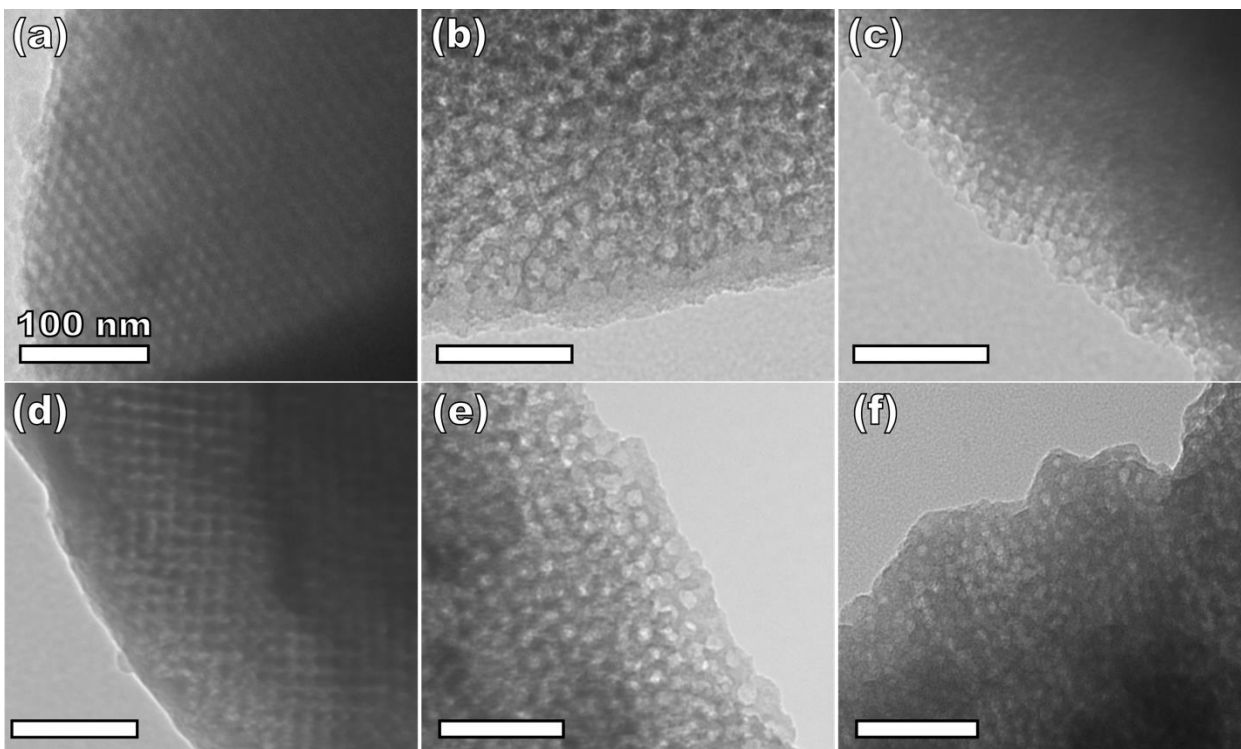


Figure 2. 9 – TEM of carbonized samples from the series OS1–EtOH with material:template ratios of 0.75 (a), 0.85 (b), 0.95 (c), 1.00 (d), 1.15 (e), and 1.30 (f).

Sample series OS1-EtOH was subsequently carbonized at high temperature and characterized by a combination of SAXS, TEM, and BET. The SAXS data of the carbonized OS1–EtOH series again exhibited monotonic lattice expansion, albeit with a ~25% contraction in  $d$ -spacing relative to the as-made samples (Figure 2.8). As expected, the carbon precursors had a mass yield of 30–34% upon carbonization. TEM images of the carbonized series are shown in Figure 2.9. Hundreds of measurements were made upon the TEM images to collect the statistically significant descriptors of the nanostructure from unobstructed images. Here, all samples with M:T > 0.75 had a relatively constant pore size of ~10.7 nm, a 39% contraction from the original template dimension (Table 2.5). Similarly the wall thickness was found to monotonically increase from 7.77–10.35 nm with

increasing material content until M:T = 1.3, the point beyond which the material appeared to phase separate from the micelles.

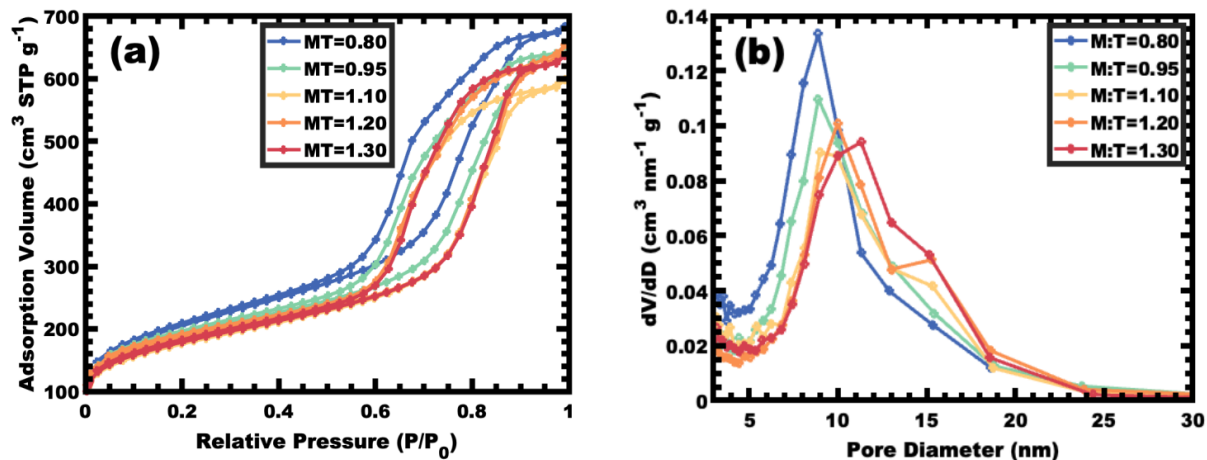


Figure 2. 10 – Nitrogen physisorption isotherms for selected samples from the series OS1–EtOH (a) along with the corresponding BJH pore size analysis from the adsorption branch of the isotherm (b).

Table 2. 4 – Nitrogen physisorption isotherms for select samples from series OS1-EtOH (a) along with the corresponding BJH pore size analysis from the adsorption branch of the isotherm (b).

M:T Ratio	Total surface area (m <sup>2</sup> g <sup>-1</sup> )	Mesopore surface area (m <sup>2</sup> g <sup>-1</sup> )	Total pore volume (cm <sup>3</sup> g <sup>-1</sup> )	Mesopore volume (cm <sup>3</sup> g <sup>-1</sup> )
0.80	732.5	405.4	1.06	0.89
0.95	677.8	341.9	1.01	0.84
1.10	624.1	305.4	0.93	0.76
1.20	658.4	304.2	1.01	0.84
1.30	634.2	313.9	0.99	0.83
1.40	627.1	224.2	1.01	0.82
1.50	535.4	218.6	0.90	0.74
1.65	537.0	206.5	0.90	0.75

The corresponding nitrogen physisorption isotherms and Barrett, Joyner, Halenda method (BJH) analysis are shown in Figure 2.10. The isotherms exhibit classic type IV shape with relatively constant offset between adsorption and desorption branches suggestive of open-ended pores rather than *e.g.*, ink-bottle pores. The BJH pore size distributions were

calculated from the adsorption branch of the isotherms where the templated mesopore volume-weighted average pore diameters ranged from 8.71–10.27 nm (Figure 2.10b and Table 2.5). There was a monotonic size trend in average BJH pore size with M:T where the samples with thinner walls exhibited progressively further pore contraction following carbonization, a trend that is also apparent with SAXS *d*-spacing contraction (Figure A.9). The samples with thinner walls (lower M:T) perhaps experienced greater lattice contraction following carbonization as a result of their lower structural integrity. However, samples with M:T > 1.3 exhibited a larger constant pore size of ~16.6 nm (Fig. A.10). This suggests that the non-proportionate contraction tapers off with increasing M:T until reaching a constant value, similar to the original micelle diameter prior to use as templates (Figure 2.4).

Table 2. 5 – Measurements from series OS1-EtOH after carbonization

M:T Ratio	<i>d</i> -Spacing (nm)	Average TEM pore diameter <sup>a</sup> (nm)	Standard deviation of TEM pore diameter <sup>b</sup> (nm)	Average BJH pore diameter <sup>c</sup> (nm)	Average wall thickness <sup>a</sup> (nm)	Standard deviation of wall thickness <sup>b</sup> (nm)	Percent change in wall thickness (%)
0.75	15.41	10.52 ± 0.17	1.77		7.77 ± 0.16	1.58	N/A
0.80	17.66			8.71			
0.85	17.66	10.45 ± 0.12	1.67		8.02 ± 0.10	1.47	3.2
0.90	18.22	10.93 ± 0.17	1.50		8.65 ± 0.14	1.36	11.3
0.95	19.05			9.34			
1.00	18.73	10.80 ± 0.14	1.40		9.07 ± 0.19	1.86	16.7
1.10	20.27			9.79			
1.15	19.86	10.82 ± 0.18	1.80		9.91 ± 0.17	1.68	27.5
1.20	20.89			10.11			
1.25	21.25	10.61 ± 0.13	1.67		9.96 ± 0.12	1.64	28.2
1.30	21.65	10.58 ± 0.16	1.63	10.27	10.35 ± 0.17	1.78	33.2

<sup>a</sup>Average values are reported ± the standard-error-of-the-mean to indicate the uncertainty in the reported value. <sup>b</sup>The standard deviation of the measured metric are presented to

indicate the statistical distribution of measured values. °The average BJH pore diameter was calculated as a volume-weighted average.

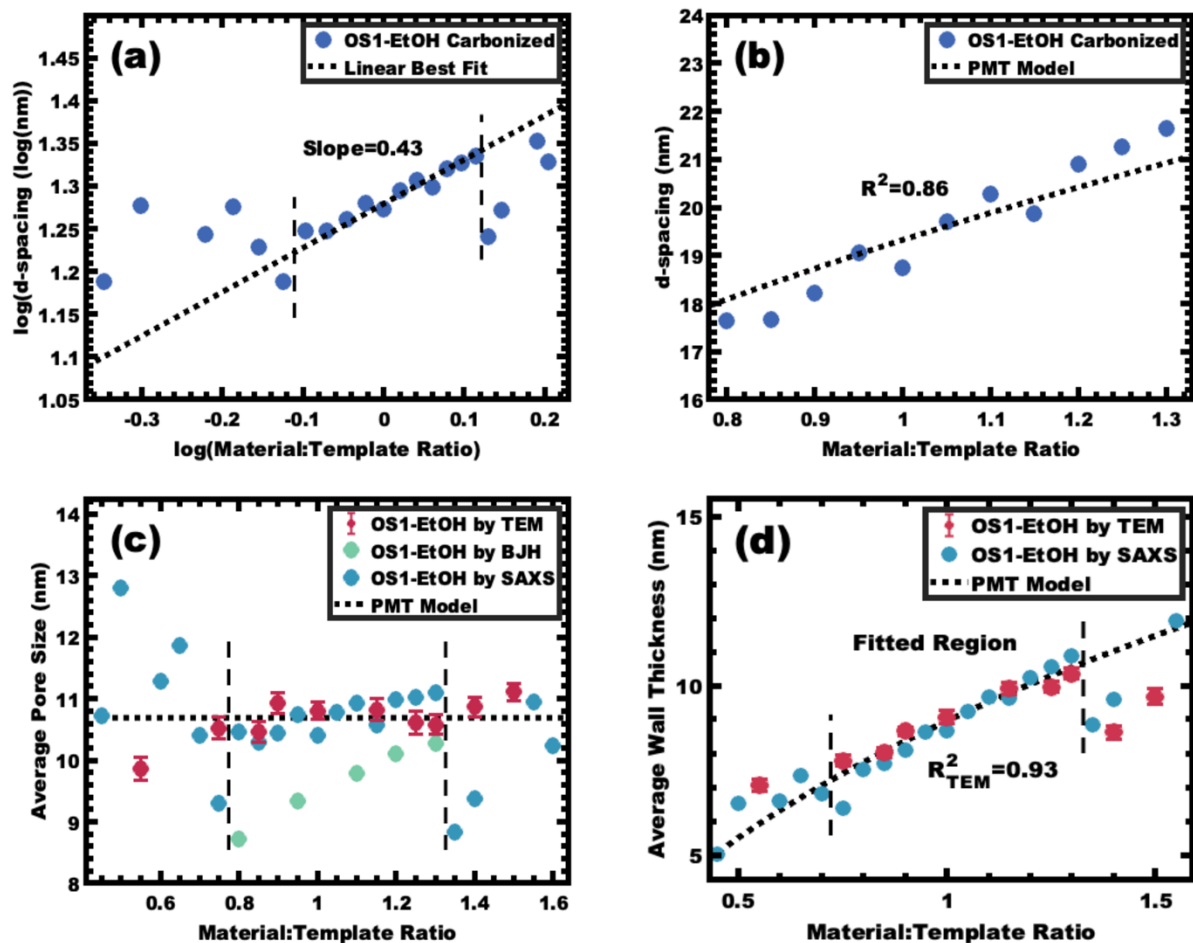


Figure 2.11 – Analysis of samples from series OS1–EtOH following carbonization. The trends in SAXS peak position were examined using the same log–log (a) and linear–linear (b) plots as before. The slope of data in the log–log coordinate space is 0.43 instead of the predicted 1/3. The bounds of the as-made PMT window are denoted with vertical dashed lines. The average pore size (c) and wall thickness (d) were calculated using the best-fit model and were compared to the dimensions determined by direct measurement from TEM images.

Please note however, that the physisorption data includes contributions from any phase separated carbon precursors whereas the SAXS analysis and TEM data were principally corresponding to micelle templated materials. The lack of monotonic trend in mesopore

volume and surface are (Table 2.4) was attributed to this variable material contraction combined with the partial phase separation of material precursors (Fig. A.7 and A.9).

The same modelling and log–log analysis of  $d$ -spacing vs. M:T ratio was used for sample series OS1–EtOH after carbonization. A linear region with a slope of 1/3 is predicted by the PMT model (Figure 2.11a), however the higher best-fit slope of  $\sim 0.4$  was attributed to non-proportionate shrinkage of feature sizes during the high temperature carbonization. Regardless, the trends in  $d$ -spacing were well fitted with the PMT model having a goodness of fit  $R^2 = 0.86$  (Figure 2.11b and Table 2.3). The best-fit model interpretation of the SAXS data also confirmed the relatively constant pore size of  $\sim 10.7$  nm, consistent with both the TEM and BJH statistics (Figure 2.11c). The best-fit PMT model also agreed well with the trend in average TEM wall thickness (Figure 2.11d) with a goodness of fit  $R^2 = 0.93$ . Please note that the inclusion of varying BJH pore size in the model led to lower quality fits so a constant average pore diameter was used for modelling. Despite the non-proportional shrinkage during carbonization, the resulting material exhibited a relatively constant pore diameter with monotonically increasing wall thickness. Thus, the development of glassy-PMT approach enabled custom tailored porous carbon materials with monotonic wall thickness control despite the challengingly slow materials chemistry.

## 2.5 CONCLUSIONS

Porous nanoscale carbon materials are widely used in diverse fields, yet the tailored synthesis of these materials has remained elusive. Persistent micelle templates (PMTs) recently emerged as a novel approach to prepare nanoscale porous materials based uniquely upon kinetic control of polymer micelles. Under kinetic control, micelles maintain a

constant average template diameter despite the challenging solution conditions. However, a drawback with prior PMT demonstrations was limited micelle persistence after solvent evaporation, necessitating rapid thermal cross-linking of material precursors to preserve micelle persistence. This caveat has prevented the application of traditional PMT methods to porous carbons as the materials chemistry generally progresses with slower kinetics and involves the critical transition from a solvent-rich to a materials-rich environment. Thus, a new PMT modality with greatly enhanced persistence was developed to enable the synthesis of custom-tailored porous carbons. A comprehensive set of 5 design guidelines were developed to enable persistent micelle templates with glassy micelle cores (glassy-PMT). In particular, these guidelines show the realization of glassy-PMT from a multistep procedure that traverses from non-selective solvent to purely selective solvent(s) for the corona block that are simultaneously non-solvents for the core block. Our unique solvent pathway yields micelles that are present exclusively in PS non-solvents with cores that are fully immobile and free of plasticizing agents (*i.e.*, glassy). This highly specific processing route is likely part of why others have not broadly utilized such glassy persistent micelle templates despite the popularity of suitable PEO-*b*-PS and PEO-*b*-PMMA polymers. The development of glassy-PMTs also enables the first comparison of a persistent micelle template both before and after use as a template where the dimensions were found to be comparable and are thus the first direct evidence of the PMT mechanism. The results here with porous carbons also highlight the potential of glassy-PMTs to broadly enable tailored nanoscale control with diverse materials chemistries.

## 2.6 REFERENCES

1. Jonas, L. A. Reaction steps in gas sorption by impregnated carbon. *Carbon* **1978**, *16*, 115-119.
2. O'koye, I. P.; Benham, M.; Thomas, K. M. Adsorption of Gases and Vapors on Carbon Molecular Sieves. *Langmuir* **1997**, *13*, 4054-4059.
3. Ryoo, R.; Joo, S. H.; Jun, S. Synthesis of Highly Ordered Carbon Molecular Sieves via Template-Mediated Structural Transformation. *J. Phys. Chem. B.* **1999**, *103*, 7744-7746.
4. Benzigar, M. R.; Talapaneni, S. N.; Joseph, S.; Ramadass, K.; Singh, G.; Scaranto, J.; Ravon, U.; Al-Bahily, K.; Vinu, A. Recent advances in functionalized micro and mesoporous carbon materials: synthesis and applications. *Chem. Soc. Rev.* **2018**, *47*, 2680-2721.
5. Gang, D.; Uddin Ahmad, Z.; Lian, Q.; Yao, L.; Zappi, M. E. A review of adsorptive remediation of environmental pollutants from aqueous phase by ordered mesoporous carbon. *Chem. Eng. J.* **2021**, *403*, 126286.
6. Sircar, S.; Golden, T. C.; Rao, M. B. Activated carbon for gas separation and storage. *Carbon* **1996**, *34*, 1-12.
7. Liang, C.; Li, Z.; Dai, S. Mesoporous Carbon Materials: Synthesis and Modification. *Angew. Chem. Int. Ed.* **2008**, *47*, 3696-3717.
8. Hu, Y.; Florek, J.; Larivière, D.; Fontaine, F.; Kleitz, F. Recent Advances in the Separation of Rare Earth Elements Using Mesoporous Hybrid Materials. *Chem. Rec.* **2018**, *18*, 1261-1276.
9. Joo, S. H.; Choi, S. J.; Oh, I.; Kwak, J.; Liu, Z.; Terasaki, O.; Ryoo, R. Ordered nanoporous arrays of carbon supporting high dispersions of platinum nanoparticles. *Nature* **2001**, *412*, 169-172.
10. Lu, A.; Schmidt, W.; Matoussevitch, N.; Bönemann, H.; Spliethoff, B.; Tesche, B.; Bill, E.; Kiefer, W.; Schüth, F. Nanoengineering of a Magnetically Separable Hydrogenation Catalyst. *Angew. Chem. Int. Ed.* **2004**, *43*, 4303-4306.
11. Zhai, Y.; Dou, Y.; Zhao, D.; Fulvio, P. F.; Mayes, R. T.; Dai, S. Carbon Materials for Chemical Capacitive Energy Storage. *Adv. Funct. Mater* **2011**, *23*, 4828-4850.
12. Roberts, A. D.; Li, X.; Zhang, H. Porous carbon spheres and monoliths: morphology control, pore size tuning and their applications as Li-ion battery anode materials. *Chem. Soc. Rev.* **2014**, *43*, 4341-4256.

13. Eftekhari, A.; Fan, Z. Ordered mesoporous carbon and its applications for electrochemical energy storage and conversion. *Mater. Chem. Front* **2017**, *1*, 1001-1027.
14. Meng, Y.; Gu, D.; Zhang, F.; Shi, Y.; Yang, H.; Li, Z.; Yu, C.; Tu, B.; Zhao, D. Ordered Mesoporous Polymers and Homologous Carbon Frameworks: Amphiphilic Surfactant Templating and Direct Transformation. *Angew. Chem. Int. Ed.* **2005**, *44*, 7053-7059.
15. Zhang, F.; Meng, Y.; Gu, D.; Yan, Y.; Yu, C.; Tu, B.; Zhao, D. A facile aqueous route to synthesize highly ordered mesoporous polymers and carbon frameworks with Ia3d bicontinuous cubic structure. *J. Am. Chem. Soc.* **2005**, *127*, 13508.
16. Liang, C.; Dai, S. Synthesis of Mesoporous Carbon Materials via Enhanced Hydrogen-Bonding Interaction. *J. Am. Chem. Soc.* **2006**, *128*, 5316-5317.
17. Ma, T.; Liu, L.; Yuan, Z. Direct Synthesis of Ordered Mesoporous Carbons. *Chem. Soc. Rev* **2013**, *42*, 3977-4003.
18. Teng, H.; Wang, S. Preparation of porous carbons from phenol-formaldehyde resins with chemical and physical activation. *Carbon* **2000**, *38*, 817-824.
19. Inagaki, M.; Toyoda, M.; Soneda, Y.; Tsujimura, S.; Morishita, T. Templated mesoporous carbons: Synthesis and applications. *Carbon* **2016**, *107*, 448-473.
20. Zakhidov, A. A. Carbon Structures with Three-Dimensional Periodicity at Optical Wavelengths. *Science* **1998**, *282*, 897-901.
21. Liang, C.; Dai, S.; Guiochon, G. A Graphitized-Carbon Monolithic Column. *Anal. Chem.* **2003**, *75*, 4904-4912.
22. Tanev, P. T.; Pinnavaia, T. J. A Neutral Templating Route to Mesoporous Molecular Sieves. *Science* **1995**, *267*, 865-867.
23. Zhao, D.; Huo, Q.; Feng, J.; Chmelka, B. F.; Stucky, G. D. Nonionic Triblock and Star Diblock Copolymer and Oligomeric Surfactant Syntheses of Highly Ordered, Hydrothermally Stable, Mesoporous Silica Structures. *J. Am. Chem. Soc.* **1998**, *120*, 6024-6036.
24. Donnet, J. -B.; Bansal, R. C.; Dekker, M. *Carbon Fibers*; Wiley: New York, 1990; .
25. Liang, C.; Hong, K.; Guiochon, G. A.; Mays, J. W.; Dai, S. Synthesis of a Large-Scale Highly Ordered Porous Carbon Film by Self-Assembly of Block Copolymers. *Angew. Chem. Int. Ed.* **2004**, *43*, 5785-5789.

26. Luz, A. P.; Renda, C. G.; Lucas, A. A.; Bertholdo, R.; Aneziris, C. G.; Pandolfelli, V. C. Graphitization of phenolic resins for carbon-based refractories. *Ceram. Int* **2017**, *43*, 8171-8182.
27. Deng, Y.; Yu, T.; Wan, Y.; Shi, Y.; Meng, Y.; Gu, D.; Zhang, L.; Huang, Y.; Liu, C.; Wu, X.; Zhao, D. Ordered Mesoporous Silicas and Carbons with Large Accessible Pores Templated from Amphiphilic Diblock Copolymer Poly(ethylene oxide)-b-polystyrene. *J. Am. Chem. Soc.* **2007**, *129*, 1690-1697.
28. Chen, D.; Li, Z.; Wan, Y.; Tu, X.; Shi, Y.; Chen, Z.; Shen, W.; Yu, C.; Tu, B.; Zhao, D. Anionic surfactant induced mesophase transformation to synthesize highly ordered large-pore mesoporous silica structures. *J. Mater. Chem* **2006**, *16*, 1511.
29. Fei, H.; Li, W.; Bhardwaj, A.; Nuguri, S.; Ribbe, A.; Watkins, J. J. Ordered Nanoporous Carbons with Broadly Tunable Pore Size Using Bottlebrush Block Copolymer Templates. *J. Am. Chem. Soc.* **2019**, *141*, 17006-17014.
30. Zhu, X. X.; Banana, K.; Yen, R. Pore Size Control in Cross-Linked Polymer Resins by Reverse Micellar Imprinting. *Macromolecules* **1997**, *30*, 3031-3035.
31. Lee, K. T.; Oh, S. M. Novel synthesis of porous carbons with tunable pore size by surfactant-templated sol-gel process and carbonisation. *Chem. Commun.* **2002**, 2722-2723.
32. Ghimbeu, C. M.; Vidal, L.; Delmotte, L.; Le Meins, J.; Vix-Guterl, C. Catalyst-free soft-template synthesis of ordered mesoporous carbon tailored using phloroglucinol/glyoxylic acid environmentally friendly precursors. *Green Chem.* **2014**, *16*, 3079-3088.
33. Zhang, Y.; Yuan, Z.; Zhou, Y. Effect of furfural alcohol/phenol-formaldehyde resin mass ratio on the properties of porous carbon. *Mater. Lett.* **2013**, *109*, 124-126.
34. Lipic, P. M.; Bates, F. S.; Hillmyer, M. A. Nanostructured Thermosets from Self-Assembled Amphiphilic Block Copolymer/Epoxy Resin Mixtures. *J. Am. Chem. Soc.* **1998**, *120*, 8963-8970.
35. Meng, Y.; Gu, D.; Zhang, F.; Shi, Y.; Cheng, L.; Feng, D.; Wu, Z.; Chen, Z.; Wan, Y.; Stein, A.; Zhao, D. A Family of Highly Ordered Mesoporous Polymer Resin and Carbon Structures from Organic-Organic Self-Assembly. *Chem. Mater.* **2006**, *18*, 4447-4464.
36. Huang, Y.; Cai, H.; Yu, T.; Sun, X.; Tu, B.; Zhao, D. Highly Ordered Mesoporous Carbonaceous Frameworks from a Template of a Mixed Amphiphilic Triblock-Copolymer System of PEO-PPO-PEO and Reverse PPO-PEO-PPO. *Chem. Asian J.* **2007**, *2*, 1282-1289.

37. Tanaka, S.; Doi, A.; Nakatani, N.; Katayama, Y.; Miyake, Y. Synthesis of ordered mesoporous carbon films, powders, and fibers by direct triblock-copolymer-templating method using an ethanol/water system. *Carbon* **2009**, *47*, 2688-2698.
38. Lee, K.; Song, H.; Lee, K. H.; Choi, S. H.; Jang, J. H.; Char, K.; Son, J. G. Nickel Nanofoam/Different Phases of Ordered Mesoporous Carbon Composite Electrodes for Superior Capacitive Energy Storage. *ACS Appl. Mater. Interfaces* **2016**, *8*, 22516-22525.
39. Lee, J.; Kim, J.; Hyeon, T. Recent Progress in the Synthesis of Porous Carbon Materials. *Adv. Mater.* **2006**, *18*, 2073-2094.
40. Herou, S.; Ribadeneyra, M. C.; Madhu, R.; Araullo-Peters, V.; Jensen, A.; Schlee, P.; Titirici, M. Ordered mesoporous carbons from lignin: a new class of biobased electrodes for supercapacitors. *Green Chem.* **2018**, *21*, 550-559.
41. Zhang, J.; Deng, Y.; Wei, J.; Sun, Z.; Gu, D.; Bongard, H.; Liu, C.; Wu, H.; Tu, B.; Schüth, F.; Zhao, D. Design of Amphiphilic ABC Triblock Copolymer for Templating Synthesis of Large-Pore Ordered Mesoporous Carbons with Tunable Pore Wall Thickness. *Chem. Mater.* **2009**, *21*, 3996-4005.
42. Deng, Y.; Yu, T.; Wan, Y.; Shi, Y.; Meng, Y.; Gu, D.; Zhang, L.; Huang, Y.; Liu, C.; Wu, X.; Zhao, D. Ordered Mesoporous Silicas and Carbons with Large Accessible Pores Templated from Amphiphilic Diblock Copolymer Poly(ethylene oxide)-b-polystyrene. *J. Am. Chem. Soc.* **2007**, *129*, 1690-1697.
43. Peng, L.; Hung, C.; Wang, S.; Zhang, X.; Zhu, X.; Zhao, Z.; Wang, C.; Tang, Y.; Li, W.; Zhao, D. Versatile Nanoemulsion Assembly Approach to Synthesize Functional Mesoporous Carbon Nanospheres with Tunable Pore Sizes and Architectures. *J. Am. Chem. Soc.* **2019**, *141*, 7073-7080.
44. Trivedi, M.; Peng, F.; Xia, X.; Sepulveda-Medina, P. I.; Vogt, B. D. Control of Pore Size in Ordered Mesoporous Carbon-Silica by Hansen Solubility Parameters of Swelling Agent. *Langmuir* **2019**, *35*, 14049-14059.
45. Liu, C.; Yu, M.; Li, Y.; Li, J.; Wang, J.; Yu, C.; Wang, L. Synthesis of mesoporous carbon nanoparticles with large and tunable pore sizes. *Nanoscale* **2015**, *7*, 11580-11590.
46. Lokupitiya, H. N.; Jones, A.; Reid, B.; Guldin, S.; Stefik, M. Ordered Mesoporous to Macroporous Oxides with Tunable Isomorphic Architectures: Solution Criteria for Persistent Micelle Templates. *Chem. Mater.* **2016**, *28*, 1653-1667.
47. Lan, K.; Liu, Y.; Zhang, W.; Liu, Y.; Elzatahry, A.; Wang, R.; Xia, Y.; Al-Dhayan, D.; Zheng, N.; Zhao, D. Uniform Ordered Two-Dimensional Mesoporous TiO<sub>2</sub>

Nanosheets from Hydrothermal-Induced Solvent-Confined Monomicelle Assembly. *J. Am. Chem. Soc.* **2018**, *140*.

48. Tan, H.; Tang, J.; Henzie, J.; Li, Y.; Xu, X.; Chen, T.; Wang, Z.; Wang, J.; Ide, Y.; Bando, Y.; Yamauchi, Y. Assembly of Hollow Carbon Nanospheres on Graphene Nanosheets and Creation of Iron–Nitrogen-Doped Porous Carbon for Oxygen Reduction. *ACS Nano* **2018**, *12*.
49. Sarkar, A.; Stefik, M. How to make persistent micelle templates in 24 hours and know it using X-ray scattering. *J. Mater. Chem. A* **2017**, *5*, 11840-11853.
50. Sarkar, A.; Evans, L.; Stefik, M. Expanded Kinetic Control for Persistent Micelle Templates with Solvent Selection. *Langmuir* **2018**, *34*, 5738-5749.
51. Lantz, K. A.; Clamp, N. B.; van den Bergh, W.; Sarkar, A.; Stefik, M. Full Gamut Wall Tunability from Persistent Micelle Templates via Ex Situ Hydrolysis. *Small* **2019**, *15*, 1900393-1900403.
52. Sarkar, A.; Thyagarajan, A.; Cole, A.; Stefik, M. Widely tunable persistent micelle templates via homopolymer swelling. *Soft Mater* **2019**, *15*, 5193-5203.
53. Deng, Y.; Liu, J.; Liu, C.; Gu, D.; Sun, Z.; Wei, J.; Zhang, J.; Zhang, L.; Tu, B.; Zhao, D. Ultra-Large-Pore Mesoporous Carbons Templated from Poly(ethylene oxide)-b-Polystyrene Diblock Copolymer by Adding Polystyrene Homopolymer as a Pore Expander. *Chem. Mater.* **2008**, *20*, 7281-7286.
54. Deng, Y.; Liu, C.; Gu, D.; Yu, T.; Tu, B.; Zhao, D. Thick wall mesoporous carbons with a large pore structure templated from a weakly hydrophobic PEO–PMMA diblock copolymer. *J. Mater. Chem.* **2008**, *18*, 91-97.
55. Williams, D. B. G.; Lawton, M. Drying of Organic Solvents: Quantitative Evaluation of the Efficiency of Several Desiccants. *J. Org. Chem.* **2010**, *75*, 8351-8354.
56. Whitfield, R.; Anastasaki, A.; Nikolaou, V.; Jones, G. R.; Engelis, N. G.; Discekici, E. H.; Fleischmann, C.; Willenbacher, J.; Hawker, C. J.; Haddleton, D. M. Universal Conditions for the Controlled Polymerization of Acrylates, Methacrylates, and Styrene via Cu(0)-RDRP. *J. Am. Chem. Soc.* **2017**, *139*, 1003-1010.
57. Scott, T. A. Refractive Index of Ethanol–Water Mixtures and Density and Refractive Index of Ethanol–Water–Ethyl Ether Mixtures. *J. Phys. Chem.* **1946**, *50*, 406-412.
58. Aminabhavi, T. M.; Gopalakrishna, B. Density, Viscosity, Refractive Index, and Speed of Sound in Aqueous Mixtures of N,N-Dimethylformamide, Dimethyl Sulfoxide, N,N-Dimethylacetamide, Acetonitrile, Ethylene Glycol, Diethylene Glycol, 1,4-Dioxane, Tetrahydrofuran, 2-Methoxyethanol, and 2-Ethoxyethanol at 298.15 K. *J. Chem. Eng. Data* **1995**, *40*, 856-861.

59. Foster, J. C.; Carrazzone, R. J.; Spear, N. J.; Radzinski, S. C.; Arrington, K. J.; Matson, J. B. Tuning H<sub>2</sub>S Release by Controlling Mobility in a Micelle Core. *Macromolecules* **2019**, *52*, 1104-1111.
60. Löbbling, T. I.; Ikkala, O.; Gröschel, A. H.; Müller, A. H. E. Controlling Multicompartment Morphologies Using Solvent Conditions and Chemical Modification. *ACS Macro Lett.* **2016**, *5*, 1044-1048.
61. Choi, S.; Lodge, T. P.; Bates, F. S. Mechanism of Molecular Exchange in Diblock Copolymer Micelles: Hypersensitivity to Core Chain Length. *Phys. Rev. Lett.* **2010**, *104*, 047802.
62. Choi, S.; Bates, F. S.; Lodge, T. P. Molecular Exchange in Ordered Diblock Copolymer Micelles. *Macromolecules* **2011**, *44*, 3594-3604.
63. Faucher, J. A. The dependence of glass transition temperature on molecular weight for poly(propylene oxide) and poly(butylene oxide). *Polym. Lett.* **1965**, *3*, 143-145.
64. Stefik, M.; Song, J.; Sai, H.; Guldin, S.; Boldrighini, P.; Orilall, M. C.; Steiner, U.; Gruner, S. M.; Wiesner, U. Ordered mesoporous titania from highly amphiphilic block copolymers: tuned solution conditions enable highly ordered morphologies and ultra-large mesopores. *J. Mater. Chem. A* **2015**, *3*, 11478-11492.
65. Alberius, P. C. A.; Frindell, K. L.; Hayward, R. C.; Kramer, E. J.; Stucky, G. D.; Chmelka, B. F. General Predictive Syntheses of Cubic, Hexagonal, and Lamellar Silica and Titania Mesostructured Thin Films. *Chem. Mater* **2002**, *14*, 3284-3294.
66. Fox, T. G.; Flory, P. J. Second-Order Transition Temperatures and Related Properties of Polystyrene. I. Influence of Molecular Weight. *J. Appl. Phys.* **1950**, *21*, 581-591.
67. Fox, T. G.; Flory, P. J. The glass temperature and related properties of polystyrene. Influence of molecular weight. *J. Polym. Sci.* **1954**, *14*, 315-319.
68. Brandrup, J.; Immergut, E. H.; Grulke, E. A. *Polymer Handbook*; Wiley-Interscience: Boca Raton, FL, 1999.

CHAPTER 3: UNIMER SUPPRESSION ENABLES  
SUPERSATURATED HOMOPOLYMER SWOLLEN MICELLE  
STATES WITH LONG-TERM STABILITY AFTER GLASSY  
ENTRAPMENT<sup>2</sup>

---

<sup>2</sup> Adapted from Williams, E. R.; Ruff, C. X.; Stefik, M. Unimer Suppression Enables Supersaturated Homopolymer Swollen Micelle States with Long-Term Stability after Glassy Entrapment. *Submitted*.

### 3.1 ABSTRACT

The size of polymer micelles is critical for a range of applications where the ability to adjust and lock in specific stable sizes has remained largely elusive. While micelle swelling agents are well known, their dynamic re-equilibration in solution implies limited stability. Here, a processing sequence is studied where homopolymer swelling is combined with glassy-core (“persistent”) micelles. This path-dependent process was found to sensitively depend on unimer concentration as revealed by DLS, SAXS, and TEM analysis. Here, lower-selectivity solvents led to the formation of unimer-homopolymer aggregates and eventual precipitation. In contrast, higher-selectivity solvent combinations enabled supersaturated homopolymer swelling of micelles favored by rapid homopolymer insertion. The demonstrated 39.8–99.6 nm exceeded prior equilibrium demonstrations and subsequent core vitrification enabled size persistence beyond 6 months. Lastly, micelle core size analysis upon swelling indicated a plateau in the interfacial area per chain, suggesting a critical interfacial density for corona chains to screen core-solvent interactions.

## 3.2 INTRODUCTION

Amphiphilic block polymer micelles have wide-ranging applications in the fields of drug delivery,<sup>1-6</sup> nanoreactors,<sup>7-10</sup> and as templates for organizing nanostructured materials.<sup>11,12</sup> When in solution, the equilibrium size of a micelle is decided by a balance of entropic and enthalpic contributions to the free energy. Notably the entropic contribution of core chain stretching to fill space and the enthalpic contribution of the micelle-solvent interface.<sup>13</sup> Equilibrium micelle sizes are well known to be adjustable with hydrophobic core swelling molecules. For example, organic solvent such as 1,3,5-trimethylbenzene,<sup>14</sup> other hydrocarbons<sup>15-20</sup> and even high-pressure gasses can swell micelle cores.<sup>21</sup> Thus, a range of micelle sizes are generally achievable from a single block polymer with a properly selected swelling agent.<sup>19,22</sup> Homopolymer swelling agents benefit from being non-volatile, however, these too are generally reported with narrow tunability. For example, PEO-*b*-PS micelles swollen with PS homopolymer in THF led to an increase in micelle size from 26.0–39.4 nm with up to 20 wt% PS where higher loadings led to uncontrolled and multimodal size distributions.<sup>23</sup> More recently, kinetically trapped (“persistent”) micelles of poly(ethylene oxide-*b*-hexyl acrylate) (PEO-*b*-PHA) were shown to be swellable with PHA homopolymer from 13.3–41.9 nm before transitioning to multimodal size distributions.<sup>24</sup> These swollen persistent micelles were noted to exhibit dynamic homopolymer exchange i.e., active diffusion of homopolymer through the solvent phase from one micelle to another. Thus, the swollen state was only metastable, leading to PHA homopolymer phase separation within a day.

Applications that depend upon specific micelle dimensions benefit from robust size persistence. However, dynamic (equilibrating) micelles are naturally unstable in the sense that their aggregation number is depended upon the local environmental conditions (e.g., temperature, solvent etc.). As noted above, the stability of persistent micelles<sup>25</sup> swollen with homopolymer can also be limited by the active exchange of homopolymer chains.<sup>24</sup> Here, the requirement for low molecular mass homopolymer naturally poses a challenge to  $\chi N$  based control, where  $\chi$  is the effective interaction parameter between the homopolymer and the solvent ( $\chi_{\text{hPS-solvent}}$ ) and  $N$  is proportional to the degree of polymerization.<sup>24-29</sup> Glassy-core micelles offer a more robust modality of arresting chain exchange through core block vitrification rather than a fickle  $\chi N$  barrier, however, this approach has yet to be elaborated with homopolymer swelling. A recent study of glassy persistent micelles enumerated a set of design criteria necessary for glassy kinetic control: (1) the block polymer should feature a high- $T_g$  core block, (2) the core block molecular mass must be sufficient to realize high- $T_g$  behavior, and (3) all plasticizing solvents for the core block (THF, DCM, etc.) must be removed through e.g., dialysis or selective distillation after micelle formation. A distinct advantage of glassy persistent micelles is that they retain their dimensions essentially indefinitely in the absence of plasticizers or elevated temperatures. With homopolymer swollen glassy micelles being understudied, there remain many practical questions as to what changes occur at each stage of processing and how these changes correspond to fundamental driving forces.

Herein, a sequence of detailed characterizations are used to understand the changes occurring throughout the processing pathway of homopolymer-swollen glassy persistent micelles for the first time. It is first shown that the progression from non-selective to

selective solvents brings about micellization of the PEO-*b*-PS diblock and that subsequently added homopolymer preferentially resides in the solution phase until a critical selective solvent composition is reached that drives the homopolymer into dynamic micelles. Lastly, these swollen dynamic micelles are vitrified through the removal of all plasticizing solvent, thus being dispersed in purely selective solvent. Careful analysis of the corresponding micelle dimensions as a function of homopolymer loading revealed a trend towards constant interfacial chain density, suggesting a critical chain density to limit the core-solvent interfacial energy.

### 3.3 EXPERIMENTAL METHODS

#### MATERIALS

Anisole (99%, BeanTown Chemical), chloroform (>99% Aldrich), ethanol (EtOH, 200 proof, Deacon Laboratories), methanol (MeOH, 99.8%, Fisher), and methylene chloride (DCM, 99%, Fisher) were stored over 50 vol% molecular sieves (3Å, 8–12 mesh, Acros Organics) for a week prior to use.<sup>30</sup> Cu(I)Br (99.99%, Aldrich), N,N,N',N'',N''-pentamethyldiethylenetriamine (PMDETA, 98+%, Acros Organics), N,N'-dicyclohexylcarbodiimide (DCC, 99.8% BeanTown Chemical) and N,N-dimethylformamide (DMF, 99.8%, Acros Organics) were all stored in an argon glovebox. L-ascorbic acid (ACS Grade, VWR), 2-bromopropionic acid (>99%, Aldrich), Cu(II)Br (99%, Sigma), ethyl 2-bromopropionate (EBPA, 99%, Aldrich), poly(ethylene oxide) methyl ether (PEO,  $M_n = 5,000 \text{ g mol}^{-1}$ , Sigma), formaldehyde (37% in aq. solution stabilized with 10–15% methanol, Alfa Aesar), hexanes (>98.5%, Fisher), phenol (crystals, ACS Grade, VWR), 4-(dimethylamino)pyridine (DMAP, 99%, Aldrich), and sodium

hydroxide (Macron, 99+%) were all used as received. Styrene (99%, stabilized, Acros Organics) was passed over a basic alumina column just prior to use to remove inhibitor.

#### SYNTHESIS OF THE (5k)PEO-BR MACROINITIATOR

A Steglich esterification was used to produce a macroinitiator for atom-transfer radical polymerization (ATRP). The macroinitiator synthesis is explained elsewhere in greater detail.<sup>26</sup> In brief, 20 g of 5,000 g mol<sup>-1</sup> (4.0 mmol) PEO methyl ether was dissolved in 100 mL of anhydrous chloroform. Next, 1.33 mL (8.00 mmol) of 2-bromopropionic acid was added dropwise with stirring. The flask was then chilled with an ice water bath for 10 minutes prior to the addition of 1.65 g (8.00 mmol) of DCC and 0.489 g (3.20 mmol) of DMAP. The flask was then allowed to stir for another 10 minutes before the ice bath was removed. The reaction was stirred at room temperature for 18 hours. Once the reaction had finished, the crude mixture was gravity filtered through a Whatman 2V filter paper with a diameter of 270 mm to remove the urea by-product. The solid by-product was discarded while the macroinitiator filtrate was retained. This filtrate was then concentrated into a viscous liquid by the removal of excess chloroform through rotary evaporation. The solid product was collected and allowed to dry in a vacuum chamber overnight without heating.

#### SYNTHESIS OF THE OS DIBLOCK

The PEO-*b*-PS diblock was prepared by activators generated by electron transfer atom-transfer radical polymerization (AGET-ATRP)<sup>31</sup> using the following molar ratios: (5k)PEO-Br : PMDETA : Cu(II)Br : Ascorbic Acid : Styrene of 1.00 : 1.00 : 0.45 : 450. Styrene monomer was passed over a basic alumina column immediately prior to use to

remove inhibitor. In a 100 mL round-bottom flask, 30.9 mL (270.0 mmol) of styrene was added to 3.00 g (0.600 mmol) of the previously synthesized (5k)PEO-Br macroinitiator and sealed with a rubber septum. This reaction mixture was then sparged with nitrogen gas for 20 minutes. Separately, stock solutions of ascorbic acid and Cu(II)Br were prepared in 50/50 vol.% mixtures of DMF/anisole with concentrations of 12.5 and 30 mg mL<sup>-1</sup>, respectively. These solutions were also sparged with nitrogen for 10 minutes prior to taking aliquots for the polymerization. Next, 4.46 mL (0.600 mmol) of the Cu(II)Br and 3.80 mL (0.270 mmol) of the ascorbic acid stock solutions were injected into the reaction mixture. This was followed by the injection of 125 µL (0.600 mmol) of PMDETA after which time the reaction mixture was placed in an oil bath preheated to 110 °C. The reaction was allowed to proceed for 18 hours. The reaction mixture was then placed in the freezer for 1 hour and vented to air to terminate the polymerization. The crude reaction mixture was then solubilized with DCM and passed over a basic alumina column to remove copper salts. The product was then concentrated by rotary evaporation to a viscous liquid and precipitated in 10× volume excess of room-temperature MeOH by a dropwise addition. The product was then collected by gravity filtration and dried under vacuum without heat prior to characterization.

#### SYNTHESIS OF THE hPS HOMOPOLYMER

The hPS homopolymer was prepared by ATRP<sup>32</sup> using the following molar ratios of EBPA : PMDETA : Cu(I)Br : Styrene of 1.00 : 1.00 : 1.00 : 100. Styrene monomer was passed over a basic alumina column immediately prior to use to remove inhibitor. A volume of 6.32 mL (55.2 mmol) of styrene was combined with 71.7 µL (0.552 mmol) of EBPA in a

25 mL round-bottom flask and sealed with a rubber septum. In an argon glovebox, 79.2 mg (0.552 mmol) of Cu(I)Br was dissolved in 115.3  $\mu$ L (0.552 mmol) of PMDETA and 0.40 mL of toluene. This solution was then injected into the reaction flask which was placed in a preheated oil bath set to 110 °C. The reaction was allowed to polymerize for 18 hours. The reaction mixture was then placed in the freezer for 1 hour and vented to air to terminate the polymerization. The crude reaction mixture was then solubilized with methylene chloride and passed over a basic alumina column to remove copper salts. The product was then concentrated by rotary evaporation to a viscous liquid and precipitated in 10 $\times$  volume excess of room temperature MeOH by a dropwise addition. The product was collected by gravity filtration and dried under vacuum without heat prior to characterization.

#### SYNTHESIS OF PF-RESOL CARBON PRECURSORS

Phenol-formaldehyde based carbon precursors were prepared in a previously reported manner<sup>33</sup> but with a refined protocol for removal of the NaCl by-product. In a typical synthesis, 3.05 g (32.40 mmol) of phenol crystals were dissolved in 0.65 mL (4.06 mmol) of a 20 wt% NaOH (aq) solution. Next, 5.25 g (64.93 mmol) of the 37% formaldehyde solution was added, and the reaction was heated to 80 °C for 1 hour, during which time a color change from clear to a pale yellow was noted. The reaction mixture was then neutralized with 37% HCl and NaCl by-product removed by successive crystallizations from hot isopropanol at 80 °C. This process was repeated until no more NaCl crystals were evident by eye. Excess isopropanol was then removed by evaporation under reduced pressure to yield the final phenol-formaldehyde carbon resol.

## POLYMER CHARACTERIZATION

The molar mass of the OS diblock was determined using nuclear magnetic resonance (NMR) spectroscopy while gel permeation chromatography (GPC) was used to evaluate the molar mass of the hPS diblock as well as the molar mass dispersities ( $D$ ) of both polymers. All proton NMR ( $^1\text{H-NMR}$ ) spectra were collected using a Bruker Avance III HD 300. The molar mass ( $M_n$ ) of the OS diblock was determined by integration ratios between the aromatic styrene  $-\text{C}_6\text{H}_5$  signal ( $\delta = 6.30\text{--}7.26$  ppm) and the known (5k)PEO ether signal  $-\text{OCH}_2\text{CH}_2-$  signal ( $\delta = 3.66$  ppm). All GPC data were collected using a Waters gel permeation chromatography GPC instrument equipped with a 515 HPLC pump, a 2410 refractive index detector and three styragel columns (HR1, HR3, HR4) in the effective molecular mass range of 0.1–5, 0.5–30, 5–600  $\text{kg mol}^{-1}$ , respectively. The eluent used was THF at a temperature of 30 °C and a flow rate of 1  $\text{mL min}^{-1}$ . The instrument was calibrated with polystyrene standards (2570, 1090, 579, 246, 130, 67.5, 34.8, 18.1, 10.4, 3.4, and 1.6  $\text{kg mol}^{-1}$ ) received from Polymer Laboratories. The GPC samples were prepared by dissolution in THF at a concentration of  $\sim 10$   $\text{mg mL}^{-1}$  and were filtered through a syringe filter with a pore diameter of 0.2  $\mu\text{m}$  just prior to injection.

## PREPARATION OF GLASSY MICELLE STOCK SWOLLEN WITH hPS

A typical synthesis involved dissolving 150 mg of OS in 3 mL of DCM. To this solution was added 1 mL of EtOH in a dropwise manner with frequent wrist stirring. The solution was then placed on a shaker at 300 RPM for 15 mins. This process was repeated until 5 mL of EtOH had been added. The concentration of the OS was 15  $\text{mg mL}^{-1}$  for the 50/50 and 58/42 vol% EtOH/DCM samples and 18.7  $\text{mg/mL}$  for the 63/37 vol% EtOH/DCM

sample. In a separate vial, the desired amount of polystyrene homopolymer (hPS) was dissolved in DCM and EtOH was added such that the final concentration was  $10 \text{ mg mL}^{-1}$  and the solution composition was 40 vol% EtOH, 60 vol% DCM. The hPS solution was then slowly added dropwise to the OS solution, stirring vigorously. The resulting micelle solution was then quenched by a dropwise addition of the micelle solution into 50 mL of EtOH with vigorous stirring. DCM was then removed from the solution by rotary evaporation at  $40 \text{ }^\circ\text{C}$ .

### SAXS CHARACTERIZATION

Small-angle X-ray Scattering (SAXS) measurements were performed on micelle stocks in solution and carbon powders after aging heat treatments. X-ray experiments were conducted using a SAXSLab Ganesha instrument at the South Carolina SAXS Collaborative (SCSC). A Xenocs GeniX 3D microfocus source was used with a copper target to generate a monochromatic beam with a wavelength of 0.154 nm. The instrument was calibrated just prior to any measurement using the National Institute of Standards and Technology (NIST) reference material 640d silicon powder with a peak position of  $2\theta = 28.44^\circ$ , where  $2\theta$  refers to the total scattering angle. A Pilatus 300k detector (Dectris) was used to collect the two-dimensional (2D) scattering pattern with nominal pixel dimensions of  $172 \times 172 \text{ } \mu\text{m}^2$ . The SAXS data were acquired with an X-ray flux of  $\sim 1.2 \text{ M}$  photons per second incident upon the sample with a sample-to-detector distance of 1502 mm. Micelle solutions were loaded into a 0.9 mm outer diameter borosilicate glass capillary (Charlessupper) followed by a flame sealing treatment and an additional sealing with candle wax. The 2D images were azimuthally integrated to yield the scattering vector and

intensity using SAXSGUI software. Unless otherwise stated, micelles in solution were fitted using the program SASFit to a sphere with Gaussian chains model incorporating a dozier background term to account for high- $q$  “blob” scattering. Some samples were fitted using McSAS version 1.3.1 using a simple sphere model with one active parameter and 200 refinement repetitions.

#### TRANSMISSION ELECTRON MICROSCOPY (TEM)

Electron microscopy images were collected in bright-field imaging mode using a JEOL 1400 Plus Transmission Electron Microscope with an accelerating voltage of 120keV. TEM grids were prepared by placing a 20  $\mu\text{L}$  drop at 5 mg mL<sup>-1</sup> concentration onto a carbon coated grid and allowing the sample to sit unperturbed for 5 minutes. Staining was performed by adding a 20  $\mu\text{L}$  drop of 1 wt% aqueous uranyl acetate solution and wicking the grid dry after 10 minutes.

### 3.4 RESULTS AND DISCUSSION

The ability to widely adjust micelle sizes and lock in specific desired dimensions has remained especially elusive over the years. As introduced above, prior micelle swelling demonstrations either lacked size-persistence due to dynamic block polymer exchange or lack longevity due to the dynamic exchange of homopolymer. Achieving kinetic control over both block polymer and homopolymer chains has remained challenging, with there currently being no prior report of processing conditions that lead to kinetic entrapment of both simultaneously. This challenge is in part due to a limited understanding of the sequence of events that can occur during homopolymer swelling which are further

complicated by plasticization/vitrification when using glassy-core micelles. The strategy herein developed features homopolymer swelling for widely adjustable micelle core size through the incorporation of a glassy core block and glassy homopolymer for long-term size-persistence following vitrification. Such kinetically controlled formation processes are naturally path dependent. The method studied here is based upon three steps: (1) micellization of the diblock polymer, (2) incorporation of the homopolymer, and (3) vitrification of the micelle cores. A poly(ethylene oxide-*b*-styrene) (PEO-*b*-PS, **OS**) was chosen as a prototypical amphiphilic block polymer which has the ability to form micelles with a glassy PS core and a solvated PEO corona in selective (hydrophilic) solvents. The following two sections detail the processing of block polymer alone and then block polymer with homopolymer.

#### MICELLIZATION OF PEO-*b*-PS

The processing began with the block polymer being dispersed in a non-selective “good solvent” for both blocks. For PEO-*b*-PS, dichloromethane (DCM) was selected as the first solvent amongst many candidates that are plasticizing/good solvents including tetrahydrofuran (THF), N,N-dimethylformamide (DMF), chloroform, acetonitrile, ethyl acetate and toluene. The choice of DCM here is particularly motivated due to its ease of removal through selective distillation due to its low boiling point. The solution containing **OS** in DCM was examined by DLS (Figure 3.1) where the ~8 nm hydrodynamic diameter indicates the presence of free diblock (unimer) chains without larger features suggesting a lack of micelle formation. Selective solvent was next used to induce micellization. As the final goal is to disperse glassy micelles in this selective solvent, it is important that is also

be non-plasticizing towards the polystyrene core block to enable subsequent vitrification. A test towards this end is to check whether the block polymer or homopolymer are directly dispersible in this solvent. Here, direct dispersibility would indicate plasticization i.e., a solvent that is not suitable for glassy core micelles.<sup>34</sup> For the present case of **OS**, ethanol (EtOH), methanol (MeOH), and water (H<sub>2</sub>O) were all found to be non-plasticizing and sufficiently selective. This extent of selectivity is important to later control the localization of PS homopolymer (**hPS**), *vide infra*.

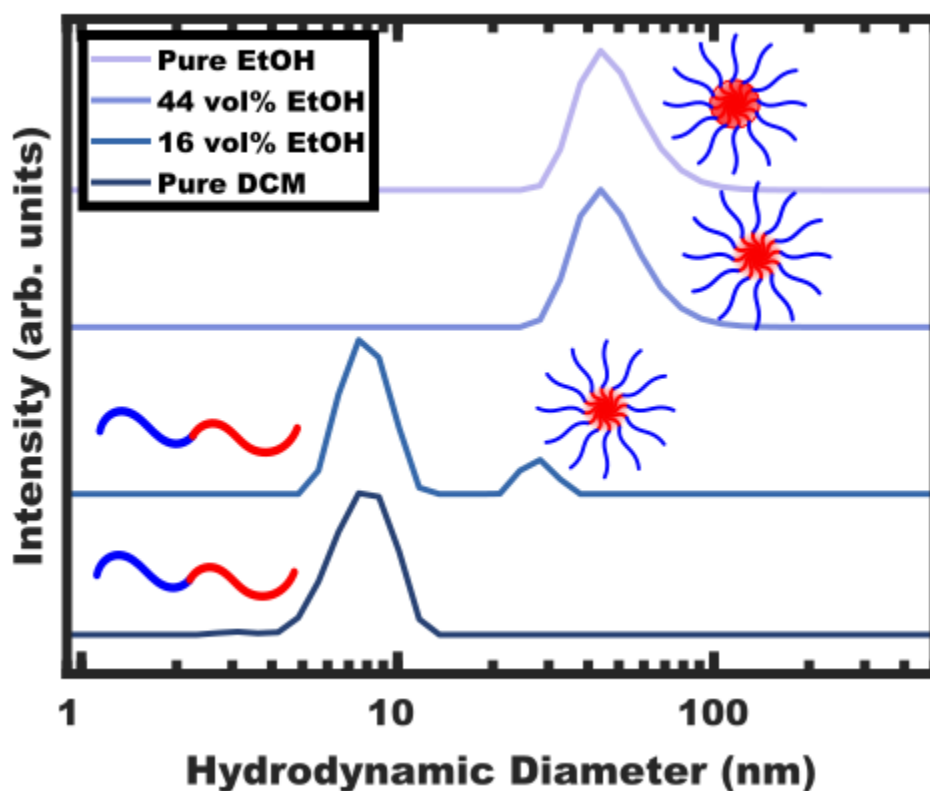


*Figure 3. 1* – DLS data during **OS** dispersion in non-selective solvent (pure DCM) and gradual **OS** micellization through the addition of selective solvent (EtOH). Finally, selective distillation resulted in glassy-core micelles dispersed in a purely selective solvent (pure EtOH). The volume fraction of EtOH is given with respect to the total solution volume. The plots were offset vertically for clarity.

EtOH was selected to induce micellization of the **OS** block polymer. The progressive aggregation of **OS** with EtOH addition was tracked by DLS (Figure 3.1) where the hydrodynamic diameter of free chains ( $< \sim 10$  nm) is distinctly different from their micelle counterparts ( $> \sim 20$  nm). Micellization first became apparent at 16 vol% EtOH where the DLS intensity data corresponded to a majority of unimers with a minority of  $\sim 30$  nm micelles. Here, any observable quantity of free unimers indicates dynamic micelles with a constant unimer concentration equal to the critical micelle concentration (CMC). Further increasing the EtOH content to 44 vol% lead to a lack of observable unimers (decreasing

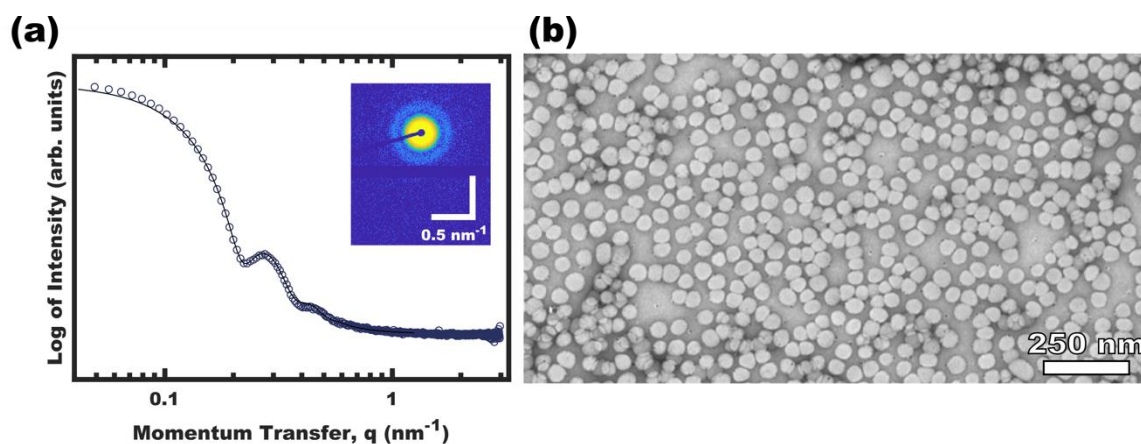


*Figure 3. 2* – Representative SAXS and TEM data for **OS** micelles in pure EtOH. The 2D SAXS pattern (inset, log(intensity) color scale) was radially integrated to yield the reduced plot which was fitted with a micelle form factor model (a). The TEM micrograph of **OS** micelles after staining with 1% uranyl acetate to enhance the contrast between PS (light) and PEO (dark) (b).

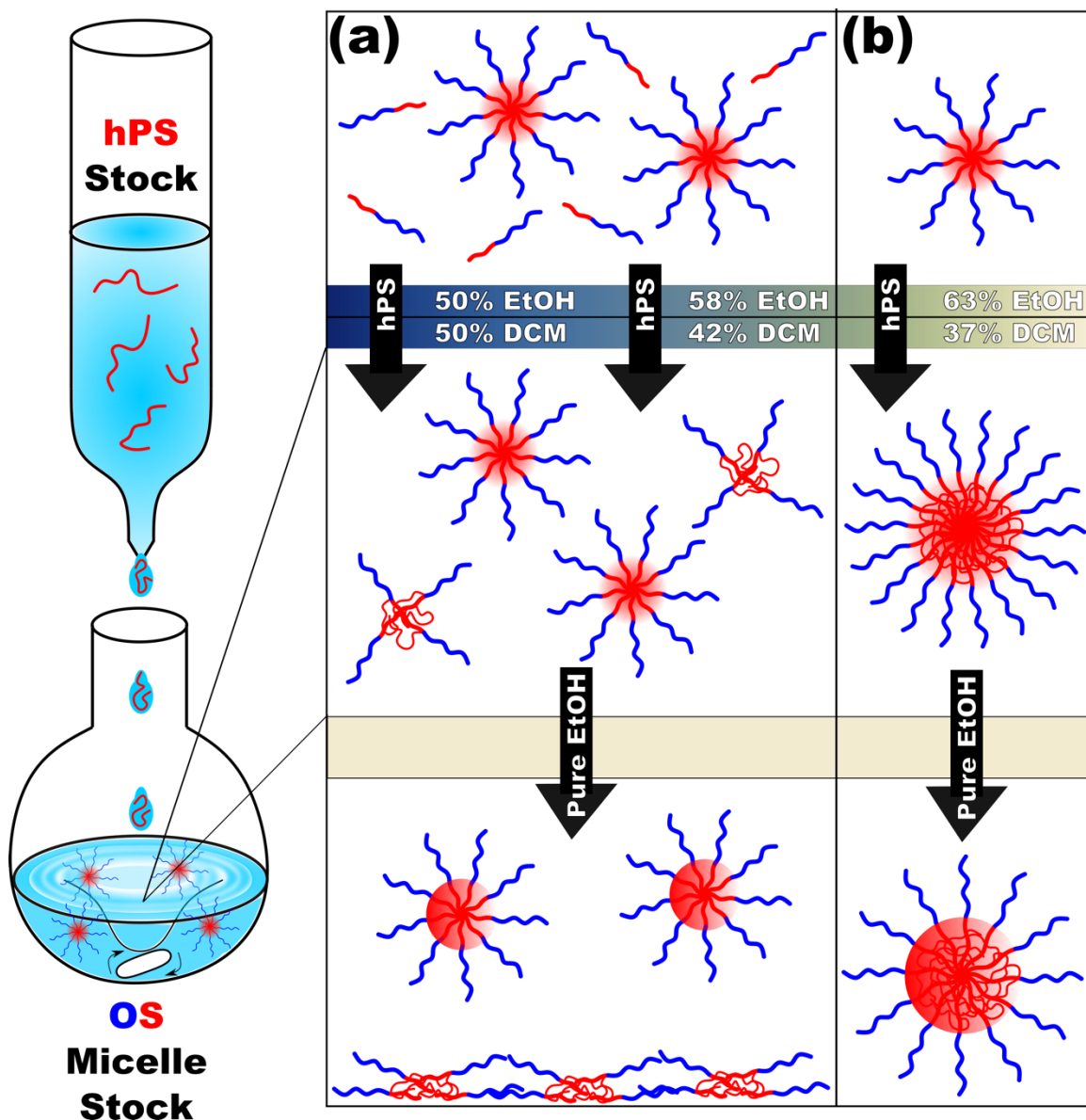
CMC) and a corresponding increase in the micelle hydrodynamic diameter to  $\sim 48$  nm. Please note that the lack of observable unimers by DLS does not indicate kinetic entrapment since dilute unimers are obscured by the higher scattering strength of the micelles ( $I \propto d_{micelle}^6$ ).<sup>27</sup> Selective removal of the DCM to yield pure EtOH as the solvent resulted in a similar  $\sim 48$  nm micelle hydrodynamic diameter without apparent unimers.

The **OS** micelles in pure EtOH were also examined by SAXS and TEM (Figure 3.2). The solution SAXS data were well-fitted using a micelle form factor with a core diameter of  $39.8 \pm 0.02$  nm. This dimension was consistent with the TEM data where the micelle cores (light) were apparent after staining with an average core size of  $42.1 \pm 0.4$  nm. **OS** micelles in pure EtOH are kinetically trapped as described previously,<sup>34</sup> however, the micelle core size has negligible tunability.<sup>35,36</sup>

#### ADDITION OF HOMOPOLYMER MICELLES: ROLE OF SOLVENT SELECTIVITY

Micelle solutions were next combined with homopolymer solutions. Here, the insertion and retention of the homopolymer chains necessitates (1) that the solution is sufficiently selective that the homopolymer preferentially resides within the micelles while also (2) not being so selective that the homopolymer precipitates out of solution nor (3) vitrifies the micelle cores, locking out further homopolymer swelling. The **hPS** used herein was insoluble in typical PS non-solvents (See Appendix B) and was screened with DCM/EtOH mixtures to assess its tolerance towards cosolvent mixtures. In principle, these three conditions are satisfied by the gradual addition of selective solvent (EtOH) to a single solution of **OS** and **hPS** polymers in good solvent (DCM). Here, DLS reveals **OS** micellization as early as 16 vol% EtOH whereas **hPS** is still soluble until ~45 vol% EtOH. Despite this apparent plausibility, the gradual increase in solvent selectivity rather led to precipitation. The homopolymer swelling of micelles with relatively low solvent selectivity is limited e.g., a prior report had a maximum of 20 wt% PS in PEO-*b*-PS when dispersed in THF.<sup>23</sup> In contrast, our prior study of micelle swelling showed much higher supersaturated (metastable) loadings<sup>24</sup> of homopolymer as a function of solvent selectivity.

Thus, the precipitation here with gradual EtOH addition indicates that the **hPS** loadings are also supersaturated. A strategy was developed where pre-formed micelles serve as “sinks” to entrap **hPS** in micelles faster than it can precipitate. Here, **hPS** was dispersed as dilute unimers in DCM with EtOH being added until the final solution composition was 60 vol% DCM, 40 vol% EtOH at a concentration of 10 mg mL<sup>-1</sup>. These solutions were then added to preformed **OS** micelle solutions with varying DCM content. The use of dilute unimers is important such that individual **hPS** chains are more likely to enter a micelle rather than aggregate with each other and form precipitants.



*Scheme 3.1* – A stock solution of **hPS** is added dropwise to an **OS** micelle solution (left). The **OS** unimer concentration depends upon the amount of selective solvent (top panel) and determines the outcome from the homopolymer addition (middle panel) as well as the outcome after selective distillation (bottom panel). Here, compositions with unimers present (a) will form small **hPS** aggregates stabilized by **OS** chains that later precipitate. In contrast, higher-selectivity compositions with minimal unimers (b) result in homopolymer swelling of the micelle cores which remain stable after transfer to a selective solvent.

Following this plan, **hPS** dispersions were added to pre-formed **OS** micelles in DCM/EtOH mixtures of varying selectivity (Scheme B.1). Micelle solutions with solvent compositions ranging from 50–63 vol% EtOH were examined. Please note that the **hPS**

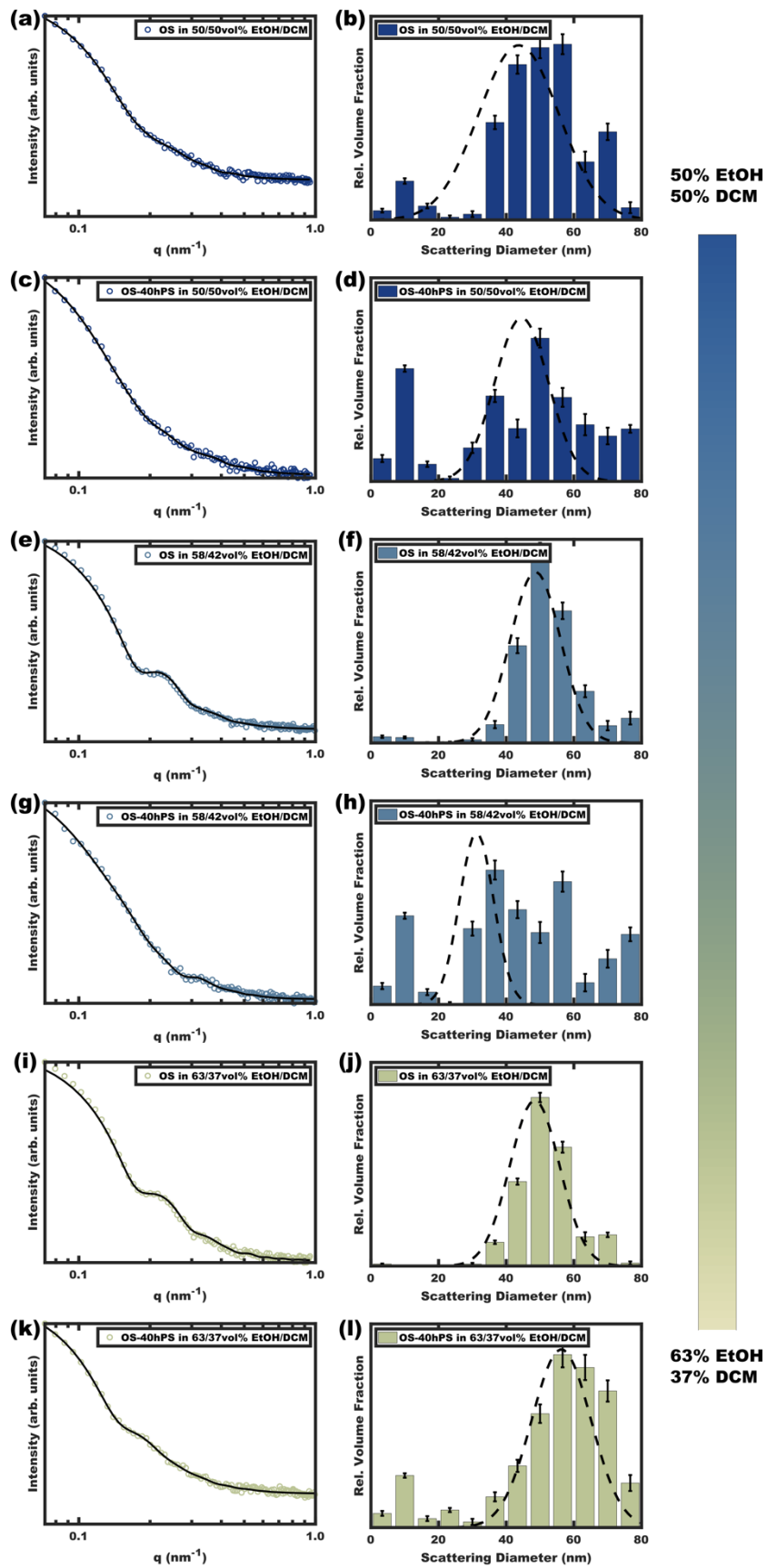


*Figure 3. 3* – Scattering curves (a, c, e, g, i, k) for pure **OS** micelles as compared to those with 40 wt% **hPS** (**OS–40hPS**) were measured with different EtOH/DCM compositions for the **OS** solution. Form factor analysis using a single Gaussian size distribution (dashed lines) led to illogical interpretations (e.g., micelles shrinking in the presence of **hPS**). Thus, additional Monte Carlo fitting was used to reveal additional smaller size clusters (b, d, f, h, j, l). The error bars correspond to uncertainty of the y-values.

used here is insoluble in all of these compositions, thus there is an enthalpic driving force for **hPS** to avoid interfaces with the solvent phase. Two options for **hPS** are thus apparent: precipitation or combination with **OS** amphiphiles. Again, these experiments were biased towards the latter outcome by using dilute **hPS** solutions. Figure 3.3 shows the SAXS scattering profiles and corresponding best-fit for **OS** micelles populations before and after the addition of **hPS**. The **OS** solutions were varied in their EtOH/DCM ratios containing: 50, 58, and 63 vol% EtOH. The SAXS data were first analyzed using a micelle form factor model with a Gaussian distribution of aggregation numbers. The corresponding best-fits indicated that homopolymer only led to core expansion for the 63 vol% EtOH sample whereas the 50 and 58 vol% EtOH samples either remained largely unchanged or contracted somewhat (Figure 3.3, dashed Gaussian distributions). This indicates that homopolymer swelling of micelle cores only occurs with sufficiently selective compositions. Curiously, the 50 and 58 vol% EtOH solutions did not initially exhibit precipitation which raises the question where did the **hPS** go since it is not soluble in these at these solvent compositions and at this concentration? The SAXS data were re-analyzed using a Monte Carlo fitting routine for spherical form factors without an assumed distribution profile. The number of micelle sizes were constrained to limit the extent of over-fitting. The resulting best-fits (Figure 3.3) indicated that the **OS** micelles contained minor **OS** unimer content for the 50 and 58 vol% EtOH solutions where the addition of

**hPS** then led to additional ~10 nm aggregates. This perspective is consistent with the formation of unimer-homopolymer aggregates to minimize interfacial enthalpy. In contrast, this analysis for the 63 vol% EtOH samples did not identify unimers in the **OS** solution and rather led to an increase in micelle size upon homopolymer addition. This collection of observations indicates that higher-selectivity solvents (lower CMC value) are critical for homopolymers to swell micelle cores rather than form separate unimer-homopolymer aggregates.

#### VITRIFICATION OF THE SWOLLEN GLASSY MICELLES

Having identified the conditions to realize swollen micelles with supersaturated homopolymer loadings, the next step was vitrification via the removal of plasticizers/good solvents (DCM). Again, the appropriate selection of non-selective and selective solvents based upon boiling point makes this purification facile *via* selective distillation.<sup>34,36</sup> It should also be pointed out that such solvent exchanges are also generally possible *via* dialysis regardless of the boiling points. Having  $T_g > RT$  is also an essential attribute where the Flory-Fox equation<sup>37,38</sup> predicts the  $T_g$  of the PS in the **OS** diblock polymer to be ~97.5 °C whereas the  $T_g$  of the **hPS** is estimated at ~90 °C. Thus, both the **OS** diblock and the **hPS** homopolymer are expected to be well within the high- $T_g$  regime and suitable for vitrification.

Micelles were then swollen with various amounts of **hPS** and were vitrified by quenching in a large excess of EtOH followed by the selective distillation of DCM to leave purely EtOH as the solvent. Whereas micelle-homopolymer mixtures prepared using

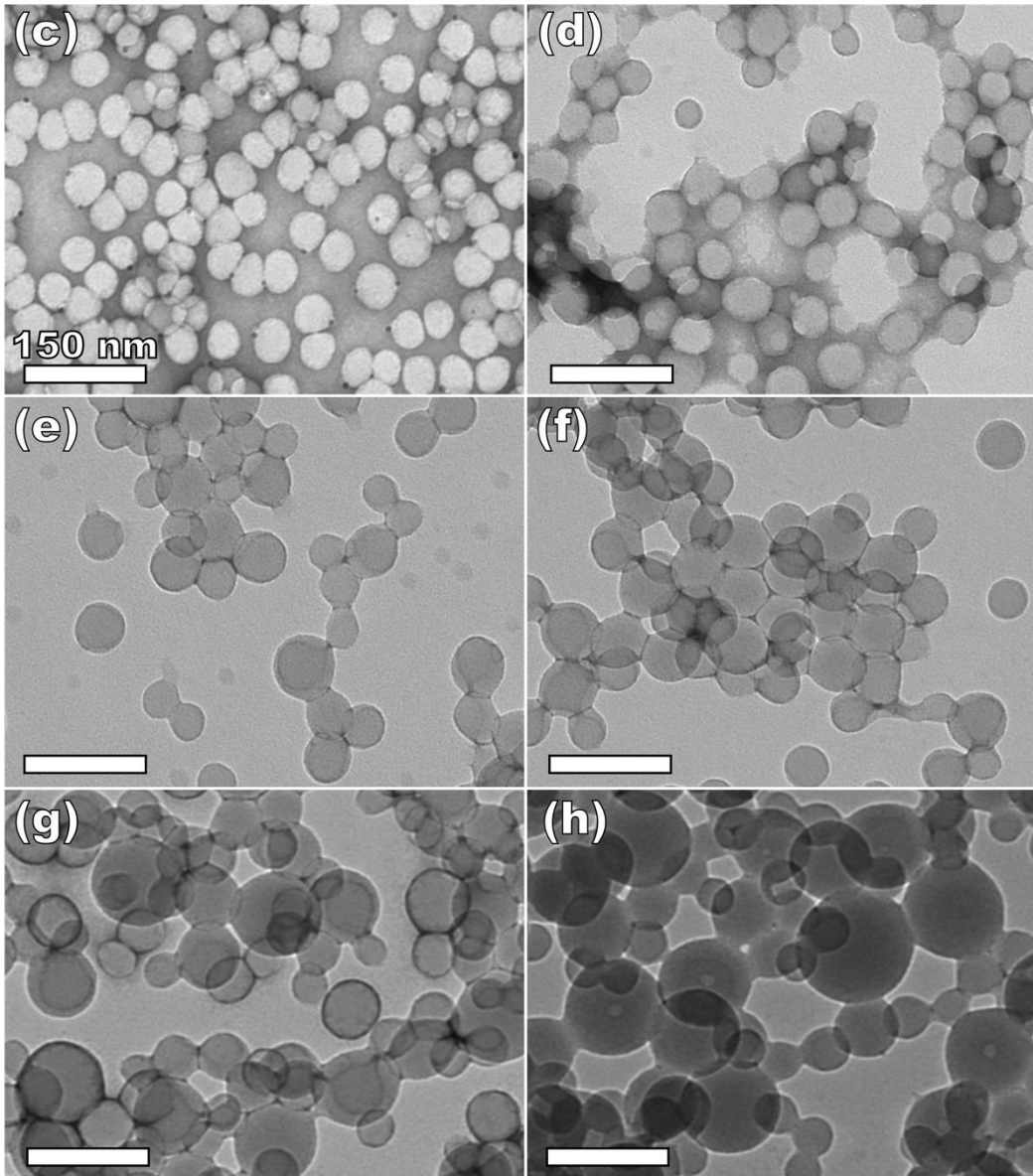
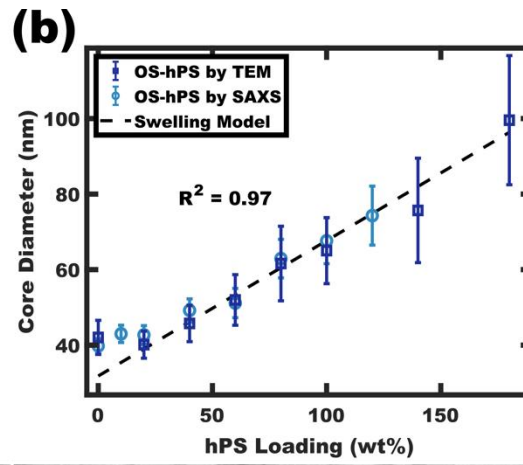
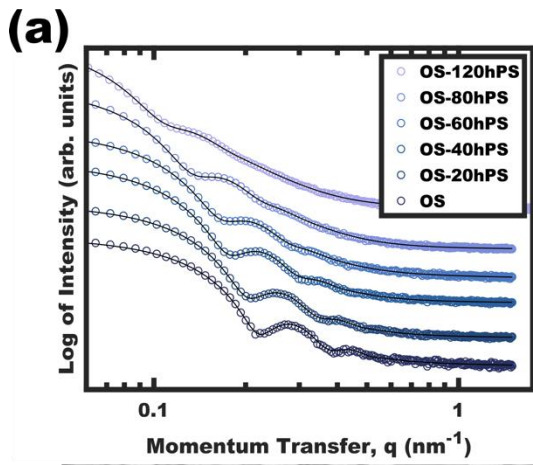


*Figure 3. 4* – SAXS and TEM for **OS** micelles with increasing homopolymer loading. SAXS curves (a) were fitted to derive the core diameter distributions (b). TEM images for **OS** (c), **OS-60hPS** (d), **OS-80hPS** (e), **OS-100hPS** (f), **OS-140hPS** (g), and **OS-180hPS** (h) are shown with 1 wt% uranyl acetate stain to improve contrast. The core diameter distributions from these TEM data are also presented alongside the SAXS fit values (b). SAXS plots were offset vertically for clarity. The TEM background varied from dark to light depending on the amount of unbound staining agent present after drying. The dashed line in (b) is based upon Eq. B8 where constant interfacial **OS** chain density leads to a linear swollen micelle size trajectory as a function of **hPS** loading.

micelles in 50 and 58 vol% EtOH resulted in some precipitation upon DCM removal, those prepared using micelles in 63 vol% EtOH led to stable dispersions. Figure 3.4a shows the corresponding solution SAXS profiles of the vitrified **OS** micelles swollen with increasing amounts of **hPS** in pure EtOH. Across the series, a consistent leftward shift is noted for the scattering features corresponding to an increase in micelle core ( $d = 2\pi/q$ ) with **hPS** addition. The best-fit micelle core dimensions from SAXS fitting are plotted as a function of the homopolymer loading (w.r.t **OS** mass) in Figure 3.4b. The curious linear correlation of core size to homopolymer loading will be elaborated upon in the next section. The immobile nature of the core block after vitrification also permits imaging by TEM since the micelles are stable (Figure 3.4c–h). The direct TEM measurements of core size are also plotted in Figure 3.4b and were statistically indistinguishable from the solution SAXS interpretations from form factor analysis. Here, an increase of 59.8 nm from 39.8–99.6 nm is observed with up to 180 wt% homopolymer loading across the series. The corresponding TEM size distributional profiles are presented in Appendix B, Figure B.7. This close agreement across two separate techniques (solution SAXS vs. dried TEM) demonstrates the size integrity and stability of these glassy swollen micelles.

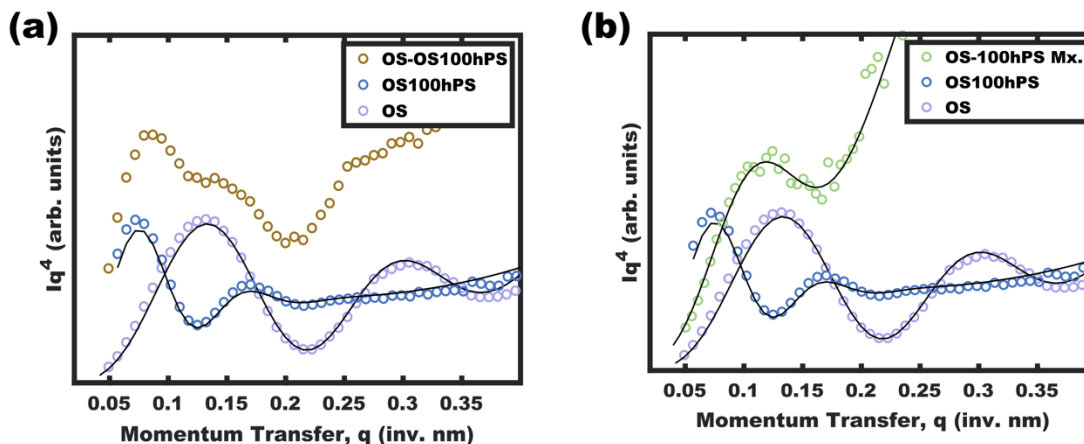


Figure 3. 5 – SAXS data and best-fits for **OS** and **OS-100hPS** micelle stocks measured both separately and after combination in pure EtOH to yield a bimodal distribution (a). The mixture was then measured again after the addition of 30 vol% DCM with stirring for 1.5 hrs to yield a new equilibrated size distribution (b). Values are presented in  $Iq^4$  vs.  $q$  coordinate spaces to highlight small changes in micelle form factor oscillations.

#### DYNAMIC CHAIN EXCHANGE AND SCALING LAWS

One may reasonably wonder whether these observations reflect a pseudo-equilibrium (supersaturated) or a purely kinetically trapped state. Indeed, the curious pseudolinear relationship of core diameter to **hPS** loading (Fig. 3.4b) is inconsistent with persistent micelles at the time of **hPS** swelling where a pseudo-cube root dependence would be expected, this due to the natural scaling relationship between a volume and a linear dimension (core diameter). First, the dynamic exchange of **hPS** is examined by combining unswollen **OS** micelles with **hPS** swollen micelles (**OS-100hPS**). Figure 3.5 shows the solution SAXS pattern for unswollen **OS** micelles (39.8 nm), those swollen with 100 wt% **hPS** (67.6 nm), and their combination where features of both size distributions are apparent when dispersed in EtOH. Next, 30 vol% DCM as added to this mixture and after 1.5 hrs of stirring, a single size distribution was apparent (45.4 nm), indicating dynamic exchange of **hPS** and possibly also **OS**. Please note that the SAXS scattering profiles are presented in

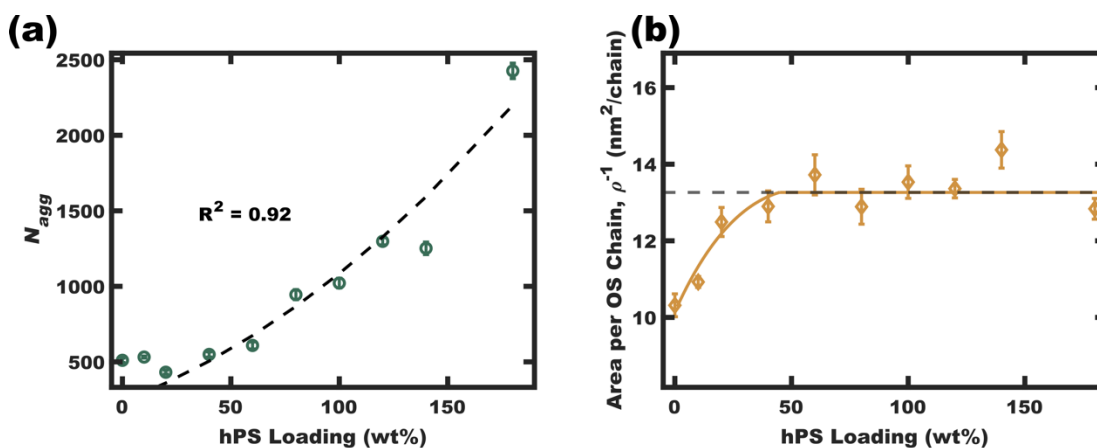


Figure 3. 6 – The swollen micelle aggregation numbers ( $N_{agg}$ ) were calculated using Equation B.5 for varying extents of swelling (a). The interfacial area per **OS** chain was found to plateau at high **hPS** loadings, suggesting a critical interfacial **OS** chain density (b). This plateau density (average value for 50–180 wt% **hPS**, b dashed line) led to an anticipated parabolic swelling trajectory for  $N_{agg}$  based on Equation B.10 (a dashed line). Error bars correspond to the propagated uncertainty from a combination of TEM and SAXS measurements.

$lq^4$  vs.  $q$  coordinate space to highlight feature sizes since the purely spherical form factor has undamped oscillations in this coordinate space.

Having confirmed that **hPS** exchange is active for supersaturated swollen micelles (while in EtOH/DCM mixtures), the dynamic exchange of **OS** chains was next examined by calculating the aggregation number ( $N_{agg}$ ). A simple equation was derived to calculate the  $N_{agg}$  for homopolymer swollen micelles based on volume conservation (see Appendix B for derivation and variable definitions).

$$N_{agg} = \frac{\pi d_{core}^3}{6V_{BCP}(\phi_S + \xi)} \quad (\text{Equation 3.1})$$

The trend of  $N_{agg}$  for the series of swollen micelles revealed a marked non-linear increase from ~500–2500 chains per micelles as a function of **hPS** loading (Fig. 3.6a). This change in  $N_{agg}$  as a function of **hPS** loading confirms dynamic **OS** chain exchange between

micelles while in EtOH/DCM mixtures, suggesting that this behavior reflects a pseudo-equilibrium (supersaturated) state.

As the equilibrium diameter of a micelle is significantly influenced by interfacial enthalpy and core chain stretching,<sup>13</sup> the significant increase in micelle core diameter with **hPS** swelling may be partially decoupled from chain stretching constraints since the **hPS** can occupy the center of the micelle cores. Thus, the localization of **hPS** in the center of the micelle cores would certainly reduce entropy losses resulting from core chain stretching. As such, the interfacial density of chains ( $\rho$ , Eq. B.6) was next examined as this determines how well core-solvent interactions are screened for each swollen micelle state. The interfacial area per chain ( $\rho^{-1}$ ) is presented as a function of **hPS** loading in Figure 3.6b. This plot shows an initial increase in interfacial area per **OS** chain from  $\sim 10.5$  for **OS** micelles to a plateau average of  $\sim 13.2$  nm<sup>2</sup> per **OS** chain for most of the swelling series. This plateau suggests that the pseudo-equilibrium exchange of both **OS** and **hPS** is governed by micelles optimizing the screening of core-solvent interactions. Too high of a  $\rho$  and the chains are sterically hindered (chain crowding) while too low of a  $\rho$  (rich in PEO-PS interfaces) results in a system that does not sufficiently screen the PS-solvent interactions. This trend towards a constant  $\rho$  furthermore implies specific quantitative expectations for each of the swelling trajectories presented thus far, including the parabolic trend of  $N_{agg}$  and the linear dependence of swollen micelle diameter upon **hPS** loading (Fig. 3.6a fitted with Eq. B.8, Fig. 3.3b fitted with Eq. B.10). Though we<sup>24</sup> and others<sup>23</sup> have noted e.g., linear trends of core size with homopolymer loading, to the best of our knowledge, none have before noted this effect of constant interfacial chain density. The swollen micelle core diameters and aggregation number thus appear to be the result of a

pseudo-equilibrium (supersaturated) state governed largely by interfacial chain density. This critical value for interfacial chain density also explains the precipitation of the homopolymer-unimer aggregates. The resulting precipitates were collected by centrifugation, dried under vacuum, and analyzed by  $^1\text{H-NMR}$  (Fig. B.8). Though the overall solutions corresponded to 100 wt% **hPS**, these precipitates rather corresponded to 357 wt% **hPS**. This  $\xi$  value and the  $\sim 10$  nm core diameter of the homopolymer-unimer aggregates identified by Monte Carlo analysis of SAXS scattering patterns (Fig. 3.3d, h) corresponds to an area per corona chain of  $16710 \text{ nm}^2$  per chain ( $\rho = 5.98 \times 10^{-5}$  chains/ $\text{nm}^2$ ). Thus, the precipitation of these homopolymer-unimer aggregates is expected from the correspondingly low corona chain density when these aggregates were transferred to pure EtOH.

#### LONG-TERM STABILITY OF SWOLLEN GLASSY MICELLES

The stability of the resulting glassy swollen micelles was assessed over the course of several months after transferring to a pure EtOH solvent. As noted earlier, our prior report of homopolymer swollen persistent micelles had a limited lifespan of about a day before the non-glassy homopolymer would phase separate (again supersaturated). Figure 3.7 presents the solution SAXS scattering profiles for various swollen micelles both “as-made” and after 6 months of storage. The micelle core size distributions were analyzed by again fitting the SAXS data where the resulting average micelle diameters were essentially identical to the corresponding as-made samples with less than 1% difference (Table 3.1). Thus, this path-dependent processing sequence is the first report to combine both both wide-ranging micelle sizes with long-term stability.

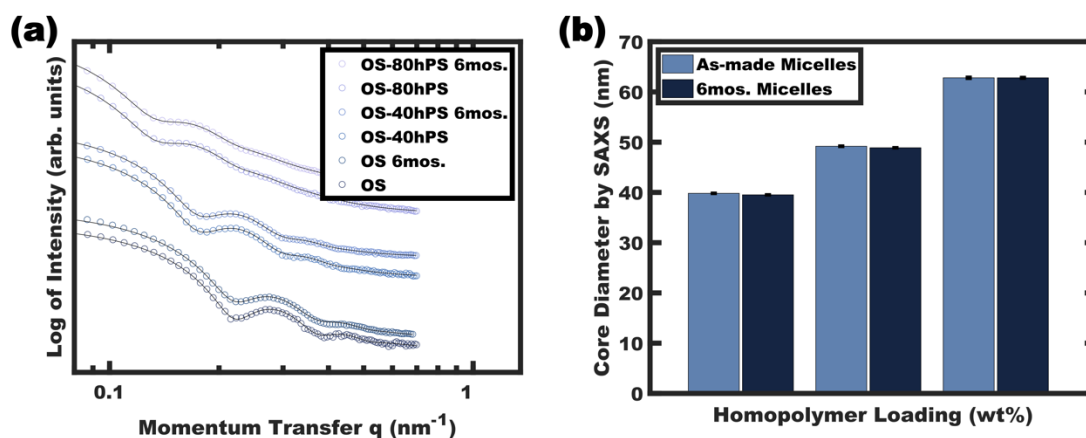


Figure 3. 7 – SAXS data of (swollen) glassy-core micelles as-made and after a 6-month quiescent period (6 mos.) (a). The best-fit average core diameters were compared, including the error of the fit values (b). SAXS data were offset vertically for clarity.

Table 3. 1 – Micelle size metrics from analysis of SAXS data for the swollen **OS-hPS** micelles as a function of storage time.

Sample	Sit Time (months)	As-made Diameter by SAXS (nm) <sup>a</sup>	After Storage Diameter by SAXS (nm) <sup>a</sup>	% Difference
OS	6	$39.82 \pm 0.05$	$39.52 \pm 0.04$	0.75
OS-40hPS	6	$49.19 \pm 0.07$	$48.89 \pm 0.04$	0.61
OS-80hPS	6	$62.81 \pm 0.14$	$62.86 \pm 0.10$	0.07

<sup>a</sup>As determined by form factor analysis (see Appendix B) on micelle solutions in pure EtOH.

## STABILITY AS MICELLE TEMPLATES

The kinetic entrapment of micelles is also verifiable by using a titration series that combines micelle templates with material precursors. Here, variation in the amount of material precursors shifts the solution composition and thus shifts the equilibrium micelle size. Methodology developed for analyzing persistent micelle templates (PMTs) has been widely used to detect onsets of micelle chain exchange.<sup>24-29,34,36,39</sup> A previously developed PMT SAXS model can either identify dynamic micelle behavior or consistency with persistent micelle behavior.<sup>26,27</sup> This model specifically quantifies a

quasi-cube root expectation for how the material-to-template ratio (amount of material added) alters the SAXS  $d$ -spacing.

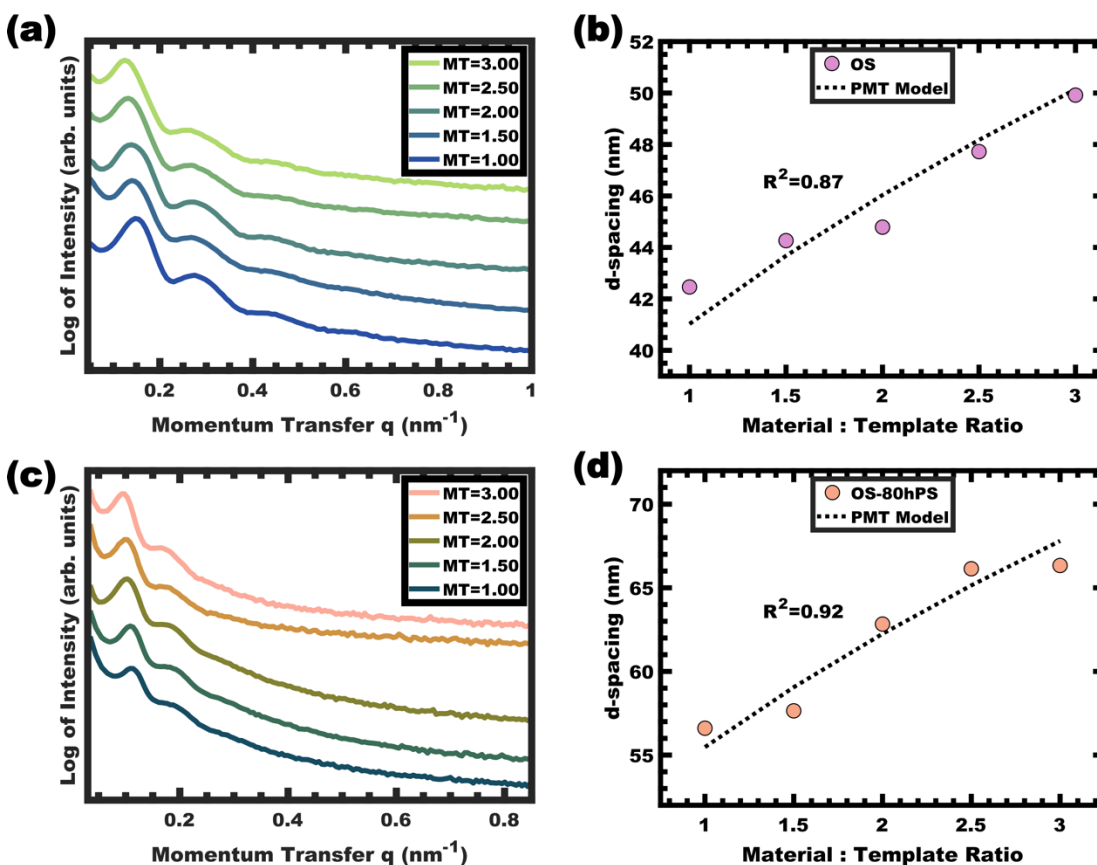


Figure 3. 8 – SAXS of as-made carbon materials templated using OS (a) and OS-80hPS micelles (c). The corresponding  $d$ -spacings were compared to model predictions for persistent micelles (PMT model) as a function of the material : template ratio (b, d). SAXS plots are offset vertically for clarity.

This test was performed using phenol-formaldehyde carbon precursors as described previously.<sup>34</sup> In brief, the shifts of the structure factor peaks were quantitatively consistent with PMT behavior (Figure 3.8) by a well matched PMT SAXS model. These two example titration series are both consistent with deeply trapped micelles due to their glassy cores. This demonstration is yet further evidence supporting the extraordinary stability of these glassy core swollen persistent micelles.

### 3.5 CONCLUSIONS

This manuscript examined the necessary conditions to enable supersaturated homopolymer swelling of PEO-*b*-PS micelles. Solvent mixtures with lower selectivity and higher CMC values were found to result in homopolymer-unimer aggregates that eventually precipitated. In contrast, highly selective solvent mixtures with lower CMC values were found to enable supersaturated homopolymer swelling of micelles. This approach enabled micelle size tunability from 39.8–99.6 nm with 180 wt% homopolymer loading which far exceeded prior equilibrium demonstrations with the subsequent core vitrification enabling size persistence beyond 6 months. Control experiments with mixtures of unswollen and swollen micelles confirmed dynamic homopolymer exchange where subsequent calculations of aggregation number also confirmed the dynamic exchange of the block polymer. The curious trends with homopolymer loading, including a linear increase of micelle core size and parabolic increase of aggregation number, were both consistent with a pseudo-equilibrium that preserves a constant interfacial area per polymer chain. Such a pseudo-equilibrium is consistent with relaxed constraints for core block chain stretching where the swollen micelle states are largely governed by interfacial energy as screen by the block polymer chains.

### 3.6 REFERENCES

1. Ulbrich, K.; Holá, K.; Šubr, V.; Bakandritsos, A.; Tuček, J.; Zbořil, R. Targeted Drug Delivery with Polymers and Magnetic Nanoparticles: Covalent and Noncovalent Approaches, Release Control, and Clinical Studies. *Chem. Rev.* **2016**, *116*, 5338-5431.
2. Chen, G.; Roy, I.; Yang, C.; Prasad, P. N. Nanochemistry and Nanomedicine for Nanoparticle-based Diagnostics and Therapy. *Chem. Rev.* **2016**, *116*, 2826-2885.

3. Ahmad, Z.; Shah, A.; Siddiq, M.; Kraatz, H. Polymeric micelles as drug delivery vehicles. *RSC Adv.* **2014**, *4*, 17028-17038.
4. Kataoka, K.; Harada, A.; Nagasaki, Y. Block copolymer micelles for drug delivery: design, characterization and biological significance. *Adv. Drug Deliv. Rev.* **2001**, *47*, 113-131.
5. Sandeep, K.; Nekkanti, V. Insoluble drug delivery strategies: review of recent advances and business prospects. *Acta pharmaceutica Sinica. B* **2015**, *5*, 442-453.
6. Cabral, H.; Miyata, K.; Osada, K.; Kataoka, K. Block Copolymer Micelles in Nanomedicine Applications. *Chem. Rev.* **2018**, *118*, 6844-6892.
7. Bronstein, L.; Krämer, E.; Berton, B.; Burger, C.; Förster, S.; Antonietti, M. Successive Use of Amphiphilic Block Copolymers as Nanoreactors and Templates: Preparation of Porous Silica with Metal Nanoparticles. *Chem. Mater.* **1999**, *11*, 1402-1405.
8. Khullar, P.; Singh, V.; Mahal, A.; Kumar, H.; Kaur, G.; Bakshi, M. S. Block Copolymer Micelles as Nanoreactors for Self-Assembled Morphologies of Gold Nanoparticles. *J. Phys. Chem. B* **2013**, *117*, 3028-3039.
9. Gaitzsch, J.; Huang, X.; Voit, B. Engineering Functional Polymer Capsules toward Smart Nanoreactors. *Chem. Rev.* **2015**, *116*, 1063-1093.
10. Würbser, M. A.; Schwarz, P. S.; Heckel, J.; Bergmann, A. M.; Walther, A.; Boekhoven, J. Chemically Fueled Block Copolymer Self-Assembly into Transient Nanoreactors. *ChemSystemsChem* **2021**, *3*, 2100015.
11. Bagshaw, E.; Proust, T. J.; Pinnavaia, T. J. Templating of Mesoporous Molecular Sieves by Nonionic Polyethylene Oxide Surfactants. *Science* **1995**, *269*, 1242-1244.
12. Tanev, P. T.; Pinnavaia, T. J. A Neutral Templating Route to Mesoporous Molecular Sieves. *Science* **1995**, *267*, 865-867.
13. Halperin, A.; Alexander, S. Polymeric Micelles: Their Relaxation Kinetics. *Macromolecules* **1989**, *22*, 2403-2412.
14. Fan, J.; Yu, C.; Lei, J.; Zhang, Q.; Li, T.; Tu, B.; Zhou, W.; Zhao, D. Low-Temperature Strategy to Synthesize Highly Ordered Mesoporous Silicas with Very Large Pores. *J. Am. Chem. Soc.* **2005**, *127*, 10794-10795.
15. Kimura, T.; Sugahara, Y.; Kuroda, K. Synthesis of mesoporous aluminophosphates using surfactants with long alkyl chain lengths and triisopropylbenzene as a solubilizing agent. *Chem. Commun.* **1998**, 559-560.

16. Sayari, A.; Kruk, M.; Jaroniec, M.; Moudrakovski, I. L. New Approaches to Pore Size Engineering of Mesoporous Silicates. *Adv. Mater.* **1998**, *10*, 1376-1379.
17. Blin, J. L.; Otyjacques, C.; Herrier, G.; Su, B. Pore Size Engineering of Mesoporous Silicas Using Decane as Expander. *Langmuir* **2000**, *16*, 4229-4236.
18. Kruk, M.; Cao, L. Pore Size Tailoring in Large-Pore SBA-15 Silica Synthesized in the Presence of Hexane. *Langmuir* **2007**, *23*, 7247-7254.
19. Kruk, M. Access to Ultralarge-Pore Ordered Mesoporous Materials through Selection of Surfactant/Swelling-Agent Micellar Templates. *Acc. Chem. Res.* **2012**, *45*, 1678-1687.
20. Trivedi, M.; Peng, F.; Xia, X.; Sepulveda-Medina, P. I.; Vogt, B. D. Control of Pore Size in Ordered Mesoporous Carbon-Silica by Hansen Solubility Parameters of Swelling Agent. *Langmuir* **2019**, *35*, 14049-14059.
21. O'Callaghan, J. M.; McNamara, H.; Copley, M. P.; Hanrahan, J. P.; Morris, M. A.; Steytler, D. C.; Heenan, R. K.; Holmes, J. D. Swelling of Ionic and Nonionic Surfactant Micelles by High Pressure Gases. *Langmuir* **2010**, *26*, 7725-7731.
22. Alvarez-Fernandez, A.; Fornerod, M. J.; Reid, B.; Guldin, S. Solvent Vapor Annealing for Controlled Pore Expansion of Block Copolymer-Assembled Inorganic Mesoporous Films. *Langmuir* **2022**, *38*, 3297-3304.
23. Deng, Y.; Liu, J.; Liu, C.; Gu, D.; Sun, Z.; Wei, J.; Zhang, J.; Zhang, L.; Tu, B.; Zhao, D. Ultra-Large-Pore Mesoporous Carbons Templated from Poly(ethylene oxide)-b-Polystyrene Diblock Copolymer by Adding Polystyrene Homopolymer as a Pore Expander. *Chem. Mater* **2008**, *20*, 7281-7286.
24. Sarkar, A.; Thyagarajan, A.; Cole, A.; Stefik, M. Widely tunable persistent micelle templates via homopolymer swelling. *Soft Mater* **2019**, *15*, 5193-5203.
25. Lokupitiya, H. N.; Jones, A.; Reid, B.; Guldin, S.; Stefik, M. Ordered Mesoporous to Macroporous Oxides with Tunable Isomorphic Architectures: Solution Criteria for Persistent Micelle Templates. *Chem. Mater* **2016**, *28*, 1653-1667.
26. Sarkar, A.; Stefik, M. How to make persistent micelle templates in 24 hours and know it using X-ray scattering. *J. Mater. Chem. A* **2017**, *5*, 11840-11853.
27. Sarkar, A.; Evans, L.; Stefik, M. Expanded Kinetic Control for Persistent Micelle Templates with Solvent Selection. *Langmuir* **2018**, *34*, 5738-5749.
28. Lantz, K. A.; Clamp, N. B.; van den Bergh, W.; Sarkar, A.; Stefik, M. Full Gamut Wall Tunability from Persistent Micelle Templates via Ex Situ Hydrolysis. *Small* **2019**, *15*, 1900393-1900403.

29. Williams, E. R.; Wessel van den Bergh; Morgan Stefik High- $\chi$ , low-N micelles from partially perfluorinated block polymers. *Soft Matter* **2022**, *18*, 7917-7930.
30. Williams, D. B. G.; Lawton, M. Drying of Organic Solvents: Quantitative Evaluation of the Efficiency of Several Desiccants. *J. Org. Chem.* **2010**, *75*, 8351-8354.
31. Min, K.; Gao, H.; Matyjaszewski, K. Preparation of Homopolymers and Block Copolymers in Miniemulsion by ATRP Using Activators Generated by Electron Transfer (AGET). *J. Am. Chem. Soc.* **2005**, *127*, 3825-3830.
32. Matyjaszewski, K.; Xia, J. Atom Transfer Radical Polymerization. *Chem. Rev.* **2001**, *101*, 2921-2990.
33. Meng, Y.; Gu, D.; Zhang, F.; Shi, Y.; Yang, H.; Li, Z.; Yu, C.; Tu, B.; Zhao, D. Ordered Mesoporous Polymers and Homologous Carbon Frameworks: Amphiphilic Surfactant Templating and Direct Transformation. *Angew. Chem. Int. Ed.* **2005**, *44*, 7053-7059.
34. Williams, E. R.; McMahon, P. L.; Reynolds, J. E.; Snider, J. L.; Stavila, V.; Allendorf, M. D.; Stefik, M. Tailored porous carbons enabled by persistent micelles with glassy cores. *Mater. Adv.* **2021**, *2*, 5381-5395.
35. Larison, T.; Stefik, M. Persistent Micelle Corona Chemistry Enables Constant Micelle Core Size with Independent Control of Functionality and Polyelectrolyte Response. *Langmuir* **2021**, *37*, 9817-9825.
36. van den Bergh, W.; Williams, E. R.; Vest, N. A.; Chiang, P.; Stefik, M. Mesoporous TiO<sub>2</sub> Microparticles with Tailored Surfaces, Pores, Walls, and Particle Dimensions Using Persistent Micelle Templates. *Langmuir* **2021**, *37*, 12874-12886.
37. Fox, T. G.; Flory, P. J. Second-Order Transition Temperatures and Related Properties of Polystyrene. I. Influence of Molecular Weight. *J. Appl. Phys.* **1950**, *21*, 581-591.
38. Fox, T. G.; Flory, P. J. The glass temperature and related properties of polystyrene. Influence of molecular weight. *J. Polym. Sci.* **1954**, *14*, 315-319.
39. Stefik, M. Single-variable porous nanomaterial series from polymer structure-directing agents. *J. Mater. Res.* **2022**, *37*, 25-42.

CHAPTER 4: HIGH- $\chi$ , Low- $N$  MICELLES FROM PARTIALLY  
PERFLUORINATED BLOCK POLYMERS<sup>3</sup>

---

<sup>3</sup> Reproduced from Williams, E. R.; van den Bergh, W.; Stefik, M. *Soft Matter* **2022**, *18*, 7917–7930 with permission from the Royal Society of Chemistry.

## 4.1 ABSTRACT

Kinetically trapped (“persistent”) micelles enable emerging applications requiring a constant core diameter. Preserving a  $\chi N$  barrier to chain exchange with low- $N$  requires a commensurately higher  $\chi_{\text{core-solvent}}$  for micelle persistence. Low- $N$ , high- $\chi$  micelles containing fluorophobic interactions were studied using poly(ethylene oxide-*b*-perfluorooctyl acrylate)s ( $\text{O}_{45}\text{F}_x$ ,  $x = 8, 11$ ) in methanolic solutions. DLS analysis of micelles revealed chain exchange only for  $\text{O}_{45}\text{F}_8$  while SAXS analysis suggested elongated core block conformations commensurate with the contour lengths. Micelle chain exchange from solution perturbations were examined by characterizing their behavior as templates for inorganic materials *via* SAXS and SEM. In contrast to the  $\text{F}_8$  analog, the larger  $\chi N$  barrier for the  $\text{O}_{45}\text{F}_{11}$  enabled persistent micelle behavior in both thin films and bulk samples despite the low  $T_g$  micelle core. Careful measurements of micelle core diameters and pore sizes revealed that the nanoparticle distribution extended through the corona and  $0.52 \pm 0.15$  nm into the core–corona interface, highlighting thermodynamics favoring both locations simultaneously.

## 4.2 INTRODUCTION

The self-assembly of block polymers is the basis for countless modern applications and areas of active research.<sup>1-4</sup> The phase separation of polymer blocks is driven by  $\chi N$ , the product of the Flory–Huggins interaction parameter with the degree of polymerization.<sup>5</sup> One amongst many unique features of high- $\chi$  polymers is their ability to maintain phase separation with exceedingly low molecular masses (low  $N$ ).<sup>6</sup> This capability has been of broad interest recently for the field of block polymer lithography in the pursuit of even smaller feature sizes.<sup>7-11</sup> While self-consistent mean-field theory is only strictly rigorous in the limit of  $N \rightarrow \infty$ , it has proven surprisingly useful down to  $N \sim 10$ – $20$  where the corresponding chains could reasonably be considered oligomers.<sup>6</sup> Micelles are a distinct context for block polymers where their kinetics in the low- $N$ , high- $\chi$  regime remains underexplored.

During equilibration, micelles are known to change both their size and morphology in response to changing solution conditions.<sup>12-17</sup> To date, several mechanisms such as single-chain exchange (SCE)<sup>18-20</sup> and micelle fusion/fission<sup>21,22</sup> have been identified as supporting this equilibration. Interestingly, the predominant mechanism appears to be governed by how far removed the system is from its equilibrium state<sup>23-26</sup> with single-chain mechanisms considered to dominate both small-molecule surfactants and block polymer micelles that are near equilibrium.<sup>18-20,27,28</sup> Analogous to bulk polymer melts, the product  $\chi N$  also plays a pivotal role in SCE kinetics where the relevant  $\chi$  is between the core-forming block and the solvent ( $\chi_{\text{core-solvent}}$ ) and the relevant  $N$  corresponds to the length of the core block. This  $\chi N$  product is thus part of the activation energy for single-chain exchange when the core block is extracted into the solvent phase.<sup>18</sup> Modern models for



border). The star and square denote the high- $\chi$ , low- $N$  polymers from this study, O<sub>45</sub>F<sub>11</sub> and O<sub>45</sub>F<sub>8</sub>, respectively.

where maintenance of a constant micelle core diameter offers distinct advantages. Scheme 4.1 surveys the landscape of persistent *vs.* dynamic micelle behaviors with respect to  $N$  where there is a notable lack of persistent micelles in the low- $N$  regime (see Appendix C). Points featuring a black border had a  $\chi_{\text{core-solvent}}$  determined from SANS data whereas those with a blue border were crudely estimated using solubility parameters. The gradual transition from dynamic behavior (red) to persistent (blue) as a function of  $\chi N$  is represented with a gradient background color. This is analogous to glass transition behavior where the binary labels of persistent (circles) *vs.* dynamic (diamonds) micelles span a continuum of kinetics. The works are broadly separated as those which note kinetic entrapment<sup>36–38,42</sup> (circles) *versus* those that note dynamic exchange<sup>18,19,29,43–48</sup> (diamonds). Persistent micelles are generally found for  $\chi N > \sim 300$  for nearly all works shown here with some disagreement for lower values that particularly depend upon the quantification method. It is noted that prior persistent micelle reports tailored the core block molar mass ( $\propto N$ ),<sup>34</sup> solvent conditions,<sup>36</sup> core crystallinity<sup>49</sup> or immobilized glassy cores.<sup>40,41,50,51</sup> In principle,  $\chi N \sim 300$  barrier could be maintained in the limit  $N \rightarrow 1$  (using the monomer volume as the lattice site volume) by a commensurate increase in  $\chi_{\text{core-solvent}}$  and it thus remains an open question as to a low- $N$  limit for micelle persistence. It should be noted that most polymers are not ideal candidates for low- $N$  kinetic micelle entrapment. For example, a number of commodity block polymers often feature low to moderate- $\chi$  core-forming blocks such as poly(propylene oxide)<sup>52</sup> and poly(methyl methacrylate) when

compared to alcoholic/aqueous solvents.<sup>53</sup> Thus, the molar mass needed for persistence would be well outside what could reasonably be considered the low- $N$  regime.

This challenge of micelle persistence in the low- $N$  regime is herein examined with a perfluorinated motif in the core-forming block. Perfluorinated alkanes stand out as a unique class of molecules where their fluorophobic interactions render them remarkably immiscible with dissimilar polymers and solvents alike in a phenomenon known as the fluorophobic effect.<sup>54-56</sup> It thus follows that block polymers including a perfluorinated motif often possess especially high- $\chi$  values, including  $\chi_{A-B}$  and  $\chi_{\text{core-solvent}}$ .<sup>57</sup> Interestingly, this fluorophobic effect is in part a result of the greater relative volume occupied by these molecules in solution through the adoption of a helical configuration caused by the larger size of the fluorine atoms when compared to hydrogen.<sup>58,59</sup> As such, the work required to displace favorable intermolecular interaction between polar solvent molecules in accommodating the larger fluorocarbons (*e.g.*, hydrogen bonding, electrostatic interactions, *etc.*) is not offset by favorable fluorocarbon interactions with the solvent as the former is already highly polarized.<sup>59,60</sup>

Herein, we examine the low- $N$  limits for micelle persistence with a series of poly(ethylene oxide-*b*-perfluorooctyl acrylate)s (PEO-*b*-PFOA, O<sub>45</sub>F<sub>X</sub>). Micelle solution behavior is first examined with DLS and SAXS before interrogating micelle persistence *via* their use as templates. Please note that PFOA is not expected to crystallize since fluorinated acrylates are amorphous.<sup>61</sup> It will be shown that the large  $\chi_{\text{core-solvent}}$  afforded by the perfluorinated core-forming segment enabled persistent micelles with as few as 11 mer units whereas prior demonstrations often required values in excess of 50 or even 100 to realize similar persistent micelle behavior.<sup>34,36</sup> The remarkable persistence of low- $N$

perfluorinated micelle templates are shown through an expansive 45 sample series with multiple processing techniques. Simulations and experiments have examined the placement of nanoparticles within block polymers on several occasions where the general predictions and observations either (1) place the nanoparticles at the interface of block polymers to increase translational entropy,<sup>62–67</sup> (2) mix the nanoparticles with a block due to selective and attractive interactions,<sup>68–72</sup> or (3) phase separate the nanoparticles.<sup>73,74</sup> Here a combination of SAXS and SEM data showed that the average micelle core size was larger than the average templated pore size, suggesting that the inorganic nanoparticles were dispersed throughout the corona and into the core–corona interface. This observation highlights that predictions 1 and 2 are not mutually exclusive.

#### 4.3 EXPERIMENTAL METHODS MATERIALS

Titanium tetrakisopropoxide (TTiP, 99% Acros), *N,N'*-dicyclohexylcarbodiimide (DCC, 99% Beantown Chemical), Cu(I) Br (99.99%, Aldrich), and the ligand tris[2-(dimethylamino)ethyl]-amine (Me<sub>6</sub>TREN) were all stored in an argon glovebox prior to use. Methanol (MeOH, 99.8%, Fisher), chloroform (>99.5%, Fisher), and toluene (>99.5%, Fisher) were dried at room temperature over 50% w/w of molecular sieves (3Å 8–12 mesh, Acros Organics) for a week prior to use.<sup>75</sup> Hexanes (99%, Fisher) were used as received. The monomer *1H,1H,2H,2H*-perfluorooctyl acrylate (FOA, 97%, Sigma) was stored in the refrigerator and passed over a basic alumina column to remove inhibitor just prior to use. Concentrated 12 M HCl (37%, ACS Grade, VWR), poly(ethylene glycol)monomethyl ether (PEO-OH,  $M_n = 2000 \text{ g mol}^{-1}$ , Alfa Aesar), 2-bromopropionic acid (98%, Beantown Chemical), 4-(dimethylaminopyridine) (DMAP, 99%, Aldrich) were all used as received.

## SYNTHESIS OF PEO-*b*-PFOA DIBLOCKS O<sub>45</sub>F<sub>11</sub> and O<sub>45</sub>F<sub>8</sub>

High- $\chi$  diblock polymers were synthesized using an ATRP macroinitiator followed by the controlled chain extension using FOA. The macroinitiator was prepared with the following ratios of PEO-OH : 2-bromopropionic acid : DMAP : DCC of 1.0 : 2.0 : 0.8 : 2.0.<sup>35</sup> A general synthesis involved the dissolution of 20 g of PEO-OH in 100 mL of anhydrous MeOH-free chloroform. To this solution was added 3.59 mL of 2-bromopropionic acid in a dropwise fashion. The solution was then placed in an ice water bath for 10 minutes. Next, 4.12 g of DCC and 0.97 g of DMAP were added. The reaction was allowed to stir unperturbed for 18 hours. After completion, the contents were gravity filtered through a Whatman V2 filter paper (diameter 270 mm) to remove the urea by-product. The product was collected and concentrated to a highly viscous liquid by rotary evaporation. The crude macroinitiator was then precipitated in 500 mL of ice-cold hexanes by a dropwise addition and recovered. Residual urea by-product was removed by dissolution in 50 mL of chloroform followed by gentle shaking with an equivalent volume of deionized water. This process was repeated for a total of three times. The purified macroinitiator (PEO-Br) was dried under vacuum without heat prior to characterization. The O<sub>45</sub>F<sub>11</sub> block polymer was synthesized with the following molar ratios of PEO-Br : Me<sub>6</sub>TREN : Cu(I) Br : FOA of 1.0 : 0.5 : 0.5 : 12. A standard synthesis involved the combination of 2.00 g of PEO-Br with 3.2 mL of inhibitor-free FOA monomer and 9 mL of toluene in a 25 mL Schlenk flask. This mixture was then degassed by 3 freeze-pump-thaw cycles of 20 min each before being moved into an argon glovebox to be opened under an inert atmosphere. While in the glovebox, 71.7 mg of Cu(I) Br and 133.6  $\mu$ L of Me<sub>6</sub>TREN were added. The reaction was

then removed from the glovebox and placed in a pre-heated oil bath at 90 °C and allowed to polymerize for 42 hrs. Afterwards, the flask was placed in the freezer for 2 hrs and then vented to air to terminate the polymerization. The crude product was then solubilized with THF and passed over a column of basic alumina to remove copper salts. The product was dialyzed against a 50 : 50 mixture of THF and MeOH to remove unreacted initiator. Unreacted FOA monomer was subsequently removed by dissolving the crude diblock in THF and a dropwise precipitation in 500 mL of room temperature hexanes. The purified product was then collected and dried under vacuum for 24 hrs without heat.

## POLYMER CHARACTERIZATION

The molar mass of PFOA and dispersity ( $D$ ) of all polymers were determined using nuclear magnetic resonance (NMR) spectroscopy and gel permeation chromatography (GPC), respectively. All proton NMR ( $^1\text{H-NMR}$ ) spectra were collected using a Bruker Avance III HD 300. The molar mass ( $M_n$ ) of the PFOA diblocks was determined by integration ratios between the FOA ester  $-\text{COOCH}_2-$  signal ( $\delta = 4.35$  ppm) and the known (2k)PEO ether signal  $-\text{OCH}_2\text{CH}_2-$  signal ( $\delta = 3.66$  ppm). All GPC data were collected using a Waters gel permeation chromatography GPC instrument equipped with a 515 HPLC pump, a 2410 refractive index detector and three styragel columns (HR1, HR3, and HR4) in the effective molecular mass range of 0.1–5, 0.5–30, and 5–600 kg mol $^{-1}$ , respectively. The eluent used was THF at a temperature of 30 °C and a flow rate of 1 mL min $^{-1}$ . The instrument was calibrated with polystyrene standards 92570, 1090, 579, 246, 130, 67.5, 34.8, 18.1, 10.4, 3.4 and 1.6 kg mol $^{-1}$ ) received from Polymer Laboratories. The GPC samples were

prepared by dissolution in THF with a concentration of  $\sim 10 \text{ mg mL}^{-1}$  and were filtered through a syringe filter with a pore diameter of  $0.2 \text{ }\mu\text{m}$  just prior to injection.

#### PREPARATION OF MICELLE SOLUTIONS

Micelle solutions were prepared by dissolving the  $\text{O}_{45}\text{F}_x$  polymer in anhydrous MeOH. The polymers directly dispersed with only minor agitation. The micelle solutions for templating were prepared by dissolving 50 mg of dried PEO-*b*-PFOA polymer in 5.0 g (6.3 mL) of anhydrous MeOH. Next, 70.8  $\mu\text{L}$  of HCl (aq) was added in preparation for nanoparticle addition. The resulting micelle solution was sonicated for 5 mins at room temperature with the intent to enable chain exchange under kinetically limited conditions.<sup>76</sup>

#### DLS MEASUREMENTS

Dynamic light scattering (DLS) measurements were performed on the  $\text{O}_{45}\text{F}_{11}$  and  $\text{O}_{45}\text{F}_8$  polymers under different solution conditions. The DLS measurements of the hydrodynamic diameter were performed using a Zetasizer Nanoseries ZEN3690 instrument. Solutions for DLS were prepared at a polymer concentration of  $\sim 10 \text{ mg mL}^{-1}$  and were filtered through a  $0.2 \text{ }\mu\text{m}$  syringe filter prior to measuring. All measurements were performed six times to confirm reproducibility. All DLS measurements were conducted at  $25 \text{ }^\circ\text{C}$ . Viscosities of 0.659 cP and 0.782 cP along with refractive indices of 1.334 and 1.336 were used for the 98% MeOH, 2%  $\text{H}_2\text{O}$  and 90% MeOH, 10%  $\text{H}_2\text{O}$  solutions, respectively.<sup>77,78</sup>

## SAXS OF MICELLES

Micelle solutions for SAXS were prepared in an identical fashion as those used for spin coating. In brief, the polymer of choice was dispersed in anhydrous MeOH followed by 1.4 vol% HCl addition such that the final polymer concentration was  $10 \text{ mg mL}^{-1}$ . Samples were passed through a  $0.2 \text{ }\mu\text{m}$  syringe filter prior to loading in a  $0.8 \text{ mm}$  diameter class capillary (Charlessupper). Capillaries were first flame-sealed followed by an additional sealing with hot candle wax. A blank sample consisting of a capillary with only MeOH (aq) was measured under the same conditions. All samples were acquired for 150 minutes at room temperature. SAXS data were background subtracted with SAXSGUI software using the same solvent mixtures in Charlessupper  $0.8 \text{ mm}$  diameter capillaries. These capillaries yielded reproducible signal that was several orders of magnitude weaker than the sample signal.

## *Ex situ* TTIP HYDROLYSIS AND MICELLE TEMPLATING

Standard PMT *modus operandi* calls for titrating in increasing amounts of material precursors to effect increases in wall thickness. An *ex situ*  $\text{TiO}_2$  nanoparticle solution was prepared by quickly adding  $3.00 \text{ mL}$  of TtiP to a  $20 \text{ mL}$  scintillation vial containing  $1.2 \text{ mL}$  of conc. HCl (aq) and  $2.0 \text{ mL}$  of anhydrous MeOH stirring rapidly at  $600 \text{ rpm}$  with a magnetic stir bar.<sup>37</sup> Please note that this process is highly exothermic and should be performed cautiously. The resulting material stock solution was allowed to stir for a few minutes after hydrolysis to cool back to room temperature. A predetermined amount of sol stock was added to a  $0.5 \text{ mL}$  aliquot of the micelle stock to realize the desired material-to-template (M:T) mass ratio. After combining the two, the mixture was agitated slightly by

hand before spin coating. This process was repeated for all samples across the entire M:T range. A 10  $\mu\text{L}$  aliquot of this solution was then spin coated for 30 sec at 1500 rpm with a 15% relative humidity, after which time it was immediately transferred to a pre-heated hotplate at 250  $^{\circ}\text{C}$  where it was left to age for 2 hrs. Samples spun on silicon substrates were prepared in an identical fashion and were subjected to an additional aging treatment at 150  $^{\circ}\text{C}$  for 18 hrs. Samples were calcined in a furnace at 360  $^{\circ}\text{C}$  for 24 hrs with a 5  $^{\circ}\text{C min}^{-1}$  ramp rate.

#### BULK EVAPORATIVE CASTING

A 5.0 g solution of micelles as described above was used. Next, a predetermined amount of  $\text{TiO}_2$  material stock (as prepared previously) was combined with the micelle stock and cast in a Teflon dish with a diameter of 4 cm. The material and micelles were allowed to undergo evaporation-induced self-assembly overnight without added heat. Once dry, the samples were aged at 80  $^{\circ}\text{C}$  for 24 hrs prior to removal of the micelle template. Samples were then calcined at 300  $^{\circ}\text{C}$  for 0.5 hrs with a ramp rate of 5  $^{\circ}\text{C min}^{-1}$ .

#### X-RAY MEASUREMENTS

X-ray measurements were performed at the South Carolina SAXS Collaborative (SCSC) using a SAXSLab Ganesha instrument. A Xenocs GeniX 3D microfocus source was used with a copper target to produce a monochromatic beam with a wavelength of 0.154 nm. The instrument was calibrated prior to use with a National Institute of Standards and Technology (NIST) reference material 640d silicon powder with a peak position of 28.44 $^{\circ}$   $2\theta$ , where  $2\theta$  refers to the total scattering angle. A Pilatus 300k detector (Dectris) was used

to collect a two-dimensional (2D) scattering pattern with the nominal pixel dimensions of  $172 \times 172 \mu\text{m}^2$ . The SAXS data were acquired with an X-ray flux of  $\sim 4.1$  M photons per second incident upon the sample and a sample-to-detector distance of 1040 mm. A transmission SAXS geometry was used to measure the purely in-plane features of the thin film samples. A high-tilt measurement with a  $45^\circ$  incident angle was used to simultaneously measure the in-plane and out-of-plane contributions. The 2D images were azimuthally integrated to yield the scattering vector and intensity. The tilted data were integrated over limited azimuthal angle ranges along orthogonal directions. Peak positions were fitted using custom MATLAB software. The SAXS measurements were reported as the average  $\pm$  the standard-error-of-the-mean. Micelle SAXS measurements were fitted using a model for hard spheres with Gaussian chains and a Dozier scattering background to account for high- $q$  “blob” scattering.

#### SCANNING ELECTRON MICROSCOPY (SEM)

Top-view images of calcined films on silicon were acquired with a Zeiss Ultraplus thermal field emission SEM using an accelerating voltage of 5 keV and an in-lens secondary electron detector. The working distance was maintained at  $\sim 4$  mm as well as constant magnification across the series. Hundreds of SEM measurements were made on each sample to yield statistically significant metrics of pore diameter and wall-thickness. Data are presented as average values with the standard error-of-the-mean. SEM metrics were validated using a NIST gold nanoparticle standard of nominal diameter 10 nm (Reference Material 8011) deposited on Si wafers of  $\sim 3 \times 3 \text{ cm}^2$ . Samples were prepared by placing a drop of 3-aminopropyltriethoxysilane on a substrate treated with oxygen plasma. This was

allowed to react for ~2 hrs, after which time the excess silane was rinsed off with isopropanol followed by deionized water. A drop of the nanoparticle solution was then deposited on the derivatized substrate and allowed to dry for ~1 hr, after which it was briefly washed with isopropanol and gently blown dry.

#### 4.4 RESULTS AND DISCUSSION

The kinetic control of micelles depends upon the thermodynamic barriers to chain exchange processes. It is well established that the rate of SCE decreases strongly with increasing  $\chi N$ .<sup>18–20,47,79–81</sup> However, the kinetic control of block polymer micelles in this low- $N$ , high- $\chi$  regime remains underexplored despite suitable candidates for high- $\chi$  polymers.<sup>10,48,57</sup> Herein persistent micelle behavior under high- $\chi$ , low- $N$  micelle conditions are examined in solution as well as after their use as templates for inorganic nanoparticles. In the latter case, the pore size serves as a proxy for the nominal micelle core size. Two high- $\chi$ , low- $N$  PEO-*b*-PFOAs were prepared using Atom-Transfer Radical Polymerization, resulting in block polymers O<sub>45</sub>F<sub>11</sub> and O<sub>45</sub>F<sub>8</sub>. It is noted that the low degree of polymerization of the FOA block leads to a comb-like architecture with ~16–22 bonds along the backbone and 11 bonds along the side group. The aspect ratio of these polymers may play a role in their dynamics. The corresponding molecular attributes were characterized by <sup>1</sup>H-NMR (Fig. 4.1) and GPC (Fig. 4.2). Both polymers readily dispersed in MeOH and formed micelles. All micelle characterizations were performed in a specific composition of aqueous methanol for compatibility with micelle template experiments which need HCl for nanoparticle stability and a quickly evaporating solvent (MeOH) (Fig. 4.3).

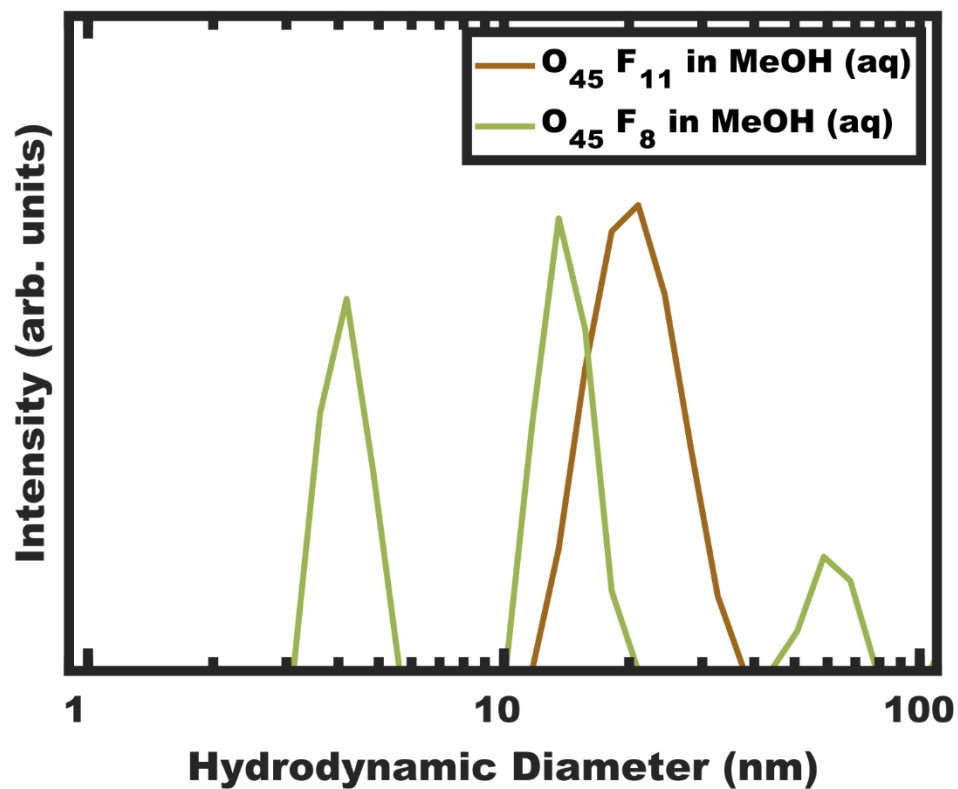
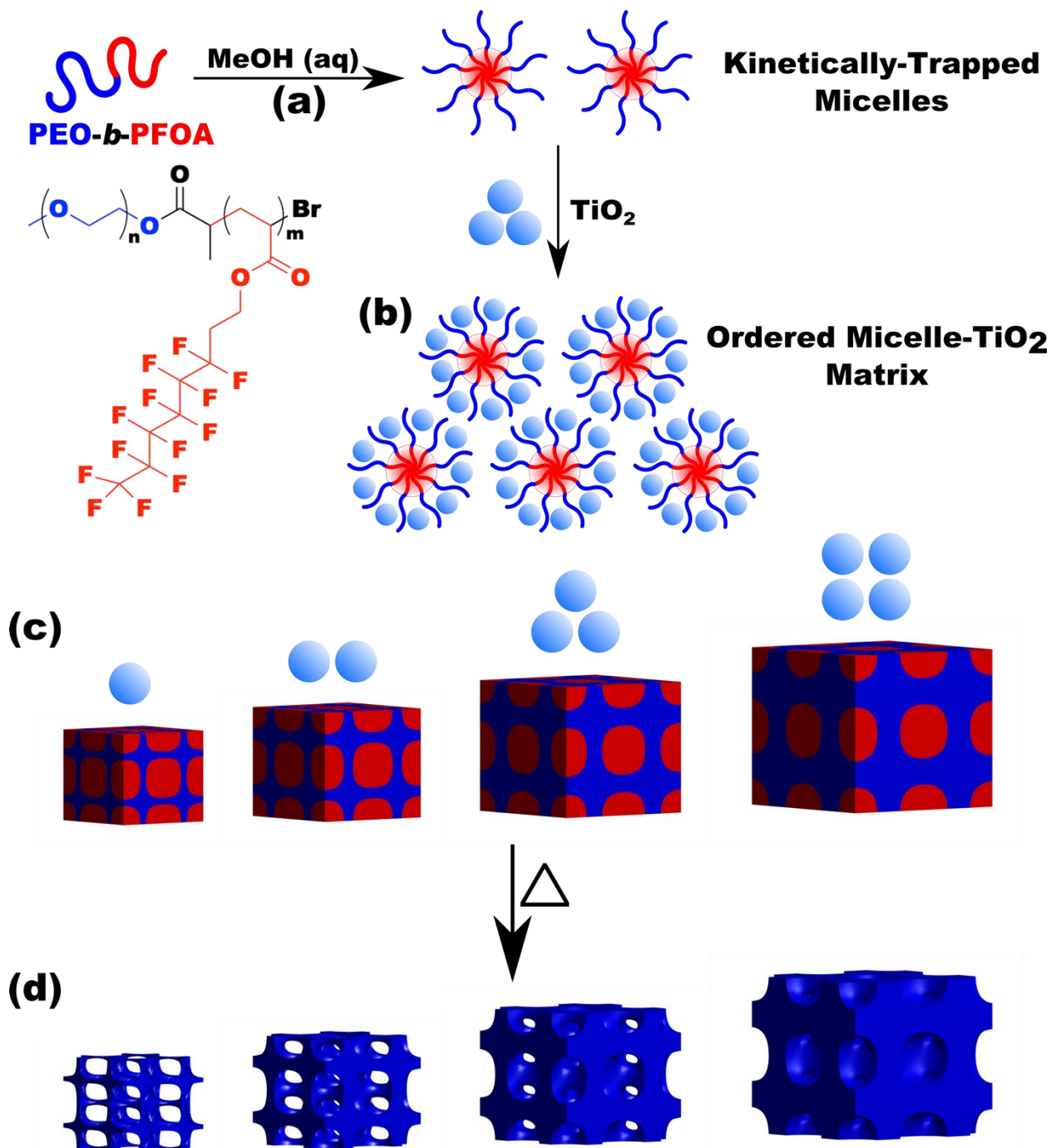


*Figure 4. 1* – DLS intensity data for micelle solutions O<sub>45</sub>F<sub>11</sub> and O<sub>45</sub>F<sub>8</sub> in MeOH (aq) with 1.4 vol% HCl. The data were obtained at a concentration of 10 mg mL<sup>-1</sup>.

Micelles from each polymer were first evaluated using a combination of DLS and SAXS. Subsequent analysis after their use as templates for inorganic nanoparticles can reveal micelle size changes as a result of dynamic chain exchange resulting from the perturbations to the solution composition (Scheme 4.1).



*Scheme 4. 2* – Overview showing the use of micelles as templates. A diblock polymer is dispersed in a selective solvent to yield micelles (a). Material precursors (nanoparticles) are next added where there is a preferential interaction with the micelle *via* hydrophilic interactions (b). If the micelle is kinetically trapped (persistent) then the template/pore size remains constant while the wall thickness is independently tailored by the amount of

material precursors (c). Subsequent heat treatment removes the polymer and yields porous nanomaterials where the pore size arises from the micelle core diameter (d).

Here, the use of poly(ethylene oxide) corona blocks enables well-known selective interactions with typical hydrophilic oxide nanoparticles such that the nanoparticles are predominately located throughout the corona region.<sup>82–85</sup> Finally, the templated pore dimensions are compared with respect to the parent micelle core size to infer the nanoparticle spatial distribution in proximity of the core–corona interface.

#### DLS OF O<sub>45</sub>F<sub>11</sub> AND O<sub>45</sub>F<sub>8</sub> MICELLES

A signature of persistent micelles is the preservation of a constant aggregation number ( $N_{agg}$ ) by inhibiting chain exchange. SCE operates with a stable population of free chains (unimers) in solution to support continuous equilibration. DLS measurements provide a facile and direct method for detecting the presence of such unimers, whose hydrodynamic diameter (<10 nm) is often distinguishable from their micelle counterparts. It should however be noted that the absence of detectable unimers in solution does not guarantee kinetic entrapment as the population of unimers may simply be below the limit of detection for the instrument.<sup>36</sup> Furthermore, light scattering carries a natural bias towards larger objects (intensity  $\propto$  size<sup>6</sup>) which can obscure the observation of trace unimers. Therefore, analysis of micelle solution DLS data allows for a binary assessment of micelle dynamics in solution as (1) certainly dynamic or (2) either persistent or dynamic (ambiguous).

DLS measurements were performed on the polymers O<sub>45</sub>F<sub>11</sub> and O<sub>45</sub>F<sub>8</sub> in MeOH (aq) (see Experimental). Please note that the addition of HCl (aq) was not found to have a significant impact on the resulting micelle hydrodynamic diameters measured by DLS (Fig. 4.4). DLS of the O<sub>45</sub>F<sub>11</sub> polymer solution revealed a relatively uniform population of micelles with

~24 nm hydrodynamic diameter without detectable unimers below 10 nm (Fig. 4.3). The addition of HCl (aq) increased the micelle hydrodynamic diameters which is consistent with expanded corona conformations<sup>36</sup> or dynamic micelles with increasing the  $\chi_{\text{core-solvent}}$  (Fig. 4.4). This suggests that MeOH (aq) is not only a selective solvent for PEO but also a good candidate for kinetic entrapment. Please note that the apparent absence of unimers here does not prove kinetic entrapment but suggests that O<sub>45</sub>F<sub>11</sub> may have formed persistent micelles. In contrast, O<sub>45</sub>F<sub>8</sub> was similarly dispersed in MeOH and properly acidified with DLS analysis again revealing a mixture of unimers or low number aggregates in addition to micelles and larger micelle-aggregates. To increase  $\chi$ , up to 10.0 vol% water was added to the methanolic O<sub>45</sub>F<sub>8</sub> solution where DLS again detected unimers consistent with dynamic micelles. It is curious that the 3 fewer FOA repeat units on O<sub>45</sub>F<sub>8</sub> resulted in markedly different solution behavior. Thus, a difference in aggregation behavior was identified by DLS where only O<sub>45</sub>F<sub>8</sub> had detectable chain exchange in MeOH whereas O<sub>45</sub>F<sub>11</sub> did not.

The concentration dependent micelle characteristics of the O<sub>45</sub>F<sub>11</sub> polymer were also examined with DLS. The polymer solution (fixed solvent composition) was examined from 5.0 – 0.25 mg mL<sup>-1</sup> of O<sub>45</sub>F<sub>11</sub> (Fig 4.5). Throughout this range ~24 nm micelles were apparent with addition aggregates of micelles appearing at the lowest concentrations. Such aggregates of micelles have been noted before with PEO containing micelles where the hydrodynamic diameter increase with concentration was attributed to the aggregation of multiple micelles rather than a uniform increase in micelle diameter.<sup>51</sup> The lack of apparent unimers (<10 nm), however, indicates a very low CMC value as expected from persistent

micelles. Please note that the CMC for similar fluoropolymers were found to be around 1.4 mg L<sup>-1</sup>.<sup>86</sup>

#### SAXS OF O<sub>45</sub>F<sub>11</sub> AND O<sub>45</sub>F<sub>8</sub> MICELLES

Analysis of SAXS data was used to assess the diameter and conformation of the PFOA blocks. The SAXS scattering intensity arises from the contrast in scattering length density ( $\rho$ ) where the difference between the perfluorinated PFOA core and MeOH (aq) is expected to dominate. The corresponding data for O<sub>45</sub>F<sub>11</sub> and O<sub>45</sub>F<sub>8</sub> micelles are shown in Figure 4.6.

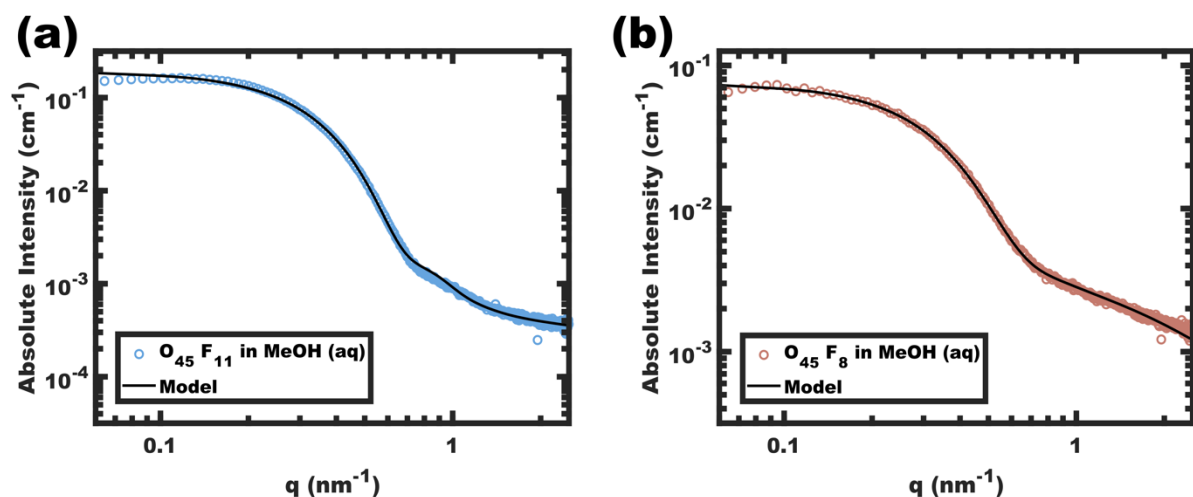


Figure 4. 2 – Absolute intensity SAXS data for micelle solutions O<sub>45</sub>F<sub>11</sub> (a) and O<sub>45</sub>F<sub>8</sub> (b) in MeOH (aq) with 1.4 vol% HCl. The data were obtained at a polymer concentration of 10 mg mL<sup>-1</sup>. Solid lines correspond to the model best-fits.

The SAXS patterns resemble the form factor of polydisperse spherical scatterers. Please note that aggregation of micelles have been noted before for PEO containing micelles,<sup>51,87</sup> where there is a distinct separation between the micelle form factor and aggregate structure factor when present.<sup>88</sup> Absolute scattering data were fitted using a model for hard spheres with Gaussian chains and a Dozier scattering background to account for high- $q$  “blob”

scattering. The resulting fit parameters included average core diameters of 11.24 and 9.04 nm for the O<sub>45</sub>F<sub>11</sub> and O<sub>45</sub>F<sub>8</sub> micelles, respectively. The 11.24 nm core diameter somewhat exceeds the ~8.6 nm estimated end-to-end contour length expected for two completely outstretched F<sub>11</sub> blocks (Fig. 4.7). An elongated conformation state here is perhaps expected considering the high  $\chi_{\text{core-solvent}}$ . Indeed, others have noted micelle dimensions commensurate with the core block contour length in systems with perfluorinated core-forming segments,<sup>89</sup> with the degree of chain stretching increasing with decreasing core block  $N$ .<sup>90-93</sup> After considering the estimated molar volume for the PFOA core, the aggregation numbers for the O<sub>45</sub>F<sub>11</sub> and O<sub>45</sub>F<sub>8</sub> micelles were estimated at 109 and 78, respectively. Fluorinated surfactants are also known to have an affinity for dissolving gasses such as O<sub>2</sub> and CO<sub>2</sub>,<sup>94</sup> which may increase the micelle core size. In evaluating this possibility, micelles of O<sub>45</sub>F<sub>11</sub> were compared after several treatments: degassed by freeze-pump-thaw, degassing by sonication, saturating with O<sub>2</sub>, and saturating with CO<sub>2</sub>. Analysis of the corresponding SAXS data revealed that all micelle core diameters were similarly elongated and were in close agreement (~7% difference) (Figure 4.8). In other words, extended core block conformations were found regardless of the presence of dissolved gasses. Naturally, the chain extension caused by high- $\chi$  conditions mitigates feature size shrinking with low- $N$  polymers, somewhat obfuscating a typical objective of smaller feature sizes. A perhaps underappreciated advantage of chains elongated to the contour length is that this tradeoff has reached a terminus; in other words, lower- $N$  species with yet higher- $\chi$  values offer a path to smaller feature sizes.

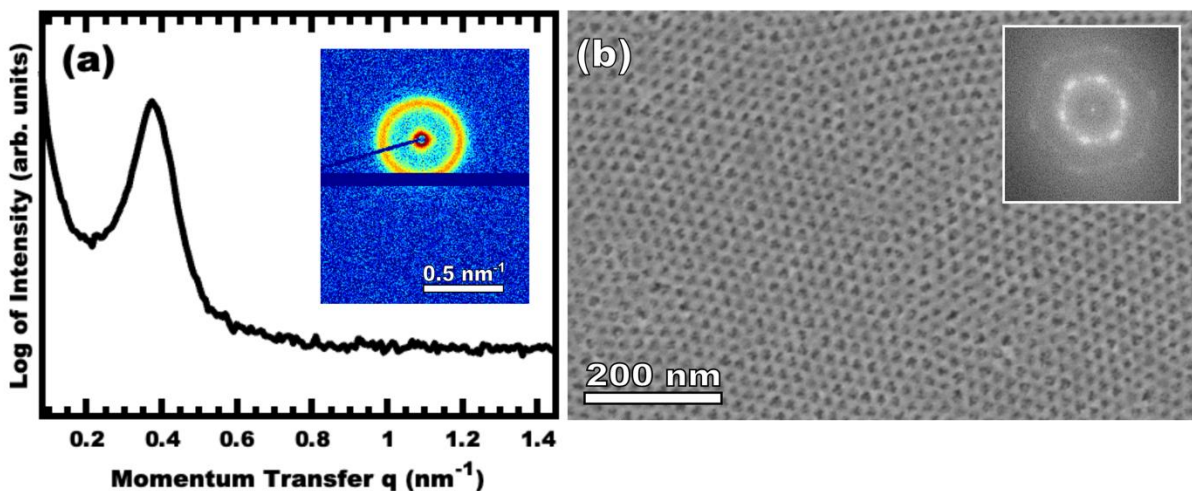


Figure 4. 3 – Representative data for sample O<sub>45</sub>F<sub>11</sub>–1.00. The integrated SAXS pattern is shown in (a) with the 2D pattern inset. The color scale corresponds to the log-scale of X-ray scattering intensity. The SEM image (b) has light areas corresponding to titania with the dark areas corresponding to the former location of the micelle cores (pores) with the FFT inset.

#### O<sub>45</sub>F<sub>11</sub> MICELLES: DYNAMIC OR PERSISTENT?

The micelle core dimensions were next examined after use as templates in diverse conditions to assess micelle persistence or lack thereof. A single sample is first presented in detail before describing subsequent series of experiments. Micelle templates were combined with titania nanoparticles (“material precursors”), followed by evaporation and thermal treatments to remove the polymer and leave behind pores in the former location of the micelle cores (Scheme 4.1).

Sample O<sub>45</sub>F<sub>11</sub>–1.00 was prepared using sufficient material precursors to yield a material-to-template (M:T) mass ratio of 1.00. Figure 4.9 shows the corresponding SAXS and SEM data. The electron micrograph after polymer removal shows a continuous network of titania walls (light) amongst spherical pores (dark) (Fig. 4.9b). The evenly spaced and uniform arrangement of spheres is reflected in the inset fast Fourier transform

containing two concentric textured rings. Statistical descriptors were derived from hundreds of measurements upon SEM images to yield an average pore diameter of  $11.59 \pm 0.79$  nm and an average wall thickness of  $4.58 \pm 0.27$  nm. The SAXS-derived average micelle core diameter of  $11.08 \pm 0.03$  nm was in close agreement with the SEM average pore diameter of  $11.59 \pm 0.79$  nm after the templating process. The corresponding SAXS pattern (Fig. 4.9a) features a single isotropic scattering peak with a  $d$ -spacing ( $2\pi/q^*$ ) of 16.43 nm. The isotropic 2D pattern (inset) reflects the random in-plane orientation over the macroscopic few  $\text{mm}^2$  of the SAXS beam. Furthermore, the lack of apparent higher-order SAXS reflections suggests predominantly short-range order features that are typical for PMT samples.<sup>35–38,40,41</sup> Please note that the SAXS  $d$ -spacing of 16.43 nm is similar to the sum of the SEM pore and wall dimensions. This correspondence of feature size and  $d$ -spacing is typical for randomly packed spheres.<sup>95–98</sup> Furthermore, this correlation is quantitatively predictable using the PMT model<sup>35</sup> which is based upon a simple conservation of volume argument. The model quantitatively predicts sample  $d$ -spacings when the micelles are persistent (constant core size) where increasing the amount of titania material precursors (increasing M:T ratio) leads to lattice expansion as the added inorganic is directed to the micelle coronae and pushes the micelles further apart. In the next section, this geometric architecture-micelle relationship will be used to track changes to the micelle core diameter and volume.

The  $\text{O}_{45}\text{F}_{11}$  micelle persistence in MeOH (aq) was evaluated by varying the M:T ratio from 0.50–6.00. Increasing the M:T ratio both increases the amount of charged nanoparticle interactions with the PEO coronas and increases the trace water content in solution, both of which could alter the equilibrium aggregation number. A correspondingly

changed micelle core size would indicate dynamic micelles undergoing chain exchange towards the new equilibrium conditions whereas an invariant core size suggests kinetic control. Indeed, the general case for dynamic micelle templates is a simultaneous variance in both the pore and wall feature sizes as

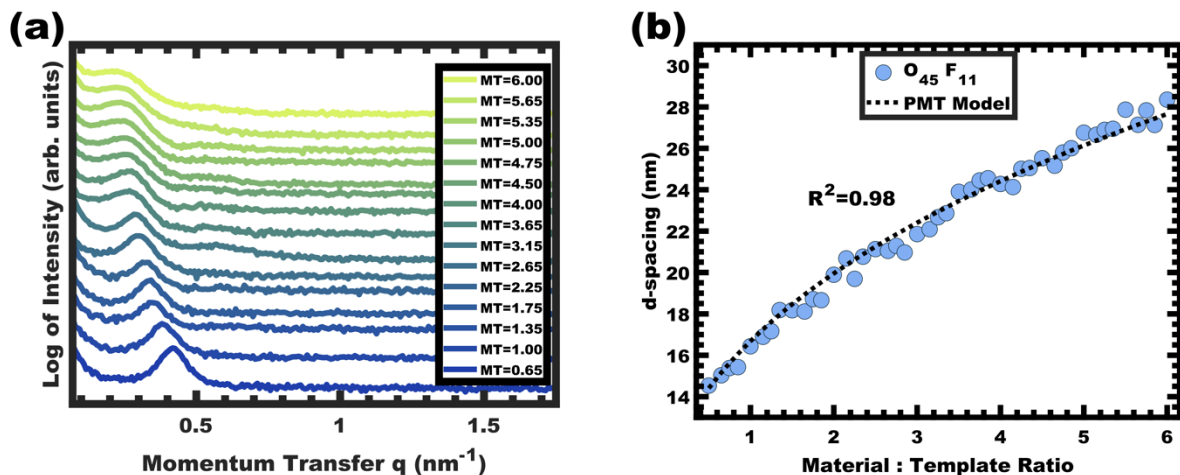


Figure 4. 4 – Analysis of films from the  $O_{45}F_{11}$  thin film series featuring increasing material-to-template (M:T) ratio. The monotonic leftward shift of the SAXS first-peak position in (a) indicates lattice expansion with increasing  $d$ -spacings ( $d = 2\pi/q$ ). The lattice expansion was quantitatively consistent with the PMT model, suggesting constant template/pore diameter (b). The SAXS data were offset vertically for clarity.

micelles attempt to reach a thermodynamic equilibrium *i.e.*, a balance of interfacial enthalpy and chain stretching. The SAXS data for the  $O_{45}F_{11}$  M:T series are shown in Figure 4.10a. The increase of M:T ratio results in a monotonic leftward shift of SAXS curves towards lower  $q$  values (higher  $d$ -spacings), indicative of the lattice expansion behavior consistent with PMTs.

This expansion of  $d$ -spacing is quantitatively expected to follow a pseudo-cube root relationship of  $d$ -spacing to M:T ratio, reflecting the underlying conservation of volume and the natural relationship of a linear dimension to a volume ratio. Fitting of the PMT model parameters, however, requires knowledge of the pore size.<sup>35</sup> A convenient log re-

arrangement eliminates this need for pore size knowledge and a subsequent approximation yields an expected straight line with a slope of  $\sim 1/3$  for  $\log(d\text{-spacing})$  vs.  $\log(M:T)$ .<sup>36</sup> This log–log coordinate space thus expedites the identification of consistency with PMT conditions prior to pore size inputs from electron microscopy. In the case of  $O_{45}F_{11}$ , the linear best-fit slope of 0.30 was consistent with PMT behavior. This suggests that micelle chain exchange was arrested on the timescale of

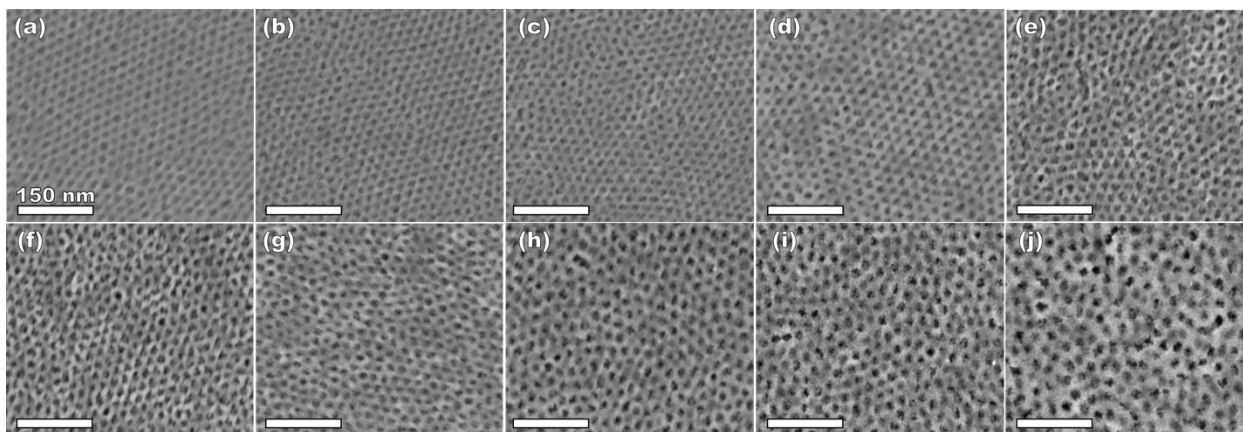


Figure 4. 5 – SEM images for a sample series prepared using  $O_{45}F_{11}$  micelle templates. The images are arranged in order of increasing material-to-template ratios: (a) 1.0, (b) 1.5, (c) 2.0, (d) 2.5, (e) 3.0, (f) 3.5, (g) 4.0, (h) 4.5, (i) 5.0, (j) 6.0.

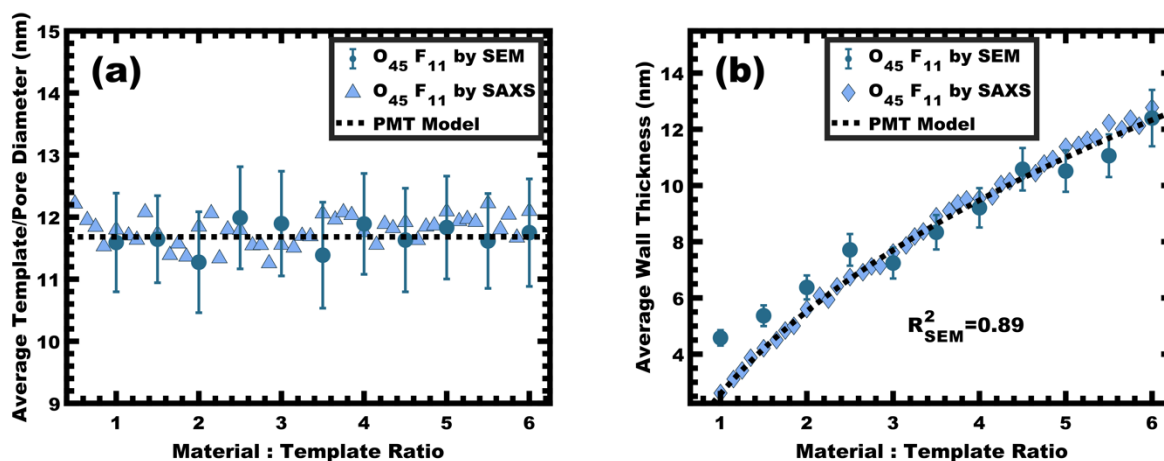


Figure 4. 6 – The average template/pore diameter (a) and wall thickness (b) for  $O_{45}F_{11}$  thin films were determined from hundreds of measurements on SEM images and were compared with a best-fit of the PMT model (dashed line). Additionally, these metrics were

calculated from SAXS  $d$ -spacing based upon the best-fit of the PMT model. The agreement of measured values with the PMT model is consistent with constant micelle core size. Error bars correspond to the standard-error-of-the-mean.

the experiment despite the exceedingly small PFOA block. Following the log–log analysis, measurements of the pore size and SAXS lattice expansion were used to assess consistency with persistent micelles. Measurements upon numerous SEM images of this series yielded a relatively constant average pore diameter of  $11.68 \pm 0.81$  nm that was consistent with kinetically trapped micelles. The SEM images also revealed that the average wall thickness expanded from  $4.58 \pm 0.27$  nm to  $12.40 \pm 1.00$  nm (~170% increase) as the M:T ratio monotonically increased (Fig. 4.11 and 4.12b). The PMT model was fitted to the observed lattice expansion including SEM metrics where the resulting best-fit closely matched the experimental  $d$ -spacing trend with a goodness-of-fit  $R^2 = 0.98$  (Fig. 4.10b). Furthermore, the observed  $d$ -spacing can be deconvolved into the underlying template/pore diameter and wall thickness using these best-fit parameters which closely matched the direct and model-independent measurements from SEM (Fig. 4.12). Thus,  $O_{45}F_{11}$  micelles in MeOH (aq) were most consistent with kinetic entrapment. This PMT series also demonstrated an unprecedented 2.7 $\times$  change in average wall thickness across a 45-sample series which is 90% larger than any prior PMT demonstration,<sup>36</sup> suggesting particularly persistent micelles are feasible in the high- $\chi$ , low- $N$  regime (Scheme 4.1).

#### $O_{45}F_8$ MICELLES: DYNAMIC OR PERSISTENT?

The analogous  $O_{45}F_8$  was next investigated in the same fashion with an M:T series spanning from 1.0–3.0. With so few repeat FOA units, the change of an average degree of polymerization from 11 to 8 appears minor but nonetheless constitutes a 27% decrease.

Figure 4.13 shows the resulting SAXS data for this series where the structure factor was significantly broader than the prior sample and the peak position varied sporadically with increasing M:T (Figure 4.13b) which is inconsistent with persistent micelle behavior. The corresponding  $d$ -spacing trend in log–log coordinate space is similarly unpredictable where the linear best-fit yields a slope of 0.08 with  $R^2 = -0.10$  (Fig 4.13b). Such sporadic  $d$ -spacing trends are often observed for dynamic and non-equilibrated micelles<sup>36,40</sup> where the resulting micelle size, size distribution, and structure factor are expected to vary the  $d$ -spacing in a non-monotonic fashion. Thus, the micelles prepared from O<sub>45</sub>F<sub>8</sub> in MeOH (aq) were most consistent with dynamic chain exchange.

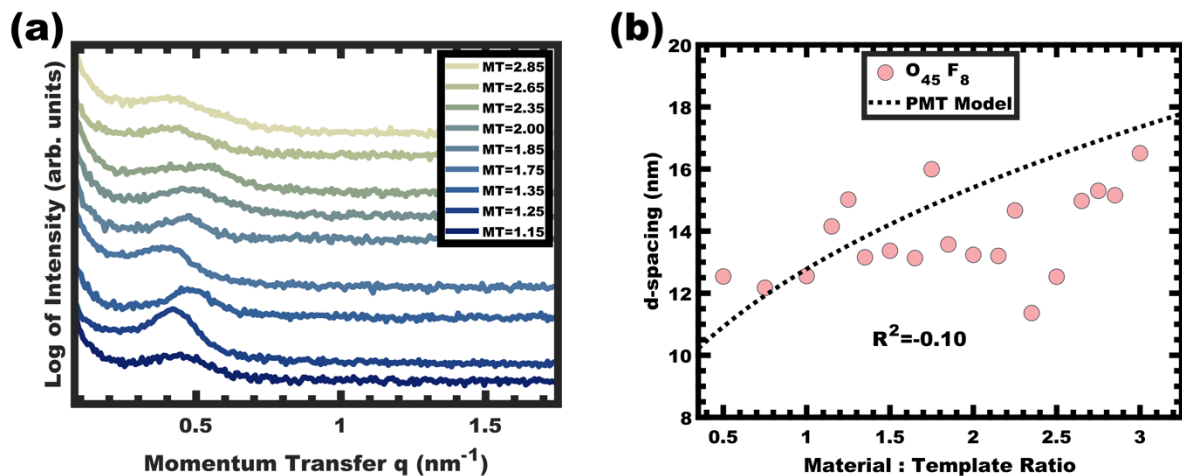


Figure 4. 7 – SAXS patterns for O<sub>45</sub>F<sub>8</sub> thin film series (a) did not exhibit the expected monotonic trend in peak shift (data offset vertically for clarity). The corresponding peak  $d$ -spacings were not consistent with the PMT model, suggesting active chain exchange (b).

#### EVALUATION OF THE $\chi N$ VALUE FROM SOLUBILITY PARAMETERS

The  $\chi N$  values were compared for the two considered polymer solutions. The estimation of  $\chi$  values from Hildebrand solubility parameters ( $\delta$ ) are semi-quantitative at best but are

distinctively convenient and often monotonic with reality (at least for minor changes).<sup>99</sup>

The relationship<sup>100</sup> is:

$$\chi_{1,2} = \frac{v}{k_b T} (\delta_1 - \delta_2)^2$$

where  $v$  is the repeat unit volume (FOA volume in PFOA),  $k_b$  is the Boltzmann constant,  $T$  is the absolute temperature in kelvin, and the  $\delta$  terms correspond to Hildebrand solubility parameters associated with the two-component interface under consideration. Hildebrand solubility parameters are determined by a range of methods where the magnitude corresponds to the volume-weighted energy of self-self-intermolecular interactions (cohesive energy density). Here, the molar volume of FOA was calculated to be  $0.501 \text{ nm}^3$  from group approximations.<sup>101</sup> Caution should be taken when comparing  $\chi$  values calculated using different molar volume ( $v$ ) values where a common lattice volume of  $0.118 \text{ nm}^3$  is sometimes assumed for comparisons without mer-volume effects. Regardless of which convention is used, the corresponding  $\chi N$  product is not affected. For the present system, Hildebrand solubility parameters of  $14.5 \sqrt{\text{MPa}}$  for PFOA<sup>102</sup> and  $30.0 \sqrt{\text{MPa}}$  for the MeOH (aq)<sup>103</sup> solution yielded an estimation of  $\chi_{\text{core-solvent}} = 29.2$ . It is worth noting that  $\chi_{\text{core-solvent}}$  is often substantially larger than  $\chi_{\text{A-B}}$  even when one polymer block has the same repeat unit structure as the solvent.<sup>104,105</sup> For example, a polymer-polymer blend  $\chi_{\text{A-B}}$  can be as low as  $10^{-2} - 10^{-3}$ , however,  $\chi_{\text{core-solvent}}$  values even in good solvents tend towards a lower limit of  $\sim 0.34$ .<sup>104,106,107</sup> The two studied conditions were thus estimated to have  $\chi N = 321$  for O<sub>45</sub>F<sub>11</sub> persistent micelles and  $\chi N = 234$  for O<sub>45</sub>F<sub>8</sub> dynamic micelles, both well within what would be called the strong segregation regime for bulk block polymers. Again, note the hazardous application of self-consistent mean-field theory to an oligomeric system

that is far from the limit of  $N \rightarrow \infty$ . A prior study of 43.5 kg mol<sup>-1</sup> PEO-*b*-PHA, for example, exhibited a transition from persistent micelles to dynamic micelles when similarly estimated  $\chi N$  values transitioned from  $\sim 140$  to 122, considerably lower than the present case, albeit still within the strong segregation limit.<sup>34</sup> The significant contrast between F<sub>11</sub> and F<sub>8</sub>-based micelle behavior reveals the previously reported “hypersensitivity to chain length”<sup>18</sup> within a curious low- $N$  regime where very minor changes to  $N$  have large ramifications to micelle kinetics.

#### MORE DIRECT MICELLE MEASUREMENTS *via* BULK CASTING

The persistent O<sub>45</sub>F<sub>11</sub> micelles were next examined with more challenging (slow) bulk casting. From a micelle persistence perspective, there are added challenges in bulk processing relative to fast evaporation during spin coating in the above examples. Such challenges are due in large part to the more gradual decrease in  $\chi$  during solvent evaporation coupled with the extended evaporation time for bulk casting. To the best of our knowledge, there are no examples of bulk PMTs processed by casting. In brief, the O<sub>45</sub>F<sub>11</sub> micelle template solutions were combined with titania nanoparticles as described above (see Experimental) and were evaporated in Teflon dishes at room temperature. A series of samples were prepared with M:T = 1.0 – 6.5. The SAXS patterns for this sample series exhibited a leftward shift towards lower  $q$ -values consistent with the  $d$ -spacing lattice expansion expected for persistent micelle templates (Figure 4.14a).

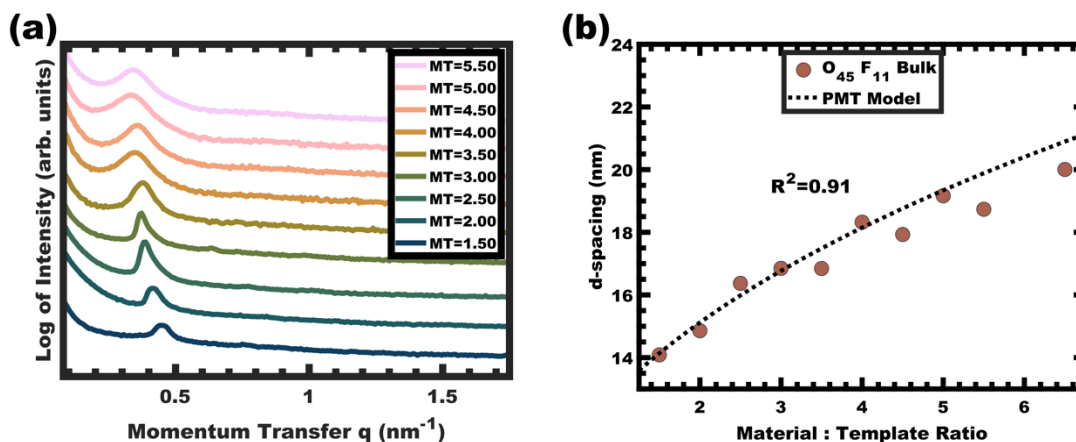


Figure 4. 8 – SAXS patterns for a bulk cast series from  $O_{45}F_{11}$  micelles. The monotonic leftward shift in  $q$ -space (a) indicates lattice expansion with increasing material-to-template ratio (offset vertically for clarity). The lattice expansion was quantitatively consistent with the PMT model (b), suggesting constant micelle core size.

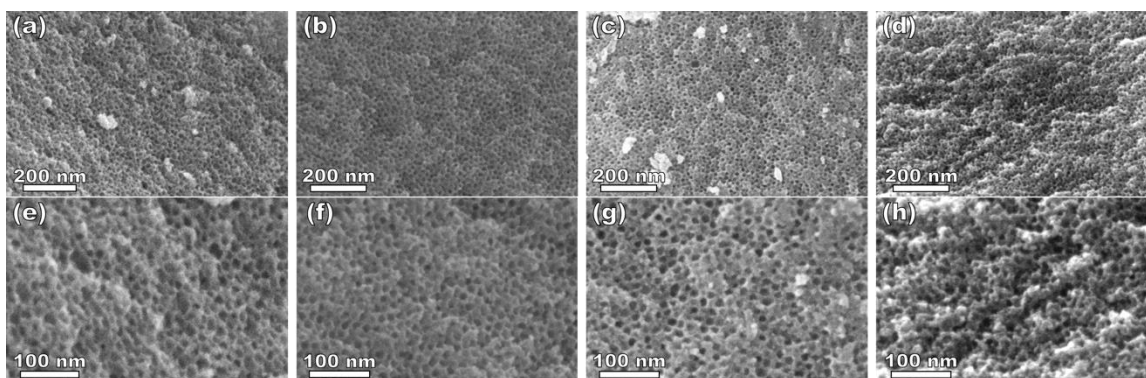


Figure 4. 9 – SEM images of bulk titania samples prepared by casting  $O_{45}F_{11}$  micelle templates with material precursors. The images are arranged in order of increasing material-to-template ratios: 1.50 (a and e), 3.00 (b and f), 3.50 (c and g), 4.00 (d and h).

Again, the log–log coordinate space was used to identify regions of consistency with PMT behavior. A linear trend was identified from M:T = 1.5–6.5 with a linear best-fit slope of 0.23 that was lower than the expected approximate slope of 1/3 but nevertheless was well-fitted by the PMT model without approximations (Figure 4.14b). The corresponding SEM data presented in Figure 4.15 are consistent with randomly packed spherical micelles albeit with less order than their sin coated counterparts. The analysis of hundreds of

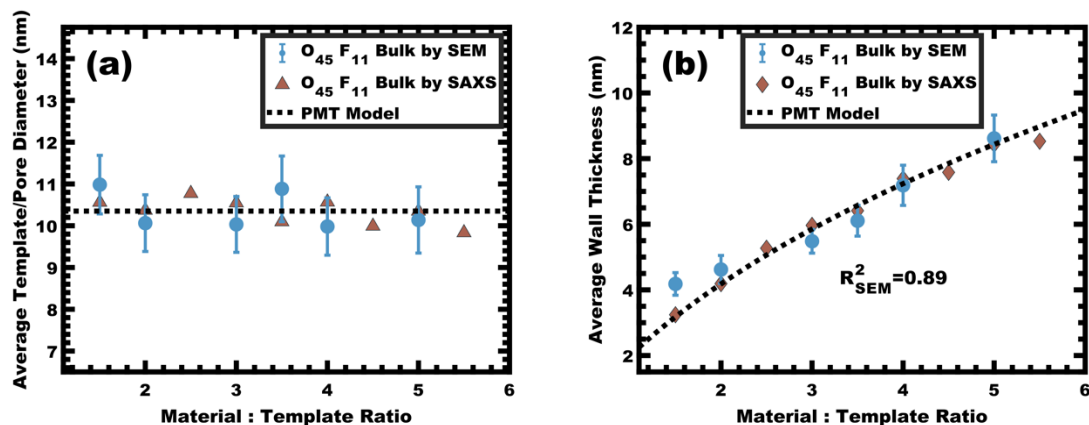
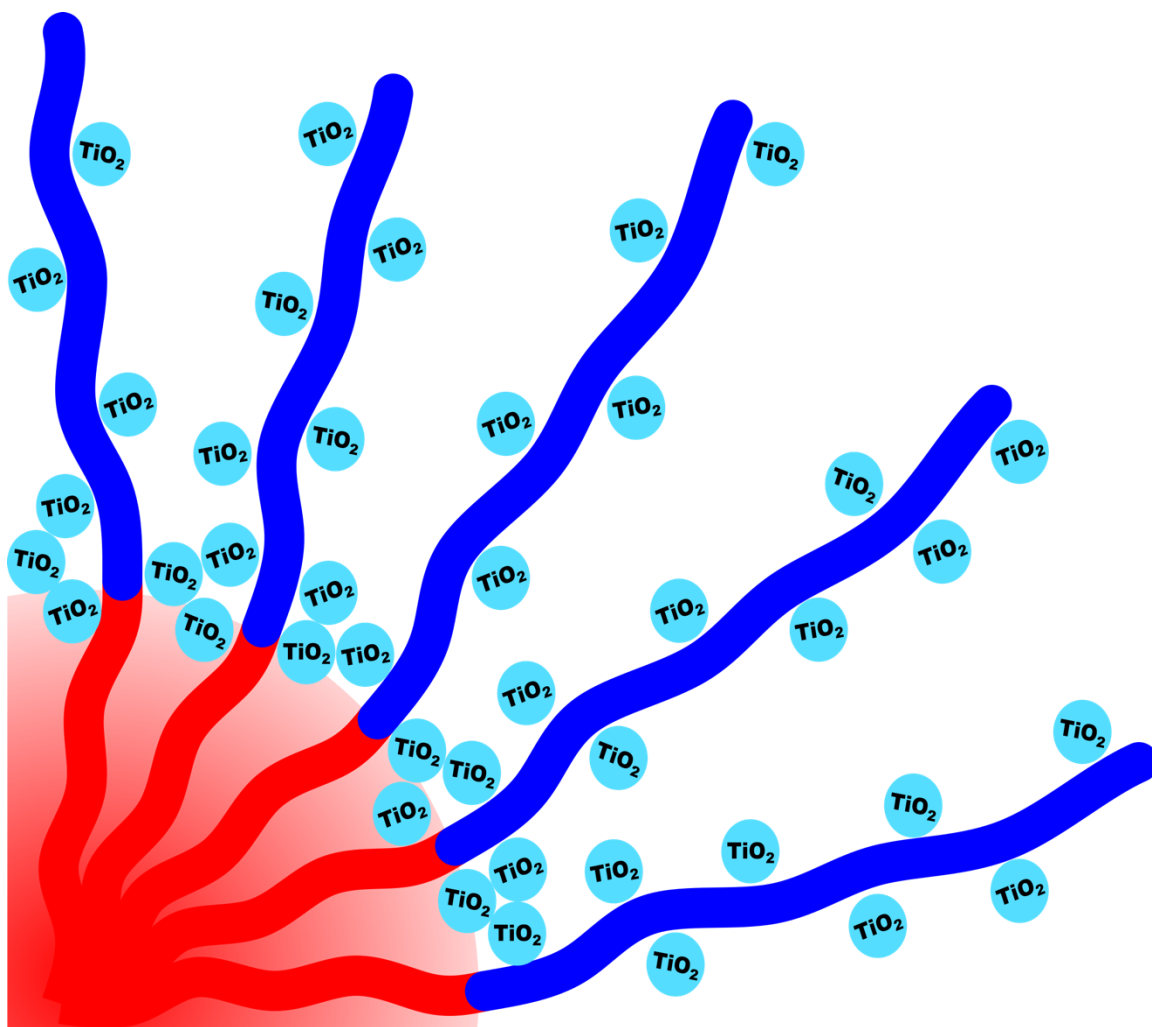


Figure 4. 10 – The average template/pore diameters (a) and wall thicknesses (b) were determined using measurements on SEM images. Additionally, these metrics were calculated from SAXS  $d$ -spacing based on the PMT model using best-fit parameters. The agreement of measured values with the PMT model is consistent with constant micelle core size. Error bars correspond to the standard-error-of-the-mean.

measurements from SEM images revealed a relatively constant average template/pore size of  $10.35 \pm 0.29$  nm (Fig. 4.16a). Similarly, the average wall thickness measured from SEM images monotonically increased from  $4.18 \pm 0.71$  nm with increasing material addition. The template/pore size and wall thickness metrics calculated using SAXS data and the PMT model best-fit closely correspond to the model-free and direct measurements by SEM with the latter having a goodness-of-fit  $R^2 = 0.89$  (Figure 4.16b). Thus, both the SAXS and SEM data were consistent with persistent micelles for the bulk processed  $O_{45}F_{11}$  micelles despite the slow processing. This first example of bulk PMT samples highlights the deep extent of kinetic entrapment for these high- $\chi$ , low- $N$  micelles.

## NANOPARTICLE DISTRIBUTION IN MICELLES

The micelle core dimensions were next compared to the resulting pore dimensions to measure the distribution of nanoparticles with respect to the core–corona interface. Again,



*Scheme 4. 3* – Depiction of nanoparticles preferentially interacting with the corona blocks while simultaneously being localized within the core–corona interface.

PEO based polymers are typically reported to distribute hydrophilic nanoparticles throughout that block.<sup>108</sup> As described above, the core diameter of O<sub>45</sub>F<sub>11</sub> micelles was 11.24 nm as determined by SAXS form factor fitting. However, the bulk processed O<sub>45</sub>F<sub>11</sub> micelle templates exhibited an average pore diameter of  $10.35 \pm 0.29$  nm. This difference of  $0.89 \pm 0.03$  nm is statistically significant and warrants further understanding. While the inorganic is expected to contract because of thermal processing, that change cannot explain this difference since contraction of the inorganic would rather enlarge the pore diameter.

However, the opposite is the case where the pore size is smaller than the micelle core size, suggesting that the nanoparticle distribution extends through the corona and  $\sim 0.45$  nm beyond the core–corona interface (Scheme 4.3). This is particularly surprising considering the fluorophobic interaction between the nanoparticles and FOA, suggesting that the driving force for this phenomenon is translation entropy as predicted by previous computations.<sup>62,63</sup> Prior mixtures of block polymers and nanoparticles have tended towards a nanoparticle preference of one domain or the interface of the two domains, depending on the nature of the nanoparticle–polymer interaction and polymer architecture.<sup>70,109–111</sup> In contrast, the present data report a case where both distribution types are apparent simultaneously which is consistent with several prior reports of mismatched dimensions or predominant placement at the interface with minor nanoparticle content within another block.<sup>40,112–114</sup> It is worth pointing out that the thermodynamic driving forces that favor these two different nanoparticle distributions are not mutually exclusive. This interpretation is further supported by analysis of the spin coated samples. During thin film processing, shrinkage due to solvent evaporation and inorganic condensation is principally accommodated in the out-of-plane direction due to good adhesion with the substrate. This distortion is not apparent by standard top-down SEM or transmission SAXS but is apparent with cross-sectional SEM and tilted/grazing incidence SAXS (See Appendix C).<sup>115</sup> This distortion was included when analyzing spin coated samples by using data acquired with the samples tilted at  $45^\circ$  relative to the incident X-ray beam. The ellipsoidal structure factor was extrapolated to calculate the purely out-of-plane dimension. The structure factor distortion was assumed to be equal to the micelle template distortion. Thus, combining the in-plane template diameter from SEM with this SAXS-derived distortion factor yielded the

corresponding out-of-plane pore diameter of  $8.40 \pm 0.17$  nm. The volume of this ellipsoidal template was equivalent to an undistorted sphere with a diameter of  $10.46 \pm 0.21$  nm which is statistically indistinguishable from the bulk sample template diameter of  $10.35 \pm 0.29$  nm (~1% difference). This is the first geometric comparison of identical PMTs applied to bulk and thin film samples. Thus, both undistorted bulk samples and distorted thin film samples exhibited pore dimensions that were consistent with nanoparticles extending both through the micelle corona and into the corona–core interface where such a dual preference may be a common though underappreciated phenomenon.

#### 4.5 CONCLUSION

Perfluorinated amphiphiles represent a fascinating and unique class of high- $\chi$  polymers whose potential for a variety of applications are continuing to be realized. Such polymers constitute a special class of candidates for kinetic entrapment as the high- $\chi$  values lower the required  $N$  for kinetically trapped, persistent micelles. Herein, it was shown that micellization and subsequent kinetic entrapment of the high- $\chi$ , low- $N$  polymer poly(ethylene oxide-*b*-perfluorooctyl acrylate) (PEO-*b*-PFOA) can be achieved in methanolic (aq) solutions with  $N = 11$  whereas dynamic micelles were found with  $N = 8$ . The resulting O<sub>45</sub>F<sub>11</sub> persistent micelles exhibited remarkable levels of persistence, enabling the most expansive persistent micelle template series to date with a 45-sample series spanning 170% increase in wall thickness tunability. The deeply trapped character of these O<sub>45</sub>F<sub>11</sub> micelles enabled the first demonstration of bulk PMT casting with extended micelle persistence throughout the necessarily slow evaporation process. Careful comparison of the micelle core dimensions to the resulting pore dimensions revealed that

the inorganic nanoparticle distribution extended throughout the corona and ~0.45 nm past the core–corona interface.

#### 4.6 REFERENCES

1. Mai, Y.; Eisenberg, A. Self-assembly of block copolymers. *Chem. Soc. Rev.* **2012**, *41*, 5969-5985.
2. Feng, H.; Lu, X.; Wang, W.; Kang, N.; Mays, J. W. Block Copolymers: Synthesis, Self-Assembly, and Applications. *Polymers* **2017**, *9*, 494.
3. Epps III, T. H.; O'Reilly, R. K. Block copolymers: controlling nanostructure to generate functional materials - synthesis, characterization, and engineering. *Chem. Sci.* **2016**, *7*, 1674-1689.
4. Liu, Y.; Goebel, J.; Yin, Y. Templated synthesis of nanostructured materials. *Chem. Soc. Rev.* **2013**, *42*, 2610-2653.
5. Leibler, L. Theory of Microphase Separation in Block Copolymers. *Macromolecules* **1980**, *13*, 1602-1617.
6. Sinturel, C.; Bates, F. S.; Hillmyer, M. A. High  $\chi$ -Low N Block Polymers: How Far Can We Go? *ACS Macro Lett.* **2015**, *4*, 1044-1050.
7. Bates, C. M.; Seshimo, T.; Maher, M. J.; Durand, W. J.; Cushen, J. D.; Dean, L. M.; Blachut, G.; Ellison, C. J.; Willson, C. G. Polarity-Switching Top Coats Enable Orientation of Sub-10-nm Block Copolymer Domains. *Science* **2012**, *338*, 775-779.
8. Bates, C. M.; Maher, M. J.; Janes, D. W.; Ellison, C. J.; Willson, C. G. Block Copolymer Lithography. *Macromolecules* **2014**, *47*, 2-12.
9. Luo, Y.; Montarnal, D.; Kim, S.; Shi, W.; Barteau, K. P.; Pester, C. W.; Hustad, P. D.; Christianson, M. D.; Fredrickson, G. H.; Kramer, E. J.; Hawker, C. J. Poly(dimethylsiloxane-b-methyl methacrylate): A Promising Candidate for Sub-10 nm Patterning. *Macromolecules* **2015**, *48*, 3422-3430.
10. Yoshida, K.; Tian, L.; Miyagi, K.; Yamazaki, A.; Mamiya, H.; Yamamoto, T.; Tajima, K.; Isono, T.; Satoh, T. Facile and Efficient Modification of Polystyrene-block-poly(methyl methacrylate) for Achieving Sub-10 nm Feature Size. *Macromolecules* **2018**, *51*, 8064-8072.
11. Chevalier, X.; Gomes Correia, C.; Pound-Lana, G.; Bézard, P.; Sérég , M.; Petit-Etienne, C.; Gay, G.; Cunge, G.; Cabannes-Bou , B.; Nicolet, C.; Navarro, C.;

- Cayrefourcq, I.; Müller, M.; Hadziioannou, G.; Iliopoulos, I.; Fleury, G.; Zelsmann, M. Lithographically Defined Cross-Linkable Top Coats for Nanomanufacturing with High- $\chi$  Block Copolymers. *ACS Appl. Mater. Interfaces* **2021**, *13*, 11224-11236.
12. Yu, G.; Eisenberg, A. Multiple Morphologies Formed from an Amphiphilic ABC Triblock Copolymer in Solution. *Macromolecules* **1998**, *31*, 5546-5549.
  13. Yu, K.; Bartels, C.; Eisenberg, A. Trapping of Intermediate Structures of the Morphological Transition of Vesicles to Inverted Hexagonally Packed Rods in Dilute Solutions of PS-*b*-PEO. *Langmuir* **1999**, *15*, 7157-7167.
  14. Zhang, L.; Eisenberg, A. Thermodynamic vs Kinetic Aspects in the Formation and Morphological Transitions of Crew-Cut Aggregates Produced by Self-Assembly of Polystyrene-*b*-poly(acrylic acid) Block Copolymers in Dilute Solution. *Macromolecules* **1999**, *32*, 2239-2249.
  15. Luo, L.; Eisenberg, A. Thermodynamic Size Control of Block Copolymer Vesicles in Solution. *Langmuir* **2001**, *17*, 6804-6811.
  16. Bhargava, P.; Zheng, J. X.; Li, P.; Quirk, R. P.; Harris, F. W.; Cheng, S. Z. D. Self-Assembled Polystyrene-block-poly(ethylene oxide) Micelle Morphologies in Solution. *Macromolecules* **2006**, *39*, 4880-4888.
  17. Bhargava, P.; Tu, Y.; Zheng, J. X.; Xiong, H.; Quirk, R. P.; Cheng, S. Z. D. Temperature-Induced Reversible Morphological Changes of Polystyrene-block-Poly(ethylene Oxide) Micelles in Solution. *J. Am. Chem. Soc.* **2007**, *129*, 1113-1121.
  18. Choi, S.; Lodge, T. P.; Bates, F. S. Mechanism of Molecular Exchange in Diblock Copolymer Micelles: Hypersensitivity to Core Chain Length. *Phys. Rev. Lett.* **2010**, *104*, 047802.
  19. Choi, S.; Bates, F. S.; Lodge, T. P. Molecular Exchange in Ordered Diblock Copolymer Micelles. *Macromolecules* **2011**, *44*, 3594-3604.
  20. Lu, J.; Bates, F. S.; Lodge, T. P. Chain Exchange in Binary Copolymer Micelles at Equilibrium: Confirmation of the Independent Chain Hypothesis. *ACS Macro Lett.* **2013**, *2*, 451-455.
  21. Parent, L. R.; Bakalis, E.; Ramírez-Hernández, A.; Kammeyer, J. K.; Park, C.; De Pablo, J.; Zerbetto, F.; Patterson, J. P.; Gianneschi, N. C. Directly Observing Micelle Fusion and Growth in Solution by Liquid-Cell Transmission Electron Microscopy. *J. Am. Chem. Soc.* **2017**, *139*, 17140-17151.
  22. Kelley, E. G.; Murphy, R. P.; Seppala, J. E.; Smart, T. P.; Hann, S. D.; Sullivan, M. O.; Epps, T. H. Size evolution of highly amphiphilic macromolecular solution assemblies via a distinct bimodal pathway. *Nat. Commun.* **2014**, *5*, 3599-3609.

23. Denkova, A. G.; Mendes, E.; Coppens, M. Non-equilibrium dynamics of block copolymer micelles in solution: recent insights and open questions. *Soft Matter* **2010**, *6*, 2351-2357.
24. Nicolai, T.; Colombani, O.; Chassenieux, C. Dynamic polymeric micelles versus frozen nanoparticles formed by block copolymers. *Soft Matter* **2010**, *6*, 3111-3118.
25. Dormidontova, E. E. Micellization Kinetics in Block Copolymer Solutions: Scaling Model. *Macromolecules* **1999**, *32*, 7630-7644.
26. Meli, L.; Santiago, J. M.; Lodge, T. P. Path-Dependent Morphology and Relaxation Kinetics of Highly Amphiphilic Diblock Copolymer Micelles in Ionic Liquids. *Macromolecules* **2010**, *43*, 2018-2027.
27. Halperin, A.; Alexander, S. Polymeric Micelles: Their Relaxation Kinetics. *Macromolecules* **1989**, *22*, 2403-2412.
28. Lund, R.; Willner, L.; Richter, D.; Dormidontova, E. E. Equilibrium Chain Exchange Kinetics of Diblock Copolymer Micelles: Tuning and Logarithmic Relaxation. *Macromolecules* **2006**, *39*, 4566-4575.
29. Wang, E.; Zhu, J.; Zhao, D.; Xie, S.; Bates, F. S.; Lodge, T. P. Effect of Solvent Selectivity on Chain Exchange Kinetics in Block Copolymer Micelles. *Macromolecules* **2020**, *53*, 417-426.
30. Mahmud, A.; Xiong, X.; Lavasanifar, A. Novel Self-Associating Poly(ethylene oxide)-block-poly( $\epsilon$ -caprolactone) Block Copolymers with Functional Side Groups on the Polyester Block for Drug Delivery. *Macromolecules* **2006**, *39*, 9419-9428.
31. Li, F.; Danquah, M.; Mahato, R. I. Synthesis and Characterization of Amphiphilic Lipopolymers for Micellar Drug Delivery. *Biomacromolecules* **2010**, *11*, 2610-2620.
32. Zhang, Y.; Li, Q.; Welsh, W. J.; Moghe, P. V.; Uhrich, K. E. Micellar and structural stability of nanoscale amphiphilic polymers: Implications for anti-atherosclerotic bioactivity. *Biomaterials* **2015**, *84*, 230-240.
33. Sun, X.; Wang, G.; Zhang, H.; Hu, S.; Liu, X.; Tang, J.; Shen, Y. The Blood Clearance Kinetics and Pathway of Polymeric Micelles in Cancer Drug Delivery. *ACS Nano* **2018**, *12*, 6179-6192.
34. Lokupitiya, H. N.; Jones, A.; Reid, B.; Guldin, S.; Stefik, M. Ordered Mesoporous to Macroporous Oxides with Tunable Isomorphic Architectures: Solution Criteria for Persistent Micelle Templates. *Chem. Mater.* **2016**, *28*, 1653-1667.
35. Sarkar, A.; Stefik, M. How to make persistent micelle templates in 24 hours and know it using X-ray scattering. *J. Mater. Chem. A* **2017**, *5*, 11840-11853.

36. Sarkar, A.; Evans, L.; Stefik, M. Expanded Kinetic Control for Persistent Micelle Templates with Solvent Selection. *Langmuir* **2018**, *34*, 5738-5749.
37. Lantz, K. A.; Clamp, N. B.; van den Bergh, W.; Sarkar, A.; Stefik, M. Full Gamut Wall Tunability from Persistent Micelle Templates via Ex Situ Hydrolysis. *Small* **2019**, *15*, 1900393-1900403.
38. Sarkar, A.; Thyagarajan, A.; Cole, A.; Stefik, M. Widely tunable persistent micelle templates via homopolymer swelling. *Soft Mater* **2019**, *15*, 5193-5203.
39. van den Bergh, W.; Lokupitiya, H. N.; Vest, N. A.; Reid, B.; Guldin, S.; Stefik, M. Nanostructure Dependence of T-Nb2O5 Intercalation Pseudocapacitance Probed Using Tunable Isomorphic Architectures. *Adv. Funct. Mater.* **2021**, *31*, 2007826-2007837.
40. Williams, E. R.; McMahon, P. L.; Reynolds, J. E.; Snider, J. L.; Stavila, V.; Allendorf, M. D.; Stefik, M. Tailored porous carbons enabled by persistent micelles with glassy cores. *Mater. Adv.* **2021**, *2*, 5381-5395.
41. van den Bergh, W.; Williams, E. R.; Vest, N. A.; Chiang, P.; Stefik, M. Mesoporous TiO2 Microparticles with Tailored Surfaces, Pores, Walls, and Particle Dimensions Using Persistent Micelle Templates. *Langmuir* **2021**, *37*, 12874-12886.
42. Lantz, K. A.; Sarkar, A.; Littrell, K. C.; Li, T.; Hong, K.; Stefik, M. Cavitation Enables Switchable and Rapid Block Polymer Exchange under High- $\chi$ N Conditions. *Macromolecules* **2018**, *51*, 6967-6975.
43. Won, Y.; Davis, H. T.; Bates, F. S. Molecular Exchange in PEO–PB Micelles in Water. *Macromolecules* **2003**, *36*, 953-955.
44. Lu, J.; Choi, S.; Bates, F. S.; Lodge, T. P. Molecular Exchange in Diblock Copolymer Micelles: Bimodal Distribution in Core-Block Molecular Weights. *ACS Macro Lett.* **2012**, *1*, 982-985.
45. Zinn, T.; Willner, L.; Lund, R.; Pipich, V.; Richter, D. Equilibrium exchange kinetics in n-alkyl–PEO polymeric micelles: single exponential relaxation and chain length dependence. *Soft Matter* **2012**, *8*, 623-626.
46. Murphy, R. P.; Kelley, E. G.; Rogers, S. A.; Sullivan, M. O.; Epps, T. H. Unlocking Chain Exchange in Highly Amphiphilic Block Polymer Micellar Systems: Influence of Agitation. *ACS Macro Lett.* **2014**, *3*, 1106-1111.
47. Ma, Y.; Lodge, T. P. Chain Exchange Kinetics in Diblock Copolymer Micelles in Ionic Liquids: The Role of  $\chi$ . *Macromolecules* **2016**, *49*, 9542-9552.

48. Kim, S.; Lee, S.; Choi, S.; Char, K. Chain Exchange Kinetics of Bottlebrush Block Copolymer Micelles. *Macromolecules* **2021**, *54*, 4739-4746.
49. König, N.; Willner, L.; Pipich, V.; Zinn, T.; Lund, R. Cooperativity during Melting and Molecular Exchange in Micelles with Crystalline Cores. *Phys. Rev. Lett.* **2019**, *122*, 78001-78007.
50. Larison, T.; Stefik, M. Persistent Micelle Corona Chemistry Enables Constant Micelle Core Size with Independent Control of Functionality and Polyelectrolyte Response. *Langmuir* **2021**, *37*, 9817-9825.
51. Xu, R.; Winnik, M. A.; Hallett, F. R.; Riess, G.; Croucher, M. D. Light-scattering study of the association behavior of styrene-ethylene oxide block copolymers in aqueous solution. *Macromolecules* **1991**, *24*, 87-93.
52. Hamley, I. W.; Castelletto, V.; Yang, Z.; Price, C.; Booth, C. Melt Phase Behavior of Poly(oxyethylene)-Poly(oxypropylene) Diblock Copolymers. *Macromolecules* **2001**, *34*, 4079-4081.
53. Mu, D.; Huang, X.; Lu, Z.; Sun, C. Computer simulation study on the compatibility of poly blends. *Chem. Phys* **2008**, *348*, 122-129.
54. Percec, V.; Johansson, G.; Ungar, G.; Zhou, J. Fluorophobic Effect Induces the Self-Assembly of Semifluorinated Tapered Monodendrons Containing Crown Ethers into Supramolecular Columnar Dendrimers Which Exhibit a Homeotropic Hexagonal Columnar Liquid Crystalline Phase. *J. Am. Chem. Soc* **1996**, *118*, 9855-9866.
55. Shen, J.; Hogen-Esch, T. Block Copolymer-like Self-Assembly of Fluorocarbon End-Functionalized Polystyrene and Polybutylmethacrylate. *J. Am. Chem. Soc.* **2008**, *130*, 10866-10867.
56. Johansson, G.; Percec, V.; Ungar, G.; Smith, K. Fluorophobic Effect Generates a Systematic Approach to the Synthesis of the Simplest Class of Rodlike Liquid Crystals Containing a Single Benzene Unit. *Chem. Mater.* **1997**, *9*, 164-175.
57. Hillmyer, M. A.; Lodge, T. P. Synthesis and self-assembly of fluorinated block copolymers. *J. Polym. Sci. Part A: Polym. Chem.* **2002**, *40*, 1-8.
58. Bunn, C. W.; Howells, E. R. Structures of Molecules and Crystals of Fluoro- Carbons. *Nature* **1954**, *174*, 549-551.
59. Dalvi, V. H.; Rossky, P. J. Molecular origins of fluorocarbon hydrophobicity. *Proc. Natl. Acad. Sci.* **2010**, *107*, 13603-13607.
60. Haynes, W. M. *CRC Handbook of Chemistry and Physics*; Taylor & Francis Group: Boca Raton, FL, 2011, pp 12-14.

61. Wang, Q.; Zhang, Q.; Zhan, X.; Chen, F. Structure and surface properties of polyacrylates with short fluorocarbon side chain: Role of the main chain and spacer group. *J. Polym. Sci. Part A, Polym. Chem.* **2010**, *48*, 2584-2593.
62. Lee, J.; Thompson, R. B.; Jasnow, D.; Balazs, A. C. Entropically driven formation of hierarchically ordered nanocomposites. *Phys. Rev. Lett.* **2002**, *89*, 155503.
63. Schultz, A. J.; Hall, C. K.; Genzer, J. Computer Simulation of Block Copolymer/Nanoparticle Composites. *Macromolecules* **2005**, *38*, 3007-3016.
64. Sanchez-Gaytan, B.; Cui, W.; Kim, Y.; Mendez-Polanco, M.; Duncan, T.; Fryd, M.; Wayland, B.; Park, S. Interfacial Assembly of Nanoparticles in Discrete Block-Copolymer Aggregates. *Angew. Chem., Int. Ed.* **2007**, *46*, 9235-9238.
65. Li, Q.; He, J.; Glogowski, E.; Li, X.; Wang, J.; Emrick, T.; Russell, T. P. Responsive Assemblies: Gold Nanoparticles with Mixed Ligands in Microphase Separated Block Copolymers. *Adv. Mater.* **2008**, *20*, 1462-1466.
66. Sanchez-Gaytan, B. L.; Li, S.; Kamps, A. C.; Hickey, R. J.; Clarke, N.; Fryd, M.; Wayland, B. B.; Park, S. Controlling the Radial Position of Nanoparticles in Amphiphilic Block-Copolymer Assemblies. *J. Phys. Chem.* **2011**, *115*, 7836-7842.
67. Lamarre, S. S.; Lemay, C.; Labrecque, C.; Ritcey, A. M. Controlled 2D Organization of Gold Nanoparticles in Block Copolymer Monolayers. *Langmuir* **2013**, *29*, 10891-10898.
68. Bockstaller, M. R.; Lapetnikov, Y.; Margel, S.; Thomas, E. L. Size-Selective Organization of Enthalpic Compatibilized Nanocrystals in Ternary Block Copolymer/Particle Mixtures. *J. Am. Chem. Soc.* **2003**, *125*, 5276-5277.
69. Chiu, J. J.; Kim, B. J.; Kramer, E. J.; Pine, D. J. Control of Nanoparticle Location in Block Copolymers. *J. Am. Chem. Soc.* **2005**, *127*, 5036-5037.
70. Mai, Y.; Eisenberg, A. Selective Localization of Preformed Nanoparticles in Morphologically Controllable Block Copolymer Aggregates in Solution. *Acc. Chem. Res.* **2012**, *45*, 1657-1666.
71. Bae, J.; Lawrence, J.; Miesch, C.; Ribbe, A.; Li, W.; Emrick, T.; Zhu, J.; Hayward, R. C. Multifunctional Nanoparticle-Loaded Spherical and Wormlike Micelles Formed by Interfacial Instabilities. *Adv. Mater.* **2012**, *24*, 2735-2741.
72. Luo, Q.; Hickey, R. J.; Park, S. Controlling the Location of Nanoparticles in Colloidal Assemblies of Amphiphilic Polymers by Tuning Nanoparticle Surface Chemistry. *ACS Macro. Lett.* **2013**, *2*, 107-111.

73. Balazs, A. C.; Emrick, T.; Russell, T. P. Nanoparticle Polymer Composites: Where Two Small Worlds Meet. *Science* **2006**, *314*, 1107-1110.
74. Mei, S.; Cao, J.; Lu, Y. Controllable assembly of two types of metal nanoparticles onto block copolymer nanospheres with ordered spatial distribution. *J. Mater. Chem. A* **2015**, *3*, 3382-3389.
75. Williams, D. B. G.; Lawton, M. Drying of Organic Solvents: Quantitative Evaluation of the Efficiency of Several Desiccants. *J. Org. Chem.* **2010**, *75*, 8351-8354.
76. Lokupitiya, H. N.; Stefik, M. Cavitation-enabled rapid and tunable evolution of high- $\chi_N$  micelles as templates for ordered mesoporous oxides. *Nanoscale* **2017**, *9*, 1393-1397.
77. Mikhail, S. Z.; Kimel, W. R. Densities and Viscosities of Methanol-Water Mixtures. *J. Chem. Eng. Data* **1961**, *6*, 533-537.
78. Iglesias, M.; Orge, B.; Tojo, J. Refractive indices, densities and excess properties on mixing of the systems acetone + methanol + water and acetone + methanol + 1-butanol at 298.15 K. *Fluid Phase Equilibria* **1996**, *126*, 203-223.
79. Wang, E.; Lu, J.; Bates, F. S.; Lodge, T. P. Effect of Corona Block Length on the Structure and Chain Exchange Kinetics of Block Copolymer Micelles. *Macromolecules* **2018**, *51*, 3563-3571.
80. Zhao, D.; Ma, Y.; Lodge, T. P. Exchange Kinetics for a Single Block Copolymer in Micelles of Two Different Sizes. *Macromolecules* **2018**, *51*, 2312-2320.
81. Ma, Y.; Lodge, T. P. Poly(methyl methacrylate)-block-poly(n-butyl methacrylate) Diblock Copolymer Micelles in an Ionic Liquid: Scaling of Core and Corona Size with Core Block Length. *Macromolecules* **2016**, *49*, 3639-3646.
82. Bagshaw, E.; Proust, T. J.; Pinnavaia, T. J. Templating of Mesoporous Molecular Sieves by Nonionic Polyethylene Oxide Surfactants. *Science* **1995**, *269*, 1242-1244.
83. Templin, M.; Franck, A.; Du Chesne, A.; Leist, H.; Zhang, Y.; Ulrich, R.; Schädler, V.; Wiesner, U. Organically Modified Aluminosilicate Mesosstructures from Block Copolymer Phases. *Science* **1997**, *278*, 1795-1798.
84. Ren, Y.; Ma, Z.; Bruce, P. G. Ordered Mesoporous Metal Oxides: Synthesis and Applications. *Chem. Soc. Rev.* **2012**, *41*, 4909-4927.
85. Liu, J.; Zou, S.; Liao, X.; Hong, Y.; Xiao, L.; Fan, J. A General Synthesis of Mesoporous Metal Oxides With Well-Dispersed Metal Nanoparticles via a Versatile Sol-Gel Process. *J. Mater. Chem. A* **2013**, *1*, 4038-4047.

86. Wei, B.; Guo, X.; Cui, Y.; Ma, S.; Li, W.; Bai, Y. Polyether fluorinated amphiphilic diblock polymer: Preparation, characterization and application as drug delivery agent. *Eur. Polym. J.* **2022**, *162*, 110872-110880.
87. Wanka, G.; Hoffmann, H.; Ulbricht, W. Phase Diagrams and Aggregation Behavior of Poly(oxyethylene)-Poly(oxypropylene)-Poly(oxyethylene) Triblock Copolymers in Aqueous Solutions. *Macromolecules* **1994**, *27*, 4145-4159.
88. Lombardo, D.; Munaò, G.; Calandra, P.; Pasqua, L.; Caccamo, M. T. Evidence of pre-micellar aggregates in aqueous solution of amphiphilic PDMS-PEO block copolymer. *Phys. Chem. Chem. Phys.* **2019**, *21*, 11983-11991.
89. Matsumoto, K.; Mazaki, H.; Matsuoka, H. Fluorinated Amphiphilic Vinyl Ether Block Copolymers: Synthesis and Characteristics of Their Micelles in Water. *Macromolecules* **2004**, *37*, 2256-2267.
90. Jada, A.; Hurtrez, G.; Siffert, B.; Riess, G. Structure of polystyrene-block-poly(ethylene oxide) diblock copolymer micelles in water. *Macromol. Chem. Phys.* **1996**, *197*, 3697-3710.
91. Mortensen, K.; Brown, W.; Almdal, K.; Alami, E.; Jada, A. Structure of PS-PEO Diblock Copolymers in Solution and the Bulk State Probed Using Dynamic Light-Scattering and Small-Angle Neutron-Scattering and Dynamic Mechanical Measurements. *Langmuir* **1997**, *13*, 3635-3645.
92. Nakano, M.; Deguchi, M.; Matsumoto, K.; Matsuoka, H.; Yamaoka, H. Self-Assembly of Poly(1,1-diethylsilabutane)-block-poly(2-hydroxyethyl methacrylate) Block Copolymer. 1. Micelle Formation and Micelle-Unimer-Reversed Micelle Transition by Solvent Composition. *Macromolecules* **1999**, *32*, 7437-7443.
93. Clatter, O.; Scherf, G.; Schillén, K.; Brown, W. Characterization of a Polyethylene oxide)-Poly(propylene oxide) Triblock Copolymer (EO27-PO39-EO27) in Aqueous Solution. *Macromolecules* **1994**, *27*, 6046-6054.
94. Norris, M. K.; Fuhrman, B. P.; Leach, C. L. Liquid ventilation: it's not science fiction anymore. *AACN Clin Issues Crit Care Nurs.* **1994**, *3*, 246-254.
95. Pedersen, J. S. Analysis of small-angle scattering data from colloids and polymer solutions: modeling and least-squares fitting. *Adv. Colloid Interface Sci.* **1997**, *70*, 171-210.
96. Schwab, M.; Stühn, B. Thermotropic transition from a state of liquid order to a macrolattice in asymmetric diblock copolymers. *Phys. Rev. Lett.* **1996**, *76*, 924-927.
97. Schwab, M.; Stühn, B. Asymmetric diblock copolymers-phase behaviour and kinetics of structure formation. *Colloid Polym. Sci.* **1997**, *275*, 341-351.

98. Wang, X.; Dormidontova, E. E.; Lodge, T. P. The Order–Disorder Transition and the Disordered Micelle Regime for Poly(ethylenepropylene-*b*-dimethylsiloxane) Spheres. *Macromolecules* **2002**, *35*, 9687-9697.
99. Stefik, M. Single-variable porous nanomaterial series from polymer structure-directing agents. *J. Mater. Res.* **2022**, *37*, 25-42.
100. Brandrup, J.; Immergut, E. H.; Grulke, E. A. *Polymer Handbook*; New York, 1999, pp 2250.
101. Grulke, E. A. Solubility Parameter Values. **2005**.
102. Kim, S.; Cho, Y.; Kim, J. H.; Song, S.; Lim, J.; Choi, S.; Char, K. Structural Analysis of Bottlebrush Block Copolymer Micelles Using Small-Angle X-ray Scattering. *ACS Macro Lett.* **2020**, *9*, 1261-1266.
103. Barton, A. F. M. Solubility Parameters. *Chem. Rev.* **1974**, *75*, 731-751.
104. Hiemenz, P. C.; Lodge, T. P. *Polymer Chemistry*; CRC Press: 2007.
105. Brandrup, J.; Immergut, E. H.; Grulke, E. A. *Polymer Handbook*; Wiley-Interscience: Boca Raton, FL, 1999; .
106. Brandrup, J.; Immergut, E. H.; Grulke, E. A.; Abe, A.; Bloch, D. R., Eds.; In *Polymer Handbook*; Wiley: New York, 1999; Vol. 89.
107. Mark, J. E. *Physical Properties of Polymers Handbook*; Springer: New York, 2007; , pp 233-257.
108. Stefik, M.; Wang, S.; Hovden, R.; Sai, H.; Tate, M. W.; Muller, D. A.; Steiner, U.; Gruner, S. M.; Wiesner, U. Networked and chiral nanocomposites from ABC triblock terpolymer coassembly with transition metal oxide nanoparticles. *J. Mater. Chem.* **2012**, *22*, 1078-1087.
109. Wang, J.; Li, W.; Zhu, J. Encapsulation of inorganic nanoparticles into block copolymer micellar aggregates: Strategies and precise localization of nanoparticles. *Polymer* **2014**, *55*, 1079-1096.
110. Liang, R.; Xu, J.; Li, W.; Liao, Y.; Wang, K.; You, J.; Zhu, J.; Jiang, W. Precise Localization of Inorganic Nanoparticles in Block Copolymer Micellar Aggregates: From Center to Interface. *Macromolecules* **2015**, *48*, 256-263.
111. Haryono, A.; Binder, W. H. Controlled Arrangements of Nanoparticle Arrays in Block-Copolymer Domains. *Small* **2006**, *2*, 600-611.

112. Chung, H.; Kim, J.; Ohno, K.; Composto, R. J. Controlling the Location of Nanoparticles in Polymer Blends by Tuning the Length and End Group of Polymer Brushes. *ACS Macro Lett.* **2012**, *1*, 252-256.
113. Guo, Y.; Harirchian-Saei, S.; Izumi, C. M. S.; Moffitt, M. G. Block Copolymer Mimetic Self-Assembly of Inorganic Nanoparticles. *ACS Nano* **2011**, *5*, 3309-3318.
114. Wang, M.; Kumar, S.; Lee, A.; Felorzabihi, N.; Shen, L.; Zhao, F.; Froimowicz, P.; Scholes, G. D.; Winnik, M. A. Nanoscale Co-organization of Quantum Dots and Conjugated Polymers Using Polymeric Micelles As Templates. *J. Am. Chem. Soc.* **2008**, *130*, 9481-9491.
115. Ruland, W.; Smarsly, B. M. Two-dimensional small-angle X-ray scattering of self-assembled nano composite films with oriented arrays of spheres: determination of lattice type, preferred orientation, deformation and imperfection. *J. Appl. Crystallogr.* **2007**, *40*, 409-417.

**CHAPTER 5: SUMMARY AND SUGGESTIONS FOR FUTURE  
WORK**

## 5.1 SUMMARY

This work aimed to leverage new mechanism of kinetic micelle control towards the tunable synthesis of porous nanomaterials for a wide host of applications. It is first shown that common methods of micelle templating such as with commercial pluronics or plasticized block polymers fail to deliver kinetic micelle control when used with slow crosslinking carbon materials. This is largely due to the critical transition from a solvent-rich to a material-rich environment, leading to the subsequent decrease in the  $\chi_{\text{core-solvent}}$  needed to retain micelle persistence with non-glassy block polymers. A set of specific design criteria are next enumerated that enabled the realization of fully immobilized (glassy) micelle character through the combination of a high- $T_g$  core-forming segment and the removal of all plasticizing solvents for this block. This was shown to enable a series of tunable porous nanomaterials where increasing amounts of carbon material effect an increase in wall thickness without compromising the average micelle diameter. Furthermore, the highly robust nature of these glassy micelles permitted their direct imaging by TEM and correlation of micelle core-pore metrics provided the first direct observation of the PMT mechanism.

Building off the development of glassy persistent micelles, a procedure was next developed that incorporated polystyrene homopolymer (hPS) into the micelle cores to enable micelle core tunability based upon homopolymer addition. While persistent micelles had indeed been swollen with core block homopolymer before, the resulting

micelles exhibited limited benchtop stability due to the dynamic exchange of the homopolymer between micelles. Here, the rapid addition of hPS to a carefully tuned solution of PEO-*b*-PS micelles was needed to realize the successful insertion and retention of the homopolymer into the cores of the diblock micelles. Following the removal of all plasticizing solvents through selective distillation, the resulting glassy swollen micelles demonstrated remarkable benchtop stability, with freshly made and six-month-old samples being statistically indistinguishable in their SAXS scattering profiles. Micelle swelling was tracked through a host of complimentary techniques with micelle metrics from solution SAXS and direct measurements from TEM images operating in close agreement for all samples. Interestingly, simple volume models (without assumptions) indicated that chain exchange was active for PEO-*b*-PS micelles during the hPS addition step, leading to drastic increases in micelle aggregation number as a function of homopolymer loading. Furthermore, analysis into micelle surface chain density revealed that systems tended towards a constant interfacial chain density to sufficiently screen core-solvent interactions as micelles increase in diameter from homopolymer loading.

Lastly, micelle persistence in the low- $N$  regime was interrogated with especially high- $\chi$  core-forming perfluorinated blocks. As all prior reports of persistent micelles required high molar masses (high  $N$ ) in order to realize micelle persistence through an enthalpic  $\chi N$  barrier or glassy character, such micelles are limited in their utility for applications requiring smaller feature sizes. A series of high- $\chi$ , low- $N$  PEO-*b*-PFOA diblocks were synthesized and their persistence evaluated through a suite of characterization techniques ranging from solution SAXS to analysis of pore and wall

measurements from their templated materials. It was found that the high- $\chi$  perfluorinated segment enabled micelle persistence with as few as 11 repeat units with such micelles demonstrating remarkable windows of persistence spanning a 45-sample series and 170% increase in wall thickness tunability. Furthermore, the elevated levels of persistence with such micelles permitted micelle persistence even with challenging bulk casting techniques. Micelle core and material pore dimensions were compared across all relevant characterization techniques to evaluate self-consistency and track micelle dimensions throughout the entire processing timeline. Interestingly, out of plane SAXS measurements revealed anisotropic pore compression in the thin film samples only which was accounted for using a simple geometric model without assumptions. After correction for pore distortions, the templated data were found to be highly consistent while slight TiO<sub>2</sub> nanoparticle penetration into the PFOA core connected the free micelle SAXS data to the thin film and bulk material datasets.

## 5.2 SUGGESTIONS FOR FUTURE WORK

The work herein detailed has filled in many gaps within the persistent micelle landscape and has likewise set the stage for many others. Due to the recent demonstration of PMT's ability to unambiguously elucidate energy storage phenomena,<sup>1</sup> the demand for improved and diversified modalities of persistence will only increase as the utility of PMT continues to be realized.<sup>2-5</sup> One such avenue for PMT expansion is in the direction of especially large pore sizes (i.e., in excess of ~200 nm). Of course, the controlled synthesis of such nanomaterials would require micelles with especially large cores resulting from substantial hydrophobic segments. Here, the polymerization of

macromonomers through especially active polymerization techniques e.g., ROMP will likely play a role. Once length scales are realized, the synthesis of hierarchical materials<sup>6</sup> will be within reach as PMT has already tamed the mesoporous regime.

### 5.3 REFERENCES

- (1) van den Bergh, W.; Lokupitiya, H.; Vest, N.; Reid, B.; Guldin, S.; Stefik, M. Tunable isomorphic architectures of T-Nb<sub>3</sub>O<sub>5</sub> quantify nanostructure dependence of intercalation pseudocapacitance upon diffusive processes. *Adv. Funct. Mater.* **2021**, *31*, 2007826.
- (2) van den Bergh, W.; Wechsler, S.; Lokupitiya, H. N.; Jarocho, L.; Heald, S.; Stefik, M. Amorphization of pseudocapacitive T-Nb<sub>2</sub>O<sub>5</sub> accelerates lithium diffusivity as revealed using isomorphic architectures. *Batter. Supercaps* **2022**, *5*, e202200056.
- (3) van den Bergh, W.; Larison, T.; Jesus Jara Fornerod, M.; Guldin, S.; Stefik, M. Faster intercalation pseudocapacitance enabled by adjustable amorphous titania where tunable isomorphic architectures reveal accelerated lithium diffusivity. *Batter. Supercaps* **2022**, *5*, e202200122.
- (4) Stefik, M. Single-variable porous nanomaterial series from polymer structure directing agents. *J. Mater. Res.* **2022**, *37*, 25–42.
- (5) van den Bergh, W.; Stefik, M.; Understanding rapid intercalation materials one parameter at a time. *Adv. Funct. Mater.* **2022**, *32*, 2204126.
- (6) Zhao, Y.; Taylor, E. E.; Hu, X.; Evanko, B.; Zheng, X.; Wang, H.; Ohnishi, R.; Tsukazaki, T.; Li, J.-F.; Stadie, N. P.; Yoo, S. J.; Stucky, G. D.; Boettcher, S. W. What structural features make porous carbons work for redox-enhanced electrochemical capacitors? *ACS Energy Lett.* **2021**, *6*, 854–861.

## APPENDIX A: CHAPTER 2 SUPPORTING INFORMATION

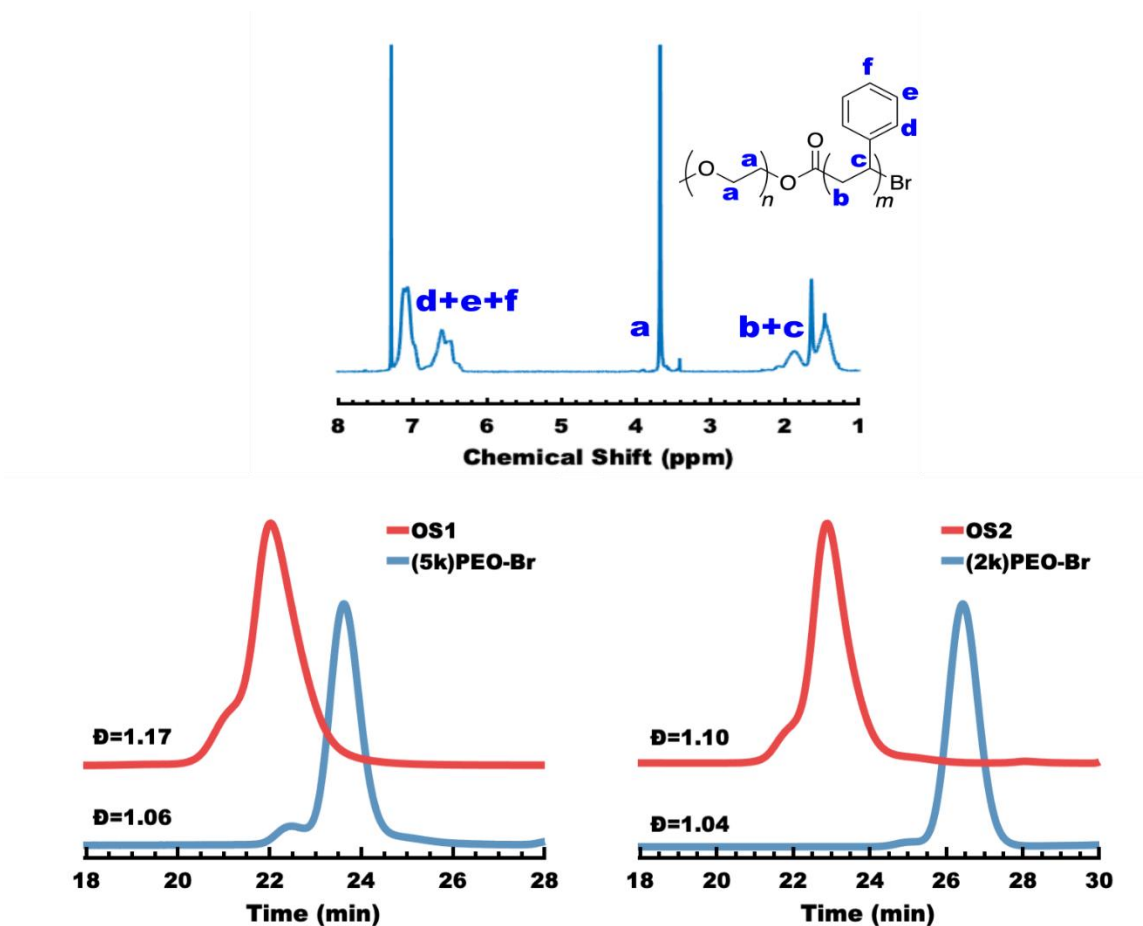


Figure A. 1 –  $^1\text{H-NMR}$  and GPC of OS1 along with the GPC of OS2 demonstrate the controlled chain extension with polystyrene and the resulting narrow molar mass dispersity. The GPC elugrams were offset vertically for clarity.

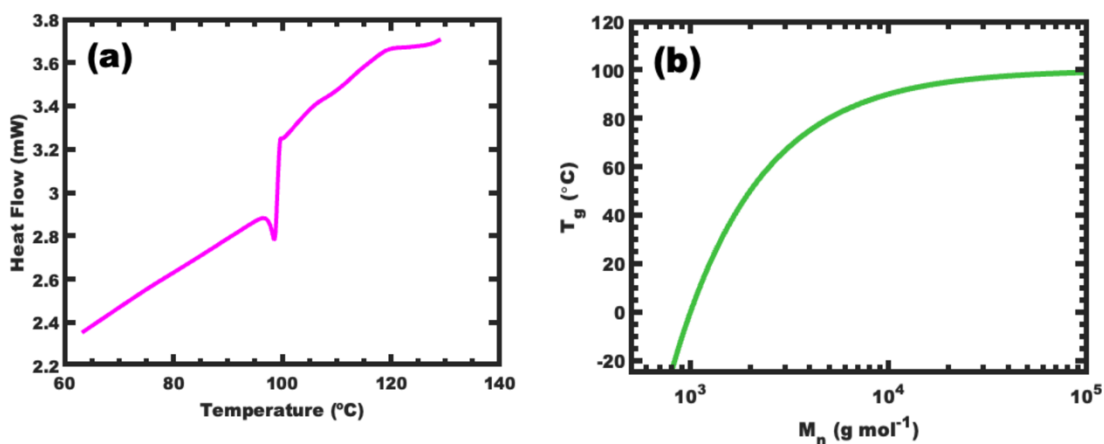


Figure A. 2 – DSC data illustrating the thermal characteristics of the diblock polymer OS1 (a). The midpoint of the  $T_g$  feature is  $99.1\text{ }^\circ\text{C}$ . Plot of the Flory-Fox prediction of PS  $T_g$  as a function of molar mass (b). This relationship predicts a  $T_g$  value of  $\sim 20\text{ }^\circ\text{C}$  for the  $\sim 800\text{ g mol}^{-1}$  PS in OS2.

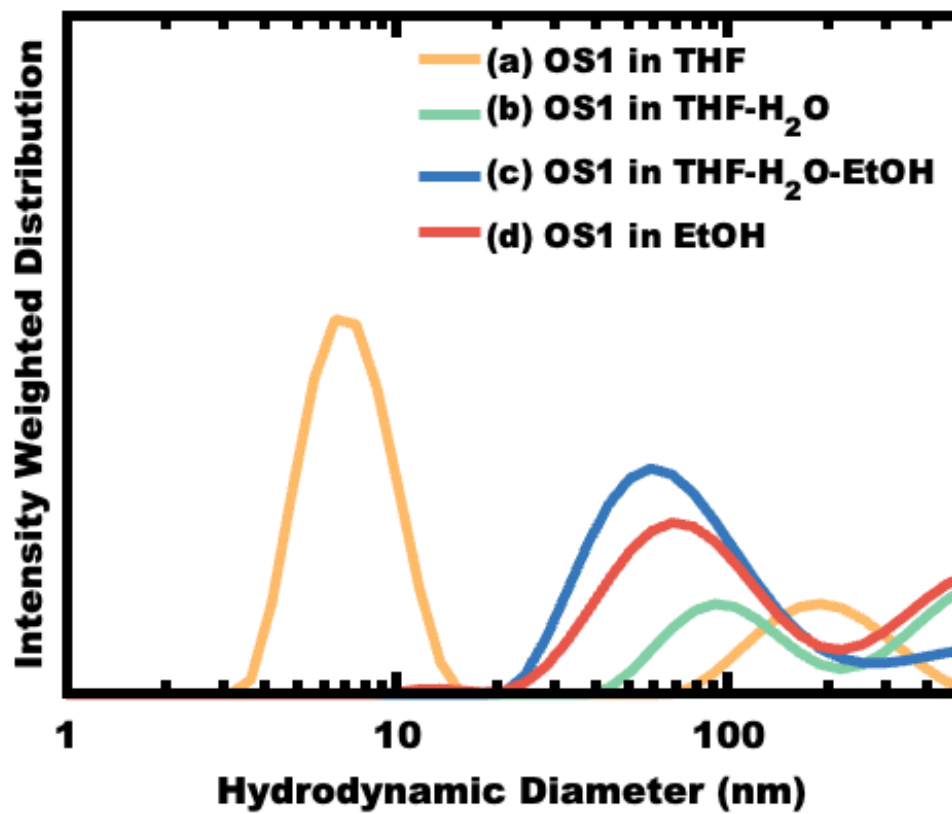


Figure A. 3 – DLS data of OS1 micelles at each processing stage.

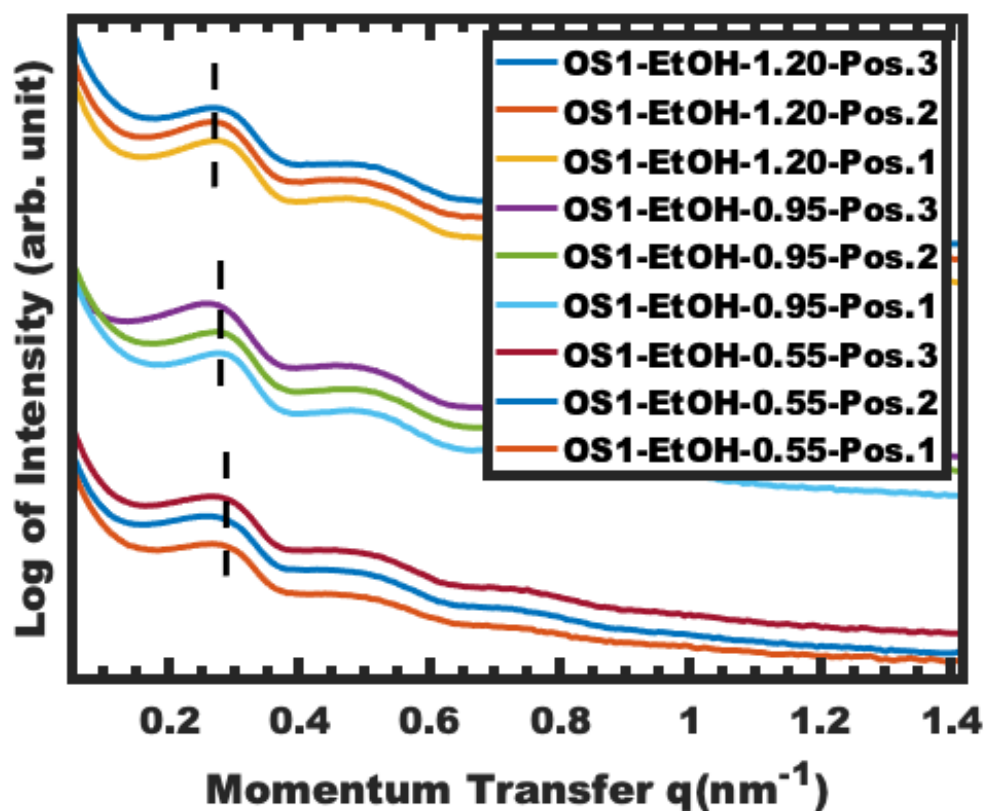


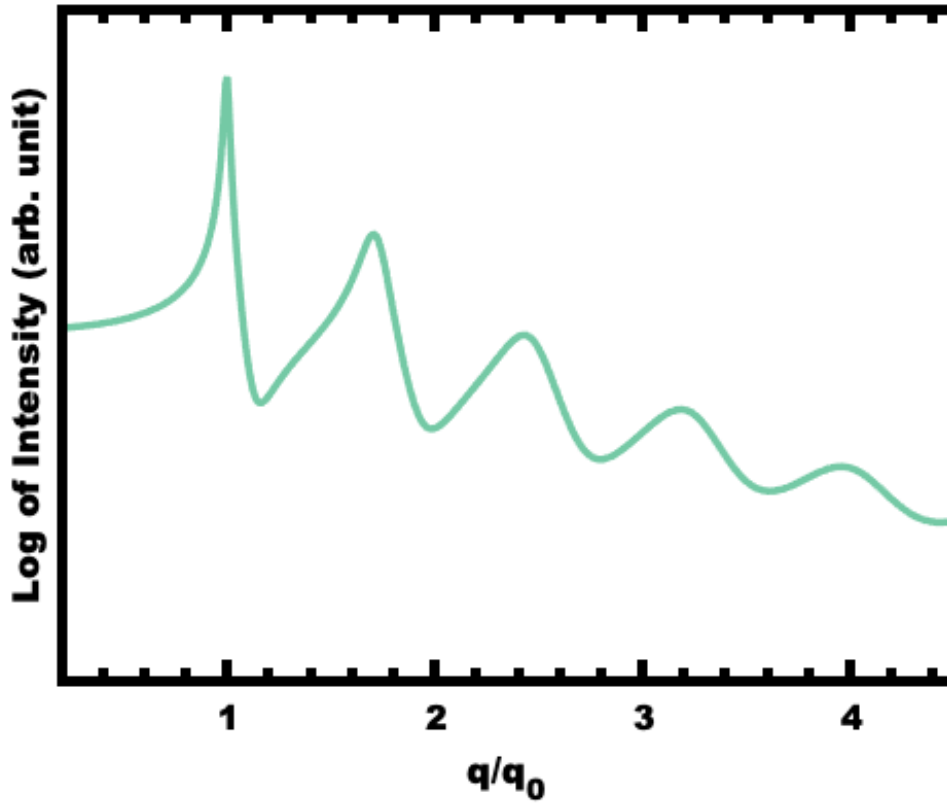
Figure A. 4 – Multiple SAXS measurements demonstrate narrow variation with as-made OS1-EtOH sample series. Samples are offset vertically for clarity.

Table A. 1 – Measurements from series OS1-EtOH as-made

M:T Ratio	$d$ -spacing (nm)	Average Template Diameter (nm) <sup>a</sup>	Standard Deviation of Template Diameter (nm) <sup>b</sup>	Average Wall Thickness (nm) <sup>b</sup>	Standard Deviation of Wall Thickness (nm) <sup>b</sup>	Percent Change in Wall Thickness (%)
0	N/A	$18.68 \pm 0.22$	3.06	N/A	N/A	N/A
0.5	25.03	$17.11 \pm 0.31$	3.12	$8.34 \pm 0.34$	3.42	N/A
0.85	24.01	$17.51 \pm 0.26$	2.61	$8.00 \pm 0.15$	1.53	N/A
0.95	24.29	$17.60 \pm 0.27$	2.70	$8.40 \pm 0.17$	1.70	5.00
1.00	23.99	$17.45 \pm 0.28$	2.83	$9.18 \pm 0.18$	1.75	14.75
1.05	24.34	$17.30 \pm 0.27$	2.68	$9.74 \pm 0.18$	1.81	21.75
1.10	25.21	$17.68 \pm 0.25$	2.50	$10.24 \pm 0.20$	2.05	28.00
1.20	25.71	$17.50 \pm 0.23$	2.31	$10.74 \pm 0.20$	2.00	34.25
1.40	25.41	$17.16 \pm 0.22$	2.21	$11.81 \pm 0.31$	1.81	47.63

<sup>a</sup>Average values are reported  $\pm$  the standard-error-of-the-mean to indicate uncertainty in the reported average value.

<sup>b</sup>The standard deviation of the measured metric are presented to indicate the statistical distribution of the measured values.



*Figure A. 5* – Simulated SAXS pattern for randomly packed hard spheres at 70 vol% and a gaussian size distribution having 6% standard deviation. The structure factor peaks have a  $q$ -spacing ratio of  $q/q_0 = 1, 1.7, 2.4, 3.1, 3.9$  where  $q_0$  is the first structure factor peak.

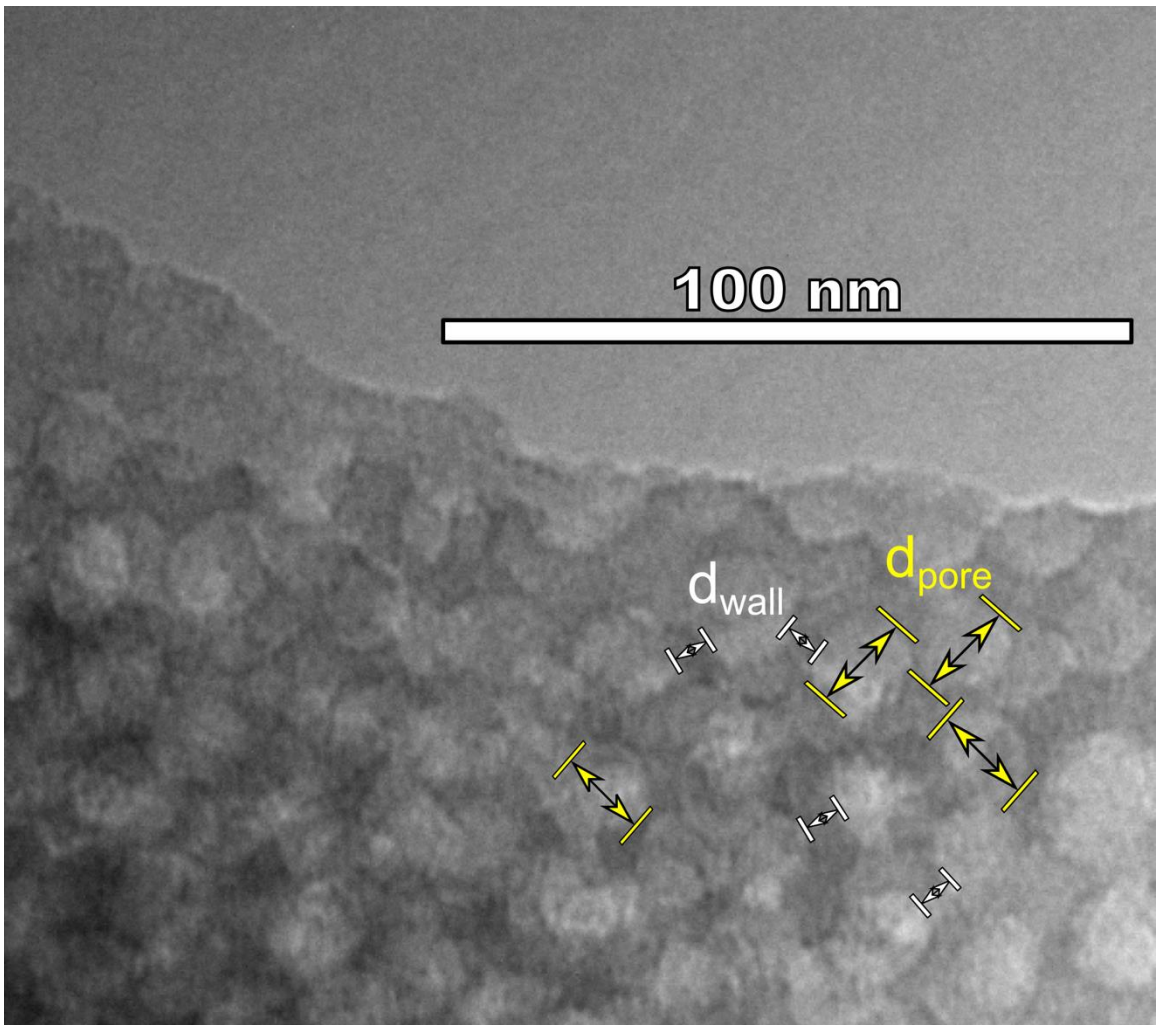


*Figure A. 6* – TEM image of OS1-EtOH-1.15 showing the wall ( $d_{\text{wall}}$ ) and pore ( $d_{\text{pore}}$ ) dimensions used for statistical analysis.

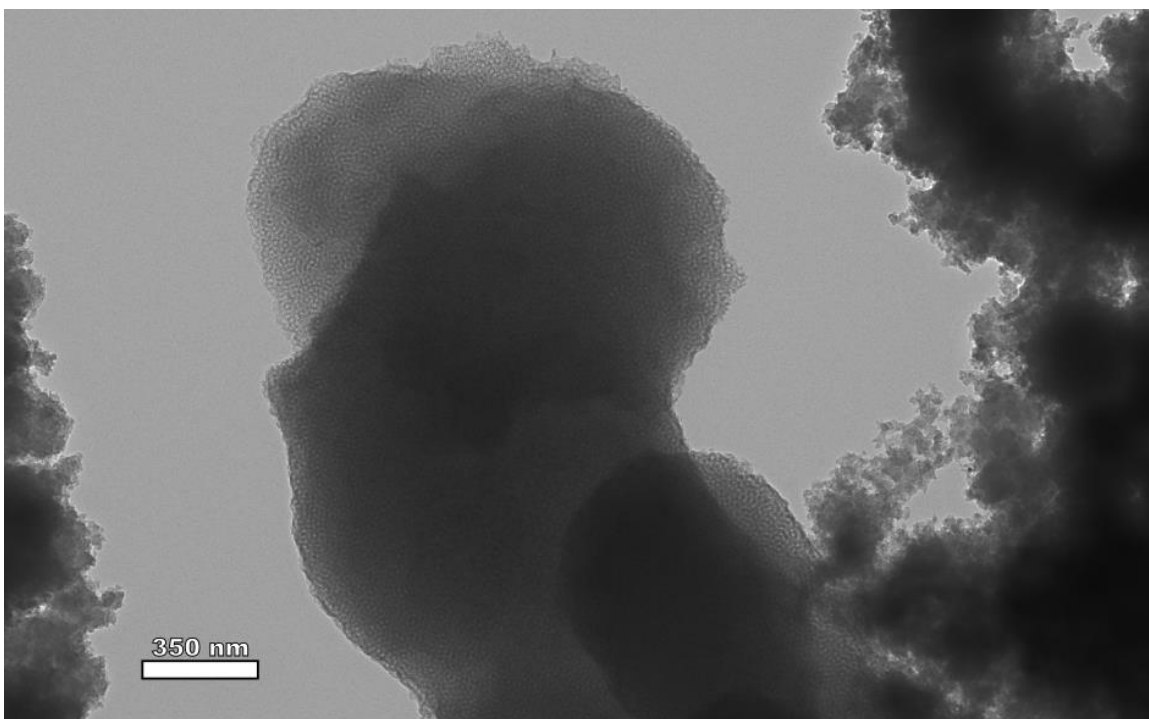


*Figure A. 7* – Porous PMT carbon (center) and non-templated carbon (edges) were both found with M:T values exceeding 1.3 and were attributed to partial phase separation of some carbon precursors from micelle templates. The samples has an M:T of 2.15 and was processed from EtOH.

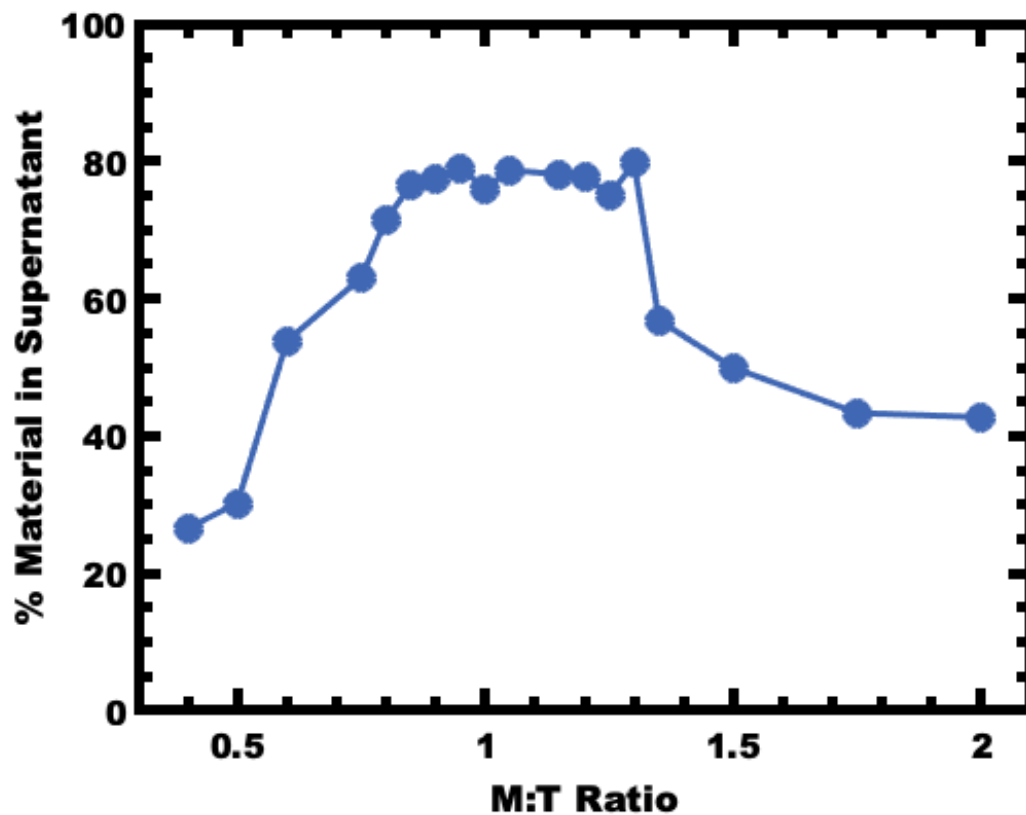


*Figure A. 8* – Mass analysis identified that the material precursors partitioned between the solvent-rich phase and the precipitated micelle-rich phase. The yield of material precursors to each phase varied with M:T ratio. These data are from the sample series OS1-EtOH.

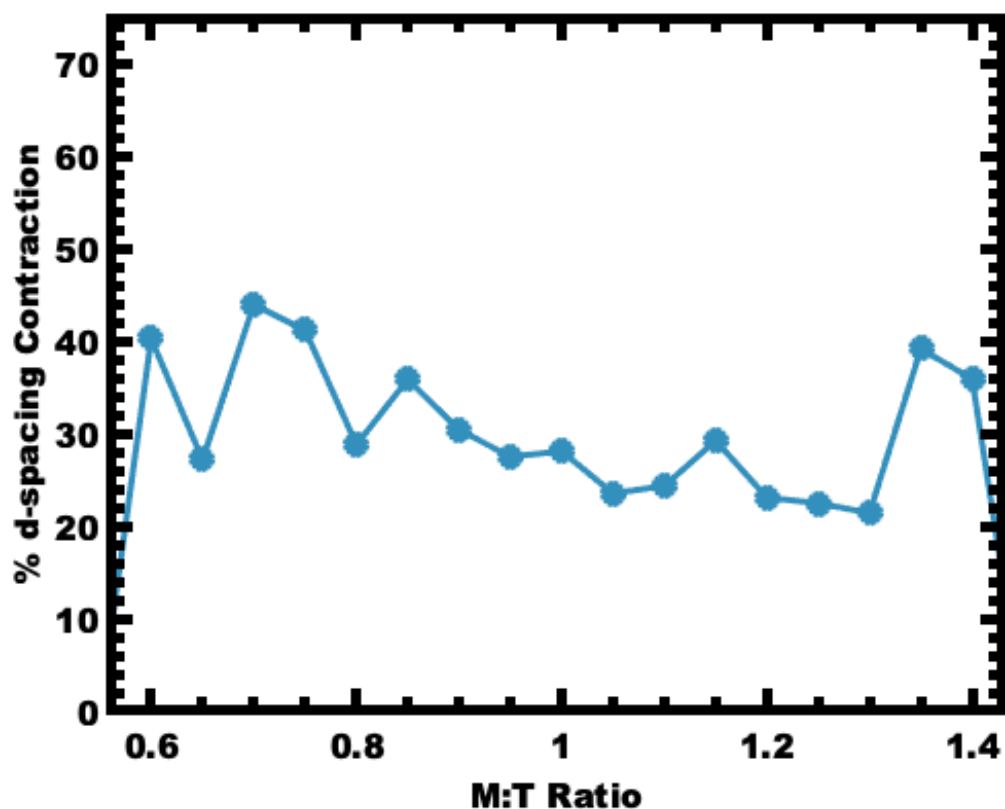


Figure A. 9 – Relevant  $d$ -spacing contraction for carbonized samples as compared to the as-made samples from the series OS1-EtOH.

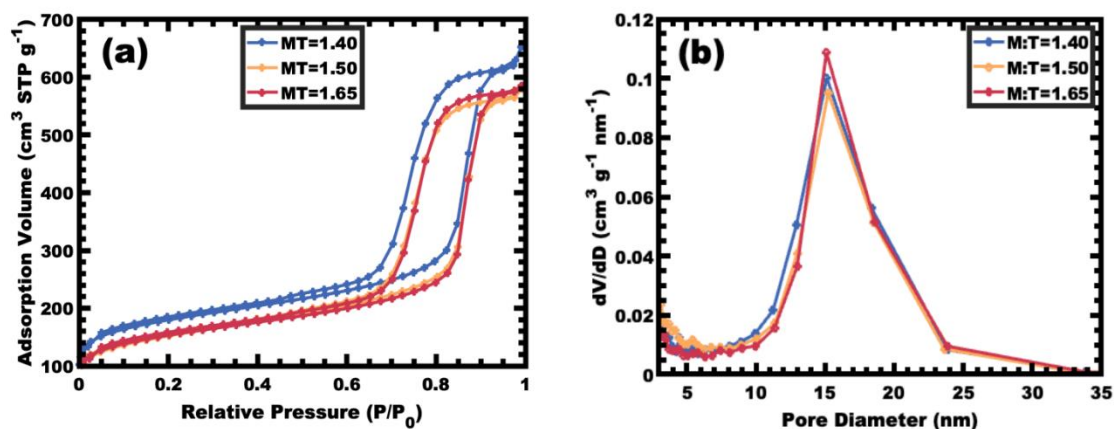
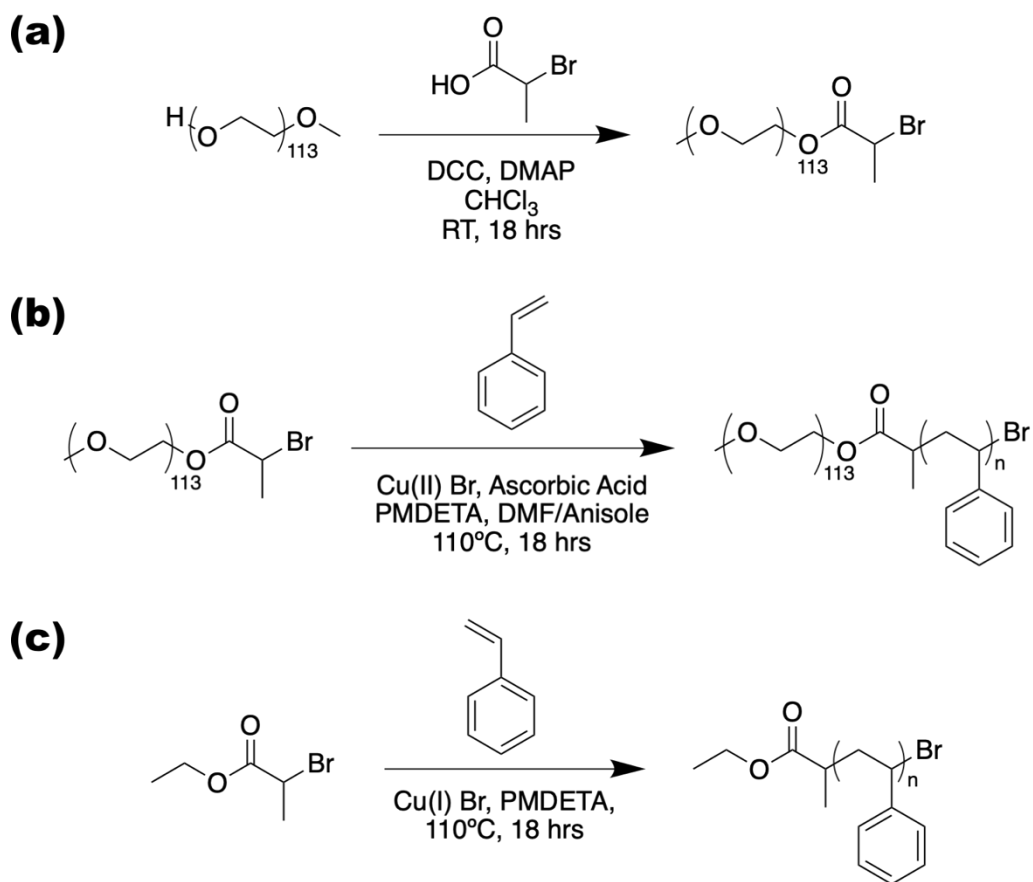


Figure A. 10 – Nitrogen physisorption isotherms for samples of the series OS1-EtOH which fell outside the fitted window (a) along with the associated BJH pore diameter analysis from the adsorption branch of the isotherm (b).

Table A. 2 – Polydispersity index (PDI) values for DLS data from intensity weighted distributions.

<b>Sample</b>	<b>Average PDI</b>
OS1 in THF	0.273
OS1 in THF-H <sub>2</sub> O	0.398
OS1 in THF-H <sub>2</sub> O-EtOH	0.499
OS1 in EtOH	0.824

## APPENDIX B: CHAPTER 3 SUPPORTING INFORMATION



*Figure B. 1* – Reaction schemes for the Steglich esterification of the (5k)PEO-OH to yield a macroinitiator for ATRP (a), followed by the synthesis of the PEO-*b*-PS (**OS**) diblock by AGET-ATRP (b). Homopolymerization of polystyrene (**hPS**) was carried out via normal ATRP (c).

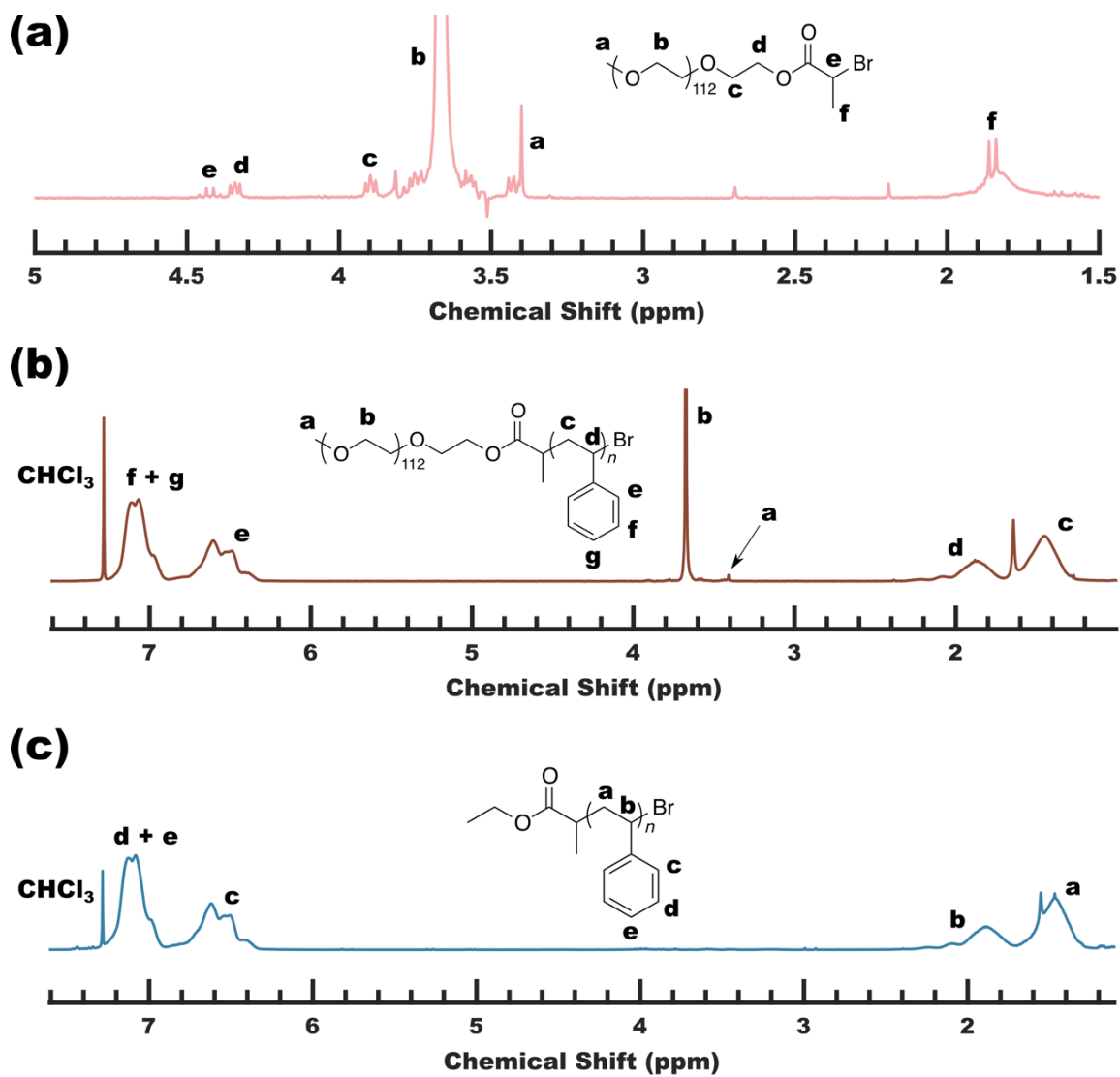


Figure B. 2 –  $^1\text{H}$ -NMR spectra of the (5k)PEO-Br macroinitiator (a), OS diblock polymer (b), and the hPS homopolymer (c). All measurements were performed in  $\text{CDCl}_3$ .

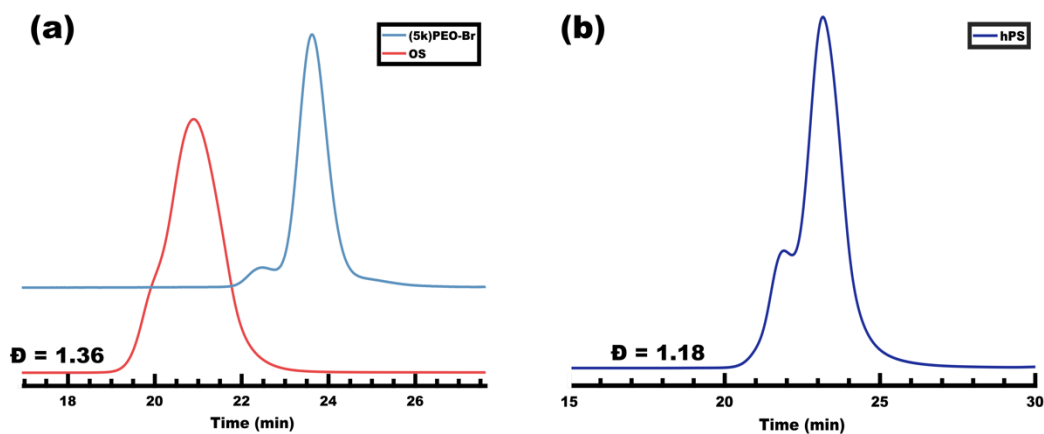


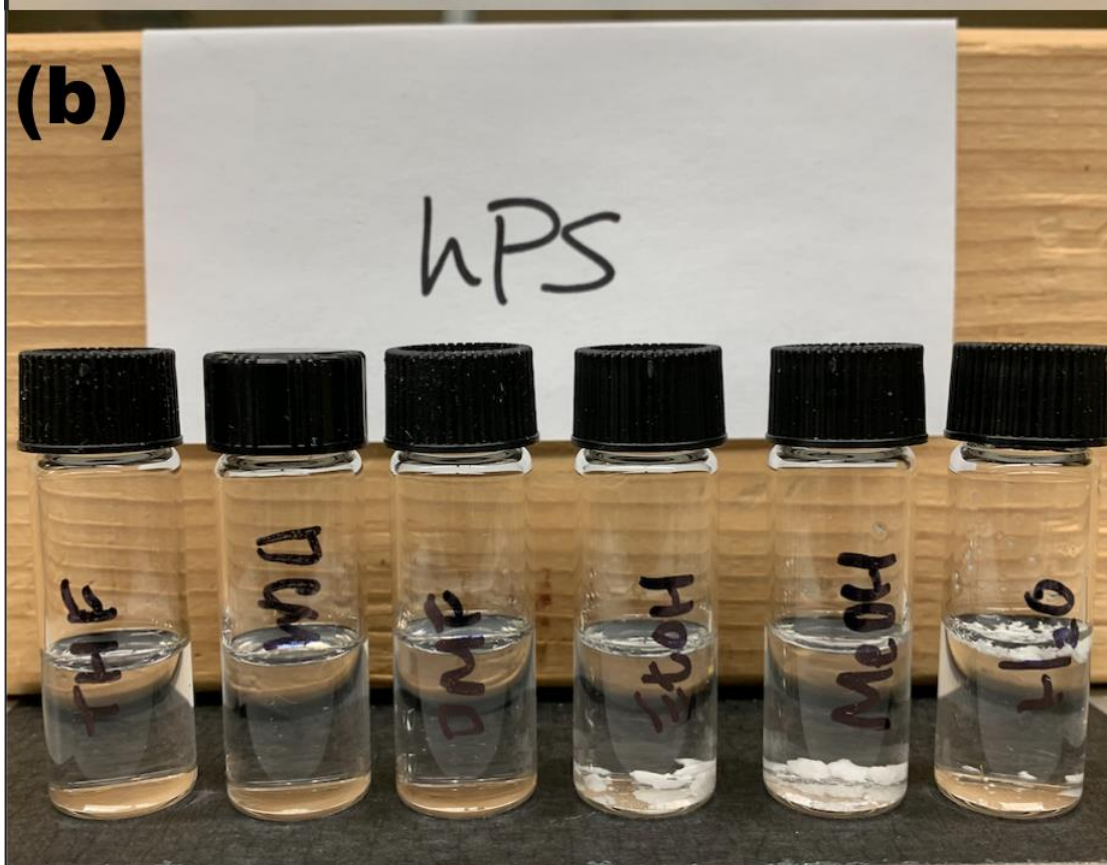
Figure B. 3 – GPC elugrams of the **OS** diblock polymer compared with the (5k)PEO-Br macroinitiator (a) and the **hPS** homopolymer (b).

Table B. 1 – Molecular characteristics of the **OS** diblock and **hPS** homopolymer.

Sample	$M_n$ of PEO ( $\text{g mol}^{-1}$ )	$M_n$ of PS ( $\text{g mol}^{-1}$ )	$\bar{D}$
<b>OS</b>	5,000	40,091 <sup>a</sup>	1.36 <sup>b</sup>
<b>hPS</b>	N/A	9,998 <sup>b</sup>	1.18 <sup>b</sup>

<sup>a</sup>Determined by <sup>1</sup>H-NMR analysis.

<sup>b</sup>Determined by GPC analysis.



*Figure B. 4* – Solubility characteristics of the **OS** (a) and **hPS** (b) polymers in a range of solvents. From left to right: THF, DCM, DMF, EtOH, MeOH, and H<sub>2</sub>O. Note the direct dispersibility of both the **OS** and **hPS** polymers in PS solvents such as THF, DCM, and DMF while both polymers are completely insoluble in PS non-solvents such as EtOH, MeOH, and H<sub>2</sub>O. Samples were prepared at a concentration of 10 mg mL<sup>-1</sup> in their respective solvents.

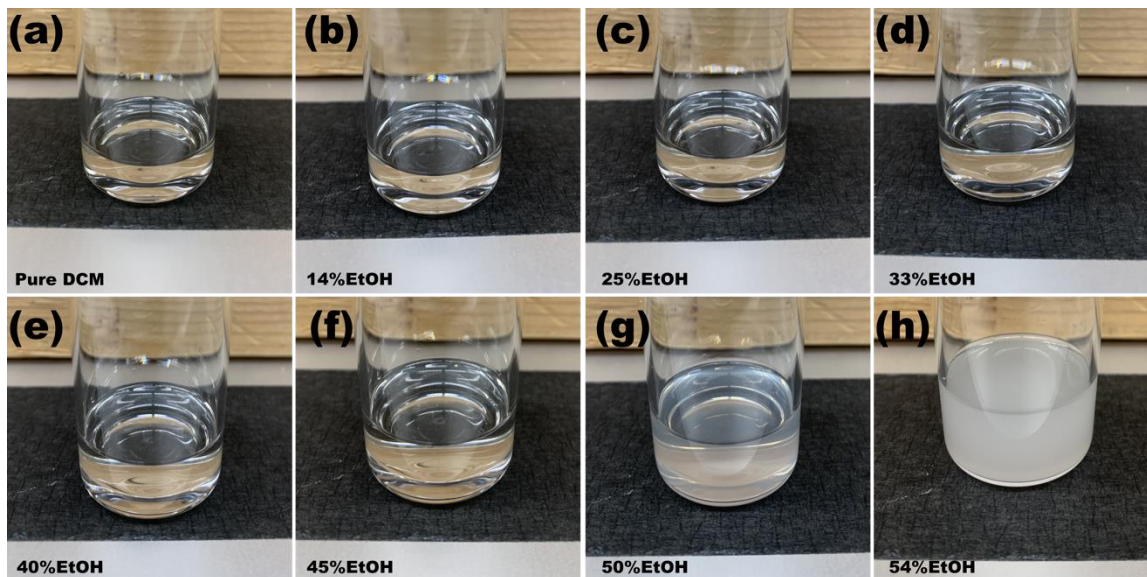


*Figure B. 5* – Solubility characteristics of the **hPS** homopolymer at a concentration of 2 mg mL<sup>-1</sup> in DCM following additions of EtOH (as vol%). The insolubility of the **hPS** becomes visually apparent around 50 vol% EtOH.

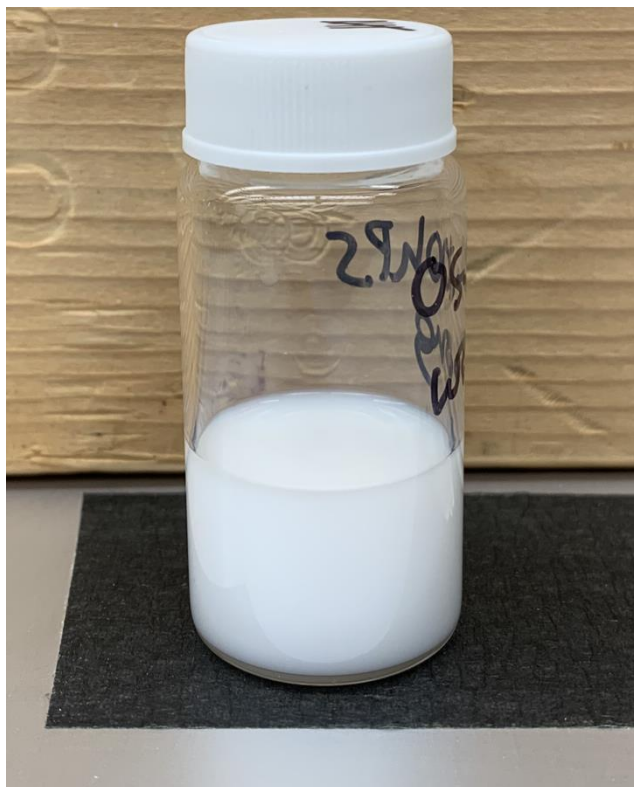


*Figure B. 6* – Direct addition of EtOH to an **OS/hPS** solution in DCM results in large-scale precipitation of the homopolymer rather than the intended incorporation into the **OS** diblock.

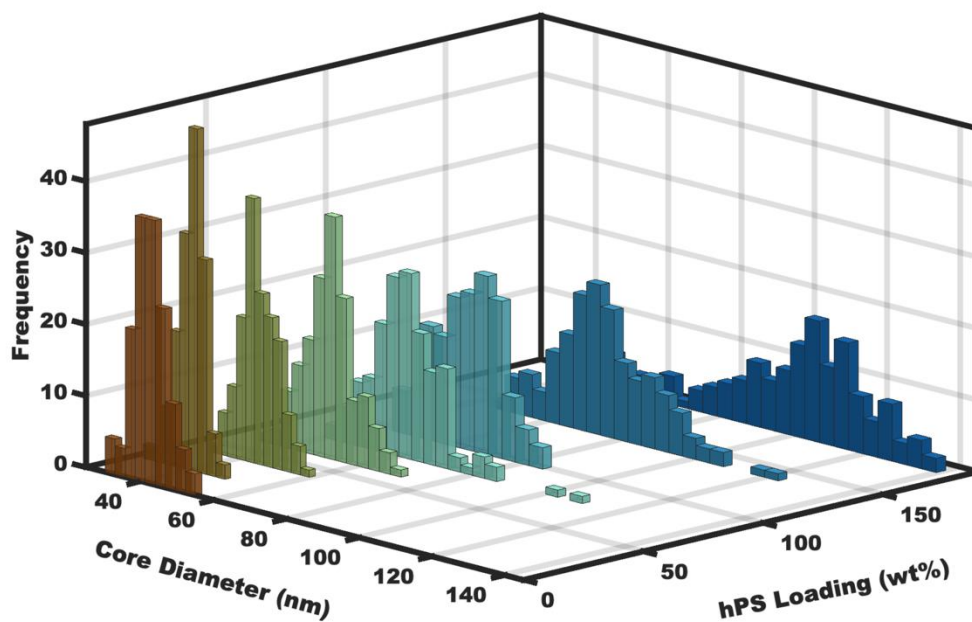


Figure B. 7 – Micelle diameter distributions from TEM data plotted as a function of homopolymer loading. The size distributions were determined from hundreds of measurements upon TEM images.

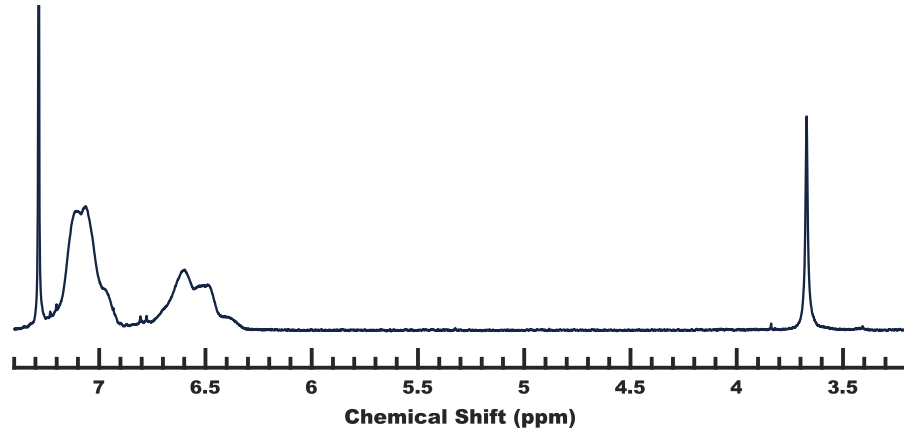


Figure B. 8 – <sup>1</sup>H-NMR analysis of the **hPS-OS** precipitants resulting from **hPS** additions to **OS** solutions that were not sufficiently selective (i.e., 50 and 58 vol% EtOH). The –OCH<sub>2</sub>CH<sub>2</sub>– signal of the (5k)PEO is apparent at δ ~3.66 ppm while the aromatic styrene –C<sub>6</sub>H<sub>5</sub> signal ranges from δ ~6.30–7.26 ppm. The solvent used was CDCl<sub>3</sub>.

#### Derivation of the variable $N_{agg}$ swelling model:

The derivation of the aggregation number for swollen micelles is based upon three simple volume expressions corresponding to an average individual micelle.

$$V_{core} = V_{HP} + V_S \quad (\text{Eq. B1})$$

$$V_{core} = \frac{4}{3} \pi \left( \frac{d_{core}}{2} \right)^3 \quad (\text{Eq. B2})$$

$$V_{HP} = \xi V_{BCP} N_{agg} \quad (\text{Eq. B3})$$

$$V_S = V_{BCP} \phi_S N_{agg} \quad (\text{Eq. B4})$$

For B1,  $V_{core}$  refers to the total volume of the micelle core  $V_{HP}$  and  $V_S$  refer to the micelle volume occupied by the homopolymer and the core block of the block polymer. For B2,  $d_{core}$  is the diameter of the micelle core. For B3,  $\xi$  is the homopolymer loading as a mass percent with respect to the mass of the **OS** diblock polymer,  $V_{BCP}$  is the volume of a single block polymer molecule, and  $N_{agg}$  is the number of block polymer chains within a micelle. For B4, furthermore,  $\phi_S$  is the PS core-content of the **OS** diblock polymer. The densities of the block polymer and the homopolymer are assumed to be approximately equivalent ( $\rho_{BCP} \approx \rho_{HP}$ ).

When equations B2-B4 are substituted into B1 and solved for  $N_{agg}$ , the following expression is obtained:

$$N_{agg} = \frac{\pi d_{core}^3}{6V_{BCP}(\phi_S + \xi)} \quad (\text{Eq. B5})$$

For the **OS** used in this study,  $V_{BCP}$  was estimated to be 79.24 nm<sup>3</sup>.

The interfacial chain density was calculated simply as the number of chains per unit of interfacial area (nm<sup>2</sup>).

$$\rho = \frac{N_{agg}}{4\pi\left(\frac{d_{core}}{2}\right)^2} = \frac{N_{agg}}{\pi d_{core}^2} \quad (\text{Eq. B6})$$

### **Micelle swelling expectations with constant $\rho$ :**

Following the observation that swollen micelles tend towards a constant interfacial chain density, this trend was captured algebraically to yield quantitative expectations for the micelle swelling trajectory.

Solving Equation B6 for  $N_{agg}$  and substituting into Equation B5 yielded:

$$\rho\pi d_{core}^2 = \frac{\pi d_{core}^3}{6V_{BCP}(\phi_S + \xi)} \quad (\text{Eq B7})$$

Solving this expression for  $d_{core}$  yields a linear swollen micelle size trajectory as a function of **hPS** loading:

$$d_{core} = 6V_{BCP}\rho(\phi_S + \xi) \quad (\text{Eq B8})$$

Furthermore, solving Eq B6 for  $d_{core}$  and substituting into Equation B5 yielded:

$$N_{agg} = \frac{\pi}{6V_{BCP}(\phi_S + \xi)} \left( \frac{N_{agg}}{\pi\rho} \right)^{\frac{3}{2}} \quad (\text{Eq B9})$$

Solving this expression for  $N_{agg}$  yields a parabolic  $N_{agg}$  trajectory as a function of **hPS** loading:

$$N_{agg} = 36\pi V_{BCP}^2 (\phi_S + \xi)^2 \rho^3 \quad (\text{Eq B10})$$

## APPENDIX C: CHAPTER 4 SUPPORTING INFORMATION

Table C. 1 – Citations for Scheme 4.1 including the  $\chi N$  values used and the relevant citation. Here, the relevant  $\chi$  value is  $\chi_{\text{core-solvent}}$ .

$N$	$\chi N$	Symbol	Border Color	Citation
11	321	Star	Blue	This Work
8	233	Square	Blue	This Work
63	403	Circle	Blue	<i>Langmuir</i> <b>2018</b> , 34, 5738 – 5749
63	676	Circle	Blue	<i>Langmuir</i> <b>2018</b> , 34, 5738 – 5749
80	849	Circle	Blue	<i>Small</i> <b>2019</b> , 15, 1900393
96	614	Circle	Blue	<i>Soft Mater</i> <b>2019</b> , 15, 5193 – 5203
278	142	Circle	Blue	<i>Chem. Mater.</i> <b>2016</b> , 28, 1653 – 1667
85	2526	Circle	Blue	<i>Nanoscale</i> <b>2017</b> , 9, 1393 – 1397
73	255	Circle	Blue	<i>Macromolecules</i> <b>2003</b> , 36, 953 – 955
250	35	Diamond	Black	<i>Macromolecules</i> <b>2011</b> , 44, 3594 – 3604
400	56	Diamond	Black	<i>Macromolecules</i> <b>2011</b> , 44, 3594 – 3604
250	18	Diamond	Black	<i>ACS Macro Lett.</i> <b>2012</b> , 1, 982 – 985
400	28	Diamond	Black	<i>ACS Macro Lett.</i> <b>2012</b> , 1, 982 – 985
169	123	Diamond	Black	<i>Macromolecules</i> <b>2016</b> , 49, 9542 – 9552
169	112	Diamond	Black	<i>Macromolecules</i> <b>2016</b> , 49, 9542 – 9552
169	101	Diamond	Black	<i>Macromolecules</i> <b>2016</b> , 49, 9542 – 9552
169	90	Diamond	Black	<i>Macromolecules</i> <b>2016</b> , 49, 9542 – 9552
246	162	Diamond	Black	<i>Macromolecules</i> <b>2016</b> , 49, 9542 – 9552
246	148	Diamond	Black	<i>Macromolecules</i> <b>2016</b> , 49, 9542 – 9552
246	130	Diamond	Black	<i>Macromolecules</i> <b>2016</b> , 49, 9542 – 9552
373	198	Diamond	Black	<i>Macromolecules</i> <b>2016</b> , 49, 9542 – 9552
269	38	Diamond	Black	<i>Macromolecules</i> <b>2018</b> , 51, 3563 – 3571
250	35	Diamond	Black	<i>Macromolecules</i> <b>2018</b> , 51, 3563 – 3571
403	141	Diamond	Black	<i>Macromolecules</i> <b>2020</b> , 53, 417 – 426
403	131	Diamond	Black	<i>Macromolecules</i> <b>2020</b> , 53, 417 – 426
90	99	Diamond	Blue	<i>Macromolecules</i> <b>2021</b> , 54, 4738 – 4746
59	207	Circle	Blue	<i>Nat. Commun.</i> <b>2013</b> , 5, 3599 – 3609
9*	64	Diamond	Blue	<i>Soft Matter</i> <b>2012</b> , 8, 623 – 626
12*	179	Diamond	Blue	<i>Soft Matter</i> <b>2012</b> , 8, 623 – 626
15* <sup>†</sup>	232	Diamond	Blue	<i>Soft Matter</i> <b>2012</b> , 8, 623 – 626

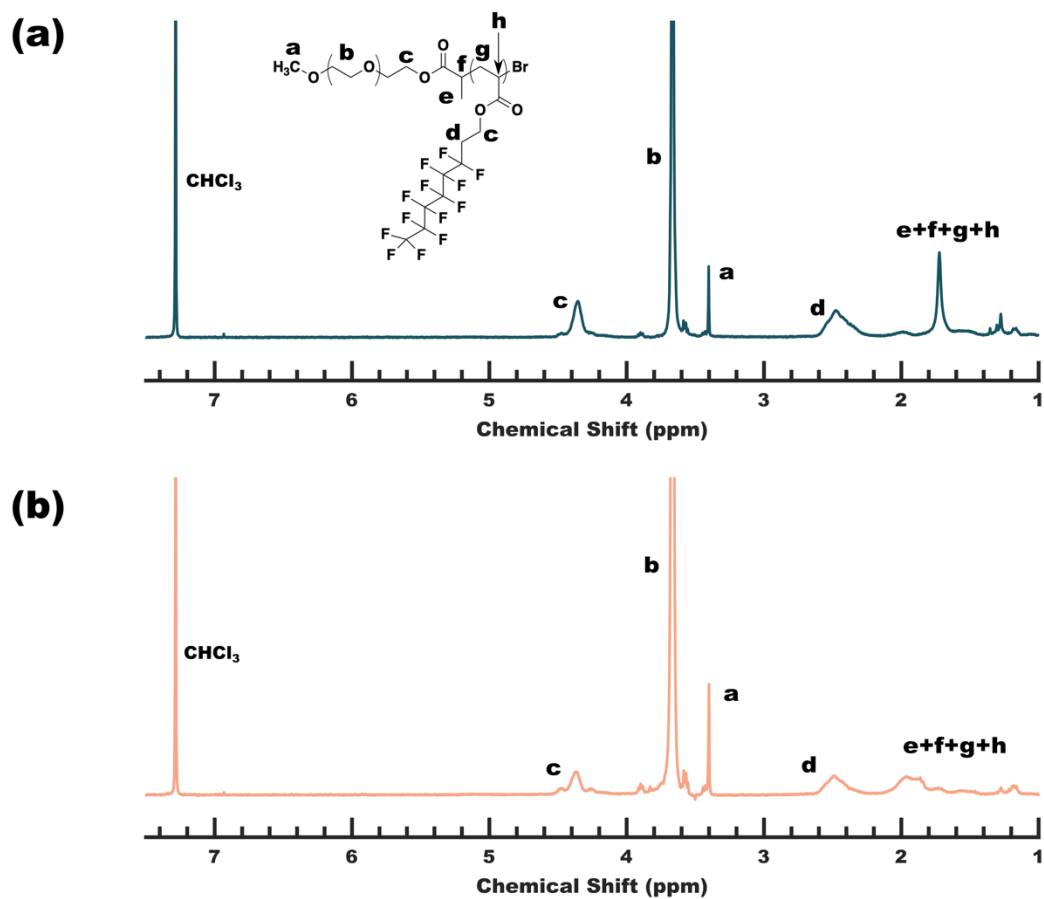


Figure C. 1 –  $^1\text{H}$ -NMR patterns for the polymers  $\text{O}_{45}\text{F}_{11}$  (a) and  $\text{O}_{45}\text{F}_8$  (b) in  $\text{CDCl}_3$ .

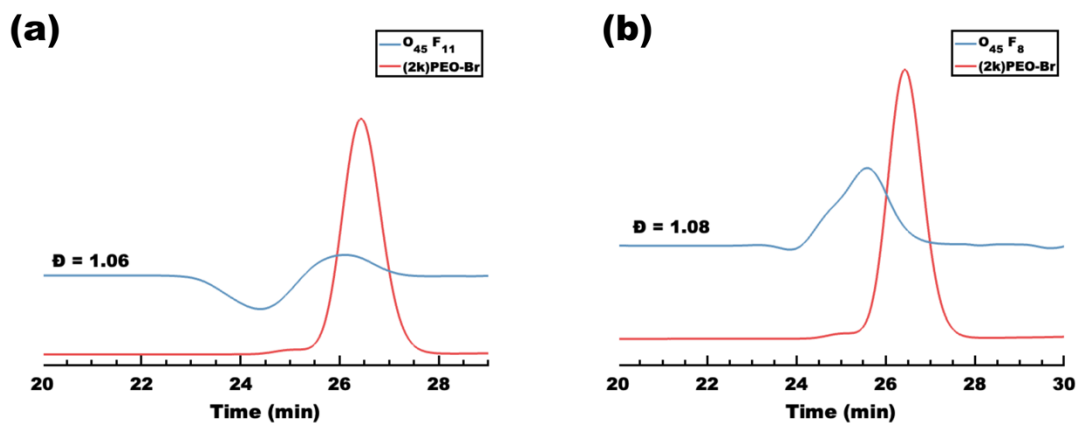


Figure C. 2 – GPC elugrams corresponding to the synthesis of  $\text{O}_{45}\text{F}_{11}$  (a) and  $\text{O}_{45}\text{F}_8$  (b).

Table C. 2 – ATRP molar ratios for the synthesis of O<sub>45</sub>F<sub>11</sub> and O<sub>45</sub>F<sub>8</sub>.

	O <sub>45</sub> F <sub>11</sub>	O <sub>45</sub> F <sub>8</sub>
(2k)PEO-Br	1.00	1.00
Me <sub>6</sub> TREN	0.5	0.5
Cu(I)Br	0.5	0.5
FOA	12.0	9.0
Toluene (%)	72.9	77.6
Temperature (°C)	90	90
Time (hrs)	42	26

Table C. 3 – Characteristics of the O<sub>45</sub>F<sub>11</sub> and O<sub>45</sub>F<sub>8</sub> polymers.

Sample:	$M_n$ , PEO (g mol <sup>-1</sup> )	$M_n$ , PFOA (g mol <sup>-1</sup> ) <sup>a</sup>	$\bar{D}^b$
O <sub>45</sub> F <sub>11</sub>	2,000	4,600	1.06
O <sub>45</sub> F <sub>8</sub>	2,000	3,300	1.08

<sup>a</sup>Determined from <sup>1</sup>H-NMR. <sup>d</sup>Determined from GPC.

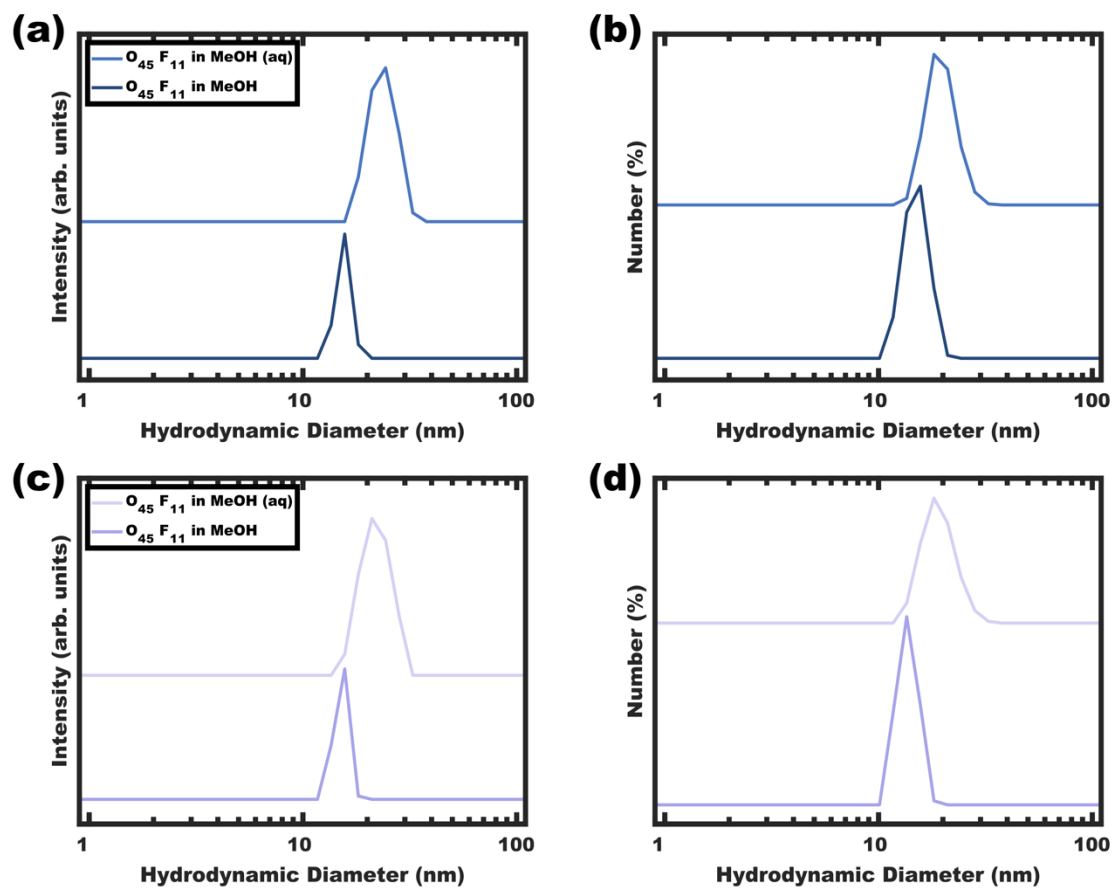


Figure C. 3 – DLS of the O<sub>45</sub>F<sub>11</sub> polymer before and after the addition of HCl either through a fast (a,b) or slow (c, d) addition rate.

*Table C. 4* – DLS hydrodynamic diameters of O<sub>45</sub>F<sub>11</sub> micelles as a function of HCl addition rate.

<b>Sample</b>	<b>Diameter in MeOH (nm)</b>	<b>Diameter in MeOH (aq) (nm)</b>
O <sub>45</sub> F <sub>11</sub> Fast Addition	15.5 ± 0.2	23.9 ± 0.7
O <sub>45</sub> F <sub>11</sub> Slow Addition	15.1 ± 0.1	22.3 ± 0.7

*Table C. 5* – DLS size metrics for Intensity and Number plots for the O<sub>45</sub>F<sub>11</sub> polymer in MeOH (aq).

<b>Run</b>	<b>Major Intensity (nm)</b>	<b>Number Value (nm)</b>
1	21.3 ± 0.2	19.2 ± 0.1
2	22.3 ± 0.1	21.5 ± 0.1
3	24.2 ± 0.1	21.7 ± 0.2
4	26.8 ± 0.2	20.9 ± 0.1
5	25.6 ± 0.2	21.6 ± 0.1
6	24.7 ± 0.1	23.0 ± 0.1
<b>Average</b>	<b>24.2 ± 0.2</b>	<b>21.3 ± 0.1</b>

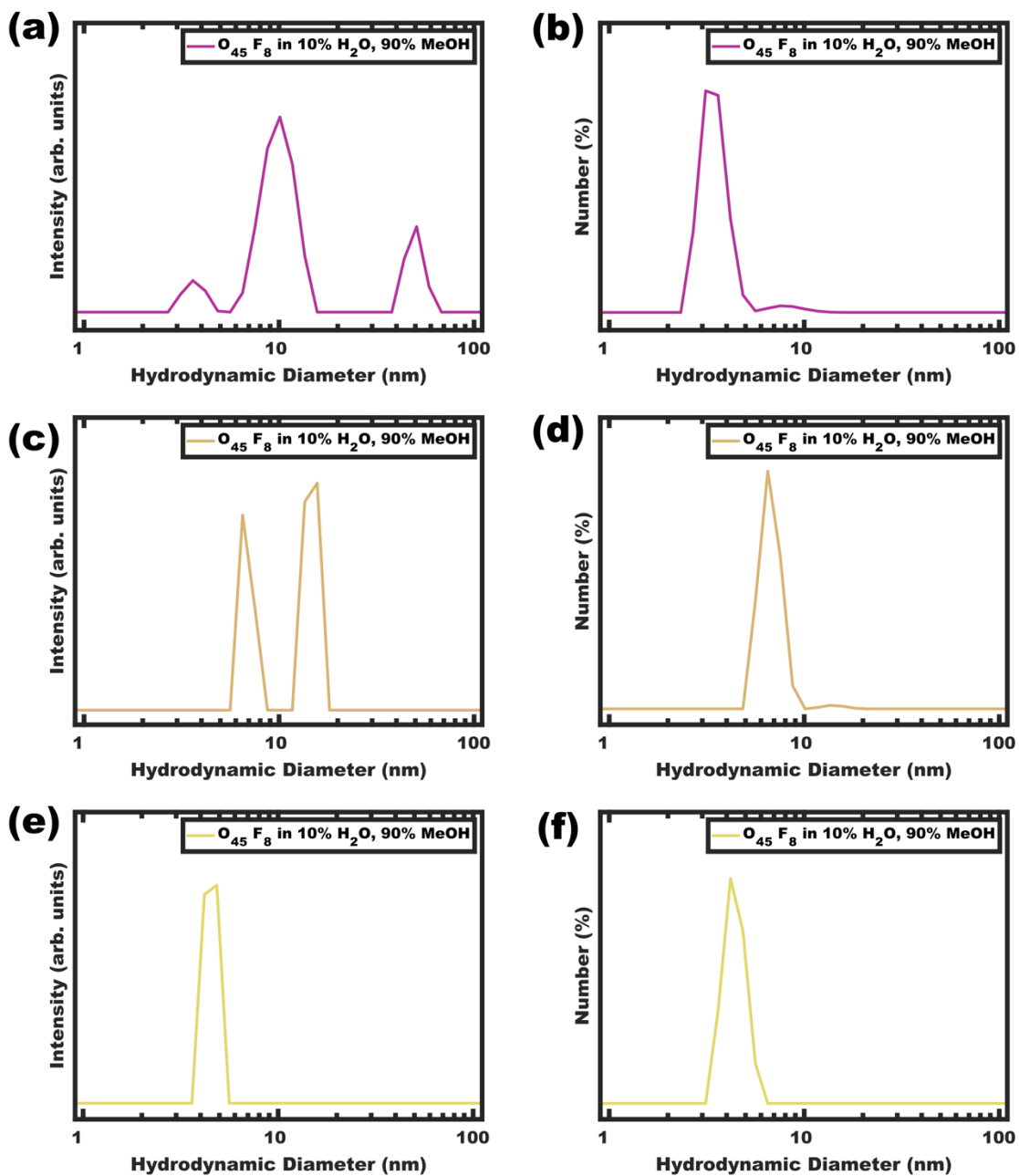


Figure C. 4 – Repeated DLS intensity (a, c, e) and number (b, d, f) distributions for  $O_{45}F_8$  micelles in 10 vol%  $H_2O$ , 90 vol% MeOH.

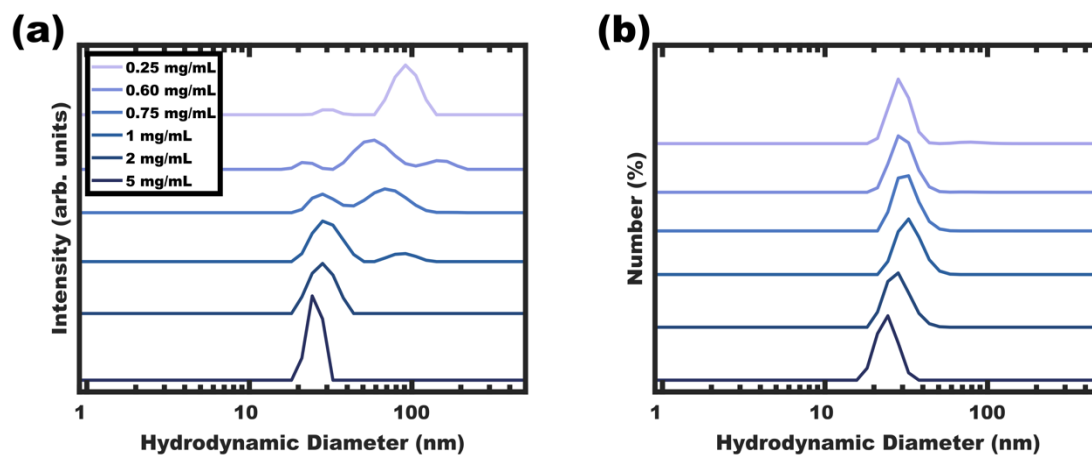


Figure C. 5 – DLS of the O<sub>45</sub>F<sub>11</sub> polymer at various concentrations in MeOH (aq).

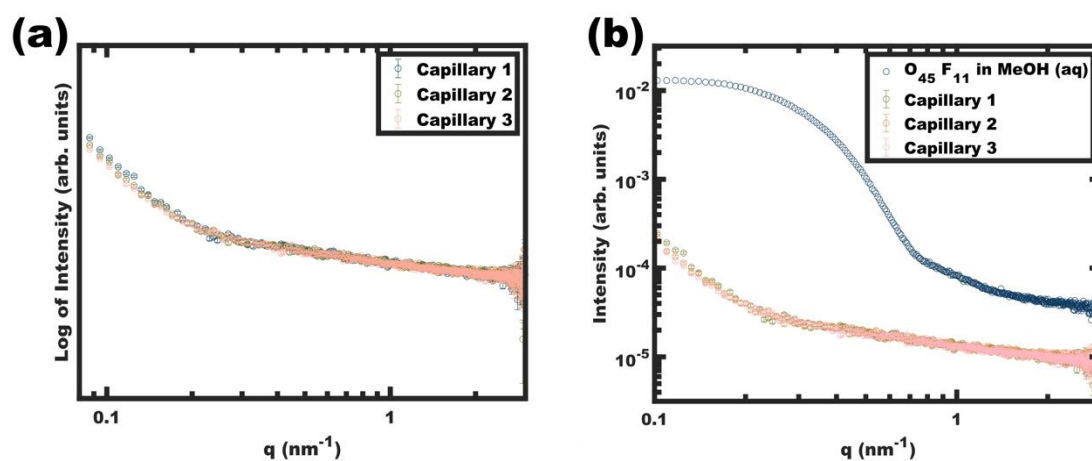
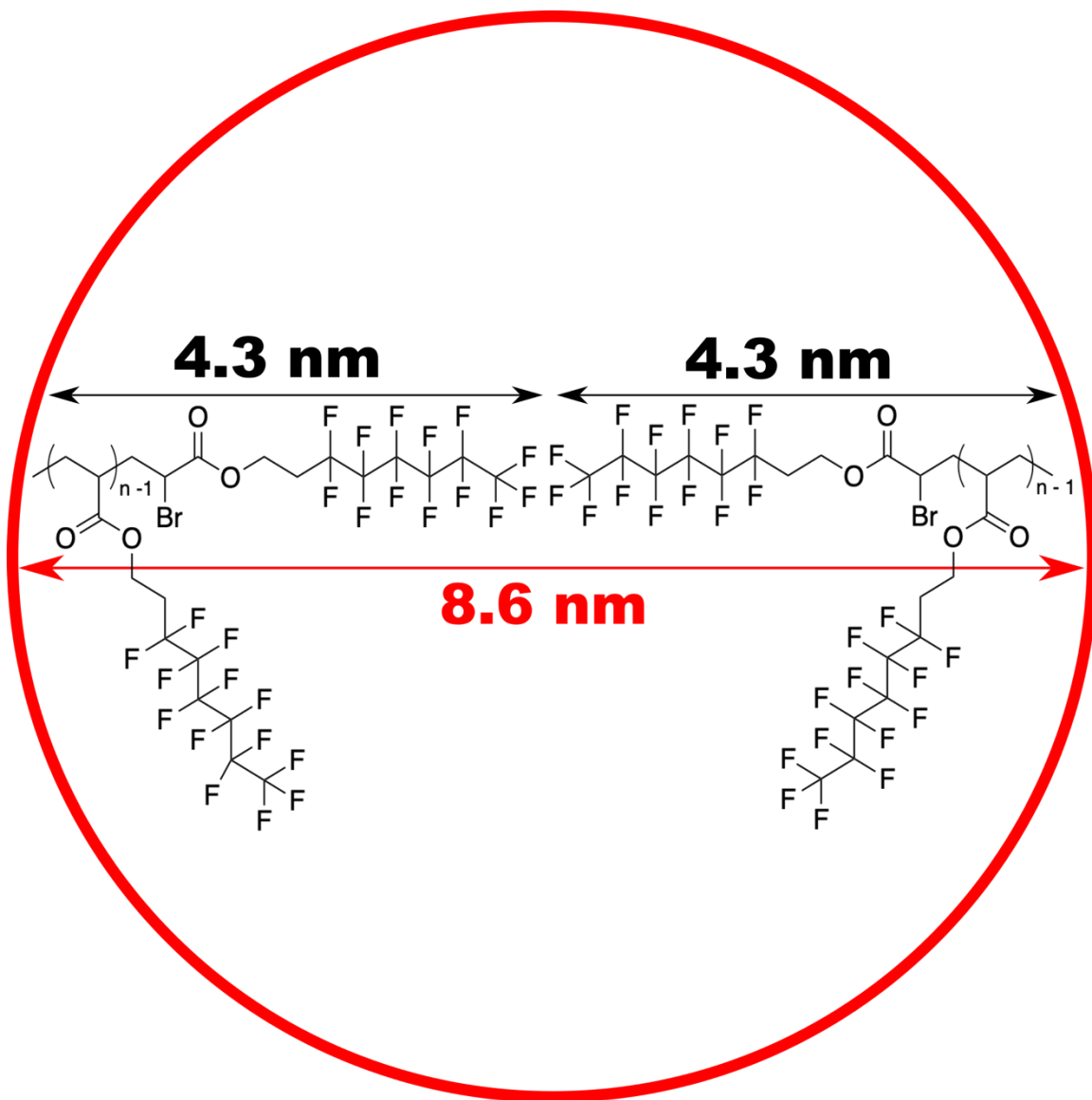


Figure C. 6 – SAXS of multiple empty glass capillaries showing a consistent background signal (a) that is several orders of magnitude weaker than the sample scattering signal (b).



*Figure C. 7* – The maximum micelle core diameter was estimated for the PFOA micelle cores from  $O_{45}F_{11}$ . The contour length for  $F_{11}$  was calculated using the trans conformation. This included the 11 repeat acrylate units along the backbone ( $1.54 \text{ \AA} \cdot \cos(35.3^\circ) \cdot 22 = 27.7 \text{ \AA}$ ). The calculation also included an extended terminal FOA mer unit. The helical conformation of the extended fluoropolymers was previously reported to have  $2.595 \text{ \AA}$  for each  $(-CF_2-CF_2-)$  unit,<sup>1</sup> i.e.,  $\sim 1.30 \text{ \AA}$  per  $(-CF_2-)$  unit. The terminal FOA conformation was approximated using this value ( $11 \cdot 1.30 \text{ \AA} = 14.3 \text{ \AA}$ ). Half of the reported<sup>2</sup>  $1.5 \text{ \AA}$  spacing between neighboring fluorines  $(-F F-)$  was included in the contour length calculation. Thus, the overall contour length was estimated as  $27.7 \text{ \AA} + 14.3 \text{ \AA} + 1.5 \text{ \AA} / 2 = 42.75 \text{ \AA}$ .

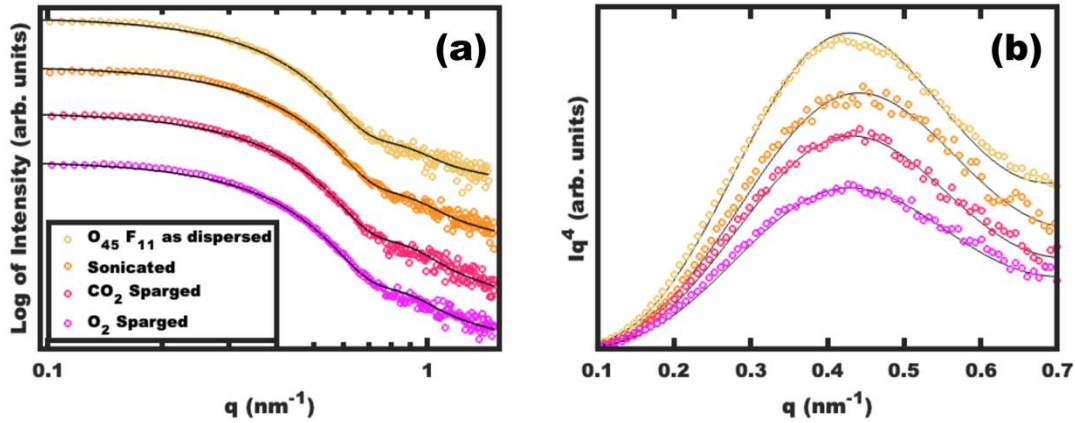


Figure C. 8 – SAXS data for O<sub>45</sub>F<sub>11</sub> micelles plotted in both I vs.  $q$  (a) and  $Iq^4$  vs.  $q$  (b) coordinate spaces. The data were obtained from a 20 mg mL<sup>-1</sup> O<sub>45</sub>F<sub>11</sub> solution in MeOH. The data were background subtracted from a MeOH capillary blank and are offset vertically for visual clarity.

Table C. 6 – The best-fit values for SAXS measurements on 10 mg mL<sup>-1</sup> solutions of O<sub>45</sub>F<sub>11</sub> micelles in MeOH as a function of different treatments.

Treatment	Diameter by SAXS Fitting (nm) <sup>1</sup>
As-dispersed	10.90 ± 0.02
Freeze-pump thaw	10.36 ± 0.01
Sonicated	10.69 ± 0.01
CO <sub>2</sub> Sparged	10.88 ± 0.02
O <sub>2</sub> Sparged	11.10 ± 0.02

<sup>1</sup>Confidence intervals were calculated through minimization of residuals on the basis of the  $\chi^2$  test.

### PMT Model

$$d_{spacing} = \frac{D}{2S} \sqrt[3]{\frac{4\pi}{3\gamma} \left( x\beta + 1 + \frac{f_{corona}}{1-f_{corona}} \right)}^{1/3} \quad (\text{Equation C1})$$

The equation for the micelle core template (MCT) model<sup>3</sup> assumes a constant micelle size across the series. Here,  $D$  represents the micelle diameter,  $\gamma$  accounts for unit cell distortion,  $x$  is the M:T ratio,  $\beta$  is the convolved density term,<sup>3</sup> and  $f_{corona}$  is the volume fraction of the hydrophilic corona-forming block (PEO). Lastly,  $S$  connects the structure factor signal from SAXS to the SEM measured micelle-to-micelle  $d$ -spacing ( $d_{m-m}$ ) using:

$$S = \frac{d_{m-m}}{d_{spacing}} = \frac{q d_{m-m}}{2\pi} \quad (\text{Equation C2})$$

The wall thickness was deconvolved from the micelle-to-micelle spacing using the following expression:

$$w = (\alpha d_{m-m} - D) \quad (\text{Equation C3})$$

where  $w$  is the wall thickness,  $\alpha$  is a fit term that accommodates the variable distribution of wall thicknesses for different orientations, and  $D$  is the template/pore diameter. For a cubic crystal system, values of  $\alpha$  are expected to range from 0.87–2.45 when using an inscribed circle to measure wall thickness.<sup>4</sup>

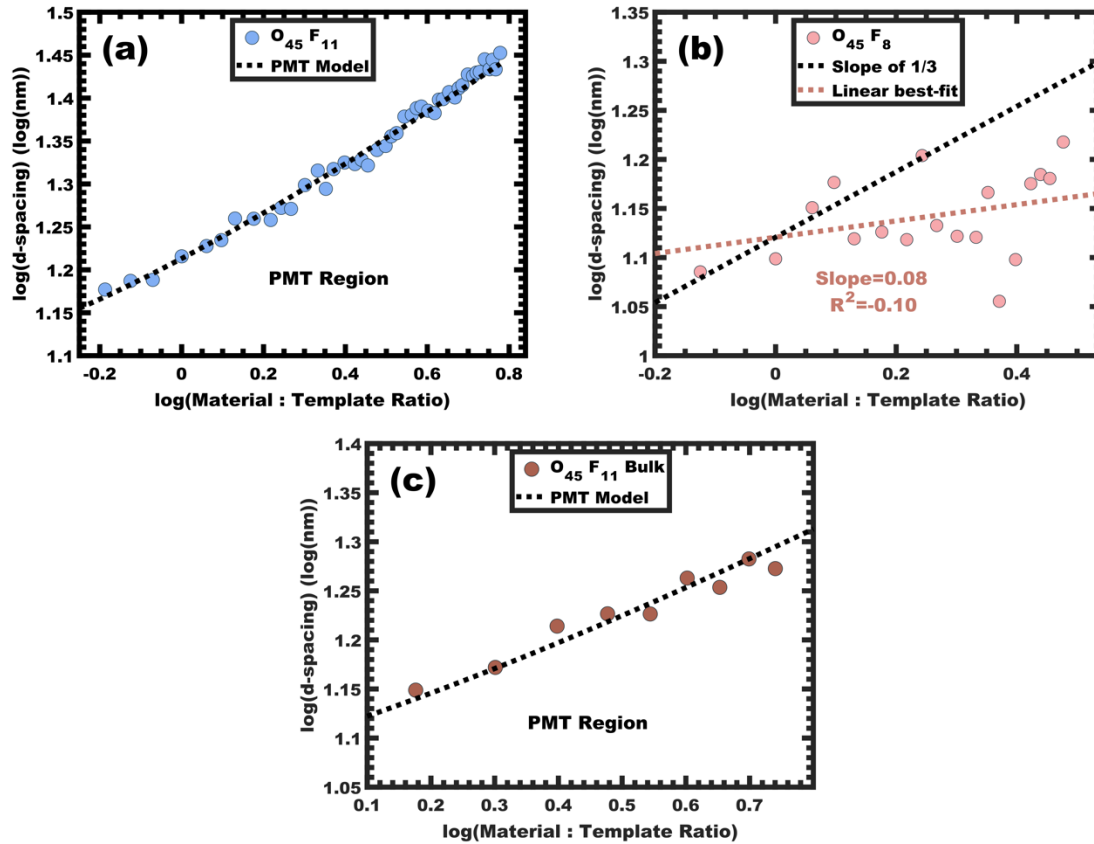


Figure C. 9 – Thin film SAXS data from  $O_{45}F_{11}$  (a),  $O_{45}F_8$  (b), and bulk  $O_{45}F_{11}$  (c) samples plotted as  $d$ -spacing vs M:T ratio in a log–log coordinate space to assess consistency with PMT trends.

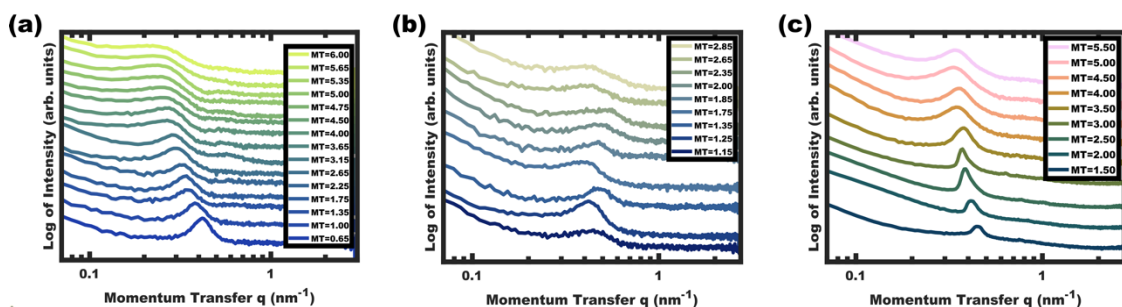


Figure C. 10 – Log-log SAXS plots for the  $O_{45}F_{11}$  thin film (a),  $O_{45}F_8$  thin film (b), and  $O_{45}F_{11}$  bulk (c) samples.

Table C. 7 – SAXS  $d$ -spacing and SEM pore diameter values from the  $O_{45}F_{11}$  thin film series. The pore size and wall thickness are reported as the average  $\pm$  the standard-error-of-the-mean.

M:T Ratio	SAXS $d$ -spacing (nm)	SEM Pore Diameter (nm)	SEM Wall Thickness (nm)
1.00	16.43	$11.59 \pm 0.79$	$4.58 \pm 0.27$
1.50	18.17	$11.64 \pm 0.70$	$5.37 \pm 0.37$
2.00	19.82	$11.27 \pm 0.81$	$6.37 \pm 0.43$
2.50	21.13	$11.99 \pm 0.82$	$7.71 \pm 0.56$
3.00	21.85	$11.90 \pm 0.84$	$7.24 \pm 0.55$
3.50	23.90	$11.39 \pm 0.85$	$8.34 \pm 0.61$
4.00	24.28	$11.89 \pm 0.81$	$9.21 \pm 0.70$
4.50	25.52	$11.63 \pm 0.83$	$10.58 \pm 0.76$
5.00	26.75	$11.83 \pm 0.82$	$10.51 \pm 0.74$
5.50	27.89	$11.62 \pm 0.76$	$11.06 \pm 0.76$
6.00	28.35	$11.75 \pm 0.86$	$12.40 \pm 1.00$

Table C. 8 – Table of PMT fit parameters for the  $O_{45}F_{11}$  thin film and bulk cast series.

	$O_{45}F_{11}$ Thin Films:	$O_{45}F_{11}$ Bulk Casts:
$\alpha^a$	0.88	0.98
$\beta^a$	3.97	2.17
$\gamma$	1.00	1.00
$f_{PEO}^b$	0.38	0.38
$S$	1.00	1.00
Template/Pore Diameter <sup>c</sup>	$11.68 \text{ nm}^d$	10.36 nm

<sup>a</sup>Determined from least squares fitting analysis within the PMT window.

<sup>b</sup>Determined from  $^1\text{H-NMR}$  analysis of the polymer.

<sup>c</sup>Determined from SEM pore size measurements within the PMT window.

<sup>d</sup>The in-plane pore dimension to be used for modelling.

Table C. 9 – SAXS  $d$ -spacing, SEM pore size and wall thickness data from the O<sub>45</sub>F<sub>11</sub> bulk cast series. The pore size and wall thickness data are reported as the average  $\pm$  the standard error-of-the-mean.

M:T Ratio	SAXS $d$ -spacing (nm)	SEM Pore Diameter (nm)	SEM Wall Thickness (nm)
1.50	14.09	10.89 $\pm$ 0.70	4.18 $\pm$ 0.34
2.00	14.86	10.06 $\pm$ 0.68	4.62 $\pm$ 0.42
3.00	16.37	10.03 $\pm$ 0.67	5.48 $\pm$ 0.36
3.50	16.85	10.88 $\pm$ 0.79	6.10 $\pm$ 0.47
4.00	18.32	9.98 $\pm$ 0.69	7.19 $\pm$ 0.61
5.00	19.17	10.14 $\pm$ 0.79	8.62 $\pm$ 0.71

### **Derivation of the SAXS $d$ -spacing deconvolution model:**

The pore volume from thin films was related to the parent micelles by quantifying evaporative distortions. The initially spherical micelles pack into an arrangement (Fig. C11a). As the material precursors begin to cross-link, the solvent continues to evaporate compressing both the micelle templates and distorting the lattice (Fig. C11b). The micelle compression ( $r_{in}/r_{out}$ ) was assumed to be equal to the lattice compression ( $a_{in}/a_{out}$ ). The Fourier transform of this real-space arrangement yields reciprocal ratios of lattice parameters where  $b_{out}/b_{in} = a_{in}/a_{out}$  (Fig. C11d). The 3D ellipsoidal structural factor in Fourier space has a major radius  $q_{out}$  and a minor radius  $q_{in}$ , corresponding to the out-of-plane and in-plane orientations, respectively. These  $q$  values are proportional to the respective lattice parameters where  $b_{out}/b_{in} = q_{out}/q_{in}$ . When the sample is rotated to  $\theta = 45^\circ$  with respect to the detector, then the corresponding plane of reciprocal space is measured (Fig. C11e). The intersection of this plane with the structure factor is drawn from an edge-on view in Figure C11f where the largest  $q_t$  contains both in-plane and out-of-plane contributions. The purely out-of-plane contributions are next extracted from this information.

The equation for such an ellipsoid is:

$$\frac{y^2}{q_{out}^2} + \frac{x^2}{q_{in}^2} = 1 \quad (\text{Equation C4})$$

The observed ellipsoid on the detector can be related to  $q_{out}$  and  $q_{in}$  by relation to  $q_t$  using an inscribed triangle and Pythagorean's theorem. The (x,y) coordinates of  $q_t$  have  $x = y$  owing to the  $45^\circ$ - $45^\circ$ - $90^\circ$  triangle where also:

$$x^2 + y^2 = q_t^2$$

This simplifies to:

$$x = y = \frac{q_t}{\sqrt{2}}$$

Thus, the  $q_t$  coordinates are  $\left(\frac{q_t}{\sqrt{2}}, \frac{q_t}{\sqrt{2}}\right)$ . Combining this known to point with the directly measured  $q_{in}$  value allows for  $q_{out}$  to be solved for using Equation C4:

$$\frac{\left(\frac{q_t}{\sqrt{2}}\right)^2}{q_{in}^2} + \frac{\left(\frac{q_t}{\sqrt{2}}\right)^2}{q_{out}^2} = 1$$

Simplification of this yields ...

$$q_{out} = \frac{q_t}{\sqrt{2 - \frac{q_t^2}{q_{in}^2}}} \quad (\text{Equation C5})$$

The value of  $q_{out}$  was calculated using data in Table C8, leading to an average ratio of:

$$\frac{q_{out}}{q_{in}} = 0.719$$

This is combined with the above statements of equality to yield:

$$\frac{q_{out}}{q_{in}} = \frac{b_{out}}{b_{in}} = \frac{a_{in}}{a_{out}} = \frac{r_{in}}{r_{out}} = 0.719$$

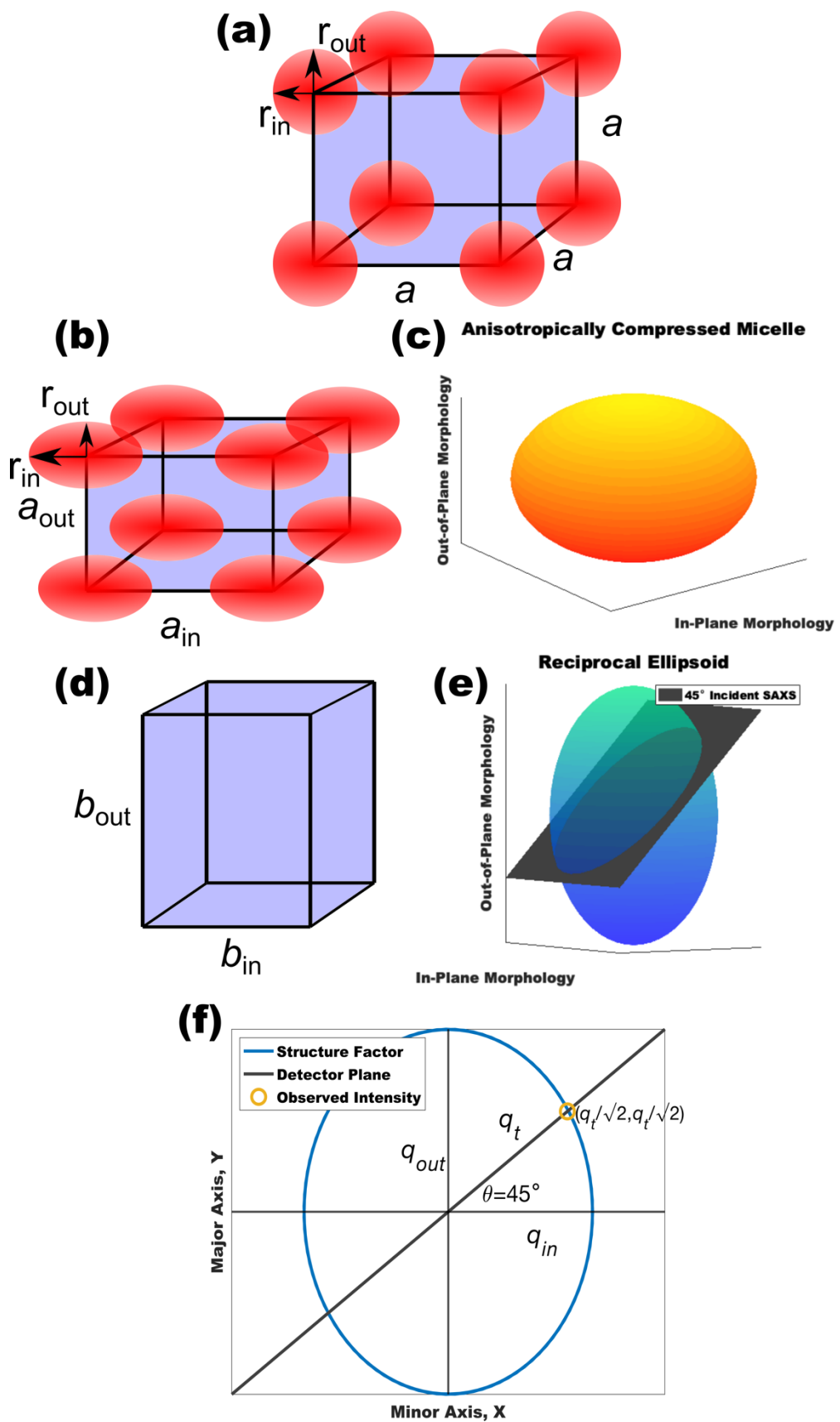


Figure C. 11 – Representation of micelle core (material pore) character throughout the material processing timeline. A non-distorted lattice of micelle cores (red) amongst the material/corona phase (blue) is considered. During the drying process, anisotropic evaporation and substrate adhesion leads to anisotropic compression of both the lattice (b) and the corresponding micelle core (c). The corresponding reciprocal space lattice has inverse anisotropy (d). The first diffraction ring is considered in this 3D Fourier space where the detector is oriented at 45° relative to the sample plane (e) to evaluate geometric considerations of incident X-rays upon such a pore geometry (e). A side-view of the detector plane in 2D is presented to relate the observed  $q$ -value to the sample distortion.

Table C. 10 – Comparison of micelle volume throughout materials processing

	<b>Micelle Core Diameter (nm)</b>	<b>Core Volume (nm<sup>3</sup>)</b>	<b>Aggregation Number<sup>b</sup></b>	<b>Equivalent Undistorted Core Diameter (nm)</b>
O <sub>45</sub> F <sub>11</sub> Micelles in MeOH (aq)	11.24 ± 0.01	743.5 ± 2.0	109 ± 0.2 <sup>c</sup>	11.24 ± 0.01
Porous O <sub>45</sub> F <sub>11</sub> Thin Films	11.68 ± 0.24 <sup>b</sup> and 8.40 ± 0.17 <sup>c</sup>	600 ± 73.9 <sup>d</sup>	N/A	10.46 ± 0.21 <sup>f</sup>
Porous O <sub>45</sub> F <sub>11</sub> Bulk Casts	10.35 ± 0.72 <sup>b</sup>	580.5 ± 121.1	N/A	10.35 ± 0.72

<sup>a</sup>Determined from micelle SAXS form factor fitting.

<sup>b</sup>The pore radius (mean ± standard error-of-the-mean) from analysis of SEM images.

<sup>c</sup>Distortion minor radius estimated by dividing the SEM major radius by the SAXS structure factor compression ratio (average IP-to-OP  $d$ -spacing ratio).

<sup>d</sup>Calculated using the adjusted volume of an ellipsoid expression (Equation C4)

<sup>e</sup>Determined by dividing the core volume by the estimated F<sub>11</sub> chain volume of 5.51 nm<sup>3</sup>.

<sup>f</sup>Calculated as the sphere diameter giving the same volume as the corresponding ellipsoidal core volume.

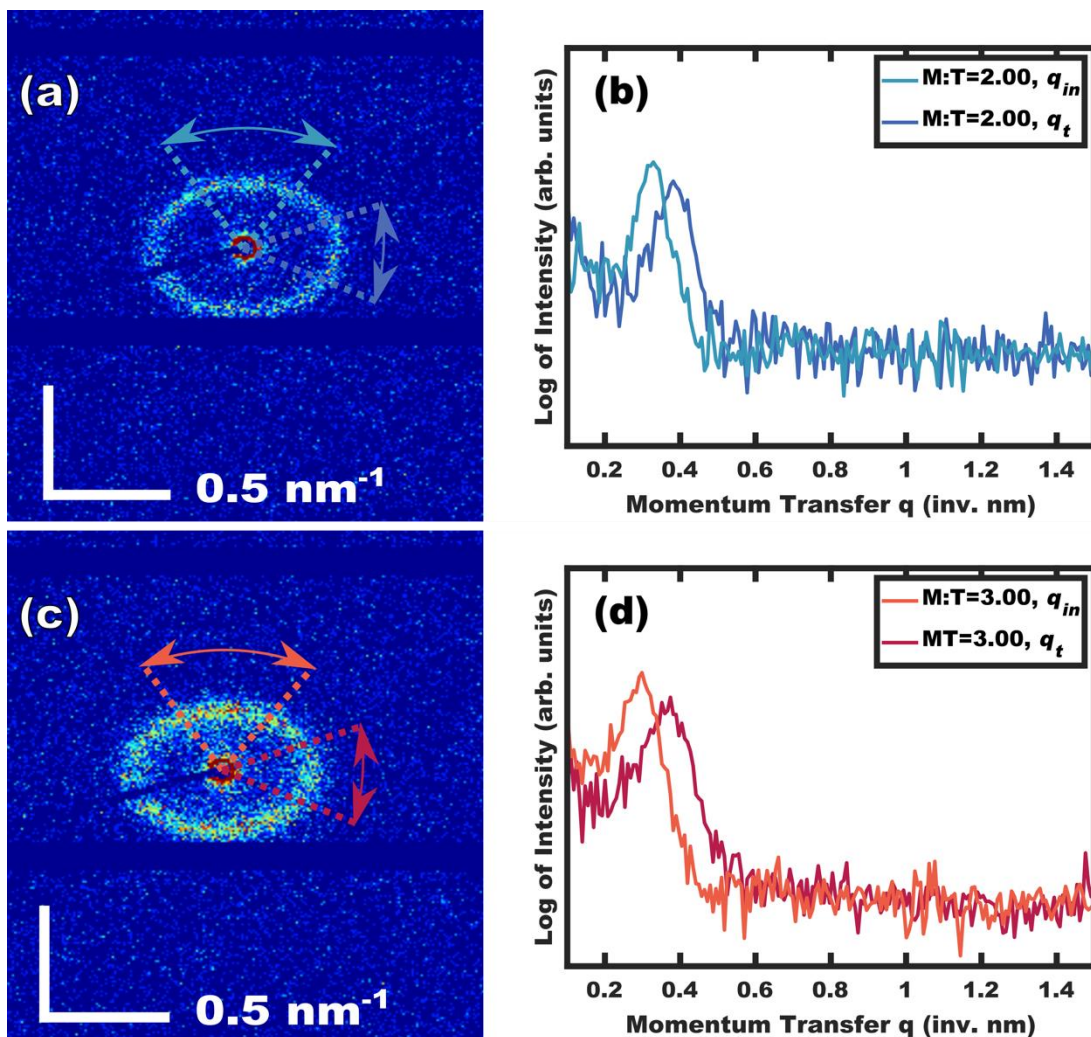


Figure C. 12 – 2D SAXS patterns acquired with the incident beam at  $45^\circ$  relative to the sample plane (a, c). Wedge integrals were calculated along the major and minor directions to measure  $q_t$  and  $q_{in}$  respectively (b, d).

### References:

1. Bunn, C. W.; Howells, E. R. Structures of Molecules and Crystals of Fluorocarbons. *Nature* **1954**, *174*, 549–551.
2. Brockway, L. O. The Internuclear Distance in the Fluorine Molecule. *J. Am. Chem. Soc.* **1938**, *60*, 1348–1349.
3. Sarkar, A.; Stefik, M. How to Make Persistent Micelle Templates in 24 Hours and Know It Using X-Ray Scattering. *J. Mater. Chem. A.* **2017**, *5*, 11840–11853.

4. Lantz, K. A.; Clamp, N. B.; van den Bergh, W.; Sarkar, A.; Stefik, M. Full Gamut Wall Tunability from Persistent Micelle Templates *via Ex-Situ* Hydrolysis. *Small* **2019**, *15*, 1900393.

